DISSERTATION

KETONES IN THE TROPOSPHERE:

STUDIES OF LOSS PROCESSES, EMISSIONS, AND PRODUCTION

Submitted by

Jared F. Brewer

Department of Atmospheric Science

In partial fulfillment of the requirements

For the Degree of Doctor of Philosophy

Colorado State University

Fort Collins, Colorado

Spring 2020

Doctoral Committee:

Co-advisor: Emily Fischer
Co-advisor: A. R. Ravishankara

Elizabeth Barnes
Shantanu Jathar

ABSTRACT

KETONES IN THE TROPOSPHERE:

STUDIES OF LOSS PROCESSES, EMISSIONS, AND PRODUCTION

Ketones play an important role in atmospheric chemistry of the troposphere because they are oxidized VOCs that are both relatively abundant with sufficiently long-lifetimes to be distributed regionally. Ketone photolysis is a potentially important source of HOx radicals in the upper troposphere; it can also serve as a source of peroxy radicals which contribute to the formation of peroxy acyl nitrate-type (PAN-type) compounds. My thesis focuses on the atmospheric processes and budgets of smaller ketones.

In this thesis, we discuss a series of four studies aimed at understanding the importance of atmospheric ketones to production of oxidants and PAN-type compounds. The four studies covered here involve laboratory measurements, interpretation of atmospheric observations, and modeling calculations.

Chapter 2 of this thesis discusses an update to and global sensitivity analysis of the global budget of acetone. We test how sensitive a global simulation of acetone is to literature-derived ranges of input factors used to represent 1) direct emissions and secondary natural sources of acetone from the biosphere; 2) loss via photolysis; and 3) dry deposition. We use the Morris method (one-at-a-time variations) to identify and prioritize potential reasons for model-measurement differences for acetone. This study helps identify what specific processes and/or geographic regions deserve further attention via modeling and/or measurements to constrain the global budget of this species. Of the sources tested, acetone is globally most sensitive to the

direct emissions from the biosphere, with other sources and sinks being important on a seasonal and regional basis.

Chapter 3 presents the results of laboratory measurements of absorption cross sections of MEK and DEK (along with their uncertainties) measured in the laboratory between 200-335 nm at temperatures ranging from 242-320 K, with a spectral resolution of 1 nm. We also report absorption cross sections for PEK at the same resolution and wavelengths at 296 K. We present a simple "two-state" physically based model to understand the temperature variation of the cross sections and to extrapolate cross sections beyond the temperatures of the measurements. The implementation of these temperature-dependent cross-sections is most important in the colder upper troposphere, where this work suggests a ~20% decrease in MEK photolysis rate relative to the previous understanding.

In Chapter 4, we present an analysis of aircraft observations of MEK in the remote marine troposphere from the Atmospheric Tomography (ATom) project. We show that the observed vertical profiles over clean oceans suggests an oceanic source of MEK. We show that the ocean serves as a source of MEK to the atmosphere during both meteorological winter and summer. MEK in clean marine air over the remote oceans correlates with both acetone and acetaldehyde, whose primary sources in the ocean water are the photooxidation of organic material.

Finally, in Chapter 5, we bring together the information gathered from Chapters 2 and 3 to improve our ability to model MEK globally and, with these and other model improvements, present the first global budget of MEK. We discuss the magnitudes, distribution, and seasonality of the sinks, sources, and atmospheric mixing ratios of MEK as well. We also present a comparison of simulated MEK abundances using a suite of available aircraft observations of MEK from around the globe. Our results suggest that MEK is much less abundant in the

atmosphere than acetone, but the fluxes of MEK into the atmosphere are about a tenth as those of acetone. The most important sources of MEK to the atmosphere are from the ocean and the oxidation of primarily anthropogenic alkanes, while the most important sinks of MEK are photolysis and oxidation by OH.

We pull the information from all these four studies to show that our knowledge of the atmospheric role of acetone and MEK are improved. We also identify gaps in our knowledge that should be pursued to further improve quantifications of the roles of ketones in the troposphere.

ACKNOWLEDGEMENTS

This research was supported primarily by NASA Award Number NNX16AI17G. Additional funding for the research discussed in Chapter 3 was provided by the European Union's Horizon 2020 research and innovation programme through the EUROCHAMP-2020 Infrastructure Activity under grant agreement No 730997. Additional funding was also provided by the CSU ASCENT Fellowship for graduate research. The research in Chapters 4 and 5 is dependent upon work supported by the National Center for Atmospheric Research, which is a major facility sponsored by the National Science Foundation under Cooperative Agreement No. 1852977. This work was funded in part by NOAA's climate and health of the atmosphere research programs. I am deeply indebted to the entirety of the ATom research and support teams from NASA, NOAA, and various universities – this research would not have possible without them. In particular, the authors would like to acknowledge our use of the ozone data collected by Dr. Thomas Ryerson, Dr. Chelsea Thompson, Jeff Peischel, and Ilann Bourgeois of NOAA. I would also like to thank Dr. James Burkholder, Dr. Dimitrios Papanastasiou, Dr. Abdelwahid Mellouki, Dr. Roisin Commane, Dr. Eric Ray, and all of the rest of my coauthors for their generous gifts of their time, mentorship, and brilliance. My thesis and my graduate school experience has been much richer for your help.

I would like to express my thanks to the members of my PhD committee, Dr. Shantanu Jathar, and Dr. Elizabeth Barnes for their review of this work and their many helpful suggestions throughout the research process. A special thank you must be extended to Dr. Barnes, to whose exemplary teaching and mentorship I am profoundly indebted. Thank you also to Dr. Delphine Farmer for her role in getting me through the PhD process.

To my advisors Dr. Emily Fischer and Dr. Ravishankara: thank you. Thank you for the years of conceptual help, the reams of rewrites, the hours of calls and meetings and help, and most of all for believing in me and helping me reach this point. I could hardly imagine a more supportive team. This has been by far the hardest thing I've ever attempted in my life, and I literally could not have done it without both of your help. Thank you for seeing my potential even before I did.

Thank you to my Masters advisors – Dr. Kevin Arrigo and Dr. Rob Dunbar – to whom I owe my love of earth science research and my ability to code Fortran, which turned out to be much more useful than I anticipated. An eternity of thank yous to Deana Fabbro-Johnston. I walked into your office in 2008 with no idea what I wanted to do and walked out with a plan for my life that turns out to have been shockingly accurate. Thank you for giving me an opportunity and helping me make a plan for how to explore my love of science and teaching.

Thanks to the members of the Fischer and Ravishankara groups past and present – Jake Zaragoza, Dr. Zitely Tzompa, Dr. Steve Brey, Jakob Lindaas, Dr. Liji David, Kate O'Dell, and Julieta Juncosa – whose technical advice, valuable discussions, and motivation were invaluable to this research. Thank you for the constant encouragement, love, and support. I am so very lucky to have known and worked with each and every one of you. I would also like to thank the entirety of the extended CSU Atmospheric Science graduate student family who have made my life a joy over the last 5 years – thank you to Dr. Rob Nelson, Dr. Marie McGraw, Colleen Brents, Ariel Schnee, Abby Worthen, Dr. Will Lassman, Rachel Severson, Dr. Erik Neilsen, Andrea Jenney, Anna Hodshire, Ed Charlesworth, Brad Wells, Alex Naegele, Dr. Stephanie Pilkington, and everyone else who makes this department and this town such a wonderful place to be a student. Thank you also to the Rocky Bards and the rest of the Wednesday night Session

at LJ's – I looked forward to every rehearsal and every session for years, and I'm so lucky to have had the opportunity to play with such talented musicians. Thank you also to dear friends Hannah Allen, David Zimmerman, Daniel Schwarz, and Dr. Mark Garret, whose phone calls and visits I still look forward to so many years later.

I would like to profusely thank my family and friends for their constant encouragement and willingness to listen and deal with the various aspects of graduate school life. Thank you to Ariana and Owen, who are my favorite people to be outside with, and who always want to know what's going on. Thank you to my parents, Dr. Wheaton Brewer and Catharine Brand, for everything. There are not enough words to express my gratitude.

DEDICATION

Ce qui est simple est toujours faux. Ce qui ne l'est pas est inutilisable.
Paul Valery

All models are wrong. Some are useful.
George Box

"Can you see anything?"
"Yes. Wonderful things."
Dr. John Hall

TABLE OF CONTENTS

CHAPTER 1: INTRODUCTION

1.1. Atmospheric Oxidation

The most important change to Earth's atmospheric composition happened 2.3 billion years ago. Prior to this point, our planet's atmosphere was primarily made of carbon dioxide (CO_2), methane (CH_4), sulfuric gases, and nitrogen (Canfield et al., 2013). This is not because elemental oxygen is in any way rare – it is believed to be the third most abundant element in the universe (Croswell, 1996). Rather, oxygen is extremely reactive, and in the ancient pre-history of earth it was primarily bound up in compounds with other elements rather than being freely available in the atmosphere. Sometime around 3 billion years ago – possibly as early as 3.5 billion and certainly by 2.7 billion - the first photosynthetic bacteria evolved a new trick: they could use the energy in sunlight to split water and CO_2 to make sugar, and in the process release molecular oxygen, O_2 (Pierson, 1994). For the first several hundred million years of photosynthesis, this process mostly did not change the atmosphere itself. Instead, the newly liberated oxygen generally returned to earth almost immediately through reaction with minerals on the surface and in the oceans – the planet itself began to rust (Canfield et al., 2013; Holland, 2006). By 2.3 billion years ago, oxygen began to accumulate in the atmosphere, where it today makes up 21% of each breath we take (Canfield et al., 2013; Holland, 2006).

Chemically, it would not be entirely wrong to think of this change as setting fire to the atmosphere. In the language of a chemist, Earth's atmosphere is an oxidizing medium: that is to say, oxygen dominates the chemistry of the atmosphere and determines the fate of nearly every trace gas released into the atmosphere. This process may most easily be understood by considering the reaction of the simplest alkane – CH_4 – with O_2 in Equation (1) below:

$$(1)\ CH_4 + 2O_2 \rightarrow 2H_2O + CO_2$$

This is the same basic reaction that occurs in a natural gas burner and, for that matter, essentially the same reaction that powers each of our cells: combine a reduced species made up mostly of carbon and hydrogen (e.g., natural gas, octane fuel, glucose) with oxygen to produce water, CO_2, and energy. Of course, both flames and cells use various other tricks of chemistry to make this reaction go more quickly. The carbon-hydrogen bonds in CH_4 are otherwise so strong that it is nearly impossible for molecular oxygen to break them. Indeed, under atmospheric conditions, reaction (1) essentially never occurs as written. A family of oxidizing radicals that are the true drivers of atmospheric oxidation: the odd hydrogen radicals ($HO_x = OH + HO_2$).

For most trace gases, OH is the dominant loss process in the troposphere. OH is sufficiently reactive that each molecule reacts with another gas and is destroyed almost as quickly as it forms – the species has a mean atmospheric lifetime of only a few seconds. Mean concentrations of OH radicals are thus highly variable, ranging up to ~10^7 molecules/cm^3 in daytime near the surface, ~10^6 molecules/cm^3 in daytime in the upper troposphere (Spivakovsky et al., 2000), and essentially 0 at night time. Even such low concentrations are sufficient to dominate atmospheric chemistry. The first reaction for the atmospheric oxidation of most VOCs takes the form:

$$RH + OH \rightarrow H_2O + R$$

In the case of CH_4, R is CH_3. Where CH_4 (i.e., RH) with its full set of four bonds was not reactive enough with oxygen to break the C-H bond quickly, the CH_3 radical will react almost immediately with O_2.

The OH and HO_2 radicals are often treated together as HO_x because the two species rapidly interconvert in the presence of NO, so the production of one HO_2 is roughly equivalent to the production of one OH. The primary HO_x source in the global troposphere is believed to be the photolysis of ozone (O_3) to produce O(^{1}D), whose subsequent reaction with water vapor

produces OH radicals (Levy, 1971). However, in regions where water vapor is scarce, such as the upper troposphere, other sources of OH become more important. One of the most important non-H_2O sources of HO_x are the ketones (McKeen et al., 1997; Singh et al., 1995; Wennberg et al., 1998).

1.2. Ketones as HO_x Sources in the Upper Troposphere

The ketones are a family of carbonyl compounds with both primary and secondary anthropogenic and natural sources. Their archetypical formula is *RC(O)R'*, where both *R* and *R'* are functional groups with at least one carbon. Ketones play an important role in atmospheric chemistry because they are both relatively abundant and relatively stable oxidized VOCs (OVOCs; H.B. Singh et al., 1994, 2000, 2001; Yañez-Serrano et al., 2016). The smallest and most abundant ketone is the three-carbon acetone ($CH_3C(O)CH_3$) (H.B. Singh et al., 1994); the four-carbon methyl ethyl ketone (MEK; $CH_3C(O)C_2H_5$) is the second most abundant ketone in the atmosphere (H.B. Singh et al., 2000; Yañez-Serrano et al., 2016). Other saturated ketones, including diethyl ketone (DEK; $C_2H_5C(O)C_2H_5$) and propyl ethyl ketone (PEK; $C_3H_7C(O)C_2H_5$) can be directly emitted into the atmosphere or secondarily produced by the oxidation of alkanes and alcohols (Siegel & Eggerdorfer, 2002; Singh et al., 2004; Yañez-Serrano et al., 2016), although we are unaware of reports of atmospheric concentrations of these compounds. Ketones have the potential to serve as an additional and significant source of HO_x radicals in the upper troposphere (McKeen et al., 1997; Singh et al., 1995; Wennberg et al., 1998). Recent work suggests that the magnitude of the HO_x source from acetone photolysis in the upper troposphere, where water vapor concentrations are small, could be as much as that via O_3 photolysis in the same region, depending upon the season (Neumaier et al., 2014). The UV absorption cross

section of DEK and PEK in the actinic region are similar to that of MEK (Brewer et al., 2019; Horowitz, 1999; Keller-Rudek et al., 2013; Martinez et al., 1992), and the rate coefficient for DEK's reaction with OH radicals is approximately 2.5 times larger than that of MEK (Burkholder et al., 2015). By analogy to acetone and MEK, DEK and PEK could potentially contribute to production of HO_x compounds in the troposphere.

1.3. Ketones and Reactive Nitrogen

In addition to their important role in atmospheric oxidation, ketones play an important part in reactive nitrogen chemistry via their part in the formation of acyl peroxy nitrates (PANs). PAN-type compounds are important reservoir species for nitrogen oxide radicals (NO_x = NO + NO_2), which transport NO_x over long distances and contribute to tropospheric ozone (O_3) production (Singh & Hanst, 1981). PANs are formed in polluted environments via the reaction between NO_x and carbonyl peroxy radicals, with a characteristic form $RC(O)OONO_2$. PANs are important because their stability depends upon ambient temperature. When warm, PAN species tend to decompose; when cold, they can be stable over a long time period, enabling long distance transport (Hudman et al., 2004; Singh, 1987). In this way PANs can introduce NO_x into remote regions of the troposphere where it otherwise might not be present and where it is most efficient at producing O_3 and OH (Fischer et al., 2010; Hudman et al., 2004; Hanwant B. Singh, 1987). Acetone is a significant precursor to PAN formation, responsible for ~9% of PAN formation globally (Fischer et al., 2014). MEK has not previously been shown to directly contribute significantly to PAN production globally, though the possibility remains that it could be regionally important in certain highly polluted areas; similarly, DEK and PEK remain total

unknowns in an atmospheric context but could potentially play a similar role due to their similar photolysis.

1.4. Photochemical Processes

Photolysis is the breaking of chemical bonds via the input of solar energy. This process represents both an important loss pathway for the ketones and the key to their atmospheric importance. Overall, solar photon absorption by a ketone in the troposphere leads to the following generalized representation:

$$\text{(R1)}\ RC(O)R' + h\nu \rightarrow\ RC(O) + R'$$

Subsequently, both R' and RCO undergo atmospheric degradation and lead to HO_x via reactions of RO radicals that are produced in the process, especially in the presence of sufficient NO_x. In reactions (R2), we show the oxidation of R' radical:

$$\text{(R2a)}\ R' + O_2 \overset{M}{\rightarrow}\ R'O_2 \overset{NO}{\rightarrow}\ R'O + NO_2$$

$$\text{(R2b)}\ R'O + O_2 \rightarrow\ R"O + HO_2$$

In the case of acetone, R' is CH_3 and R"O is CH_2O. Thus the photolysis of acetone produces two HO_x radicals and two CH_2O molecules; CH_2O can photolyze to produce additional HO_x (Cooke et al., 2010) or react with OH leading to no net loss of HO_x. If the photolysis of

MEK (R1) yields R' as CH_3, R"O will also be CH_2O. If the photolysis of MEK (R1) yields R' instead as C_2H_5, R"O is acetaldehyde ($CH_3C(O)H$). The photolysis of $CH_3C(O)H$ produces an additional HO_x molecule and another CH_2O molecule (Millet et al., 2010). Of course, acetaldehyde can also react with OH, and this fate would also generate additional HO_x through the formation of CH_2O.

The RCO radical formed via photolysis (R1) also undergoes a similar sequence of reactions in the presence of NO_x. The end result is the formation of another R radical, and its oxidation via R3 is additional HO_x production.

$$\text{(R3) } RC(O) + O_2 \rightarrow RC(O)O_2 \xrightarrow{NO} RC(O)O + NO_2 \rightarrow R + CO_2 + NO_2$$

If R is an ethyl radical (as can occur in MEK, DEK, and PEK photooxidation), then RC(O) is a propionyl radical. If R is a methyl radical (as in the case of acetone and MEK photooxidation), then RC(O) is an acetyl radical. Even in low NO_x conditions, the reaction between O_2 and a propionyl radical can serve to produce HO_x through the subsequent reactions of the peroxy radicals. In high NO_x conditions with sufficient of NO_2 present, the peroxide intermediate formed by the initial step of R3 ($RC(O)O_2$) can react with NO_2 to form a PAN-type compound ($RC(O)OONO_2$). Occasionally, the first step of reaction R3 can also lead directly to OH production via an isomerization of the carbonyl radical, leading to a series of lactone-type products and OH production (Hou & Wang, 2007; Romero et al., 2005). These yields tend to be fairly low at atmospherically relevant temperatures - between 6% (213 K, 330 hPa) and 20% (213 K, 70 hPa) for MEK (Hou & Wang, 2007; Romero et al. 2005) and at most 1-2% at

atmospherically relevant pressures for acetone (Gross et al., 2014; Papadimitriou et al., 2015). This source is not generally considered in global HO_x simulations, but has been occasionally used in laboratory studies as a means of studying ketone quantum yields (Romero et al., 2005). Overall, atmospheric ketone photolysis initiates reactions (R1 – R3) which efficiently produce HO_x radicals; in polluted environments, this process can diverge in step (R3) to produce PAN-type compounds as well.

The reaction of ketones with OH follows a similar sequence, with slightly more steps. In place of reaction R1, ketone oxidation proceeds as follows. Note that, for comprehension, one of the hydrogen atoms previously assumed to be included inside the R group is now listed as distinct – what was R in R1 is now RH_3 in R4.

$$\text{(R4) } R'C(O)RH_3 + OH \rightarrow R'C(O)RH_2 + H_2O$$

In acetone – the simplest case – R is just a single carbon, RH_3 is CH_3, and the radical product of R4 is the radical $CH_3C(O)CH_2$. This radical will quickly react with molecular oxygen in a manner analogous to R3:

$$\text{(R5) } R'C(O)RH_2 + O_2 \rightarrow R'C(O)RO_2 \overset{NO}{\rightarrow} R'C(O)RH_2O + NO_2$$

The radical product of this reaction ($R'C(O)RH_2O$) can either decompose into an aldehyde and peroxy radical or react with another oxygen molecule to abstract a second hydrogen from the RH_2O group, resulting in the production of a HO_x molecule. These paths are laid out in reactions R6 and R7, respectively.

$$\text{(R6) } R'C(O)RH_2O \rightarrow R'C(O) + RH_2O$$

$$\text{(R7) } R'C(O)RH_2O + O_2 \rightarrow R'C(O)R(O)H + HO_2$$

The decomposition case – reaction (R6) – creates the same peroxy radical as R1. Similarly, the aldehyde created in R6 will be CH_2O in the case of acetone and either CH_2O or

acetaldehyde (CH_3CHO) in the case of MEK, as was the case for the products of reaction R2b. R7 does lead to a stable dicarbonyl compound. These dicarbonyls can also consequently photolyze and react with OH, giving rise to similar product sets as the ketones from which they arose (e.g. HO_x, aldehydes, PAN-type compounds). In the case of acetone, where R is just a single carbon atom, this product is methylglyoxal; for MEK, more complex dicarbonyls can result.

1.5. Global Budgets

Atmospheric chemists rely on three tools to study the atmosphere: laboratory studies, atmospheric observations, and chemical models. Each of these tools has significant advantages and limitations. A laboratory experiment is a controlled system better suited to truly understand physical and chemical processes at the cost of a loss of complexity. Atmospheric observations capture the atmosphere as it exists, but they can be complex and necessarily limited in time and space. Atmospheric chemists therefore turn to chemical models to contextualize processes, interpret observations, and make forecasts and projections about the future (Jacob, 1999). The simplest model calculation we use to understand the role of various compounds in the atmosphere is essentially the continuity equation for a species in the atmosphere: the global budget. By tallying up the sources and sinks of a given species in the atmosphere and tracing its precursors and its products, the abundance and importance of a given species can be understood. This matters for many reasons, but one of the most notable is that the abundance of a species does not necessarily imply its chemical importance – short-lived but highly reactive compounds can be far more important to chemical processes than their concentrations suggest, as is the case with OH – and therefore understanding the sources and sinks of a compound can be just as

important as documenting its abundance. Even knowing that the model may inevitably be wrong, we can use the comparison between modeled understanding and observations to try to gain an understanding of what is and is not known about the sources, sinks, and importance of a given species in the complex atmospheric chemical system (Jacob, 1999; Oreskes et al., 1994).

Global chemical transport models (CTMs) allow us to add a layer of sophistication to what is essentially a back of the envelope calculation. They remove the flux divergence/transport question from the equation by using analyzed wind fields and allow scientists to include some basic principles about the planet that are hard to take into account in other ways. For example, any process involving exchange between the ocean and the atmosphere will likely be more important in the Southern Hemisphere; any process involving anthropogenic influence on the atmosphere is more likely to be important in the Northern Hemisphere, where 88% of Earth's population lives. The tropics hold the most productive forests and peatlands in the world, while the immediate subtropics are the site of seasonal fires, primarily of human origin. By combining our understanding of where human and natural activities take place with our understanding of atmospheric chemistry and transport, we can begin to get a handle on the fluxes and abundance of species of interest in the atmosphere.

1.6. The Importance, Abundance, and Budgets of Ketones in the Atmosphere

In the research discussed here, we have mostly focused on the two most abundant saturated atmospheric ketones, acetone and MEK. A general background on these two species is included below. In chapter 3, we also address the photochemistry of two larger saturated ketones, diethyl and propyl ethyl ketone. As discussed above, these species can be directly emitted into the atmosphere or secondarily produced by the oxidation of alkanes and alcohols (Siegel &

Eggerdorfer, 2002; Singh et al., 2004; Yañez-Serrano et al., 2016). Other unsaturated ketone species with significant atmospheric concentrations are present in the atmosphere; most notable is MVK, which is a product of isoprene oxidation in the atmosphere. While the photochemistry of these species can also be atmospherically important (Fuchs et al., 2018), this thesis is focused solely on the saturated ketones.

1.6.1. Acetone (propanone)

Acetone is the most abundant ketone in the atmosphere, and is thought to be a major source of HO_x radicals in the upper troposphere (*e.g.*, Singh et al. (1994)); its exact contribution to the overall HO_x budget is uncertain, but acetone's contribution to upper tropospheric HO_x abundance may be as high as 95% of that produced by O_3 photolysis (Neumaier et al., 2014). Acetone is also a precursor for PAN, a temporary reservoir of NO_x, and thus affects the tropospheric distribution of NO_x and O_3 (Fischer et al., 2014; Singh et al., 1994). The global budget of acetone has been periodically revisited because this species is of global importance and there are major uncertainties in important source and sink terms (Arnold et al., 2005; Fischer et al., 2010; Jacob et al., 2002; Khan et al., 2015; Singh et al., 1995).

Sources of acetone include direct emission from anthropogenic sources (Jacob et al., 2002; Singh et al., 1994), vegetation (Guenther et al., 1999, 2012; Singh et al., 1994), biomass burning (Akagi et al., 2011; Singh et al., 2000), and the ocean (Kanakidou et al., 1991; Singh et al., 1994; Tanimoto et al., 2014). Acetone is also produced in the atmosphere from the oxidation of both biogenic (Orlando et al., 2000; Pozzer et al., 2007; Reissell et al., 1999; Sindelarova et al., 2014) and anthropogenic volatile organic compounds (VOCs) (Kanakidou et al., 1991; Kasting & Singh, 1986; Pozzer et al., 2007). Acetone is lost via photolysis (Gierczak et al., 1998; Singh et

al., 1995), oxidation by OH (Jaeglé et al., 1997; Singh et al., 1995), and both terrestrial and marine surface uptake (Chatfield et al., 1987; Jacob et al., 2002; Karl et al., 2005). Jacob et al. (2002) hypothesized that the oceans provide a major source of acetone to the atmosphere and that this source is responsible for observed acetone mixing ratios of 200–500 pptv over remote regions away from land sources. A revision to the quantum yield for photolytic loss of acetone in 2004 suggested that the global acetone lifetime in the upper troposphere is 3 - 3.5 times longer than previously calculated (Arnold et al., 2005; Blitz et al., 2004; Fischer et al., 2012; Gierczak et al., 1998; Jacob et al., 2002). Fischer et al. (2012) revised the earlier Jacob et al. (2002) global budget to conclude that a large *net* ocean source is not required to reproduce the observed global patterns of acetone abundance and ocean-atmosphere fluxes.

1.6.2. Methyl Ethyl Ketone (MEK, 2-butanone)

The importance of MEK in the atmosphere remains uncertain (Singh et al., 2004; Yañez-Serrano et al., 2016). Methyl Ethyl Ketone (MEK; C_4H_8O; 2-butanone) is an oxygenated volatile compound (OVOC) that occurs in the atmosphere over a wide variety of environments with typical mixing ratios ranging from a few ppt to ~10 ppb in the most polluted environments (Sinha et al., 2014; Yañez-Serrano et al., 2016). Similar to acetone, MEK photolysis in the near-UV can produce HO_x radicals (Brewer et al., 2019; Martinez et al., 1992; Romero et al., 2005). The number of HO_x produced by photolysis of each MEK in the upper troposphere should be comparable to or higher than that from each acetone molecule in this region. The exact yield of HO_x will depend on the concentration of NO and the as-yet-uncertain quantum yields in the photolysis of MEK at upper troposphere pressures and temperatures. The sources of MEK are not fully understood (Yañez-Serrano et al., 2016). Known sources of MEK include direct

emissions from biomass burning and the terrestrial biosphere, as well as secondary production from the oxidation of anthropogenic alkanes (Cappellin et al., 2016; Jordan et al., 2009; Yañez-Serrano et al., 2016). The primary chemical sinks of MEK in the atmosphere are photolysis and reaction with OH (Chew & Atkinson, 1996; Raber & Moortgat, 1987; Romero, Blitz, Heard, Pilling, Price, & Seakins, 2005; Yañez-Serrano et al., 2016). Reactions with both nitrate (NO_3) and chlorine radicals (Cl) also occur, although these sinks are believed to be relatively minor globally (Calvert et al., 2011). MEK is also lost via dry deposition (Jordan et al., 2009; Talbot, 2005), and in this work we show that ocean exchange is also probable. Better quantification of the sources of MEK are needed to constrain the abundances, seasonality, and transport of MEK throughout the atmosphere, all of which are necessary to estimate the contribution of MEK to the HO_x budget in the upper troposphere.

1.7. Dissertation Overview

This thesis consists of four studies involving laboratory measurements, interpretation of atmospheric observations, and modeling calculations – the full breadth of atmospheric chemistry.

1.7.1. Chapter 2. A sensitivity analysis of key natural factors in the modeled global acetone budget.

Chapter two presents an update of the global acetone budget (Fischer et al., 2012; Jacob et al., 2002) based on advances in model development and observations. We test how sensitive a global simulation of acetone is to literature-derived ranges of input factors used to represent 1) direct emissions and secondary natural sources of acetone from the biosphere; 2) loss via photolysis; and 3) dry deposition. We use this approach to identify and prioritize potential reasons for model-measurement differences for acetone, in order to identify what specific

processes and/or geographic regions deserve further attention via modeling and/or measurements to constrain the global budget of this species. Of the sources tested, acetone is globally most sensitive to the direct emissions from the biosphere, with other sources and sinks being important on a seasonal and regional basis.

1.7.2. Chapter 3. Atmospheric photolysis of methyl ethyl, diethyl, and propyl ethyl ketones: temperature dependent UV absorption cross sections.

In this chapter, we report absorption cross sections of MEK and DEK (along with their uncertainties) measured in the laboratory between 200-335 nm at temperatures ranging from 242-320 K, with a spectral resolution of 1 nm. We also report absorption cross sections for PEK at the same resolution and wavelengths at 296 K. The data are also used to calculate representative first-order rate coefficients for the photodissociation (J-values) of each compound for a few representative sets of atmospheric conditions, enabling us to contextualize the atmospheric importance of the cross section temperature dependence to the photolysis rate of these compounds, as well as provide atmospheric modelers a basis for comparison to their own ketone photolysis rate calculations. We present a simple "two-state" physically based model to understand the temperature variation of the cross sections and to extrapolate cross sections beyond the temperatures of the measurements. The implementation of these temperature-dependent cross-sections is most important in the colder upper troposphere, where this work suggests a ~20% decrease in MEK photolysis rate relative to the previous understanding.

1.7.3. Chapter 4. An oceanic source of MEK to the atmosphere.

In Chapter 4, we present an analysis of aircraft observations of MEK in the remote marine troposphere from the Atmospheric Tomography (ATom) project. We show that the observed

vertical profiles over clean oceans suggests an oceanic source of MEK. We show that the ocean serves as a source of MEK to the atmosphere during in both meteorological winter and summer. There is pronounced seasonality in the MEK profiles in the extra tropical troposphere, with higher MEK mixing ratios observed in summer than in winter. MEK in clean marine air over the remote oceans correlates with both acetone and acetaldehyde, whose primary sources in the ocean water are the photooxidation of organic material. We show that even a small (>1 nM) concentration of MEK in surface waters is sufficient to allow the ocean to be a net source of MEK to the atmosphere over many ocean basins across multiple seasons.

1.7.4. Chapter 5: Global Atmospheric Budget and Importance of Methyl Ethyl Ketone (MEK): Chemical Transport Analysis and Constraints from In-Situ Aircraft Observations

In this chapter, we bring together the information gathered from the previously noted studies and present an analysis of the sinks and sources of MEK. In our simulations, MEK has direct sources from the biosphere (Jordan et al., 2009; Yañez-Serrano et al., 2016), direct anthropogenic emissions (EMEP, 2015; Hoesly et al., 2018; U. S. EPA, 2013), biomass burning (Akagi et al., 2011; Andreae, 2019), and oceanic emissions (see Chapter 4). MEK is also secondarily produced from the atmospheric oxidation of predominantly anthropogenically emitted alkanes, most importantly n-butane (Jenkin et al., 1997). Sinks for MEK in our simulation are photolysis (IUPAC, 2005), oxidation by OH, NO_3, and Cl (Calvert et al., 2011), ocean uptake (see Chapter 4), and dry deposition (Jordan et al., 2009; Talbot, 2005). This chapter discusses the magnitudes of the sinks, sources, and atmospheric mixing ratios of MEK as well as the comparison of modeled MEK to available observations.

Chapter References

Akagi, S. K., Yokelson, R. J., Wiedinmyer, C., Alvarado, M. J., Reid, J. S., Karl, T., et al. (2011). Emission factors for open and domestic biomass burning for use in atmospheric models. *Atmospheric Chemistry and Physics*, *11*(9), 4039–4072. https://doi.org/10.5194/acp-11-4039-2011

Andreae, M. O. (2019). Emission of trace gases and aerosols from biomass burning – an updated assessment. *Atmospheric Chemistry and Physics*, *19*(13), 8523–8546. https://doi.org/10.5194/acp-19-8523-2019

Arnold, S. R., Chipperfield, M. P., & Blitz, M. A. (2005). A three-dimensional model study of the effect of new temperature-dependent quantum yields for acetone photolysis. *Journal of Geophysical Research*, *110*(D22). https://doi.org/10.1029/2005jd005998

Blitz, M. A., Heard, D. E., Pilling, M. J., Arnold, S. R., & Chipperfield, M. P. (2004). Pressure and temperature-dependent quantum yields for the photodissociation of acetone between 279 and 327.5 nm. *Geophysical Research Letters*, *31*(6), n/a-n/a. https://doi.org/10.1029/2003gl018793

Brewer, J. F., Papanastasiou, D. K., Burkholder, J. B., Fischer, E. V., Ren, Y., Mellouki, A., & Ravishankara, A. R. (2019). Atmospheric Photolysis of Methyl Ethyl, Diethyl, and Propyl Ethyl Ketones: Temperature Dependent UV Absorption Cross Sections. *Journal of Geophysical Research: Atmospheres*. https://doi.org/10.1029/2019JD030391

Burkholder, J. B., Sander, S. P., Abbatt, J., Barker, J. R., Huie, R. E., Kolb, C. E., et al. (2015). Chemical Kinetics and Photochemical Data for Use in Atmospheric Studies. In *JPL Publication 15-10* (Vol. 18). Pasadena: Jet Propulsion Laboratory.

Calvert, J. G., Mellouki, A., Orlando, J. J., Pilling, M. J., & Wallington, T. J. (2011). *The Mechanisms of Atmospheric Oxidation of the Oxygenates*. New York: Oxford University Press.

Canfield, D. E., Ngombi-Pemba, L., Hammarlund, E. U., Bengtson, S., Chaussidon, M., Gauthier-Lafaye, F., et al. (2013). Oxygen dynamics in the aftermath of the Great Oxidation of Earth's atmosphere. *Proceedings of the National Academy of Sciences*, *110*(42), 16736–16741. https://doi.org/10.1073/pnas.1315570110

Chatfield, R. B., Gardner, E. P., & Calvert, J. G. (1987). Sources and Sinks of Acetone in the Troposphere: behavior of Reactive Hydrocarbons and a Stable Product. *Journal of Geophysical Research*, *92*(D4), 4208–4216.

Chew, A. A., & Atkinson, R. (1996). OH radical formation yields from the gas-phase reactions of O 3 with alkenes and monoterpenes. *J Geophys. Res.*, *101*(D22).

Cooke, M. C., Utembe, S. R., Carbajo, P. G., Archibald, A. T., Orr-Ewing, A. J., Jenkin, M. E., et al. (2010). Impacts of formaldehyde photolysis rates on tropospheric chemistry. *Atmospheric Science Letters*, n/a-n/a. https://doi.org/10.1002/asl.251

Croswell, K. (1996). *The Alchemy of the Heavens: Searching for Meaning in the Milky Way*. Anchor.

EMEP. (2015). The co-operative programme for monitoring and evaluation of the long-range transmissions of air pollutants in Europe.

Fischer, E. V., Jaffe, D. A., Reidmiller, D. R., & Jaeglé, L. (2010). Meteorological controls on observed peroxyacetyl nitrate at Mount Bachelor during the spring of 2008. *Journal of Geophysical Research*, *115*(D3). https://doi.org/10.1029/2009JD012776

Fischer, E. V., Jacob, D. J., Millet, D. B., Yantosca, R. M., & Mao, J. (2012). The role of the ocean in the global atmospheric budget of acetone. *Geophysical Research Letters*, *39*(1), n/a-n/a. https://doi.org/10.1029/2011gl050086

Fischer, E. V., Jacob, D. J., Yantosca, R. M., Sulprizio, M. P., Millet, D. B., Mao, J., et al. (2014). Atmospheric peroxyacetyl nitrate (PAN): a global budget and source attribution. *Atmospheric Chemistry and Physics*, *14*(5), 2679–2698. https://doi.org/10.5194/acp-14-2679-2014

Fuchs, H., Albrecht, S., Acir, I., Bohn, B., Breitenlechner, M., Dorn, H.-P., et al. (2018). Investigation of the oxidation of methyl vinyl ketone (MVK) by OH radicals in the atmospheric simulation chamber SAPHIR. *Atmospheric Chemistry and Physics*, *18*(11), 8001–8016. https://doi.org/10.5194/acp-18-8001-2018

Gierczak, T., Burkholder, J. B., Bauerle, S., & Ravishankara, A. R. (1998). Photochemistry of acetone under tropospheric conditions. *Chemical Physics*, *231*, 229–244.

Gross, C. B., Dillon, T. J., & Crowley, J. N. (2014). Pressure dependent OH yields in the reactions of CH3CO and HOCH2CO with O2. *Phys Chem Chem Phys*, *16*(22), 10990–8. https://doi.org/10.1039/c4cp01108b

Guenther, A., Geron, C., Pierce, T., Lamb, B., Harley, P., & Fall, R. (1999). Natural Emissions of non-methane volatile organic compounds, carbon monoxide, and oxides of nitrogen from North America. *Atmospheric Environment*.

Guenther, A., Jiang, X., Heald, C. L., Sakulyanontvittaya, T., Duhl, T., Emmons, L. K., & Wang, X. (2012). The Model of Emissions of Gases and Aerosols from Nature version 2.1 (MEGAN2.1): an extended and updated framework for modeling biogenic emissions. *Geoscientific Model Development*, *5*(6), 1471–1492. https://doi.org/10.5194/gmd-5-1471-2012

Hoesly, R. M., Smith, S. J., Feng, L., Klimont, Z., Janssens-Maenhout, G., Pitkanen, T., et al. (2018). Historical (1750–2014) anthropogenic emissions of reactive gases and aerosols from the Community Emissions Data System (CEDS). *Geoscientific Model Development*, *11*(1), 369–408. https://doi.org/10.5194/gmd-11-369-2018

Holland, H. D. (2006). The oxygenation of the atmosphere and oceans. *Philosophical Transactions of the Royal Society B: Biological Sciences*, *361*(1470), 903–915. https://doi.org/10.1098/rstb.2006.1838

Horowitz, A. (1999). *Absorption cross sections of 2-pentanone, 3-pentanone, and 3-hexanone*. The Max-Planck-Institut für Chemie, Mainz, Germany.

Hou, H., & Wang, B. (2007). Ab initio study of the reaction of propionyl (C2H5CO) radical with oxygen (O2). *J Chem Phys*, *127*(5), 054306. https://doi.org/10.1063/1.2756538

Hudman, R. C., Jacob, D. J., Cooper, O. R., Evans, M. J., Heald, C. L., Park, R. J., et al. (2004). Ozone production in transpacific Asian pollution plumes and implications for ozone air quality in California: ASIAN TRANSPACIFIC POLLUTION PLUMES. *Journal of Geophysical Research: Atmospheres*, *109*(D23). https://doi.org/10.1029/2004JD004974

IUPAC. (2005). *CH3C(O)C2H5.* (IUPAC Task Group on Atmospheric Chemical Kinetic Data Evaluation No. Data Sheet P8).

Jacob, D. J. (1999). *Introduction to Atmospheric Chemistry*. Princeton, New Jersey: Princetone University Press.

Jacob, D. J., Field, B. D., Jin, E. M., Bey, I., Li, Q., Logan, J. A., & Yantosca, R. M. (2002). Atmospheric budget of acetone. *Journal of Geophysical Research*, *107*(D10). https://doi.org/10.1029/2001jd000694

Jaeglé, L., Jacob, D. J., Wennberg, P. O., Spivakovsky, C. M., Hanisco, T. F., Lanzendorf, E. J., et al. (1997). Observed OH and HO2in the upper troposphere suggest a major source from convective injection of peroxides. *Geophysical Research Letters*, *24*(24), 3181–3184. https://doi.org/10.1029/97gl03004

Jenkin, M. E., Saunders, S. M., & Pilling, M. J. (1997). The tropospheric degradation of volatile organic compounds: a protocol for mechanism development. *Atmospheric Environment*, *31*(1), 81–104.

Jordan, C., Fitz, E., Hagan, T., Sive, B., Frinak, E., Haase, K., et al. (2009). Long-term study of VOCs measured with PTR-MS at a rural site in New Hampshire with urban influences. *Atmos. Chem. Phys.*, 21.

Kanakidou, M., Singh, H. B., Valentin, K. M., & Crutzen, P. J. (1991). A two-dimensional study of ethane and propane oxidation in the troposphere. *Journal of Geophysical Research*, *96*(D8), 15,395-15,413.

Karl, T., Harley, P., Guenther, A., Rasmussen, R., Baker, B., Jardine, L., & Nemitz, E. (2005). The bi-directional exchange of oxygenated VOCs between a loblolly pine (Pinus tadea) plantation and the atmosphere. *Atmospheric Chemistry and Physics*, *5*(11), 3015–3031.

Kasting, J. F., & Singh, H. B. (1986). Nonmethane Hydrocarbons in the Troposphere: Impact on the Odd Hydrogen and Odd Nitrogen Chemistry. *Journal of Geophysical Research*, *91*(D12), 13239–13256.

Keller-Rudek, H., Moortgat, G. K., Sander, R., & Sörensen, R. (2013). The MPI-Mainz UV/VIS spectral atlas of gaseous molecules of atmospheric interest. *Earth Syst. Sci. Data*, *5*, 365–373. https://doi.org/10.5194/essd-5-365-2013

Khan, M. A. H., Cooke, M. C., Utembe, S. R., Archibald, A. T., Maxwell, P., Morris, W. C., et al. (2015). A study of global atmospheric budget and distribution of acetone using global atmospheric model STOCHEM-CRI. *Atmospheric Environment*, *112*, 269–277. https://doi.org/10.1016/j.atmosenv.2015.04.056

Levy, H. (1971). Normal Atmosphere: Large Radical and Formaldehyde Concentrations Predicted. *Science*, *173*(3992), 141–143. https://doi.org/10.1126/science.173.3992.141

Martinez, R. D., Buitrago, A. A., Howell, N. W., Hearn, C. H., & Joens, J. A. (1992). The near U.V. absorption spectra of several aliphatic aldehydes and ketones at 300 K. *Atmospheric Environment*, *26A*(5), 785–792.

McKeen, S. A., Gierczak, T., Burkholder, J. B., Wennberg, P. O., Hanisco, T. F., Keim, E. R., et al. (1997). The photochemistry of acetone in the upper troposphere: A source of odd-hydrogen radicals. *Geophysical Research Letters*, *24*(24), 3177–3180. https://doi.org/10.1029/97gl03349

Millet, D. B., Guenther, A., Siegel, D. A., Nelson, N. B., Singh, H. B., de Gouw, J. A., et al. (2010). Global atmospheric budget of acetaldehyde: 3-D model analysis and constraints from in-situ and satellite observations. *Atmos. Chem. Phys.*, 21.

Neumaier, M., Ruhnke, R., Kirner, O., Ziereis, H., Stratmann, G., Brenninkmeijer, C. A. M., & Zahn, A. (2014). Impact of acetone (photo)oxidation on HOx production in the UT/LMS based on CARIBIC passenger aircraft observations and EMAC simulations. *Geophysical Research Letters*, *41*(9), 3289–3297. https://doi.org/10.1002/

Oreskes, N., Shrader-Frechette, K., & Belitz, K. (1994). Verification, Validation, and Confirmation of Numerical Models in the Earth Sciences. *Science*, *263*(5147), 641–646.

Orlando, J. J., Nozière, B., Tyndall, G. S., Orzechowska, G. E., Paulson, S. E., & Rudich, Y. (2000). Product studies of the OH- and ozone-initiated oxidation of some monoterpenes. *Journal of Geophysical Research*, *105*(D9), 11561. https://doi.org/10.1029/2000jd900005

Papadimitriou, V. C., Karafas, E. S., Gierczak, T., & Burkholder, J. B. (2015). CH3CO + O2 + M (M = He, N2) Reaction Rate Coefficient Measurements and Implications for the OH Radical Product Yield. *J Phys Chem A*, *119*(28), 7481–97. https://doi.org/10.1021/acs.jpca.5b00762

Pierson, B. K. (1994). The emergence, diversification, and role of photosynthetic bacteria. In S. Bengtson (Ed.), *Early Life on Earth* (pp. 161–180). New York: Columbia University Press.

Pozzer, A., Jockel, P., Tost, H., Sander, R., Ganzeveld, L., Kerkweg, A., & Lelieveld, J. (2007). Simulating organic species with the global atmospheric chemistry general circulation model ECHAM5/MESSy1: a comparison of model results with observations. *Atmospheric Chemistry and Physics*, *7*(10), 2527–2550.

Raber, W. H., & Moortgat, G. K. (1987). Photooxidation of Selected Carbonyl Compounds in Air: Methyl Ethyl Ketone, Methyl Vinyl Ketone, Methacrolein and Methylglyoxal. In J. Barker (Ed.), *Progress and Problems in Atmospheric Chemistry*. Singapore: World Scientific Publishing.

Reissell, A., Harry, C., Aschmann, S. M., Atkinson, R., & Arey, J. (1999). Formation of acetone from the OH radical- and O3-initiated reactions of a series of monoterpenes. *Journal of Geophysical Research*, *104*(D11), 13869. https://doi.org/10.1029/1999jd900198

Romero, M. T. B., Blitz, M. A., Heard, D. E., Pilling, M. J., Price, B., & Seakins, P. W. (2005). OH formation from the C2H5CO+O2 reaction: An experimental marker for the propionyl radical. *Chemical Physics Letters*, *408*(4–6), 232–236. https://doi.org/10.1016/j.cplett.2005.04.018

Romero, M. T. B., Blitz, M. A., Heard, D. E., Pilling, M. J., Price, B., Seakins, P. W., & Wang, L. (2005). Photolysis of methylethyl, diethyl and methylvinyl ketones and their role in the atmospheric HOx budget. *Faraday Discussions*, *130*, 73. https://doi.org/10.1039/b419160a

Sindelarova, K., Granier, C., Bouarar, I., Guenther, A., Tilmes, S., Stavrakou, T., et al. (2014). Global data set of biogenic VOC emissions calculated by the MEGAN model over the last 30 years. *Atmospheric Chemistry and Physics*, *14*(17), 9317–9341. https://doi.org/10.5194/acp-14-9317-2014

Singh, H. B. (1987). Reactive nitrogen in the troposphere. *Environmental Science & Technology*, *21*(4), 320–327. https://doi.org/10.1021/es00158a001

Singh, H. B., & Hanst, P. L. (1981). Peroxyacetyl nitrate (PAN) in the unpolluted atmosphere: An important reservoir for nitrogen oxides. *Geophysical Research Letters*, *8*(8), 941–944. https://doi.org/10.1029/GL008i008p00941

Singh, H. B., O'Hara, D., Herlth, D., Sachse, W., Blake, D. R., Bradshaw, J. D., et al. (1994). Acetone in the atmosphere: Distribution, sources, and sinks. *Journal of Geophysical Research*, *99*, 1805–1819.

Singh, H. B., Kanakidou, M., Crutzen, P. J., & Jacob, D. J. (1995). High concentrations and photochemical fate of oxygenated hydrocarbons in the global troposphere. *Nature*, *378*, 50–54.

Singh, H. B., Chen, Y., Tabazadeh, A., Fukui, Y., Bey, I., Yantosca, R., et al. (2000). Distribution and fate of selected oxygenated organic species in the troposphere and lower

stratosphere over the Atlantic. *Journal of Geophysical Research: Atmospheres*, *105*(D3), 3795–3805. https://doi.org/10.1029/1999jd900779

Singh, H. B., Chen, Y., Stuadt, A., Jacob, D., Blake, D., Heikes, B., & Snow, J. (2001). Evidence from the southern Pacific troposphere for large global abundances and sources of oxygenated organic compounds. *Nature*, *410*, 1078–1081.

Sinha, V., Kumar, V., & Sarkar, C. (2014). Chemical composition of pre-monsoon air in the Indo-Gangetic Plain measured using a new air quality facility and PTR-MS: high surface ozone and strong influence of biomass burning. *Atmospheric Chemistry and Physics*, *14*(12), 5921–5941. https://doi.org/10.5194/acp-14-5921-2014

Spivakovsky, C. M., Logan, J. A., Montzka, S. A., Balkanski, Y. J., Foreman-Fowler, M., Jones, D. B. A., et al. (2000). Three-dimensional climatological distribution of tropospheric OH: Update and evaluation. *Journal of Geophysical Research: Atmospheres*, *105*(D7), 8931–8980. https://doi.org/10.1029/1999jd901006

Talbot, R. (2005). Diurnal characteristics of surface level O_3 and other important trace gases in New England. *Journal of Geophysical Research*, *110*(D9). https://doi.org/10.1029/2004JD005449

Tanimoto, H., Kameyama, S., Omori, Y., Inomata, S., & Tsunogai, U. (2014). High-Resolution Measurement of Volatile Organic Compounds Dissolved in Seawater Using Equilibrator Inlet-Proton Transfer Reaction-Mass Spectrometry (EI-PTR-MS), 89–115. https://doi.org/10.5047/w-pass.a02.001

U. S. EPA. (2013). *National Emissions Inventory 2011*. (U. S. EPA, Trans.).

Wennberg, P. O., Hanisco, T. F., Jaegle, L., Jacob, D. J., Hintsa, E. J., Lanzendorf, E. J., et al. (1998). Hydrogen Radicals, Nitrogen Radicals, and the Production of O3 in the Upper Troposphere. *Science*, *279*(5347), 49–53. https://doi.org/10.1126/science.279.5347.49

Yañez-Serrano, A. M., Nolscher, A. C., Bourtsoukidis, E., Derstroff, B., Zanoni, N., Gros, V., et al. (2016). Atmospheric mixing ratios of methyl ethyl ketone (2-butanone) in tropical, boreal, temperate, and marine environments. *Atmos. Chem. Phys.*, *16*, 10965–10984. https://doi.org/10.5194/acp-16-10965-2016

CHAPTER 2: A SENSITIVITY ANALYSIS OF KEY NATURAL FACTORS IN THE MODELED GLOBAL ACETONE BUDGET [1]

2.1 Introduction

Acetone is one of the most abundant carbonyl compounds in the atmosphere, and it serves as an important source of HO_x ($OH + HO_2$) radicals in the upper troposphere and a precursor for peroxyacetyl nitrate (PAN). We present a global sensitivity analysis targeted at several major natural source and sink terms in the global acetone budget to find the input factor or factors to which the simulated acetone mixing ratio was most sensitive. The ranges of input factors were taken from literature. We calculated the influence of these factors in terms of their Elementary Effects on model output. Of the six factors tested here, the four factors with the highest contribution to total global annual model sensitivity are direct emissions of acetone from the terrestrial biosphere, acetone loss to photolysis, the concentration of acetone in the ocean mixed layer, and the dry deposition of acetone to ice-free land. The direct emissions of acetone from the terrestrial biosphere are globally important in determining acetone mixing ratios but their importance varies seasonally outside the tropics. Photolysis is most influential in the upper troposphere. Additionally, the influence of the oceanic mixed layer concentrations are relatively invariant between seasons, compared to the other factors tested. Monoterpene oxidation in the troposphere, despite the significant uncertainties in acetone yield in this process, is responsible for only a small amount of model uncertainty in the budget analysis.

In this chapter, we present an update of the global acetone budget (Fischer et al., 2012; Jacob et al., 2002) based on advances in model development and observations. Using this updated

[1] Portions of this chapter contain published work. Citation: Brewer, J. F., Bishop, M., Kelp, M., Keller, C., Ravishankara, A. R., & Fischer, E. V. (2017). A sensitivity analysis of key natural factors in the modeled global acetone budget. Journal of Geophysical Research, 122(3), 2043–2058. https://doi.org/10.1002/2016JD025935

budget, we test how sensitive a global simulation of acetone is to literature-derived ranges of input factors used to represent 1) direct emissions and secondary natural sources of acetone from the biosphere, 2) loss via photolysis and 3) dry deposition. For the purposes of this sensitivity analysis, we represent the literature-derived uncertainty ranges as uniform distributions of equally likely values. We do not assign differing trust to different literature values. We rely on the Morris Method of global sensitivity analysis, also called the Elementary Effects method of sensitivity analysis. This technique is effectively an average of derivatives over the space of input factors. It is generally considered a cost-effective method for making a sensitivity analysis of computationally expensive models [Morris, 1991; Saltelli and Annoni, 2010]. We use this approach to identify and prioritize potential reasons for model-measurement differences for acetone, in order to identify what specific processes and/or geographic regions deserve further attention by the modeling and/or measurement communities to constrain the global budget of this species.

2.2 Methods

2.2.1 GEOS-Chem Model Description

We use GEOS-Chem v10-01, a 3-D chemical transport model that includes detailed tropospheric oxidation chemistry, to simulate the global distribution of acetone (www.geos-chem.org) (Bey et al., 2001; Fischer et al., 2012; Jacob et al., 2002). GEOS-Chem is driven by NASA-GEOS5 assimilated meteorological data with 0.5◦ × 0.67◦ horizontal resolution, 47 hybrid pressure-sigma vertical levels up to 0.010 hPa, and 3–6 h temporal resolution. We degraded the horizontal resolution to 4° × 5° for input into the GEOS-Chem simulations due to computational limitations associated with the number of simulations presented here. However, there are not major differences in the acetone budget between the 4° × 5° GEOS-Chem

simulations and the higher resolution 2° × 2.5° simulations we have performed. A comparison of the acetone budget between the 4° × 5° and 2° × 2.5° simulations is included in appendix A, but the values are similar. For each analysis we used 1-year simulations for 2006, preceded by 1-year spin-ups to remove the effect of initial conditions. However, because GEOS-Chem has very little year-to-year variability in modeled acetone mixing ratios (Fischer et al., 2012, 2014), the results obtained in this work do not only apply to 2006. The global acetone budget for GEOS-Chem version 10-01 is summarized in Table 2.1.

Table 2.1: **Global and hemispheric budgets** for atmospheric acetone in GEOS-Chem v10-01 compared to Fischer et al. (2012) and Jacob et al. (2002). The 'Oxidation of Isoalkanes' category includes the source of acetone from both propane and lumped alkanes with 4 or more carbon atoms. Units are in Tg of acetone. We calculate the average monthly global acetone burden is 5.57 Tg. The average monthly acetone burden is 2.92 Tg and 2.65 Tg of acetone in the Northern and Southern Hemisphere respectively.

		This work				***Fischer et al.* [2012]**	***Jacob et al.* [2002]**
	Sources						
		NH	**SH**	**Global**			
Emissions	Anthropogenic	3.2	0.4	3.6[a]		0.7	1.1 ± 0.5
	Biomass Burning	1.1	1.5	2.6		2.8	4.5 ± 1.6
	Terrestrial Biosphere	15.3	22.0	37.1		32.0	35.0 ± 10.0
Atmospheric Production	Oxidation of Isoalkanes (Primarily Anthropogenic)	14.8	3.6	18.3		26.0	21.0 ± 5.0
	Oxidation of Biogenic VOCs	2.4	3.4	5.8		5.0	7.0 ± 3.0
	Sinks						
	Oxidation by OH	13.6	12.0	25.6		33.0	27.0
	Photolysis	9.7	11.3	21.0		19.0	46.0
	Land Uptake	7.0	5.4	12.4		12.0	9.0
	Net Ocean Exchange						
	Ocean Source	20.4	31.2	51.8		80.0	NA
	Ocean Sink	27.1	32.1	59.2		82.0	NA
	Net Exchange	-6.6	-0.9	-7.5		-2.0	NA

[a]Including biofuel use

The first global budget of acetone within GEOS-Chem was constructed by Jacob et al. (2002) and included sources from anthropogenic emissions, biomass burning, terrestrial vegetation, plant decay, photochemical production in the ocean, and the atmospheric oxidation of isoalkanes, monoterpenes, and methylbutenol. We did not test the sensitivity to the emissions of the isoalkanes, or their acetone yields, and there is evidence that the emissions of propane may

be rapidly changing (Helmig et al., 2016). Global anthropogenic emissions of propane and $>C_3$ alkanes are from the RETRO inventory (Pulles et al., 2005), and are overwritten with regional inventories for the United States (EPA/NEI2011; U. S. EPA, 2013), Europe (EMEP; EMEP, 2015; Vestreng & Klein, 2002), and Asia (MIX; Li et al., 2015)). This accounts for the difference in this source of acetone between Table 2.1 and the simulation presented in Fischer et al. (2012), which used only the base RETRO inventory without any regional inventories. Jacob et al. (2002) included losses via oxidation by OH, photolysis, and dry deposition to terrestrial environments. Fischer et al. (2012) implemented local calculations of air-sea acetone fluxes by applying the two-film model of Liss & Slater (1974) with updated liquid and gas-phase transfer velocities (Johnson, 2010; Nightingale et al., 2000) and a fixed seawater concentration of 15 nM. That simulation was able to largely reproduce global patterns of atmospheric abundances, and model calculations suggested that the ocean is in near-equilibrium with the atmosphere on a global scale. The model version presented here (v10-01) includes updates to several modules relevant for the acetone budget, including both the FASTJX photolysis module (Eastham et al., 2014), which updated the implementation of the acetone photolysis parameterization recommended by Blitz et al. (2004), and the MEGAN biosphere emissions module (Guenther et al., 2012). The revised implementation of acetone photolytic loss rates in GEOS-Chem v10-01 (discussed below) widens the differences between modeled and measurement abundances as compared to Fischer et al. (2012), and results in a 43% increase in the annual total photolysis sink for acetone compared to Fischer et al. (2012) in some regions of the globe. Both model versions perform similarly when compared to the suite of acetone observations compiled by Fischer et al. (2012): the mean bias of GEOS-Chem v9 when compared to a selection of available vertical profiles of acetone is -0.14 ppb acetone, while the mean bias of v10 is -0.12

ppb (de Gouw et al., 2001, 2006; Hornbrook et al., 2011; Jacob et al., 1996; Lelieveld, 2002; Lewis et al., 2005; Mao et al., 2006; Marandino, 2005; Murphy et al., 2010; Singh et al., 1994, 2000, 2001, 2004, 2009; Warneke & de Gouw, 2001; Williams et al., 2004). Plots summarizing comparisons of model results with observations are shown in appendix A. In general, the relative variation of acetone abundance as a function of altitude is predominantly determined by the photolytic loss rate and vertical transport, while the abundances in the boundary layer and lower troposphere are determined by both emissions and loss processes.

2.2.2 The Morris Method of Sensitivity Analysis

Sensitivity analyses are used to corroborate hypotheses, set research priorities, simplify models, identify critical or interesting regions in the space of the input factors within models, and identify factors which interact and may thus generate extreme values (Oreskes et al., 1994; Saltelli & Annoni, 2010). Here we focus on 1) research prioritization and the identification of spatial dynamics in model sensitivity, and 2) the impact of uncertainties in the representation of various processes within the GEOS-Chem model used to simulate the global distribution of acetone. As in Saltelli (2004), we seek "that factor which, on average, once fixed, would cause the greatest reduction in variance" for simulated acetone mixing ratios. This factor is therefore the most important, and it exhibits the highest sensitivity.

The Morris Method is a qualitative global one-at-a-time sensitivity analysis. One-at-a-time sensitivity analyses are generally considered to be flawed methods for use on large, complex models because they cannot detect factor interactions or non-linear sensitivities (Saltelli & Annoni, 2010). The Morris Method circumvents these problems using multiple input trajectories through the sample space to use the average of derivatives and standard deviations

over the space of input factors. Consequently, the Morris Method can achieve a relatively sophisticated sensitivity analysis using a few dozen model runs, rather than the thousands required for more comprehensive variance-based analyses (Morris, 1991; Saltelli & Annoni, 2010).

In the Morris Method, a model with ***k*** independent input factors that vary across ***p*** factor levels has an input space that can be represented as a ***k***-dimensional grid with spacing determined by ***p***. As in the case of this paper, these factors represent uncertainties in the model inputs. They are used as given in the available literature and can either represent actual ranges of possible inputs or percent variations in input factors. The distribution of elementary effects associated with the *i*th input factor is found by creating random trajectories through the input space. Each trajectory is determined by randomly selecting a starting point within the input space, and then iterating through it in increments of **p**, creating a series of input vectors which each differ from the prior trajectory entry by a single value, i.e., $<X_1, X_2, X_3, X_4>$, $<X_1, X_2+p_2, X_3, X_4>$, $<X_1, X_2+p_2, X_3, X_4+p_4>$, …, $<X_1+p_1, X_2+p_2, X_3+p_3, X_4+p_4>$. Each trajectory therefore contains (***k***+1) input vectors, where ***k*** is the number of variables tested. If the chosen **k** factors are not independent, the small number of runs required by the Morris Method will not be sufficient to determine the elementary effects, and this methodology fails.

The above process is repeated ***r*** times where ***r*** is as large as possible, given the size of the model and the computational resources available (Campolongo et al., 2007; Saltelli & Annoni, 2010). Using a larger ***r*** enables a smaller choice of ***p*** and therefore a more detailed examination of the sample space. The total number of model runs (***n***) is thus ***n*** = ***r*** x (***k***+1), where **r** is the number of trajectories and **k** is the number of input factors tested. This number ***n*** will always be considerably smaller than the thousands of runs required for variance-based sensitivity analyses

or Monte Carlo methods, and is very well suited for use with computationally expensive models (Morris, 1991).

μ* and **σ** are, respectively, the mean of the absolute values and the standard deviation of the distribution of the elementary effects. Taken together, they provide a qualitative ranking of the importance of the various factors tested, and thus are without units. **μ** is a measure of the overall influence of the factor on the output. Following Campolongo et al. (2007), we use **μ*** to discuss factor effects instead of simply using **μ**. **μ** is the mean of the distribution of the elementary effects, while **μ*** is the mean of the absolute values of the elementary effects. This alteration avoids the possibility of missing model sensitivity due to non-monotonic effects or interactions between the chosen variables. In this analysis, **μ*** represents the absolute sensitivity of the modeled acetone mixing ratios to the literature-derived uncertainty ranges of the model representations of the chosen input factors. A different **μ*** is calculated for each factor. Because this ranking is qualitative, the units of **μ*** and **σ** are ignored, as their values are only relevant for comparison both within and between the two statistics.

σ, on the other hand, estimates the standard deviation of the factor's effects, whether due to nonlinearity on the part of the tested factor and/or due to interactions with other factors. If, for a given input, we find a high **σ** value, then the elementary effects of this factor depend strongly on the initial sample point chosen, and potentially upon the values of the other input factors in the same trajectory. If we find a relatively low **σ**, then the various elementary effects have similar values no matter what starting point is chosen and are independent of the other respective input factors. The importance of the factor independence becomes especially clear here: if the chosen factors are not all independent, then **σ** will overestimate the impact of the related factors, thus rendering it non-representative. In the context of this work, **σ** represents the sensitivity of the

modeled acetone mixing ratios to non-linearities in or interactions between various input factors. Thus, if two of the chosen input factors exhibit a high **σ** value, a change in one has a relatively large impact on the effect of a change in the other.

Here, we present two complementary Morris Method analyses targeted at simulated acetone in GEOS-Chem. In the first analysis, we test the sensitivity for the five factors used to simulate acetone mixing ratios: (i) direct acetone emissions from the terrestrial biosphere, (ii) monoterpene emissions from the terrestrial biosphere, (iii) acetone yields from monoterpene oxidation, (iv) ocean mixed layer acetone concentration, and (v) acetone dry deposition over ice-free land. Two analyses were made rather than one because of computational limitations on the total number of runs we were able to execute at one time.

Our second Morris Method analysis tests the sensitivity of simulated acetone mixing ratios to three of the factors explored in the first Morris Method analysis: acetone emissions from the terrestrial biosphere, ocean mixed layer acetone concentration, acetone dry deposition. The two factors controlling secondary biogenic emissions were omitted due to their lower importance (shown below in Section 3.3). Uncertainty in the model representation of acetone photolysis was added to the analysis because model results are highly dependent on the Blitz et al. (2004) quantum yield implementation, as demonstrated by differences between the Jacob et al. (2002), Fischer et al. (2012), and v10-01 simulations. The sensitivities of the common factors (acetone emissions from the terrestrial biosphere, ocean mixed layer acetone concentration, and acetone dry deposition over ice-free land) show similar results between the two runs, with only dry deposition showing significant differences (up to 40% in specific regions) between the two model runs. To account for these differences, we present the more conservative sensitivity values for each shared factor between the two runs except where otherwise denoted. For both analyses,

we use an **r** of 8, resulting in 48 model runs for the first analysis and 40 for the second – a total of 88 model runs.

2.2.3 Bounding the Ranges of Uncertainties

As discussed above, we focus on six factors (processes) of importance for the global acetone budget for this sensitivity analysis. We summarize the available literature regarding the uncertainty range associated with each of these processes below.

2.2.3.1 Direct biogenic acetone and monoterpene emissions

Many plants emit acetone and other VOCs as a by-product of both ordinary metabolism and of plant wounding and subsequent drying (Fall, 1999; de Gouw et al., 1999). Monoterpenes consist of a large number of olefinic natural hydrocarbons. Many types of vegetation emit monoterpenes, and they are estimated to account for 15% of total global biogenic VOC emissions (Guenther et al., 2012; Sindelarova et al., 2014). The Model of Emissions of Gases and Aerosols from Nature (MEGAN) v2.1 is used to calculate acetone and monoterpene emissions within GEOS-Chem for different land cover types. The emissions of each species have specific dependencies on leaf-area index, species composition, and meteorological parameters (Guenther et al., 2012). Guenther et al. (2012) estimate that global emissions of acetone are known within a factor of two. MEGAN v2.1 calculates the emissions of 41 different types of monoterpenes (Guenther et al., 2012), but only 8 of these species (listed in Table 2.2) are incorporated into the version of GEOS-Chem used here. The lifetime of this chemical family is on the order an hour, and GEOS-Chem v10.01 does not transport them between grid boxes. As discussed next, acetone production is calculated immediately following emission using a scaling

factor. Guenther et al. (2012) estimate a higher uncertainty in monoterpene emissions compared to the emissions of acetone because no annual global assessment of these compounds has been made. They estimate that the global emissions are known within a factor of three.

In order to accommodate uncertainties on both tails of the distribution, therefore, we both multiplied the flux of acetone from the biosphere by factors of 2 and ½; similarly, we multiplied the flux of monoterpenes by 3 and 1/3. Because of their distinct light- and land-cover-type dependence, the emissions of monoterpenes are treated as independent from the direct emissions of acetone from the biosphere for this sensitivity analysis. This determination is necessary in order to make use of the Morris Method, as discussed above in Section 2.2.2.

2.2.3.2 Acetone Production from Atmospheric Oxidation of Monoterpenes

Monoterpenes are not represented in the full-chemistry version of GEOS-Chem. Their inclusion into the full chemistry version has been sporadic (*e.g.*, Fischer et al. (2014)) and has not been included in the standard public release version of the model. Fischer et al. (2014) lumped terpenes with one double bond and included the RACM2 chemical mechanism for this lumped class. In this case, their integrated acetone yield over the course of a year (as diagnosed by a difference of simulations with and without terpene chemistry) was 0.017 (1.7%). Given the uncertainty in the chemistry, we did not implement, test, and evaluate an oxidation scheme for all 8 terpene species represented in the model. It would be useful to separately carry out a sensitivity study on the oxidation mechanism of the various terpenes using the known ranges of their emission.

Currently, the full-chemistry version of GEOS-Chem calculates acetone production using a single scaling factor of 0.116, representing the yield of acetone from monoterpene oxidation,

applied to the sum of the MEGAN emissions of 8 monoterpene species. In this sensitivity analysis, we adjust this yield between 7 and 21% to account for the fact that there are multiple monoterpene species being evaluated, all of which have uncertain acetone yields during atmospheric oxidation. Using the MEGAN monoterpene speciation and the minimum and maximum acetone yields taken from the literature, we construct a fractionally-weighted average of acetone yields, with each monoterpene weighted by its fraction of the total MEGAN-emitted monoterpenes. This information is summarized in Table 2.2.

Table 2.2: Weighted monoterpene-to-acetone percentage yields. Minimum and maximum yields are weighted according to the fraction of the total monoterpenes emitted from the MEGAN model.

	Max Yields	Min Yields	Fraction Of Total	Weighted Max	Weighted Min
α-Pinene	0.20[a]	0.02[e]	0.34[h]	0.07	0.01
β-pinene	0.15[b]	0.01[e]	0.17[h]	0.03	0.00
Limonene	0.20[j]	0.004[g]	0.09 [h]	0.02	0.00
Sabinene	0.30[c]	0.16[d]	0.07[h]	0.02	0.01
Myrcene	0.51[d]	0.22[g]	0.03[h]	0.02	0.01
Δ-3-Carene	0.18[e]	0.09[g]	0.06[h]	0.01	0.01
Ocimene	0.20[f]	0.18[f]	0.23[h]	0.05	0.04
Other	0.50[j]	0.02[j]	0.01[h]	0.01	0.00
			TOTAL	0.21	0.07

[a]Vinckier et al. (1998)
[b]Wisthaler et al. (2001)
[c]Carrasco et al. (2006)
[d]Reissell et al. (1999)
[e]Orlando et al. (2000)
[f]Reissell (2002)
[g]Lee et al. (2006)
[h]Sindelarova et al. (2014)
[j]α-pinene analogue

2.2.3.3 Oceanic Acetone Concentrations

There is evidence that the ocean can serve as a significant source of acetone to the atmosphere in certain regions and a significant sink in others (Marandino, 2005; Tanimoto et al., 2014; Yang et al., 2013; Zhou & Mopper, 1997). Several very recent papers have increased our understanding of the ocean-atmosphere exchange of acetone (Beale et al., 2013, 2015; Dixon et al., 2013, 2014; Tanimoto et al., 2014; Yang et al., 2013, 2014). Enriched concentrations of acetone have been measured in the surface mixed layer (Beale et al., 2013) and surface microlayer (Zhou & Mopper, 1997). Studies suggest that acetone in the oceans has multiple sources, including exchange with the atmosphere (Beale et al., 2013; Marandino, 2005; Yang et al., 2014; Zhou & Mopper, 1997), photochemical production from colored dissolved organic matter (CDOM) (Beale et al., 2013, 2015; Dixon et al., 2014; Zhou & Mopper, 1997), and bacterial production (Nemecek-Marshall et al., 1995). Acetone in the ocean is lost to the atmosphere (Beale et al., 2013; Yang et al., 2014), oxidation in the liquid phase to CO_2 (Dixon et al., 2014), and microbial uptake (Beale et al., 2013; Dixon et al., 2014). Acetone in Atlantic surface waters has an observed seasonal cycle with a maximum in the spring and summer followed by a fall-winter minimum (Beale et al., 2015), as well as a significant meridional gradient (Yang et al., 2014).

Reported acetone abundances in the ocean mixed layer range from ~2 nM (Beale et al., 2013; Dixon et al., 2014; Zhou & Mopper, 1997) to 41 nM (Tanimoto et al., 2014), with multiple other reported values falling within that range (See Table 2.3). Generally, acetone produced in the ocean mixed layer is expected to equilibrate rapidly with the atmosphere. GEOS-Chem v10 uses a prescribed fixed mixed layer acetone concentration of 15 nM (Fischer et al., 2012) and the

subsequent ocean fluxes are parameterized using a two film model (Liss & Slater, 1974). Gas and liquid-transfer velocities are taken, respectively, from Johnson (2010) and Nightingale et al. (2000). Thus the parameterization over-simplifies the oceanic acetone in several consequential ways. In this representation there are no spatial or temporal variations in concentrations of acetone in the mixed layer, and oceanic concentrations of acetone are independent of both atmospheric acetone concentrations and incoming solar radiation. This representation, therefore, does not account for significant interactions between oceanic acetone concentrations and acetone emissions from the terrestrial biosphere. For this sensitivity analysis, we considered acetone concentrations to be between 2 and 20 nM and applied each chosen concentration as a single global value to the modeled ocean.

Table 2.3: Measurements of acetone concentrations (nM) in surface seawater. Values listed where available in the reference literature.

Mean (nM)	Min (nM)	Max (nM)	Reference
17.6	9.0	20.0	Williams et al. (2004)
14.5	1.8	27.2	Marandino et al. (2005)
19.0	4.4	41.3	Tanimoto et al. (2014)
3.0	2.0	15.0	Zhou & Mopper (1997)
7.0		10.0	Yang et al. (2013)
7.5[a], 3.0[b]	2.0	8.2	Dixon et al. (2014)
6.0	2.0	10.0	Beale et al. (2015)
13.7	3.0	36.0	Yang et al. (2014)
	5.0	14.0	Read et al. (2012)
	2.0	24.0	Beale et al. (2013)
	2.0	20.0	Dixon et al. (2013)

[a]Summer Measurement
[b]Winter measurement

There is a possibility that these measured concentrations, when determined using a membrane and gas phase analysis, like that described in Yang et al. (2014), could possibly overstate the concentrations of acetone in the water sampled due to keto-enol tautomerism – that

is, the tendency of molecules to exist in some equilibrium between keto- and -enol forms. If this equilibrium constant were high enough, the removal of 2-propanone (the keto- form of acetone) from the medium might induce the conversion of 2-propenol to 2-propanone, thus over-estimating the actual amount of acetone in the water. However, the keto-enol tautomerism for acetone in seawater is sufficiently low that we do not believe it to be a source of error in these measurements (Chatfield et al., 1987).

2.2.3.4 Dry Deposition of Acetone over Ice-Free Land

Acetone dry deposition velocities in the model are set at a constant value of 0.10 cm s^{-1} over dry land, with no deposition over snow and ice. This value produces simulated diurnal acetone cycles in eastern North America during summer months that agree with observations (Jacob et al., 2002). The current 0.10 cm s^{-1} deposition rate is designed to yield a 20% decrease in atmospheric mixing ratios of acetone relative to no deposition (Jacob et al., 2002). However, there is a large range of dry deposition velocities reported in the literature. The minimum and maximum values reported recently in the literature are 0.02 cm s^{-1} (Karl et al., 2005) and 0.14 cm s^{-1} (Karl, 2004) over forested regions. We did not consider the higher rates of dry deposition found in older studies (up to 2.6 cm s^{-1}; Judeikis, 1982) since they were exclusively based on laboratory studies under unrealistic conditions.

2.2.3.5 Acetone Photolysis Rates

Acetone is photolyzed by wavelengths in the near UV to give methyl and an acetyl radical (Calvert & Pitts, 1966; IUPAC, 2013). When a molecule of acetone is photolyzed, it can produce a total of 3.2 OH radicals over two steps (Singh et al., 1995) in the presence of sufficient NO_x, or a peroxyacetyl radical (Fischer et al., 2014). This process has been modeled in GEOS-Chem in multiple ways. In Jacob et al. (2002), acetone photolysis was modeled using the quantum yields and cross-sections from Gierczak et al. (1998), while GEOS-Chem v9.0, used in Fischer et al. (2012), includes the updated quantum yields from Blitz et al. (2004). In GEOS-Chem v10.01, the implementation of the photolysis parameterization was updated again using a customized version of the FAST-JX v7.0a, a photolysis model to simulate tropospheric photolysis (Eastham et al., 2014; Wild et al., 2000). This update was not based in new measurements, but rather because of an improved implementation of the photolysis calculation. FAST-JX v7.0a uses 18 wavelength bins covering the 177-850 nm range, at altitudes up to 60 km (Eastham et al., 2014). The acetone photolysis parameterization uses absorption cross-sections from JPL 10-06, and, for each wavelength bin, applies a quantum yield for the destruction of acetone. Combining this information with the online actinic flux calculation, FAST-JX v7.0a integrates across all wavelength bins to find a photolysis frequency (j-value) in units of *per second*. Recent revisions to FAST-JX have incorporated lower quantum yields at low-temperature-long-wavelength conditions, first described by Blitz et al. (2004) and since supported by laboratory measurements at wavelengths of 248 and 308 nm (Nadasdi et al., 2010) and 300 and 308 nm (Khamaganov & Crowley, 2013). Recent research suggests highly significant acetone photolysis at ranges up to 330 nm (Blitz et al., 2006), which have not yet been verified in laboratory studies . To account for uncertainty associated with the representation

of photolysis, we inserted a modifying scalar to all modeled acetone photolysis frequencies (j-acetone) and allowed it to vary by a factor of 2 in our sensitivity analysis.

2.2.3.6 Direct biogenic acetone and monoterpene emissions

We have chosen to represent all of the uncertainty ranges as uniform distributions of equally likely values, in order to emphasize sampling the entire sample space over a more explicit but less complete representation. If we had chosen a different distribution – the normal distribution about the 'best guess', for example – we would have fewer runs with which to span the entire space, potentially missing interactions at the extreme values. This assumption is more appropriate for some factors than others. For the cases of dry deposition velocity and the acetone yield from monoterpene oxidation, there are insufficient data to conclusively favor certain values beyond setting the limits of the sample space. In contrast, the acetone and monoterpene outputs from MEGAN represent the best estimate. Guenther et al. (2012) provide an uncertainty range associated with the total global emission, but do not recommend a distribution for the uncertainty based on the model outputs.

2.3 Elementary Effects and their interdependencies

We performed two analyses: a five-factor run, including direct acetone emissions from the terrestrial biosphere, monoterpene emissions from the terrestrial biosphere, acetone yields from monoterpene oxidation, ocean mixed layer acetone concentration, and acetone dry deposition over ice-free land, and a four-factor run which substituted photolysis uncertainty for the monoterpene oxidation and yield factors. Of the three shared factors between the two rounds of analyses (direct acetone emissions from the terrestrial biosphere, ocean mixed layer acetone

concentration, and acetone dry deposition) we present the sensitivity values calculated from the four-factor run for each shared factor between the two runs except where otherwise denoted.

Figure 2.1 presents the calculated elementary effects ($\boldsymbol{\mu}^*$) for the surface, 500 mb, and 300 mb heights, respectively. The elementary effects associated with uncertainty for acetone yield from monoterpene oxidation, dry deposition, monoterpene emissions, and acetone emissions show similar spatial patterns. All four of these processes have different vegetation type, light, and temperature dependencies. The largest emissions of acetone and monoterpenes from biogenic sources are located in the Amazon and Congo rainforests, and both these equatorial regions impact both hemispheres, depending on transport.

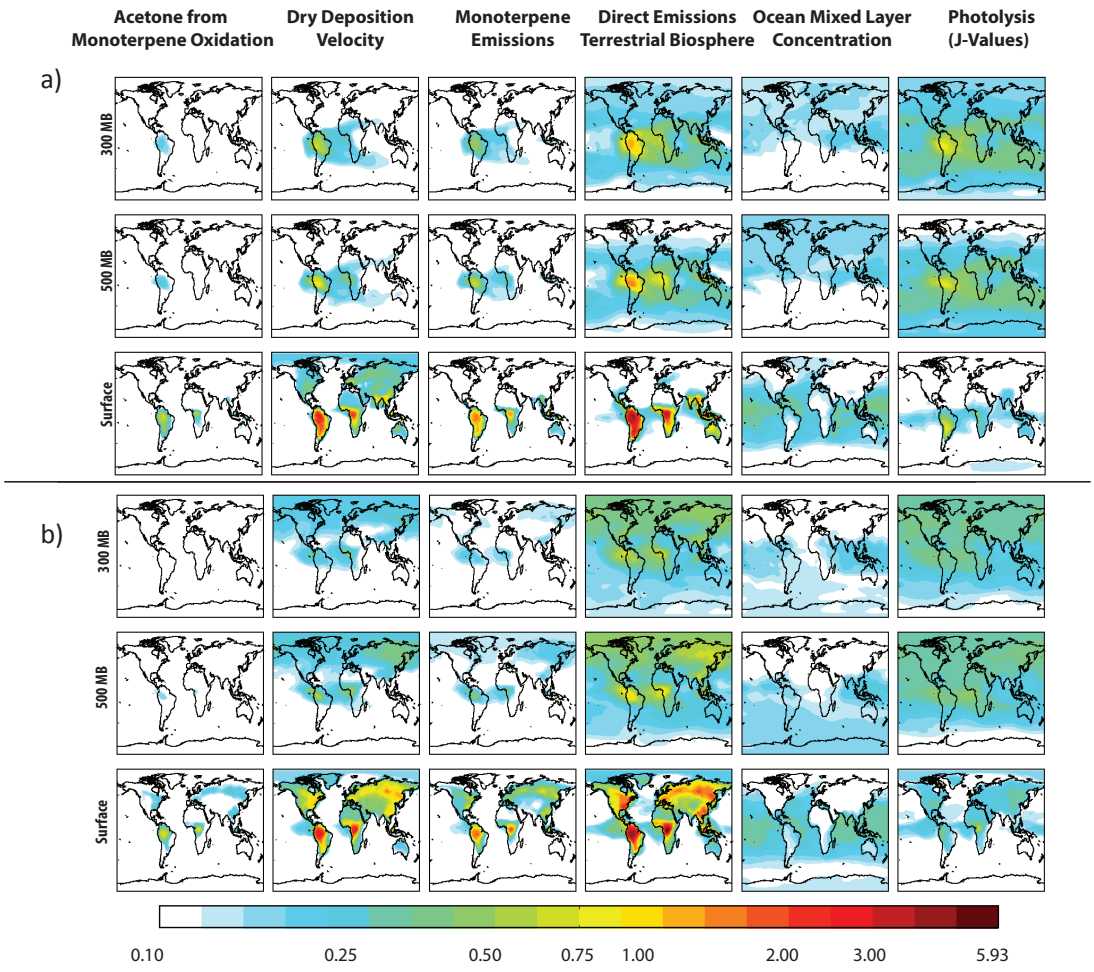

Figure 2.1: Model sensitivity (μ*) at the surface, 500 mb and 300 mb in arbitrary qualitative units for a) January and b) July. Note scale is non-linear.

Figure 2.1 shows that biogenic emissions of acetone, photolysis, and ocean mixed layer concentrations have the largest absolute effects. The uncertainty associated with the emissions of acetone from the terrestrial biosphere is most important at the surface, but the magnitude of emissions is large, and thus the scale of the impact via advection is larger than the other factors investigated here, even when further away from the primary source regions. In contrast, uncertainty associated with ocean mixed layer concentrations of acetone impact large areas of the globe, but they are not important over land when compared to emissions from the terrestrial biosphere. The impact of the ocean also decreases rapidly with altitude. The uncertainty

associated with the parameterization of photolysis in the model has a global impact. At the surface, the largest sensitivities to j-value uncertainty are seen over the continents related to the larger acetone abundance. Because the model does not exhibit significant interannual variability, we can generalize the results from these model runs for 2006 (Fischer et al., 2012).

Figure 2.2 presents the model factor interactions at three levels. The magnitude of the elementary effects (**μ***) presented in Figure 2.1 vary similarly to the sensitivity due to the interdependency between factors (**σ**) plotted in Figure 2.2. They are both comparable and have a similar spatial distribution. This is to be expected, as with **μ*,** the **σ** associated with the way acetone emissions from the biosphere are parameterized in the model is the largest factor and the most consequential. In other words, a change in the abundance of acetone due to changes in emissions will make changes in any of the loss processes more consequential.

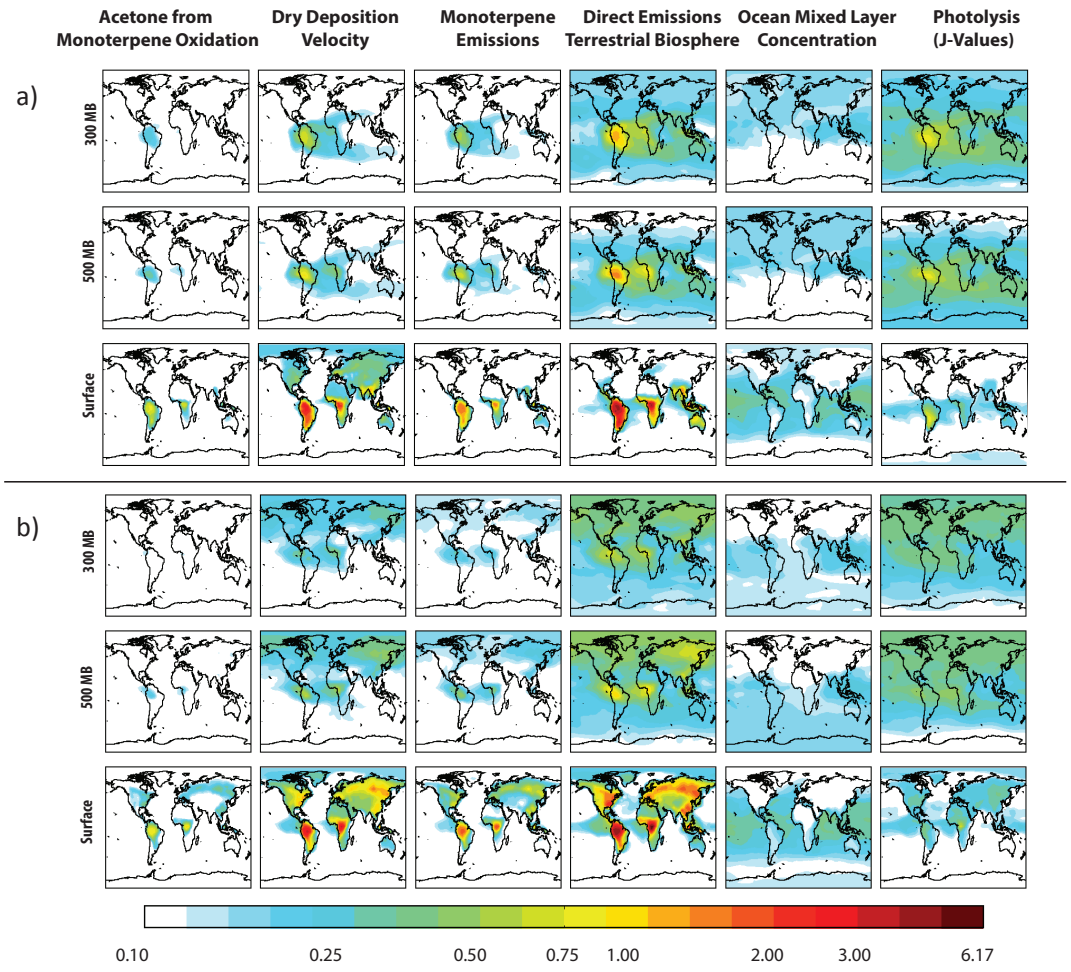

Figure 2.2: Model factor interdependencies (σ) at the surface, 500 mb and 300 mb in arbitrary qualitative units for a) January, and b) July. Note scale is not linear.

Figure 2.3 summarizes the **μ*** and **σ** presented in Figures 2.1 and 2.2 aggregated by factor across the entire globe. Additionally, Figure 2.3 distinguishes between analysis runs for the three factors tested in both analyses (direct acetone emissions from the terrestrial biosphere, ocean mixed layer acetone concentration, and acetone dry deposition). In terms of total global importance, Figure 2.3 shows a clear ranking of factor importance within the model. Uncertainties associated with emissions of acetone from the terrestrial biosphere and the representation of photolysis are the most important sources of model uncertainty in the acetone abundance for the globe, as indicated by their high **μ*** and **σ** terms, with oceanic acetone mixed

layer concentrations third. Figure 2.3 also shows that uncertainties associated with dry deposition velocity, the emissions of monoterpenes, and the acetone yield from monoterpene oxidation are less important to the simulated acetone abundances than either direct emissions from the terrestrial biosphere or photolysis. While the five-factor run displays lower sensitivities across all model runs, the qualitative relationships between the importance of the factors do not change depending on which analysis is used, with the exception of the relationship between the relative **σ** terms of the acetone emissions and photolysis factors. In the 5-factor analysis, the **σ** (interaction term) of the acetone emissions is lower than the **σ** of the photolysis term, while the **μ*** (direct influence) of the acetone emission term is larger than the **μ*** of the photolysis. This is the only non-linear relationship in the analysis; however the 5-factor analysis did not simultaneously take photolysis into account, making this comparison superficial.

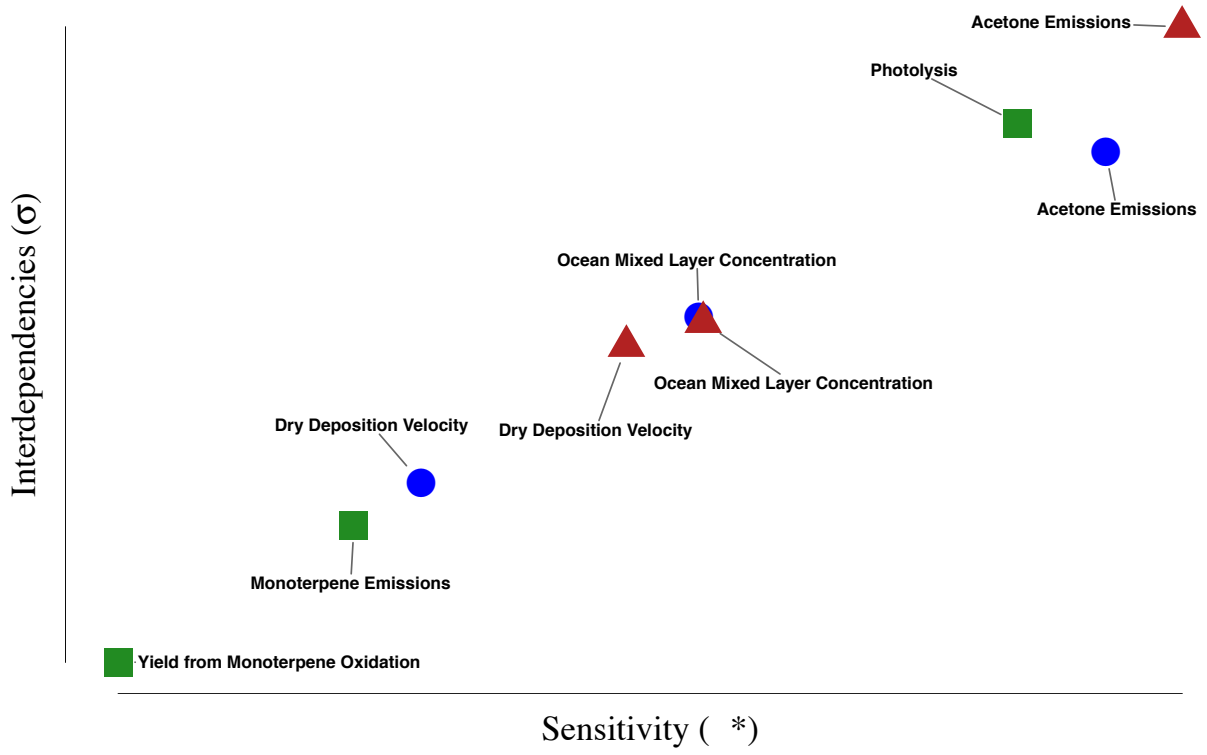

Figure 2.3: Annual total global model sensitivity (μ*) and interdepencies (σ) by factor and Morris Method run. Blue circles represent factor sensitivities from the 5-factor analysis (including monoterpene emissions and the yield from monoterpene oxidation but not photolysis). Red triangles represent factor sensitivities from the 4-factor analysis (including photolysis but not either monoterpene factor. Green squares represent factors that were only represented once. Because of this arrangement of factors within the two analyses, it is not appropriate to directly compare the 5-factor acetone emission sensitivity (in blue in the upper right of the plot) to the photolysis sensitivity, despite the fact that they appear initially to have a unique μ*-σ relationship.

Figure 2.4 shows the larger set of sensitivities from Figure 2.3 aggregated by season – summer and winter, respectively, in each hemisphere. Plotting the smaller values from Figure 2.3 does not meaningfully change the distribution of sensitivities by hemisphere. In general, sensitivity in the Northern Hemisphere is larger than in the Southern Hemisphere during both summer and winter. In both hemispheres, summer acetone mixing ratios are most sensitive to uncertainties in acetone emissions and photolysis. In the boreal summer, dry deposition is third

most important, while in the austral summer, oceanic acetone concentrations are third most important. This is due to the differences in distribution of land and ocean areas between the two hemispheres. Overall sensitivity of acetone concentrations are lower in the winter relative to the summer, most likely because of the importance of biogenic acetone sinks and sources.

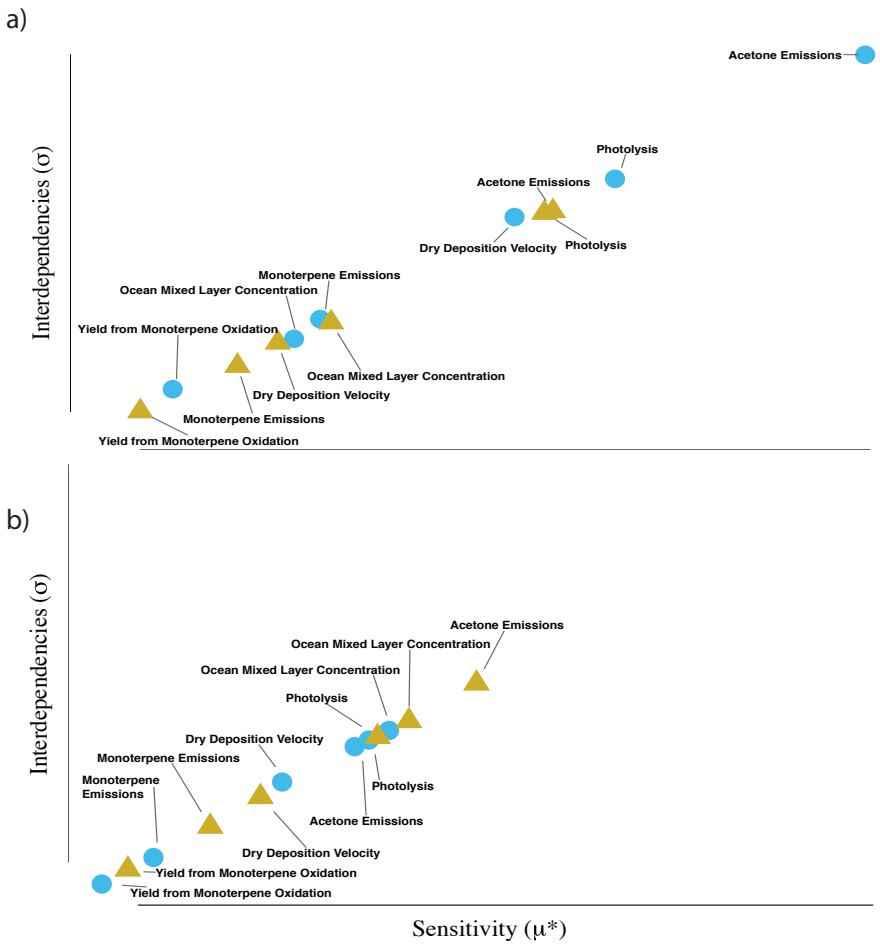

Figure 2.4: Aggregated model sensitivity (μ*) and interdepencies (σ) by hemisphere, factor, and season for the Northern (blue circles) and Southern (orange triangles) Hemispheres. Panel a) presents summer in each hemisphere (January in the SH, July in the NH), while panel b) presents winter (July in the SH, January in the NH). Panels a) and b) are plotted on the same axis.

Figure 2.5 also aggregates sensitivities by season and by region, but instead of hemispheres, it displays model sensitivity in the tropics as well as the austral and boreal subtropics. For this figure, the tropics are defined as the latitudes which fall between 30° N and

30° S. This figure treats the tropical summer as July and the tropical winter as January, but due to the lack of seasonal variability in the tropics, this assumption makes no difference to the conclusions; winter and summer sensitivities in the tropics are effectively the same.

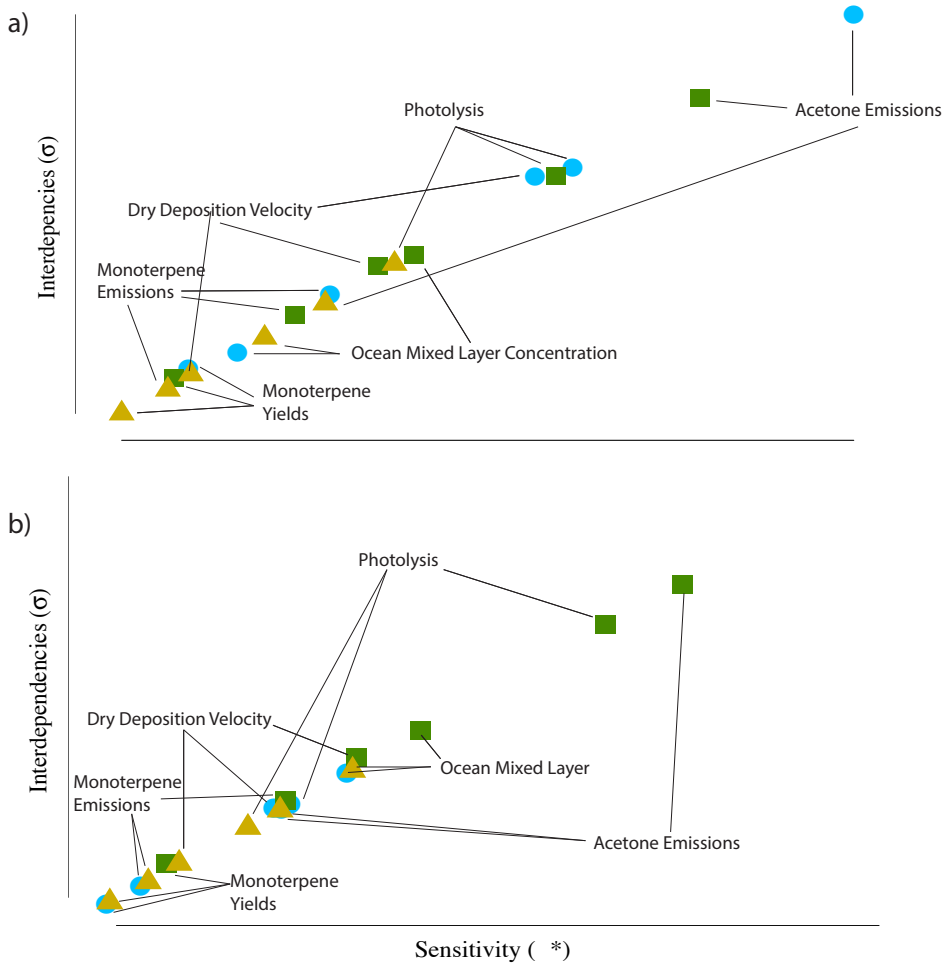

Figure 2.5: Aggregated model sensitivity (μ*) and interdependencies (σ) by region, factor, and season for the boreal (blue circles) and austral (orange triangles) subtropics, as well as the tropics (green squares). Panel a) represents summer in each region (January in the austral subtropics, July in the boreal subtropics and tropics) and panel b) presents winter (July in the austral subtropics, January in the boreal subtropics and tropics). Panels a) and b) are plotted on the same axis. Because the tropics exhibit relatively little seasonality, the choice to represent July as tropical summer is arbitrary; representing tropical summer with January data does not change the conclusions of the plot except that it represents photolysis in the tropics as slightly more important than in the Boreal Subtropics.

As Figure 2.5 shows, the sensitivity of the tropics to the most important four factors (biogenic acetone emissions, photolysis, oceanic mixed layer concentrations, and dry deposition velocity) are each larger than any of the sensitivities found during extra-tropical winters. In the summertime, direct emissions of acetone from the boreal subtropics are still the most important factor, followed by the biogenic emissions from the tropics. Photolysis is the next most important

factor in both tropical and northern subtropical regions. In the tropics, the ocean mixed layer is the third most important factor; in the boreal subtropics dry deposition is third most important. In the austral subtropics, photolysis is the most important factor, followed by direct biogenic emissions and the ocean mixed layer concentration. In all regions, the sensitivities associated with monoterpene parameterization (monoterpene emissions and monoterpene oxidation yield) are least important.

The main difference between the sensitivities of the Northern Hemisphere and Southern Hemisphere is the relative importance of the uncertainty associated with acetone concentration in the ocean mixed layer, though this is less true if the tropics are treated as a distinct region, as in Figure 2.5. The proportionately larger land surface area in the Northern Hemisphere causes the sensitivities to direct emissions of acetone from the terrestrial biosphere, the representation of photolysis, dry deposition velocity, and emissions of monoterpenes to be much larger than the ocean term in both $\boldsymbol{\mu^*}$ and $\boldsymbol{\sigma}$ at their peak summer values. The large ocean surface area in the Southern Hemisphere leads to its dominance in the Southern Hemisphere winter even when the tropics are included (as in Figure 2.4) and remains important in the Southern Hemisphere summer. In the boreal subtropics, the ocean matters very little during the summer but again becomes important in the winter. Indeed, during the winter in both subtropical regions, the oceans become the most important of the factors tested. Ocean exchange in the version of GEOS-Chem used here is parameterized using the Henry's law based Liss & Slater (1974) model. Because the Henry's law constant for acetone has a strong temperature dependence, this parameterization causes the low-latitude oceans to be a net source of acetone to the atmosphere, and there are minimal seasonal variations in this source. In contrast, cold high latitude oceans generally serve as a sink of acetone; the strength of this sink is proportional to the overlying

concentration of acetone in the air, sea surface temperatures (SST), and wind speed. During the winter at high latitudes, SST is lower and wind speed is often higher, increasing the amount of acetone sequestered into the ocean. These variables are most likely responsible for the increase in the sensitivity of the sub-polar and polar oceans shown in Figure 2.1. As previously discussed, the tropics experience almost no inter-seasonal variability in sensitivity and show a nearly identical set of sensitivities between January and July simulations.

Separating this sensitivity by altitude shows broadly similar patterns across the hemispheres. The effects of uncertainty associated with acetone emissions dominate at the surface, but the other sources of uncertainty become important aloft. The importance of uncertainty associated with the way photolysis is parameterized in the model increases with altitude, and it becomes of comparable importance above 300 mb to the uncertainty associated with direct biogenic emissions of acetone. Regardless of altitude or analysis run used, uncertainty associated with the amount of acetone in the ocean mixed layer is more consequential in the austral than the boreal troposphere.

There are other sources of model uncertainty in addition to those tested here, including other major known sources and sinks in the acetone budget (as summarized in Table 2.1) as well as more structural uncertainties involving model creation, such as oxidation schemes or transport. Evaluating structural uncertainties was beyond the scope of our work in this paper. For example, the OH fields in the models are calculated and do not have variable inputs. OH abundances vary drastically from location to location, making it challenging to systematically vary them. We have also not examined model sensitivity to the emission of alkanes, which could indeed be a very important factor over terrestrial regions. As we note in Table 2.1, the atmospheric oxidation of propane and $>C_3$ alkanes represents the third largest source of acetone

to the global budget. We anticipate high model sensitivities as a result of changing propane emissions. Propane abundances are currently changing in the Northern Hemisphere (Helmig et al., 2016), and the most recent changes have been attributed to U.S. oil and natural gas production. Constraining the emissions of propane and other light alkanes better using GEOS-Chem and unpublished observations (i.e., from field campaigns in the last year) is the subject of ongoing work in our research group and our collaborators. A full investigation of the source of acetone from the oxidation of propane and the isoalkanes will require further studies to understand the uncertainty in both the quantity and spatial distribution of the emissions, as well as the oxidation scheme. Unlike monoterpenes, the oxidation of propane and larger alkanes is treated explicitly in the chemical mechanism. However, the lumping scheme has not been revisited this decade.

2.4 Implications

There are several implications of this work. Though definitive conclusions can't be made without performing a Morris Method analysis on other models, we expect that the following general implications of this work are broadly applicable to many global chemical transport models.

1. In both hemispheres, uncertainty associated with the direct emissions of acetone from the terrestrial biosphere is the most important factor of the six sources of model uncertainty that we tested. However, the source of acetone from the terrestrial biosphere is the largest unbalanced source of acetone considered in this analysis (The raw oceanic source is larger, but it is balanced by the large ocean sink such that the *net* ocean exchange is small - see Table 2.1). Uncertainties in how acetone emissions from the terrestrial biosphere are represented have more impact on the

acetone abundances in the model even though the range of uncertainty (a factor of two) is relatively small compared to several of the other factors examined. Therefore, establishing more accurate direct biogenic emission estimates should be a major research priority for improving the acetone budget.

2. The GEOS-Chem model is relatively insensitive to variations in the acetone source from monoterpene oxidation. Monoterpene oxidation is a significant source of acetone that should be accounted for in global budget studies. We ran a simulation where we used the upper bound of both MEGAN emissions of monoterpenes and the highest literature yields from Table 2.2. This simulation produced an acetone source of the same order of magnitude as that found in (Khan et al., 2015), and represents a more than 500% increase relative to the standard version of GEOS-Chem, as represented in Table 2.1 (Kelp et al., 2015). The global total emissions of monoterpenes in Khan et al. (2015) are 127.0 Tg/yr, while the global total emissions of monoterpenes in our simulation are 123.4 Tg/yr; Khan et al. (2015) do not specify the speciation of monoterpene emissions. We provide speciation in Figure 2.2 for our simulation. However, the yield implied from Table 1 in Khan et al. (2015) is significantly higher than the literature values presented in our Table 2.2. Based upon the sensitivities of the GEOS-Chem model version presented here and the current oxidation yield ranges available in the literature, monoterpene oxidation is less important in determining acetone mixing ratios than the other factors tested here.

3. Accurately representing the amount of acetone in the ocean mixed layer is more important for simulating atmospheric abundances of acetone in the Southern Hemisphere than in the Northern Hemisphere because of the lower land surface in the NH relative to that in the SH. Accurately representing oceanic acetone exchange is also very important in modeling sub-

tropical wintertime acetone mixing ratios. In the austral winter (July), uncertainty associated with the concentration of acetone in the ocean mixed layer is of comparable importance to the uncertainty associated with direct emissions of acetone from the terrestrial biosphere. In austral summer (January), uncertainties in the representation of ocean exchange are more important to the acetone budget than they are in the boreal summer (July). The current representation of ocean exchange in our model is simplistic. On a global scale the ocean is in near-equilibrium with the atmosphere, with the ocean acting as a net sink at high latitudes and a net source in equatorial regions. Improvements to ocean exchange in global chemical transport models would include a specific mechanism for acetone production and destruction in the ocean mixed layer. Models that do not include a representation of ocean exchange of acetone are unlikely to correctly simulate atmospheric acetone abundances, particularly in the Southern Hemisphere.

4. In both hemispheres, the model is very sensitive to the representation of acetone photolysis frequency, especially in the mid to upper troposphere, where acetone is hypothesized to be an important source of HO_x. The updated acetone photolysis rates indicate that that loss via oxidation and photolysis are comparable on a global scale.

Chapter References

Beale, R., Dixon, J. L., Arnold, S. R., Liss, P. S., & Nightingale, P. D. (2013). Methanol, acetaldehyde, and acetone in the surface waters of the Atlantic Ocean. *Journal of Geophysical Research: Oceans*, *118*(10), 5412–5425. https://doi.org/10.1002/jgrc.20322

Beale, R., Dixon, J. L., Smyth, T. J., & Nightingale, P. D. (2015). Annual study of oxygenated volatile organic compounds in UK shelf waters. *Marine Chemistry*, *171*, 96–106. https://doi.org/10.1016/j.marchem.2015.02.013

Bey, I., Jacob, D. J., Yantosca, R. M., Logan, J. A., Field, B. D., Fiore, A. M., et al. (2001). Global Modeling of tropospheric chemistry with assimilated meteorology: Model description and evaluation. *Journal of Geophysical Research*, *106*(D19), 23073–23095.

Blitz, M. A., Heard, D. E., Pilling, M. J., Arnold, S. R., & Chipperfield, M. P. (2004). Pressure and temperature-dependent quantum yields for the photodissociation of acetone between 279 and 327.5 nm. *Geophysical Research Letters*, *31*(6), n/a-n/a. https://doi.org/10.1029/2003gl018793

Blitz, M. A., Heard, D. E., & Pilling, M. J. (2006). Study of Acetone Photodissociation over the Wavelength Range 248-330 nm: Evidence of a Mechanism Involving Both the Singlet and Triplet Excited States. *Journal of Physical Chemistry*, *110*, 6742–6756.

Calvert, J. G., & Pitts, J. N. (1966). *Photochemistry*. University of California, Riverside: John Wiley & Sons, Inc.

Campolongo, F., Cariboni, J., & Saltelli, A. (2007). An effective screening design for sensitivity analysis of large models. *Environmental Modelling & Software*, *22*(10), 1509–1518. https://doi.org/10.1016/j.envsoft.2006.10.004

Chatfield, R. B., Gardner, E. P., & Calvert, J. G. (1987). Sources and Sinks of Acetone in the Troposphere: behavior of Reactive Hydrocarbons and a Stable Product. *Journal of Geophysical Research*, *92*(D4), 4208–4216.

Dixon, J. L., Beale, R., & Nightingale, P. D. (2013). Production of methanol, acetaldehyde, and acetone in the Atlantic Ocean. *Geophysical Research Letters*, *40*(17), 4700–4705. https://doi.org/10.1002/grl.50922

Dixon, J. L., Beale, R., Sargeant, S. L., Tarran, G. A., & Nightingale, P. D. (2014). Microbial acetone oxidation in coastal seawater. *Front Microbiol*, *5*, 243. https://doi.org/10.3389/fmicb.2014.00243

Eastham, S. D., Weisenstein, D. K., & Barrett, S. R. H. (2014). Development and evaluation of the unified tropospheric–stratospheric chemistry extension (UCX) for the global chemistry-transport model GEOS-Chem. *Atmospheric Environment*, *89*, 52–63. https://doi.org/10.1016/j.atmosenv.2014.02.001

EMEP. (2015). The co-operative programme for monitoring and evaluation of the long-range transmissions of air pollutants in Europe.

Fall, R. (1999). *Biogenic emissions of volatile organic compounds from higher plants*. San Diego: Academic Press, San Diego.

Fischer, E. V., Jacob, D. J., Millet, D. B., Yantosca, R. M., & Mao, J. (2012). The role of the ocean in the global atmospheric budget of acetone. *Geophysical Research Letters*, *39*(1), n/a-n/a. https://doi.org/10.1029/2011gl050086

Fischer, E. V., Jacob, D. J., Yantosca, R. M., Sulprizio, M. P., Millet, D. B., Mao, J., et al. (2014). Atmospheric peroxyacetyl nitrate (PAN): a global budget and source attribution.

Atmospheric Chemistry and Physics, *14*(5), 2679–2698. https://doi.org/10.5194/acp-14-2679-2014

Gierczak, T., Burkholder, J. B., Bauerle, S., & Ravishankara, A. R. (1998). Photochemistry of acetone under tropospheric conditions. *Chemical Physics*, *231*, 229–244.

de Gouw, J. A., Howard, C. J., Custer, T. G., & Fall, R. (1999). Emissions of volatile organic compounds from cut grass and clover are enhanced during the drying process. *Geophysical Research Letters*, *26*(7), 811–814. https://doi.org/10.1029/1999gl900076

de Gouw, J. A., Warneke, C., Scheeren, H. A., van der Veen, C., Bolder, M., Scheele, M. P., et al. (2001). Overview of the trace gas measurements on board the Citation aircraft during the intensive field phase of INDOEX. *Journal of Geophysical Research: Atmospheres*, *106*(D22), 28453–28467. https://doi.org/10.1029/2000jd900810

de Gouw, J. A., Warneke, C., Stohl, A., Wollny, A. G., Brock, C. A., Cooper, O. R., et al. (2006). Volatile organic compounds composition of merged and aged forest fire plumes from Alaska and western Canada. *Journal of Geophysical Research: Atmospheres*, *111*(D10), n/a-n/a. https://doi.org/10.1029/2005jd006175

Guenther, A., Jiang, X., Heald, C. L., Sakulyanontvittaya, T., Duhl, T., Emmons, L. K., & Wang, X. (2012). The Model of Emissions of Gases and Aerosols from Nature version 2.1 (MEGAN2.1): an extended and updated framework for modeling biogenic emissions. *Geoscientific Model Development*, *5*(6), 1471–1492. https://doi.org/10.5194/gmd-5-1471-2012

Helmig, D., Rossabi, S., Hueber, J., Tans, P., Montzka, S. A., Masarie, K., et al. (2016). Reversal of global atmospheric ethane and propane trends largely due to US oil and natural gas production. *Nature Geoscience*, *9*(7), 490–495. https://doi.org/10.1038/ngeo2721

Hornbrook, R. S., Blake, D. R., Diskin, G. S., Fried, A., Fuelberg, H. E., Meinardi, S., et al. (2011). Observations of nonmethane organic compounds during ARCTAS − Part 1: Biomass burning emissions and plume enhancements. *Atmospheric Chemistry and Physics*, *11*(21), 11103–11130. https://doi.org/10.5194/acp-11-11103-2011

IUPAC. (2013). *Data Sheet P7*.

Jacob, D. J., Heikes, E. G., Fan, S. M., Logan, J. A., Mauzerall, D. L., Bradshaw, J. D., et al. (1996). Origin of ozone and NOxin the tropical troposphere: A photochemical analysis of aircraft observations over the South Atlantic basin. *Journal of Geophysical Research: Atmospheres*, *101*(D19), 24235–24250. https://doi.org/10.1029/96jd00336

Jacob, D. J., Field, B. D., Jin, E. M., Bey, I., Li, Q., Logan, J. A., & Yantosca, R. M. (2002). Atmospheric budget of acetone. *Journal of Geophysical Research*, *107*(D10). https://doi.org/10.1029/2001jd000694

Johnson, M. T. (2010). A numerical scheme to calculate temperature and salinity dependent air-water transfer velocities for any gas. *Ocean Science*, *6*(4), 913–932. https://doi.org/10.5194/os-6-913-2010

Judeikis, H. S. (1982). *Laboratory Measurements of Dry Deposition of Acetone over Adobe Clay Soil*. Washington, D.C.: American Geophysical Union.

Karl, T. (2004). Exchange processes of volatile organic compounds above a tropical rain forest: Implications for modeling tropospheric chemistry above dense vegetation. *Journal of Geophysical Research*, *109*(D18). https://doi.org/10.1029/2004jd004738

Karl, T., Harley, P., Guenther, A., Rasmussen, R., Baker, B., Jardine, L., & Nemitz, E. (2005). The bi-directional exchange of oxygenated VOCs between a loblolly pine (Pinus tadea) plantation and the atmosphere. *Atmospheric Chemistry and Physics*, *5*(11), 3015–3031.

Kelp, M., Brewer, J. F., Keller, C., & Fischer, E. V. (2015, December). *Evaluating the potential Importance of Monoterpene Degradation for Global Acetone Production*. Presented at the AGU Fall Meeting 2015, San Francisco, CA.

Khamaganov, V. G., & Crowley, J. N. (2013). Pressure dependent photolysis quantum yields for CH3C(O)CH3 at 300 and 308 nm and at 298 and 228 K. *Phys Chem Chem Phys*, *15*(25), 10500–9. https://doi.org/10.1039/c3cp50291k

Khan, M. A. H., Cooke, M. C., Utembe, S. R., Archibald, A. T., Maxwell, P., Morris, W. C., et al. (2015). A study of global atmospheric budget and distribution of acetone using global atmospheric model STOCHEM-CRI. *Atmospheric Environment*, *112*, 269–277. https://doi.org/10.1016/j.atmosenv.2015.04.056

Lelieveld, J. (2002). Global Air Pollution Crossroads over the Mediterranean. *Science*, *298*(5594), 794–799. https://doi.org/10.1126/science.1075457

Lewis, A. C., Hopkins, J. R., Carpenter, L. J., Stanton, J., Read, K. A., & Pilling, M. J. (2005). Sources and sinks of acetone, methanol, and acetaldehyde in North Atlantic marine air. *Atmospheric Chemistry and Physics*, *5*, 1963–1974.

Li, M., Q. Zhang, J. Kurokawa, J. H. Woo, K. B. He, Z. Lu, et al. (2015). MIX: a mosaic Asian anthropogenic emission inventory for the MICS-Asia and the HTAP projects. *Atmos. Chem. Phys. Discuss.*, *15*(23), 34813–34869. https://doi.org/10.5194/acpd-15-34813-2015

Liss, P., & Slater, P. G. (1974). Flux of Gases across the Air-Sea Interface. *Nature*, *247*, 181–184.

Mao, H., Talbot, R., Nielsen, C., & Sive, B. (2006). Controls on methanol and acetone in marine and continental atmospheres. *Geophysical Research Letters*, *33*(2). https://doi.org/10.1029/2005gl024810

Marandino, C. A. (2005). Oceanic uptake and the global atmospheric acetone budget. *Geophysical Research Letters*, *32*(15). https://doi.org/10.1029/2005gl023285

Morris, M. (1991). Factorial Sampling Plans for Preliminary Computational Experiments. *Technometrics*, *33*(2), 161–174.

Murphy, J. G., Oram, D. E., & Reeves, C. E. (2010). Measurements of volatile organic compounds over West Africa. *Atmospheric Chemistry and Physics*, *10*(12), 5281–5294. https://doi.org/10.5194/acp-10-5281-2010

Nadasdi, R., Zugner, G. L., Farkas, M., Dobe, S., Maeda, S., & Morokuma, K. (2010). Photochemistry of methyl ethyl ketone: quantum yields and S1/S0-diradical mechanism of photodissociation. *Chemphyschem*, *11*(18), 3883–95. https://doi.org/10.1002/cphc.201000522

Nemecek-Marshall, M., Wojciechowski, C., Kuzma, J., Silver, G. M., & Fall, R. (1995). Marine Vibrio Species Produce the Volatile Organic Compound Acetone. *Applied and Environmental Microbiology*, *61*(1), 44–47.

Nightingale, P. D., Malin, G., Law, C. S., Watson, A. J., Liss, P. S., Liddicoat, M. I., et al. (2000). In situ evaluation of air-sea gas exchange parameterizations using novel conservative and volatile tracers. *Global Biogeochemical Cycles*, *14*(1), 373–387. https://doi.org/10.1029/1999gb900091

Oreskes, N., Shrader-Frechette, K., & Belitz, K. (1994). Verification, Validation, and Confirmation of Numerical Models in the Earth Sciences. *Science*, *263*(5147), 641–646.

Pulles, T., Brand, R., van het Bolscher, M., Endresen, O., Sorgard, E., Sundet, J. K., et al. (2005). *RETRO Emission Inventory: anthropogenic emission database*. France.

Saltelli, A. (2004). *Sensitivity analysis in practice : a guide to assessing scientific models.* Hoboken, NJ.: Wiley.

Saltelli, A., & Annoni, P. (2010). How to avoid a perfunctory sensitivity analysis. *Environmental Modelling & Software*, *25*(12), 1508–1517. https://doi.org/10.1016/j.envsoft.2010.04.012

Sindelarova, K., Granier, C., Bouarar, I., Guenther, A., Tilmes, S., Stavrakou, T., et al. (2014). Global data set of biogenic VOC emissions calculated by the MEGAN model over the last 30 years. *Atmospheric Chemistry and Physics*, *14*(17), 9317–9341. https://doi.org/10.5194/acp-14-9317-2014

Singh, H. B., O'Hara, D., Herlth, D., Sachse, W., Blake, D. R., Bradshaw, J. D., et al. (1994). Acetone in the atmosphere: Distribution, sources, and sinks. *Journal of Geophysical Research*, *99*, 1805–1819.

Singh, H. B., Kanakidou, M., Crutzen, P. J., & Jacob, D. J. (1995). High concentrations and photochemical fate of oxygenated hydrocarbons in the global troposphere. *Nature*, *378*, 50–54.

Singh, H. B., Viezee, W., Chen, Y., Bradshaw, J. D., Sandholm, S., Blake, D. R., et al. (2000). Biomass burning influences on the composition of the remote South Pacific troposphere: analysis based on observations from PEM-Tropics-A. *Atmospheric Environment*, *34*, 635–644.

Singh, H. B., Chen, Y., Stuadt, A., Jacob, D., Blake, D., Heikes, B., & Snow, J. (2001). Evidence from the southern Pacific troposphere for large global abundances and sources of oxygenated organic compounds. *Nature*, *410*, 1078–1081.

Singh, H. B., Salas, L. J., Chatfield, R. B., Czech, E., Fried, A., Walega, J., et al. (2004). Analysis of the atmospheric distribution, sources, and sinks of oxygenated volatile organic chemicals based on measurements over the Pacific during TRACE-P. *Journal of Geophysical Research*, *109*(D15). https://doi.org/10.1029/2003jd003883

Singh, H. B., Brune, W. H., Crawford, J. H., Flocke, F., & Jacob, D. (2009). Chemistry and transport of pollution over the Gulf of Mexico and the Pacific: spring 2006 INTEX-B campaign overview and first results. *Atmospheric Chemistry and Physics*, *9*, 2301–2318.

Tanimoto, H., Kameyama, S., Omori, Y., Inomata, S., & Tsunogai, U. (2014). High-Resolution Measurement of Volatile Organic Compounds Dissolved in Seawater Using Equilibrator Inlet-Proton Transfer Reaction-Mass Spectrometry (EI-PTR-MS), 89–115. https://doi.org/10.5047/w-pass.a02.001

U. S. EPA. (2013). *National Emissions Inventory 2011*. (U. S. EPA, Trans.).

Vestreng, V., & Klein, H. (2002). *Emissions Data Reported to UN-ECE/EMEP: Quality assurance and trend analysis & presentation of WebDab*. Oslo, Norway: Norwegian Meteorological Institute.

Warneke, C., & de Gouw, J. A. (2001). Organic trace gas composition of the marine boundary layer over the northwest Indian Ocean in April 2000. *Atmospheric Environment*, *35*, 5923–5933.

Wild, O., Zhu, X., & Prather, M. J. (2000). Fast-J: Accurate simulaton of in- and below-cloud photolysis in tropospheric chemical models. *Journal of Atmospheric Chemistry*, *37*(3), 245–282. https://doi.org/10.1023/a:1006415919030

Williams, J., Holzinger, R., Gros, V., Xu, X., Atlas, E., & Wallace, D. W. R. (2004). Measurements of organic species in air and seawater from the tropical Atlantic. *Geophysical Research Letters*, *31*(23), n/a-n/a. https://doi.org/10.1029/2004gl020012

Yang, M., Beale, R., Smyth, T., & Blomquist, B. (2013). Measurements of OVOC fluxes by eddy covariance using a proton-transfer-reaction mass spectrometer – method development at a coastal site. *Atmospheric Chemistry and Physics*, *13*(13), 6165–6184. https://doi.org/10.5194/acp-13-6165-2013

Yang, M., Beale, R., Liss, P., Johnson, M., Blomquist, B., & Nightingale, P. (2014). Air–sea fluxes of oxygenated volatile organic compounds across the Atlantic Ocean. *Atmospheric Chemistry and Physics*, *14*(14), 7499–7517. https://doi.org/10.5194/acp-14-7499-2014

Zhou, X., & Mopper, K. (1997). Photochemical production of low-molecular-weight-carbonyl compounds in seawater and surface microlayer and their air-sea exchange. *Marine Chemistry*, *56*, 201–213.

CHAPTER 3: ATMOSPHERIC PHOTOLYSIS OF METHYL ETHYL, DIETHYL, AND PROPYL ETHYL KETONES – TEMPERATURE DEPENDENT UV ABSORPTION CROSS-SECTIONS [2]

3.1. Chapter Introduction

Ketone photolysis is a potentially important source of HO_x radicals in the upper troposphere. To represent this photolysis, models need to include actinic flux, quantum yield, and absorption cross sections over a range of atmospherically relevant conditions. This work seeks to improve the representation of ketone UV absorption by quantifying it as a function of temperature. We present observations of 1 nm resolution absorption cross sections from 200-335 nm of methyl ethyl ketone (MEK) and diethyl ketone (DEK) at temperatures between 242 and 320 K, as well as propyl ethyl ketone (PEK) cross sections at 296 K. Our measured room-temperature absorption cross sections agree to within 2%, 2% and 5% with previous studies for MEK, DEK, and PEK spectra, respectively. We parameterize the temperature dependence of the cross sections of MEK and DEK using a two-state model, which reproduces our experimental results well. With additional assumptions, this model can be applied to the temperature dependence of PEK in the absence of experimental data. This model is appropriate for atmospherically relevant temperatures both inside and outside the temperatures used in this study and is suitable for incorporation into model atmospheric photolysis schemes. R programs to facilitate usage of these data are included in appendix B. Inclusion of temperature dependent absorption cross sections in atmospheric photolysis calculations decreased the rate coefficients of MEK, DEK, and PEK

[2] Portions of this chapter contain published work. Citation: Brewer, J. F., Papanastasiou, D. K., Burkholder, J. B., Fischer, E. V., Ren, Y., Mellouki, A., & Ravishankara, A. R. (2019). Atmospheric Photolysis of Methyl Ethyl, Diethyl, and Propyl Ethyl Ketones: Temperature Dependent UV Absorption Cross Sections. Journal of Geophysical Research: Atmospheres. https://doi.org/10.1029/2019JD030391

photolysis in the upper troposphere when compared to those calculated using only the room temperature cross sections; the decrease can be as large as 20-25%.

In this chapter, we report absorption cross sections of MEK and DEK (along with their uncertainties) between 200-335 nm at temperatures ranging from 242-320 K, with a spectral resolution of 1 nm. We also report absorption cross sections for PEK at the same resolution and wavelengths at 296 K. The measured temperature dependent cross sections are parameterized for use in models. The data are also used to calculate representative first-order rate coefficients for the photodissociation (J-values) of each compound for a few representative sets of atmospheric conditions. The model calculations enable us to contextualize the atmospheric importance of the cross section temperature dependence to the photolysis rate of these compounds, as well as provide atmospheric modelers a basis for comparison to their own ketone photolysis rate calculations.

Characterization of ketone photolysis pathways is needed because the process produces HO_x. Ketones are photolyzed in the troposphere between ~290 to 350 nm. Absorption in this range is due to an electronic transition centered around the CO double bond, which is the chromophore. Following excitation to the singlet upper state, the molecule quickly undergoes intersystem crossing to a longer-lived triplet state, from which it can dissociate or be quenched (Haas, 2003). Radiative deactivation can be shown to be essentially negligible at tropospheric pressures given the rapid intersystem crossing to the triplet state and long radiative lifetime of the triplet state (Haas, 2003). The exact amount of HO_x produced from the photolysis of ketones depends on the abundance of NO_x, possibility of wet scavenging, and transport to other regions.

Keller-Rudek et al. (2013) have summarized all the available cross sections data on ketones. Multiple measurements of the absorption cross sections of MEK (Martinez et al., 1992; McMillan, 1966; Yujing & Mellouki, 2000) and DEK (Koch et al., 2008; Koch & Hanson, 2003; McMillan, 1966) exist at room temperature and higher. PEK cross sections have been reported at only room temperature. (Horowitz, 1999). Nádasdi et al. (2007) have reported MEK cross sections at atmospherically-relevant lower temperatures, but only at a few select wavelengths. Therefore, measurements of the absorption spectra of MEK and DEK at lower atmospheric temperatures are needed to accurately represent their photolysis in chemical transport models and to calculate their HO_x production potential in the troposphere, especially at the upper troposphere where the temperatures are lower than 298 K.

3.2. Materials and Methods

3.2.1. Experimental Setup

A schematic of the system used to measure the gas phase spectra of MEK, DEK, and PEK is shown in Figure 3.1. This apparatus is similar to those used in past studies for similar measurements (e.g., Papanastasiou et al. (2011)). Two absorption cells, one at room temperature and another at temperature of interest, were connected in series. The same mixture of a given ketone in a diluent gas was flowed through each absorption cell; in some instances, the measurements were made using static mixtures, which filled both cells.

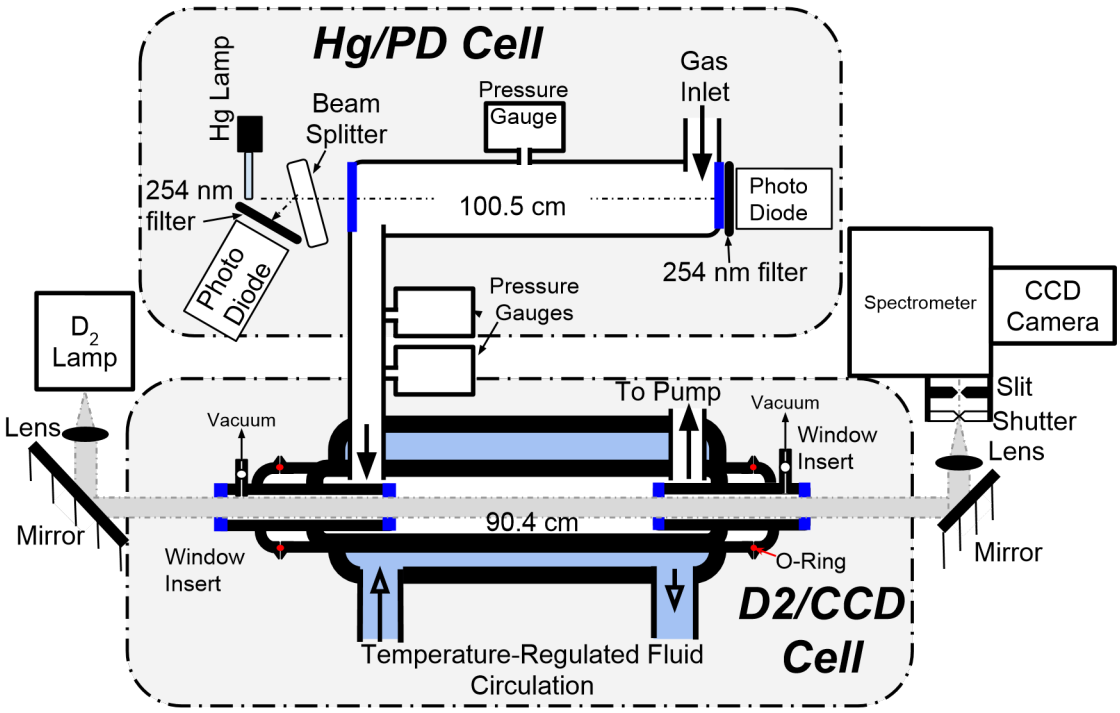

Figure 3.1- A schematic of the UV/visible absorption apparatus, which consists of two cells, one temperature controlled and illuminated with deuterium lamp (D_2/CCD Cell) and one at room temperature illuminated by a mercury lamp (Hg/PD cell). Pressure is measured using 100 and 1000 Torr capacitance manometers.

The absorption spectra of MEK, DEK and PEK were measured between 200-335 nm and at the different temperatures using the apparatus shown in Figure 3.1. This setup consisted of UV/visible light from a collimated 30 W D_2 lamp, a temperature-regulated absorption cell, an absorption cell maintained at room temperature, and a 0.5 m spectrometer equipped with a charge-coupled device (CCD) detector. The absorption cell (shown in Figure 3.1 and labeled D2/CCD cell) was a jacketed Pyrex tube (I.D. ~2.5 cm) where the temperature-controlled section was 90.5 cm long. The inset quartz windows ensured that the entire absorption path length was at the specified temperature. This cell was cooled or heated by flowing a silicone fluid from a temperature-controlled bath. The temperature was constant to within 2 K over the entire length of the tube for all temperatures except at the lowest temperature of the study where the difference

between the coolant entrance and exits ports was ~5 K. The temperature in the cell was taken to be the average of the temperature between the two ends. The measured temperatures were accurate to 0.5 K. The output of the D_2 lamp was collimated, passed through the absorption cell, and focused onto the entrance slit of the 0.5 m spectrometer which was equipped with a 512 x 2048-pixel CCD camera. Only the central (~100 x 2048 array) pixels were used. The entrance slit width was adjusted to 100 μm that yielded a resolution of ~1 nm as measured by the width of a mercury atomic line. A mechanical shutter in front of the entrance slit controlled the exposure (roughly 0.3 s) such that the CCD pixels were almost completely filled (~80-90%) when the absorption cell was empty. The absorbance at each pixel was calculated using the linearized Beer-Lambert law:

$$(3.1)\ A(\lambda) \ = \ -ln\left(\frac{I_0(\lambda)}{I(\lambda)}\right) \ = \ \sigma(\lambda, T) \times [sample] \times L$$

where $I_0(\lambda)$ and $I(\lambda)$ were the intensities measured at each wavelength with the cell either empty or filled with the non-absorbing diluent gas and with the absorbant in the cell, respectively. $\sigma(\lambda,T)$ was the ketone cross section at wavelength l and at the temperature of the cell, [sample] was the ketone concertation in the absorption cell, and L was the absorption pathlength. Typically, 120 spectra were measured and co-added to obtain each $I(\lambda)$ and $I_0(\lambda)$. The measured absorbance at each wavelength varied linearly with ketone concentration. The absorption spectrum reported in this work was measured at the highest concentration practicable for the temperature and species in question, i.e., our best quality spectrum with the highest possible absorbance (<1.1, base e absorbance) and lowest possible baseline fluctuation (<0.001 absorbance unit). The entire absorption spectrum was then converted to cross sections by scaling to the cross section at the peak of the near UV band (~280 nm) measured following a Beer's law

analysis. Ketone concentration in the absorption cells was calculated using pressure measurements and the mixing ratio of manometrically-prepared ketone/N_2 mixtures in 12 L Pyrex bulbs.

A second cell, held at room temperature, was used to measure the ketone absorbance at 254 nm. This cell (Hg/PD Cell) was 100.4 cm long with quartz windows. UV light from a penray mercury lamp (254 nm Hg line) was passed through this cell to measure the absorbance at room temperature at this one fixed wavelength. Both the input and transmitted 254 nm light intensities were measured using two photodiodes, positioned before and after the UV beam passed through the cell (Figure 3.1). This arrangement enabled precise measurements of the attenuation by continually accounting for the lamp intensity fluctuation. Absorbance was calculated using the Beer-Lambert law as in the D2/CCD cell (Equation 3.1). In the Hg/PD cell, however, $I_0(\lambda)$ and $I(\lambda)$ represented the ratios between the intensities measured by the photodiode at the far end of the cell (normalized to the measured lamp input) with and without a sample present. Absorbances over a range of concentrations were measured and plotted against the concentration calculated using manometric measurements and sample mixing ratio in the mixture of ketone in bath gas. The absorption cross section ($\boldsymbol{\sigma}_{254}$) at 254 nm was calculated using linear unweighted least squares regression. Once the absorption cross section at 254 nm was established, the ketone concentration in the temperature variable could be derived from the room temperature 254 nm measurements.

The absorption cells were flushed with bath gas (He, UHP, >99.99%) and then evacuated to measure $I_0(\lambda)$ prior to filling or flowing through them with ketones at known concentrations. Subsequent to the measurements with the ketone to obtain $I(\lambda)$, the cell was again evacuated or filled with the bath gas to obtain another value of $I_0(\lambda)$. Comparing the $I_0(\lambda)$ measured before and

after filling with the ketone mixture allowed us to verify that the lamps and optical systems were stable during the measurement of I(λ). These measurements also helped ascertain if ketones were sticking on the surfaces or the absorption cell and cold windows. We recorded six ketone spectra at each temperature with different concentrations in the cell. The system was plumbed such that sample flowed first into the Hg/PD cell, then to the D2/CCD cell; however, we repeated several of the individual experiments with the flow reversed, and the results were not different, i.e., ketone was not lost in the cells. The measured absorbance at 254 nm at 298 K in the Hg/PD cell agreed to within 1% with that in the D2/CCD cell.

A large range of ketones concentrations were used in determining the cross sections of MEK. However, the vapor pressures of DEK at 253 K and 242 K are 1.29 Torr and 0.43 Torr, respectively (Collerson et al., 1965; Majer et al., 1985) and that of PEK is ~3 Torr at 273 K (Collerson et al., 1965; Majer et al., 1985). Therefore, we were constrained to measuring DEK cross sections to T>242 K and PEK cross sections to only 298 K.

3.2.2. Materials and Handling

MEK, DEK, and PEK samples were purchased from Sigma Aldrich and had stated chemical purities of ≥ 99.7%, ≥99%, and ≥ 99%, respectively. The liquids were degassed by freeze-pump-thaw cycles prior to use. The samples were vaporized into the 12 L glass bulbs and diluted with N_2 (ultrahigh purity (UHP), >99.99%, Matheson Tri-Gas company) to a total pressure of ~800 Torr; the mixing ratios of ketones in N_2 ranged between 1-3%. The mixing ratio of ketones in these mixtures was also measured using a multipass infrared (IR) absorption cell with a total optical pathlength of 485 cm using the IR cross section from Sharpe et al. (2004). The mixing

ratios derived from IR and manometric measurements agreed to within ~2-3%. We further verified that the composition of the mixture did not change over time by repeatedly measuring the infrared absorption over the course of several weeks of the measurements.

3.3. Results

3.3.1. Measured Absorption Cross Sections

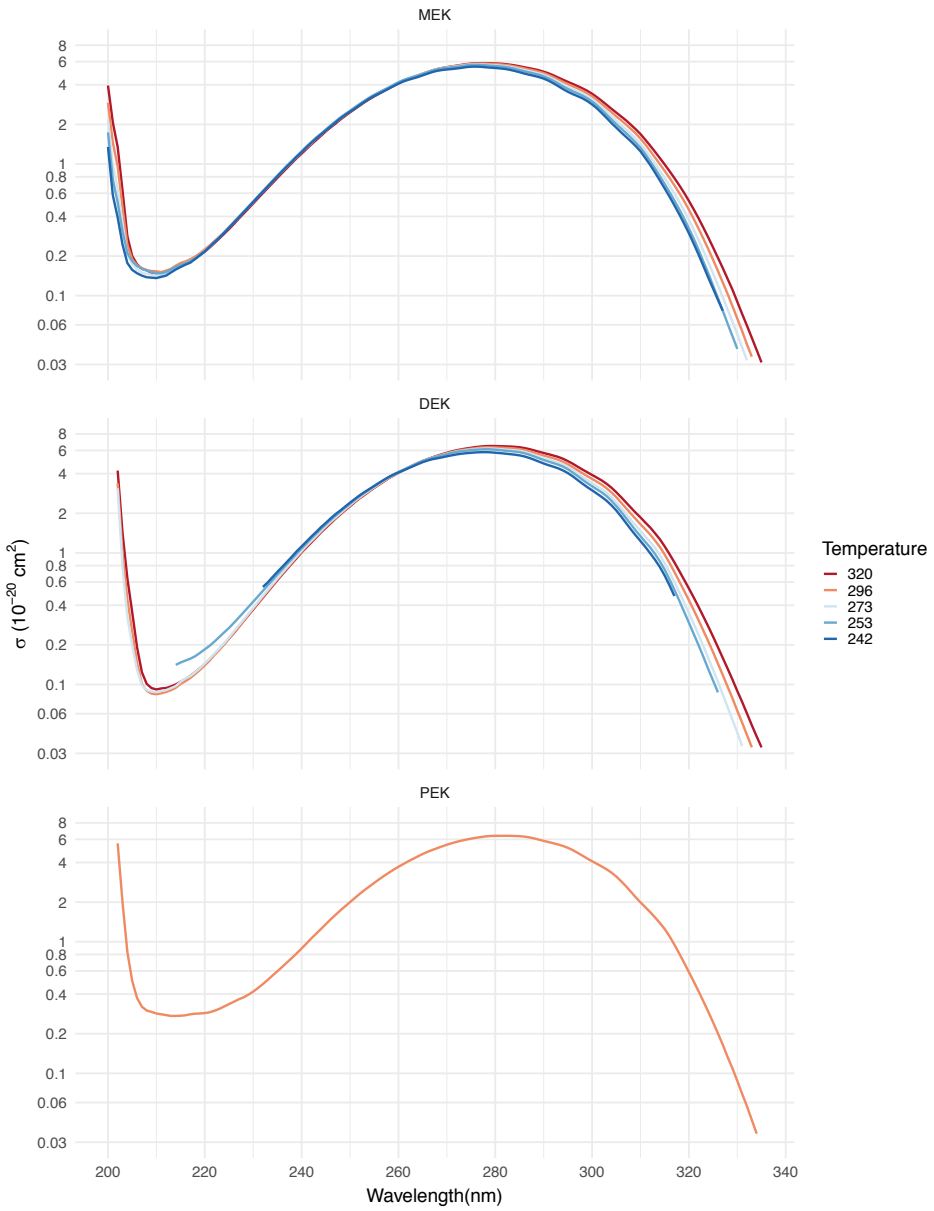

Figure 3.2 – These panels present UV absorption cross sections ($\boldsymbol{\sigma}$) in 10^{-20} cm^2 of the three species studied in this work from 200-340 nm. MEK ($C_2H_5C(O)CH_3$) and DEK ($C_2H_5C(O)C_2H_5$) cross sections at 242, 253, 273, 296, and 320 K are shown the top two panels. DEK cross sections are shorter at 242 and 253 K due to the higher uncertainty at those lower temperatures. The third panel shows the PEK ($C_2H_5C(O)C_3H_7$) cross sections at 296 K, the only temperature at which it was measured.

The top and middle panels of Figure 3.2 show the absorption cross sections of MEK and DEK at five temperatures. The lower panel shows the absorption cross sections of PEK at room temperature. These cross sections are also tabulated in appendix B (Table B1). The ketones have

large absorption cross sections at ~200 nm corresponding to the $\pi \rightarrow \pi^*$ electronic transition. These wavelengths, however, are less important for tropospheric photolysis since the actinic flux at wavelengths less than 280 nm is negligible in this region. All three species exhibit a minimum in cross sections around ~210 nm. The peak of the $n \rightarrow \pi^*$ electronic transition is around 277 nm. The absorption due to the $n \rightarrow \pi^*$ transition between ~280 and 335 nm is most relevant for tropospheric photolysis.

Figure 3.3 shows the ratios of absorption cross sections at various temperatures, $\boldsymbol{\sigma}(T)$, to those measured at 298 K, $\boldsymbol{\sigma}(298\ K)$, for both MEK and DEK. The UV absorption of MEK and DEK increases with increasing temperature at wavelengths ≥ 277 nm. As temperature increases, the absorption band broadens and the cross sections at longer wavelengths increase. Temperature dependence of the cross sections for MEK and DEK differ at short wavelengths, <240 nm. The key point to note is that the cross sections have simpler relationships with temperature within the atmospherically relevant wavelength region.

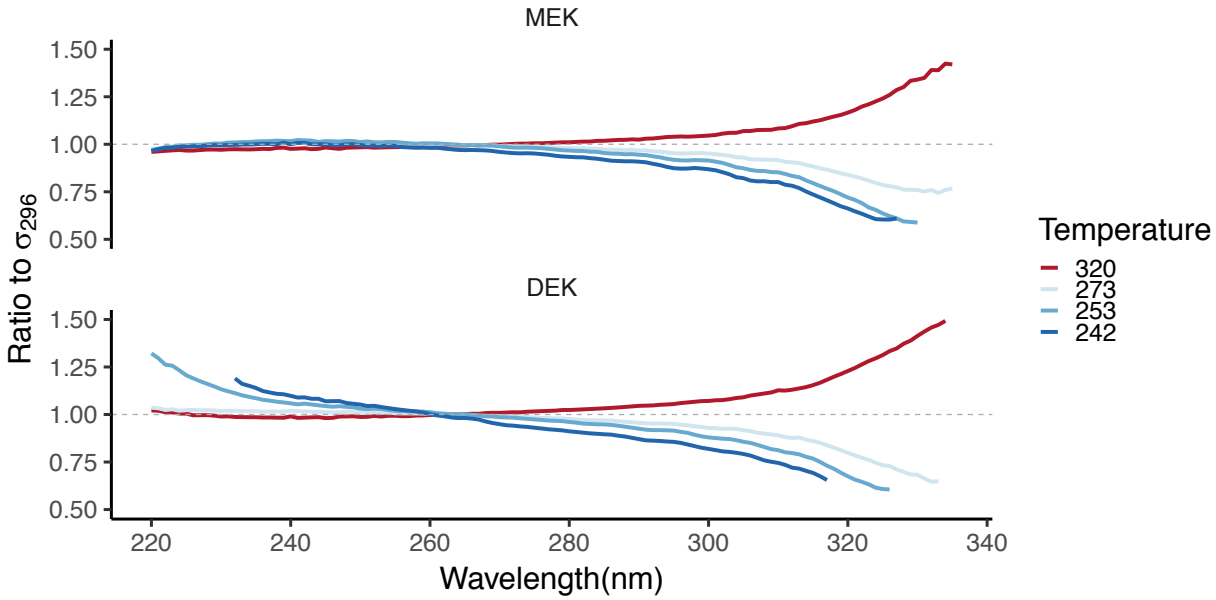

Figure 3.3 – These panels show the ratio of absorption cross sections (***σ***) of MEK and DEK at various temperatures to those measured at 298 K, as a function of wavelength.

We have also plotted the fractional uncertainties in the measured cross sections at each wavelength in appendix B (Figure B1). We report cross sections at wavelengths where absorbances were at least 0.015-0.02, ten times our detection limit of 0.0015-0.002 at the 3-sigma level. The reported uncertainty in the UV cross sections of MEK, DEK and PEK, is at the 2σ level and includes: i) the precision of the cross section at its peak (~1%); ii) the fluctuation of the D_2 light intensity (baseline stability) which is typically ~0.1% at wavelengths longer than 215 nm; iii) the accuracy of the pressure measurements (~0.5%) for the mixture preparation as well as for pressure measurement in the absorption cells; and iv) the uncertainty in the optical pathlength (~0.2 cm) Because these factors are assumed to be uncorrelated, the total uncertainty in the measured absorption was calculated by adding these contributions in quadrature. These errors contribute minimally until the cross sections decrease rapidly at the two extremes of our

measurements. At the atmospherically important wavelengths near 300 nm, the measured absorbance is uncertain to ±1.5%, except for DEK at 296 K.

3.3.2. Comparison to Prior Measurements

In Figure 3.4, we compare our measured cross sections with those from prior measurements for the compounds studied here. For comparison, we also show the cross sections for acetone.

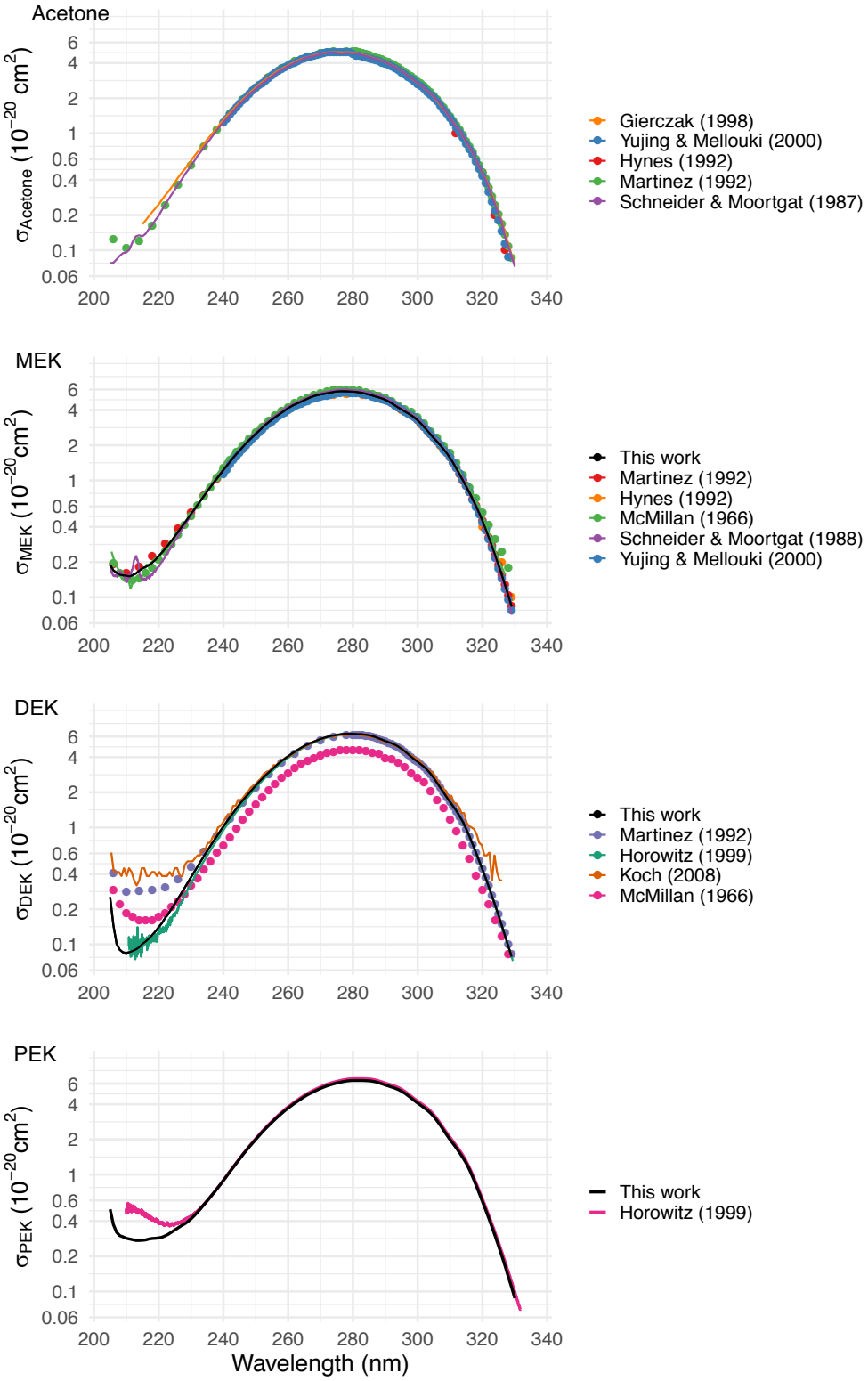

Figure 3.4 – A comparison of the UV absorption spectra in 10^{-20} cm^2 from this (black) work with those previously reported for temperature between 294-300 K by various authors as compiled by the Mainz absorption cross section database (Keller-Rudek et al., 2013).

Figure 3.4 compares the room-temperature UV absorption spectrum of MEK, DEK, PEK determined in this work with those from previous work, as well as with that of acetone. For MEK, the International Union of Pure and Applied Chemistry (IUPAC) recommends the use of cross section measurements of Martinez et al. (1992) (IUPAC, 2005). Overall, the cross sections measured in this study are in excellent agreement with the previous data from 210 – 335 nm, within 2%, 2% and 5% of the Martinez et al. (1992) and Horowitz (1999) measurements, respectively, for MEK and DEK, and PEK.

3.3.3. Temperature Dependencies of Cross Sections

In order to use our measured cross sections for interpolation between measured temperatures and for extrapolation beyond the temperatures our measurements, we have created a two-state model to represent the temperature dependence of the absorption cross section of C_3-C_6 saturated ketones. Following the method of Nicovich & Wine (1988) for H_2O_2 cross sections, we assume that the temperature dependence observed in the absorption cross sections of ketones arises from the changes in the population of the C=O stretch in the ground state. This methodology has already been used for acetone by Hynes et al. (1992), who also used the model to extrapolate MEK (using only room-temperature measurements) to other temperatures, using the dependence seen for acetone. The electronic transition in the carbonyl group is responsible for the UV absorption, and so we parameterize our two-state model using a carbonyl stretching frequency (ΔE) of the ketones. The carbonyl ΔE for aliphatic ketones is between 1705-1725 cm^{-1} (Silverstein et al., 1981); consequently, we expect that, at temperatures <350K, only the first vibrationally excited state in the C=O stretch to have significant population relative to that of the ground state, and thus a model with only two states is adequate.

We model $\boldsymbol{\sigma}(\lambda, T)$ of each ketone as a linear combination of $\boldsymbol{\sigma}_0(\lambda)$, representing the absorption cross section for electronic excitation from ground state, and $\boldsymbol{\sigma}_1(\lambda)$, representing the cross sections for electronic excitation from the first vibrational state (Nicovich & Wine, 1988). The populations in these two states are partitioned according to the fractional populations , X_0 and X_1, which are themselves functions of T and ΔE, as shown below.

$$(3.2)\ Q = 1 + e^{\frac{-\Delta E}{RT}}$$

$$(3.3)\ X_0 = \frac{1}{Q}$$

$$(3.4)\ X_1 = 1 - X_0 = \frac{Q - 1}{Q}$$

such that the overall absorption cross section is:

$$(3.5)\ \sigma(\lambda, T) = X_0(T)\sigma_0(\lambda) + X_1(T)\sigma_1(\lambda)$$

We fit the measured cross sections at each temperature to equation 3.5 while affixing ΔE at the value expected for the C=O stretch in each of the ketones. These $\boldsymbol{\sigma}_0(\lambda)$ and $\boldsymbol{\sigma}_1(\lambda)$ are shown below in the left column of Figure 3.5 for the four ketones. The second column displays model performance for each ketone compared either to our measurements (in the case of MEK and DEK) or to IUPAC recommended values (in the case of acetone). Comparable plots for PEK are displayed but the compound is treated differently due to the lack of low-temperature data; this is discussed below. The calculated values for $\boldsymbol{\sigma}_1(\lambda)$ for acetone, MEK, and DEK are realistic and comparable to those for highly absorbing species such as O_3 and NO_3 (Sander et al., 2011). We do not claim that $\boldsymbol{\sigma}_0(\lambda)$ and $\boldsymbol{\sigma}_1(\lambda)$ represent the cross sections from ground and excited states respectively, but they are consistent with a situation in which temperature changes impact the

populations of ketone molecules in the vibrational levels of the ground state, thereby facilitating the transition of those molecules to their excited state. Additionally, although this model tends to result in specific structure in the $\boldsymbol{\sigma}_1(\lambda)$ cross section and diffuse structure in the $\boldsymbol{\sigma}_0(\lambda)$, we have no data to suggest that this observation is an accurate physical representation of the two states. It would be interesting to measure the cross sections at lower temperatures and at much higher temperatures. However, our model successfully represents the measured cross sections at all temperatures and wavelengths of this study. Furthermore, in the absence of experimental data, this model provides an empirical method to calculate ketone cross sections at atmospherically relevant temperatures beyond those measured in our study.

Using our measured data and assuming $\Delta E = 1720\ cm^{-1}$, equation (3.5) gives an overdetermined system of five equations and two unknowns, and can thus be solved at each nanometer increment using a QR decomposition algorithm (Gander, 1980). This solution is shown in Figure 3.5 below. According to this solution, $\boldsymbol{\sigma}_1(\lambda)$ is ~2-3 orders of magnitude higher than $\boldsymbol{\sigma}_0(\lambda)$. The performance of this model relative to observations is shown in Figure 5b as a ratio between modeled to observed $\boldsymbol{\sigma}(\lambda, T)$. This model deviates only ~5% at longer and more atmospherically relevant wavelengths, which compares well with more traditional higher order polynomials. The observed red-shifting of $\boldsymbol{\sigma}_1$ relative to $\boldsymbol{\sigma}_0$ is also consistent with excitation from an upper vibrational state to the same electronic upper state.

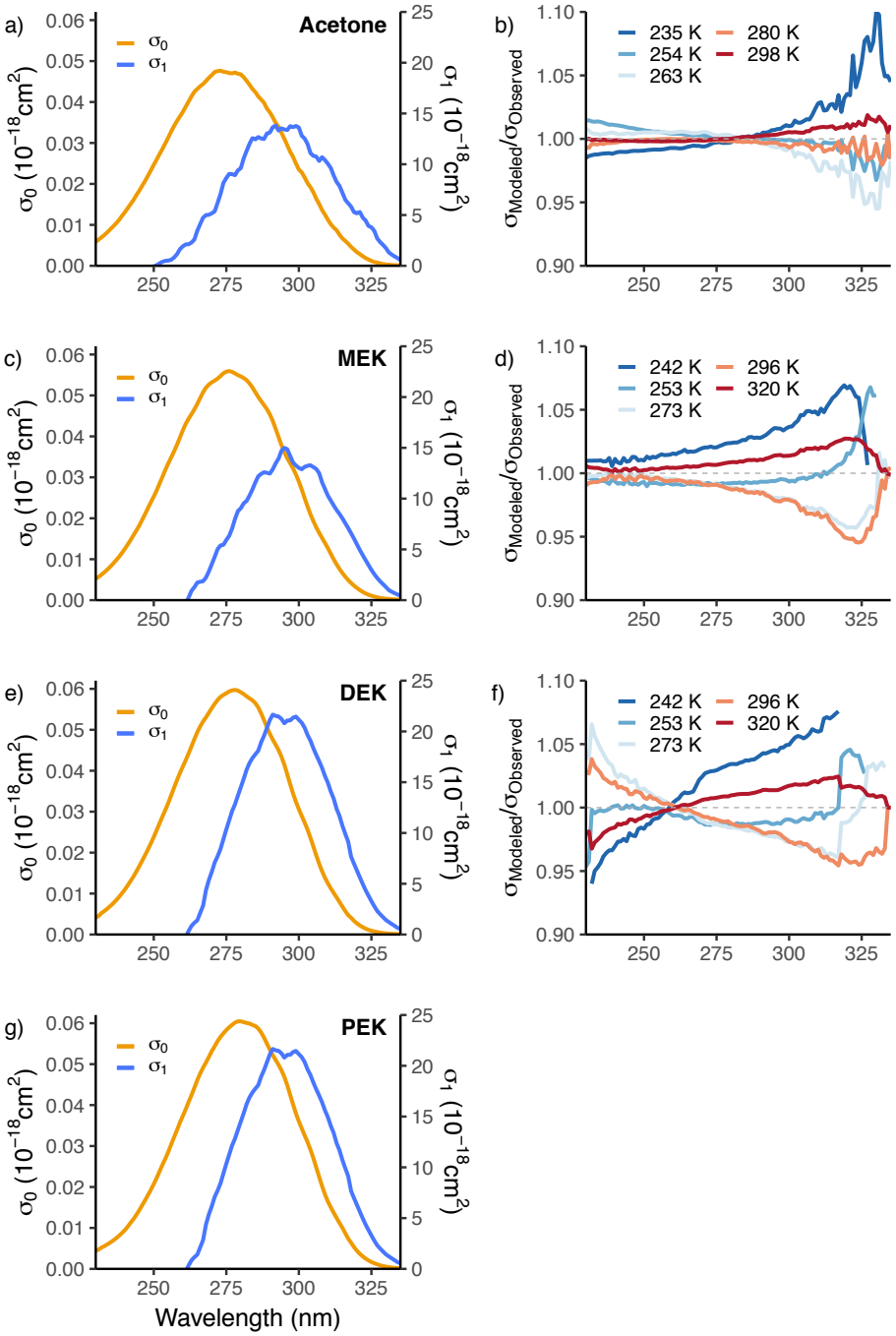

Figure 3.5 - A two-state model for C_3-C_6 saturated ketones, parameterized with a C=O stretch frequency of 1720 cm^{-1}. In all cases, the left column presents $\boldsymbol{\sigma}_0(\lambda)$ and $\boldsymbol{\sigma}_1(\lambda)$ in units of 10^{-18} cm^{-2}. $\boldsymbol{\sigma}_0(\lambda)$, displayed in orange with its values on the left y-axis, is 2-3 orders of magnitude lower than $\boldsymbol{\sigma}_1(\lambda)$, displayed in blue on the right y-axis. The right column shows the ratio of modeled $\boldsymbol{\sigma}$ to that observed at temperatures and wavelengths of our study. Panels **a)** and **b)** show the model results for acetone, using data from Gierczak et al. (1998). All other panels use data taken in this study. Panels **c)** and **d)** show the results for MEK; panels **e)** and **f)** show the results for DEK; and panel **g)** shows the model results for PEK.

In order to verify that our method works generally for short aliphatic ketones, we performed the same calculations for acetone using $\Delta E = 1720$ cm^{-1}, and the acetone spectra measured at temperatures from 235 K to 298 K by Gierczal et al. (1998). In that paper, the authors improved upon the resolution of the acetone measurements relative to Hynes et al. (1992) but found that the two-state system did not reproduce their results well. However, by using $\Delta E = 1720$ cm^{-1} and our QR decomposition methodology, we were able to produce a useful fit, comparable to the quality of fit for MEK and DEK, which is presented in Figure 3.5a) and 5b). The $\boldsymbol{\sigma}_0(\lambda)$ and $\boldsymbol{\sigma}_1(\lambda)$ values in Figure 3.5a) are comparable to those found in Figures 3.5c) and 3.5e), and the fit as shown in Figure 3.5b) is also within 5% except at the very low cross section values beyond 325 nm. The parameterized model values for $\boldsymbol{\sigma}_0(\lambda)$ and $\boldsymbol{\sigma}_1(\lambda)$ for all four compounds are tabulated in appendix B (Table B2).

Because we did not measure PEK spectra at temperatures beyond room temperature, we cannot explicitly model PEK in the same way as acetone, MEK, and DEK. However, in the absence of experimental data at temperatures other than 296 K, we can use this physical model to give us an empirical basis for PEK temperature-dependent absorption; of course, this is not verified by observations and could be uncertain. If we assume that any differences between DEK and PEK spectra are due solely to differences in the ground state absorption ($\boldsymbol{\sigma}_0$), it is possible to construct a useable model for the temperature dependence of the PEK spectra. As with DEK, we build the model using $\Delta E = 1720$ cm^{-1}, but affix $\boldsymbol{\sigma}_0(\lambda)$ such that the model correctly represents our room temperature measurements of the PEK spectrum. Figure 3.5g) thus closely resembles Figure 3.5e), with a slightly higher peak value of $\boldsymbol{\sigma}_1(\lambda)$.

We considered the possibility of deriving ΔE via optimization of $\boldsymbol{\sigma}_0(\lambda)$ and $\boldsymbol{\sigma}_1(\lambda)$, rather than using canonical values of the C=O stretch frequency, as Hynes et al. (1992) did for acetone.

We tested a range of ΔE values between 1 and 2000 cm^{-1}. The results of this analysis are included in appendix B (Figure B2). For MEK, aggregated error and the number of negative values is minimized at ΔE = 800 cm^{-1} and ΔE = 600 cm^{-1}, respectively, which is similar to ΔE = 950 cm^{-1} found by Hynes et al. (1992) for acetone. At 350 K, ΔE = 600 cm^{-1} implies that 7.8% of molecules would be in the first vibrationally excited level, which may challenge our assumption of a two-state model (i.e., the population in the next vibrational level would not be negligible). The larger value of ΔE ensures that a two-state model is reasonable over the temperature range of our study.

Regardless of which ΔE is used, this two-state model allows us to extrapolate our data to temperatures outside of the range we were able to measure. Neither choice of ΔE causes large discontinuities in $\boldsymbol{\sigma}$ relative to measured values when modeled at temperatures up to 350 K and down to 160 K. As one might expect from comparing the relative magnitudes of $\boldsymbol{\sigma}_0(\lambda)$ and $\boldsymbol{\sigma}_1(\lambda)$ in Figure 3.5a) (and 3.5c and 3.5e), the model parameterized with ΔE = 1720 cm^{-1} produces a smaller temperature response with decreasing temperatures relative to the model parameterized with ΔE = 600, while the reverse is true at temperatures >350 K. Whichever parameterization is chosen, the model produces useable results at atmospherically relevant temperatures outside the range of measurements. Figure B3 shows the performance of the model at these extreme values. For atmospheric applications, we provide models parameterized at ΔE = 1720 cm^{-1}, whose $\boldsymbol{\sigma}_0(\lambda)$ and $\boldsymbol{\sigma}_1(\lambda)$ values are provided in appendix B (Table B2). We also include an R program (Brewer_JValue_Subroutines_Code_B1.R) which can use the two-state models provided in Table B2 to output cross sections at any atmospherically relevant temperature. This code will be discussed in more detail below.

As many modeling applications of J-Value calculation take place in demanding computation environments (i.e., in the context of a globally-resolved chemical transport model), modeling applications of cross sections tend to use some form of wide-band average binning in order to efficiently and accurately compute j-values, such as the Fast-J (Wild et al., 2000) binning schemes. As such, we believe that adapting our data for a wide array of binning schemes will be most useful in facilitating its future use by the community. Thus we have produced a Fast-J (Wild et al., 2000) treatment of our cross section data, which is included in appendix B (Table B4). In appendix B, we have also included an R program capable of binning our data in other binning schemes; this code is also discussed further in section 3.3.5.

3.3.4. Calculated J-Value Comparisons

The first order rate coefficient for the removal of ketones, the J-Value (s^{-1}), is given by Equation 3.6:

$$(3.6)\ J = \int_{\lambda_1}^{\lambda_2} \sigma(\lambda, T) \times \Phi(\lambda, T, P) \times\ F(\theta, \lambda)$$

where F is the actinic flux (quanta $cm^{-2}\ s^{-1}\ nm^{-1}$), Φ is the quantum yield for the destruction of the molecule, $\sigma(\lambda, T)$ is the absorption cross section (cm^2) of the molecule, and λ_1 and λ_2 are the limits of wavelengths available in the atmosphere over which the molecule absorbs,

We have calculated J-values for each compound using model-derived clear-sky actinic flux to roughly show the photolytic loss rate coefficients for these ketones in the troposphere. We used the National Center for Atmospheric Research (NCAR) Tropospheric Ultraviolet Visible (TUV) radiative transfer model version 5.3.1 (publicly available at

https://www2.acom.ucar.edu/modeling/tropospheric-ultraviolet-and-visible-tuv-radiation-model) to simulate monthly average solar noon actinic flux in 10° latitude bins for a variety of altitudes. This model uses the top of atmosphere irradiance modified by scattering and absorption to calculate an actinic flux for a given condition using a 4-stream pseudo-spherical approximation (Madronich & Flocke, 1999).

Figure 6 shows the calculated J-values for MEK for quantum yields from IUPAC recommendations and Romero et al. (2005). For each of these quantum yields, we calculate J-values using two sets of cross sections: 1) modeled temperature-dependent cross sections as per section 3.3 of this paper; and 2) the IUPAC recommended room temperature cross sections from Martinez et al. (1992), referred to as $\boldsymbol{\sigma}_{\text{Martinez}}$ in Figure 6. Quantum yields and cross sections were calculated using the same reanalysis-derived temperature and pressure data in order to ensure that both factors vary simultaneously, as they do in the real atmosphere. Additionally, we compare these photolysis rate coefficients to the rate coefficients for removal of MEK by reaction with OH. Concentrations of OH were from Spivakovsky et al. (2000) that does not include any HO_x produced from the oxidation of MEK, DEK, or PEK. The rate coefficients for OH reaction with the various ketones are taken from the NASA JPL data evaluation (Burkholder et al., 2015). The temperature, pressure, and OH profiles used to generate this plot are included in appendix B (Table B3), as are the R programs used to calculate all the quantum yields used in this paper (Brewer_JValue_Subroutines_Code_B1.R), discussed in section 3.3.5 below.

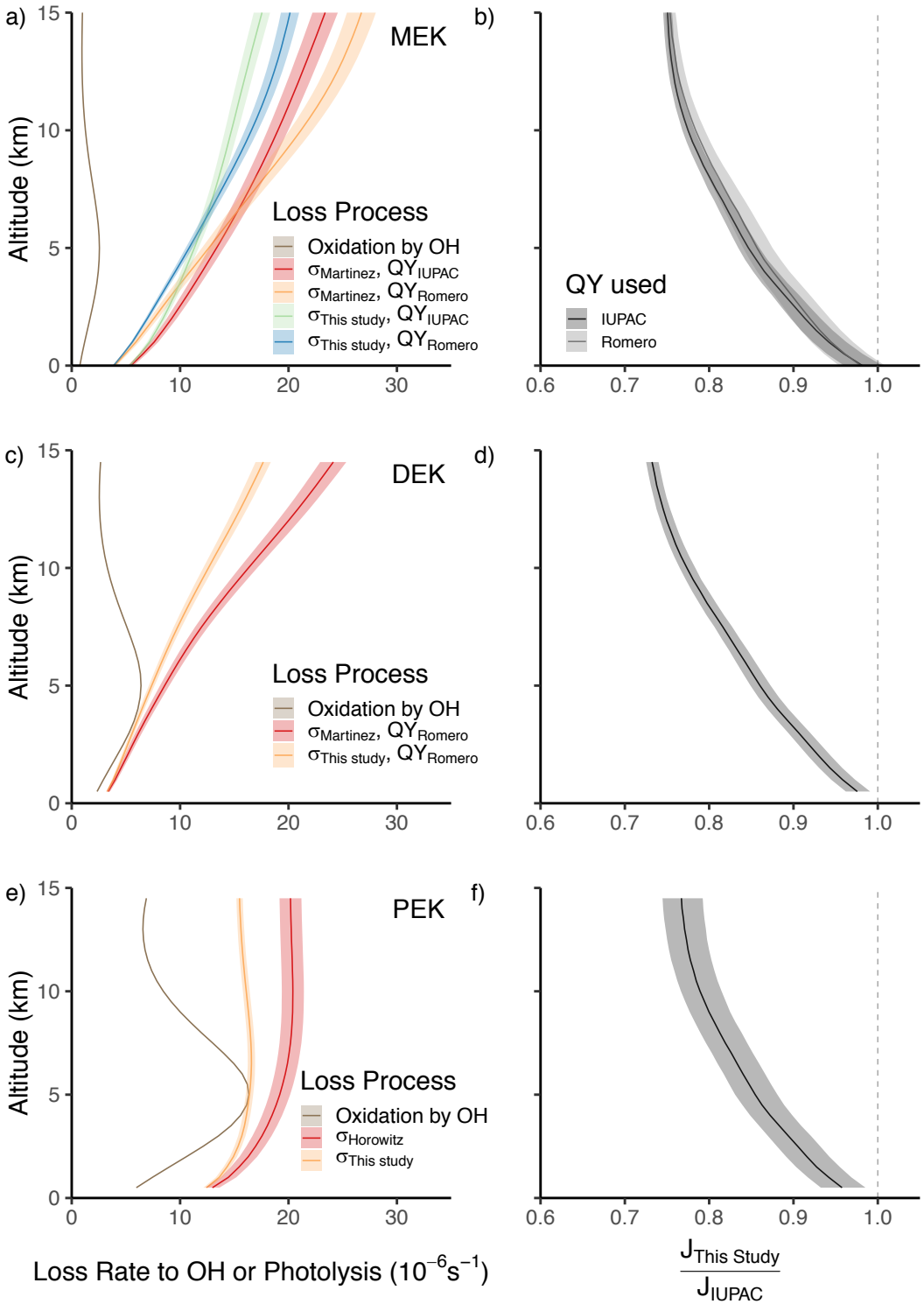

Figure 3.6 - a) photolytic and OH-reaction loss rate coefficients (10^{-6} s^{-1}) for MEK in April at the Equator with no clouds present. J-values are calculated using two different absorption cross sections (from this study and Martinez et al. (1992)) and two different quantum yield possibilities. Shaded areas in plots **a)**, **c)**, and **e)** represent the upper and lower bounds of

uncertainty in the cross sections propagated through to the J-value. The quantum yields are from the IUPAC recommendations (IUPAC, 2005) and Romero et al. (2005). **b)** the ratio of the J-values calculated with our cross sections to those using the IUPAC recommendations for each quantum yield used (IUPAC, 2005). Shaded area in plots **b)**, **d)**, and **f)** represent the ratio between the upper (and lower) bounds of this study's calculated J-values to the upper (and lower) bounds of the J-values calculated according IUPAC cross sections. Panels **c)** and **e)** show DEK and PEK J-values under the same conditions. These J-values are also calculated using two different absorption cross sections but using only the quantum yield from Romero et al. (2005) for DEK and an assumed quantum yield of 1 for PEK. J-value uncertainties in **a)**, **c)**, and **e)** reflect only the uncertainties in cross sections and not those in the various quantum yields used. Panels **d)** and **f)** show the same ratio as panel **b)**, calculated for DEK and PEK, which each use only one quantum yield.

Figure 6 shows that, for all three compounds, the inclusion of the temperature-dependent cross sections leads to a decrease in the J-value in the upper troposphere. In these specific location, season, and cloudless conditions, the change is on the order of 20-25%. Figure B4 in appendix B replicates Figure 3.6 with an assumed cloud optical depth of 25 and 100% cloud cover; the change in the J-value due to the temperature dependence is unaffected by this parameter and remains on the order of 20-25%. Because the reference IUPAC values are for 296 K, we expect a decrease in the J-value as a result of using our temperature-dependent cross sections, which decrease with temperature. In addition, panel 3.6a) shows that the choice of quantum yield is important to understanding the change of J-Value with altitude, especially under upper tropospheric conditions. Irrespective of cross section used, the inclusion of the wavelength-dependent QY from Romero et al. (2005) decreases the J-value relative to the IUPAC QY recommendation below 6 km; above 6 km, using these cross sections increases the J-Value relative to the IUPAC recommendations. Furthermore, because no experimental studies of PEK quantum yields are known, Figures 3.6e and 3.6f assume a quantum yield of 1 at all wavelengths and pressures, which accounts for the different shapes of the vertical J-value profile in Figure 3.6e as compared to Figures 3.6a and 3.6c; the calculated J values are, therefore, upper bounds for PEK loss. These observations point to a need for more detailed quantum yield

measurements for these species as well. Finally, Figure 3.6 shows that loss rates to photolysis are larger than due to reaction with OH at all altitudes for MEK and above 5 km for DEK and PEK.

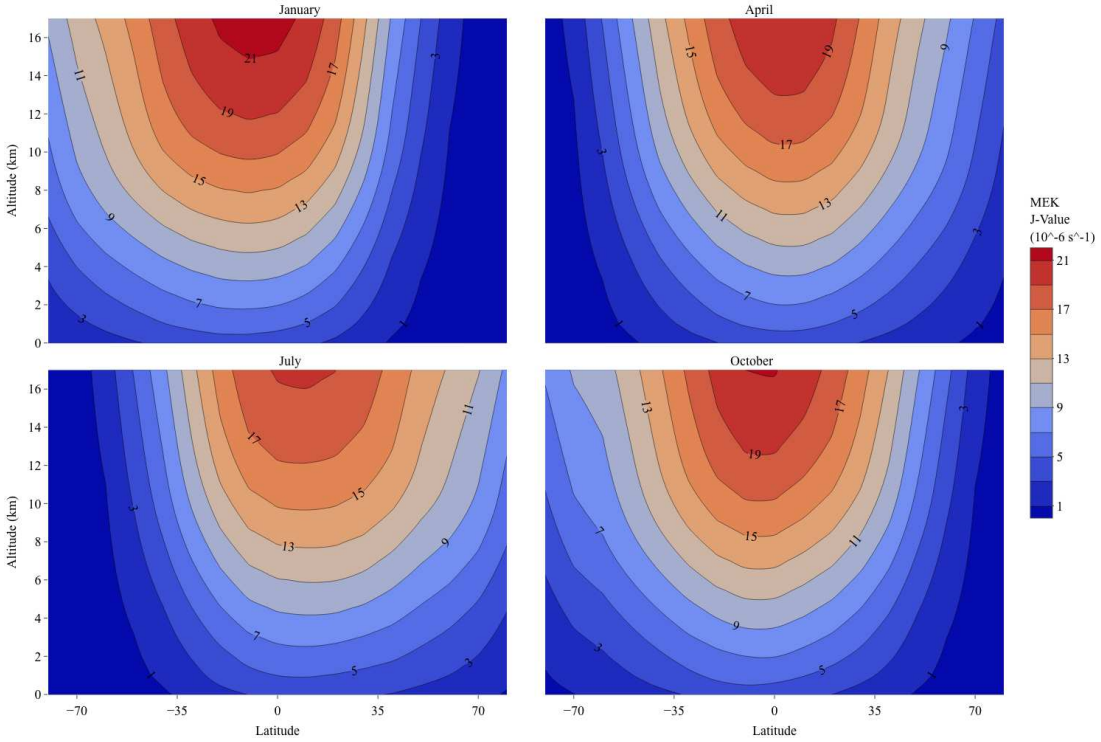

Figure 3.7 – The contours here show MEK J-values in 10^{-6} s^{-1} for four seasons. Pressures and temperatures used to generate these values are 10-year (2007-2017) monthly means from NCEP reanalysis; the cross sections used are from the 2-state model presented in this study; the quantum yields are from Romero et al. (2005). The actinic fluxes are used in this plot are solar noon values created using a customized TUV model run. We used the photochemistry-optimized standard TUV input file with the following specific conditions: 1) We used a four year pre-stratospheric O_3 depletion total O_3 column values (mean monthly values from 1978-1982) from the TOMS instrument aboard the Nimbus 7 (Keating et al., 1989); 2) We assumed clear sky, and we fixed the surface albedo value at 0.1 irrespective of surface type (i.e. water or land); 3) We used an aerosol single scattering albedo of 0.99; We used a continental aerosol profile (aerosol optical depth at 550 nm = 0.235) (Elterman, 1968); and 5) We used temperature and pressure profiles from a 2007-2017 average of monthly NCAR NCEP reanalysis data (Kalnay et al., 1996). These assumptions were chosen to create a simplified model output that others could easily replicate.

Figure 3.7 presents MEK J-values in the troposphere derived using our measured temperature-dependent cross sections at local solar noon at each 10° latitude bin (i.e. -90, -80, …, 80, 90) during four different months representative of seasons: January (Boreal Winter),

April (Boreal Spring), July (Boreal Summer), and October (Boreal Autumn). This is done to exemplify how photolysis rate coefficient changes with location and season. Photolysis rate coefficients are largest in the tropical tropopause throughout the year, with J-values reaching ~$2x10^5$ s^{-1}. However, this figure uses actinic flux characteristic of a cloudless sky and constant AOD, as such it should be primarily be treated as a comparison with modeled photolysis rates coefficients and quick look up. It is not meant to represent true atmospheric values. A similar pattern and rough values are to be expected for DEK or PEK. These rates will change depending upon the parameters specific to various atmospheric models; however, we include this generalized example for illustrative purposes. As to be expected, the photolysis maximizes in the tropical upper troposphere. From Figure 3.6, it appears that for MEK, photolysis is likely to be more important than loss to OH, regardless of the quantum yield used. For PEK and DEK, the two loss processes compete in the lower troposphere. Our study highlights the need for elucidation of the quantum yields of these species under atmospheric conditions.

3.3.5. Implementation in R

The schemes presented here have been implemented as a program in R, an open-source programming environment (R Development Core Team, 2010) which is available on all operating systems. The program (Brewer_JValue_Subroutines_Code_B1.R) makes use of multiple nested subroutines and wrapper functions in order to perform three computations:

1. Use the two-state models provided in Table B2 to output a cross section for MEK, DEK, PEK, or Acetone at any atmospherically relevant temperature.

2. Calculate the quantum yields for MEK, DEK, or PEK used in Figure 3.6.

3. Bin any quantum yield, cross section, or actinic flux according to a given wide-band binning scheme, such as those found in global models or other applications where calculation speed must be given highest priority (Wild et al., 2000).

The modular approach to the code included allows additional quantum yield schemes to be added in as separate functions, which can be called in their own right. Moreover, the code to perform the wide-band binning is extensible and should be usable for most binning schemes; the details are discussed further in the Supporting Information. Finally, this paper also includes an additional program (Brewer_JValue_Example_Code_B2.R) which gives an example implementation of the subroutines included in Brewer_JValue_Subroutines_Code_B1.R.

3.4 Conclusions

We present new measurements of MEK and DEK absorption cross sections at temperatures between 242 K - 320 K and of PEK at 298 K between 200 and 335 nm. We use these measured values to refine our understanding of the role of photolysis in the tropospheric chemistry of these compounds. We show that the measured cross sections are robustly represented by a two-state model. While we don't have data to assess the accuracy of the model at temperatures below 242 K, this model can be extrapolated to temperatures below our measurements to provide empirical, numerically stable, and physically reasonable ketone cross sections at all tropospherically relevant temperatures. We further show that this same model also allows us to simulate the

temperature dependence of acetone UV absorption cross sections and we suggest that an analogous treatment works for PEK. For MEK, DEK, and PEK, the inclusion of temperature dependence leads to a decrease in photolysis rate coefficients of up to 20-25%, when compared to photolysis rate coefficients derived using available room temperature literature recommendations. This decrease is largest in the upper troposphere (Figures 6 and 7), where ketone photolysis is thought to be most important to global oxidation potential. We provide a set of calculated J values for easy comparison at both 1 nm and wide-binned resolutions, and produce first-order estimates of photolysis rates in the troposphere. We also provide the code necessary to extend and modify this work as needed in future applications.

Chapter References

A. J. Hynes, E. A. Kenyon, A. J. Pounds, & P. H. Wine. (1992). Temperature dependent absorption cross-sections for acetone and n-butanone - implications for atmospheric lifetimes. *Spectrochimica Acta*, *48A*(9), 1235–1242.

Burkholder, J. B., Sander, S. P., Abbatt, J., Barker, J. R., Huie, R. E., Kolb, C. E., et al. (2015). Chemical Kinetics and Photochemical Data for Use in Atmospheric Studies. In *JPL Publication 15-10* (Vol. 18). Pasadena: Jet Propulsion Laboratory.

Collerson, R. R., Counsell, J. F., Handley, R., Martin, J. F., & Sprake, C. H. (1965). Purification and vapour pressures of some ketones and ethers. *Journal of the American Chemical Society*, 3697–3700.

Elterman, L. (1968). *UV, Visible, and IR Attenuation for Altitudes to 50 km* (No. AFCRL-68-0153). Cambridge, MA.

Gander, W. (1980). *Algorithms for the QR-Decomposition* (No. 80– 02). Zurich: ETH. Retrieved from http://people.inf.ethz.ch/gander/papers/qrneu.pdf

Gierczak, T., Burkholder, J. B., Bauerle, S., & Ravishankara, A. R. (1998). Photochemistry of acetone under tropospheric conditions. *Chemical Physics*, *231*, 229–244.

Horowitz, A. (1999). *Absorption cross sections of 2-pentanone, 3-pentanone, and 3-hexanone*. The Max-Planck-Institut für Chemie, Mainz, Germany.

IUPAC. (2005). *CH3C(O)C2H5.* (IUPAC Task Group on Atmospheric Chemical Kinetic Data Evaluation No. Data Sheet P8).

Kalnay, E., Kanamitsu, M., Kistler, R., Collins, W. J., Deaven, D., Gandin, L., & et al. (1996). The NCEP/NCAR 40-year Reanalysis Project. *Bulletin of the American Meteorological Society*, *773*(3), 437–472.

Keating, G. M., Pitts, M. C., & Young, D. F. (1989). Ozone Reference Models for the Middle Atmosphere. In G. M. Keating (Ed.), *Middle Atmosphere Program Handbook for MAP* (Vol. 31, pp. 37–49). University of Illinois, Urbana: SCOSTEP Secretariat.

Keller-Rudek, H., Moortgat, G. K., Sander, R., & Sörensen, R. (2013). The MPI-Mainz UV/VIS spectral atlas of gaseous molecules of atmospheric interest. *Earth Syst. Sci. Data*, *5*, 365–373. https://doi.org/10.5194/essd-5-365-2013

Madronich, S., & Flocke, F. (1999). The Role of Solar Radiation in Atmospheric Chemistry. In P. Boule (Ed.), *Environmental Photochemistry* (pp. 1–26). Berlin, Heidelberg: Springer Berlin Heidelberg.

Majer, V., Svoboda, V., & Kehiaian, H. V. (1985). *Enthalpies of vaporization of organic compounds*. Blackwell Scientific Oxford.

Martinez, R. D., Buitrago, A. A., Howell, N. W., Hearn, C. H., & Joens, J. A. (1992). The near U.V. absorption spectra of several aliphatic aldehydes and ketones at 300 K. *Atmospheric Environment*, *26A*(5), 785–792.

Nicovich, J. M., & Wine, P. H. (1988). Temperature-dependent Absorption Cross Sections for Hydrogen Peroxide Vapor. *J Geophys. Res.*, *93*(D3), 2417–2421.

Papanastasiou, D. K., Feierabend, K. J., & Burkholder, J. B. (2011). Cl2O photochemistry: Ultraviolet/vis absorption spectrum temperature dependence and O(3P) quantum yield at 193 and 248 nm. *The Journal of Chemical Physics*, *134*(20), 204310. https://doi.org/10.1063/1.3592662

R Development Core Team. (2010). R: A language and environment for statstical computing. Retrieved from http://www.r-project.org

Romero, M. T. B., Blitz, M. A., Heard, D. E., Pilling, M. J., Price, B., & Seakins, P. W. (2005). OH formation from the C2H5CO+O2 reaction: An experimental marker for the propionyl radical. *Chemical Physics Letters*, *408*(4–6), 232–236. https://doi.org/10.1016/j.cplett.2005.04.018

Sander, S. P., Abbatt, J., Barker, J. R., Burkholder, J. B., Friedl, R. R., Golden, D. M., & et al. (2011). *Chemical Kinetics and Photochemical Data for Use in Atmospheric Studies, Evaluation Number 17.* Pasadena, CA. Retrieved from http://jpldataeval.jpl.nasa.gov/

Sharpe, S. W., Johnson, T. J., Sams, R. L., Chu, P. M., Rhoderick, G. C., & Johnson, P. A. (2004). Gas-phase databases for quantitative infrared spectroscopy. *Applied Spectroscopy*.

Silverstein, R. M., Bassler, G. C., & Morrill, T. C. (1981). *Spectrometric Identification of Organic Compounds*. John Wiley & Sons.

Spivakovsky, C. M., Logan, J. A., Montzka, S. A., Balkanski, Y. J., Foreman-Fowler, M., Jones, D. B. A., et al. (2000). Three-dimensional climatological distribution of tropospheric OH: Update and evaluation. *Journal of Geophysical Research: Atmospheres*, *105*(D7), 8931–8980. https://doi.org/10.1029/1999jd901006

Wild, O., Zhu, X., & Prather, M. J. (2000). Fast-J: Accurate simulaton of in- and below-cloud photolysis in tropospheric chemical models. *Journal of Atmospheric Chemistry*, *37*(3), 245–282. https://doi.org/10.1023/a:1006415919030

CHAPTER 4: AN OCEANIC SOURCE OF MEK TO THE ATMOSPHERE [3]

4.1. Chapter Introduction

Many volatile organic compounds (VOCs) are emitted from the ocean surface from a variety of biogenic and abiogenic sources. Dimethyl sulfide (DMS), a crucial contributor to the global sulfur cycle and particle formation, is produced by phytoplankton in seawater (Kloster et al., 2006; Yu & Luo, 2010). The production of DMS is so tightly coupled to oceanic productivity that seabirds use it as a cue to find prey in the open ocean (Nevitt et al., 1995). Other VOCs have primarily photochemical sources in the ocean: acetaldehyde in the surface ocean has been shown to originate from the photolysis of chromophoric dissolved organic matter (CDOM; Keiber et al., 1990; Millet et al., 2010; Wang et al., 2019). VOCs such as methyl nitrate (CH_3ONO_2) have potentially more complicated oceanic sources. While the primary oceanic production of methyl nitrate is likely to be the photolysis of CDOM (Fisher et al., 2018; Moore & Blough, 2002), the distribution of methyl nitrate in the water column suggests the possibility of additional biological sources (Moore & Blough, 2002). Acetone has been shown to have a large oceanic emission (Fischer et al., 2012; Yang et al., 2014, 2016), though its ultimate source remains complex. Acetone is known to be produced by CDOM photolysis in seawater (Dixon et al., 2013, 2014; Keiber et al., 1990; Zhou & Mopper, 1997), while biological production has been demonstrated in laboratory studies and is considered likely to occur in the ocean as well (Dixon et al., 2013, 2014; Nemecek-Marshall et al., 1995). The two processes are not exclusively independent: in mesocosm experiments on phytoplankton blooms, Sinha et al. (2007) found that the largest

[3] Portions of this chapter contain published work. Citation: Brewer, J. F., Fischer, E. V., Commane, R., Wofsy, S. C., Daube, B. C., Apel, E. C., et al. (2020). Evidence for an Oceanic Source of Methyl Ethyl Ketone to the Atmosphere. Geophysical Research Letters, 47(4). https://doi.org/10.1029/2019GL086045

fluxes of acetone occurred during the bloom decline phase, marked by relatively high phytoplankton abundance, with less acetone during the low-biomass post-bloom phase. Based on these findings, it is likely that MEK could also have varied oceanic sources.

4.2. Methods

4.2.1. Observations of MEK

We use observational data from the first two deployments of the NASA Atmospheric Tomography (ATom) mission. The ATom project is a global survey of atmospheric chemistry, which offers a representative investigation of the composition of the remote atmosphere. ATom flights consisted of a series of ascending and descending profiles along the flight track to create a tomography of the atmosphere. The ATom-1 and ATom-2 missions took place from 29 July – 23 August 2016, and 26 January – 21 February 2017, respectively.

MEK, acetaldehyde, and acetone concentrations are available for every two minutes during ATom using the Trace Organic Gas Analyzer (TOGA) (Apel et al., 2015; Wang et al., 2019). Sampling for the abundances of methyl nitrate and DMS from the Whole Air Sampler (WAS) (Barletta et al., 2011; Colman et al., 2001) was manually controlled and unevenly spaced in time, but it averaged one measurement every ~3 minutes. The WAS samples were shipped back to the laboratory at UC Irvine and analyzed with gas chromatography (Colman et al., 2001). The lower limits of detection for MEK, acetaldehyde, and acetone were 1 ppt, 5 ppt, and 5 ppt, while those for DMS and methyl nitrate are 0.1 ppt and 0.01 ppt, respectively. Data from both WAS and TOGA registering below the limit of detection was dynamically assigned a value between 0 and the LLOD as a linear function of how many LLOD-flagged values were recorded on a given flight: the more LLOD-flagged non-NA observations, the closer the assigned value

was to 0. This methodology did not change any of the conclusions relative to filling LLOD data with half the LLOD, another common strategy. Because TOGA and WAS measurements were taken at different timesteps, we group the data from both instruments into 1-km vertical bins on ascent and descent of each flight. Carbon monoxide (CO), also used in this analysis, was measured using a Quantum Cascade Laser Spectrometer (QCLS; Accuracy 3.5 ppb, 0.15 ppb precision at 1s) (Santoni et al., 2014) and was essentially continuous with a 1 second resolution.

MEK has an estimated atmospheric lifetime against OH oxidation of ~5-6 days at OH concentrations of ~1.5×10^6 cm^{-3} (Jordan et al., 2009; Yañez-Serrano et al., 2016); its most important alkane precursors (*n*-butane and *i*-pentane) have global mean atmospheric lifetimes against OH oxidation of up to 2-4 days under the same OH concentrations, with longer lifetimes on the order of weeks possible during wintertime (Hodnebrog et al., 2018; Lee et al., 2006; Rossabi & Helmig, 2018). These lifetimes are long enough that both MEK and its precursors can be transported into the remote marine atmosphere from terrestrial sources. To isolate clean marine air masses, we define a series of conservative estimates of CO background mixing ratios by region and season. In the Southern Ocean, we define the background CO mixing ratio as 50 ppb in January-February and 60 ppb in July-August; in the South Atlantic and South Pacific we define the background CO mixing ratios as 55 ppb in January-February and 65 ppb in July-August; in the Western Tropical Pacific the values are defined as 85 ppb during January-February and 70 ppb during July-August. These values were chosen considering the GLOBALVIEW-CO observations from the same year (GLOBALVIEW-CO, 2009), and do not reflect a specific CO percentile in the ATom dataset; this choice was made because different regions and seasons sampled by ATom can have more or less data 'above background', reflecting the number of polluted airmasses sampled. We have examined the sensitivity of our

results to the choice of background: increasing background CO by 5 ppb makes little difference to our results, while reducing background values by 5 ppb reduces the number of 'clean marine' observations and renders statistical analysis difficult in some regions and seasons, especially in the South Atlantic. This sensitivity is included in the text where relevant. We use these background values to eliminate recent influence from sources of MEK on land, and thus isolate 'clean marine' air masses in which CO is produced primarily from the oxidation of long-term reservoirs of natural and anthropogenic reservoir species. In the ATom 1 and 2 datasets in the regions of interest (including data above CO background), MEK is weakly correlated with CO ($r = 0.245$, $p = 2.5 \times 10^{-19}$) because the two species share several sources (biomass burning, alkane oxidation). At CO mixing ratios at or below background, however, MEK and CO are not correlated in these regions ($r = 0.07$, $p = 0.07$).

We have grouped the ATom observations over the remote oceans by the regions shown in Figure 4.1. This figure also shows the clean-marine (colored) and anthropogenically-influenced (grey) data points, as well as the vertical distribution of the sampling (color scale). Because we are attempting to identify clean marine air masses, we have restricted this study to four relatively remote and clean regions sampled by ATom: the Western Tropical Pacific (WTP), the South Pacific (SP), the South Atlantic (SA), and the Southern Ocean (SO). There are additional ATom data in the Eastern Tropical Pacific and Tropical Atlantic, but they are largely land-influenced, and we omit them from this analysis. Stratospheric influences in the dataset were removed by using only points below 10 km. We also tested our results by including only measurements where ozone < 90 ppb to remove stratospheric influence; the results were unchanged.

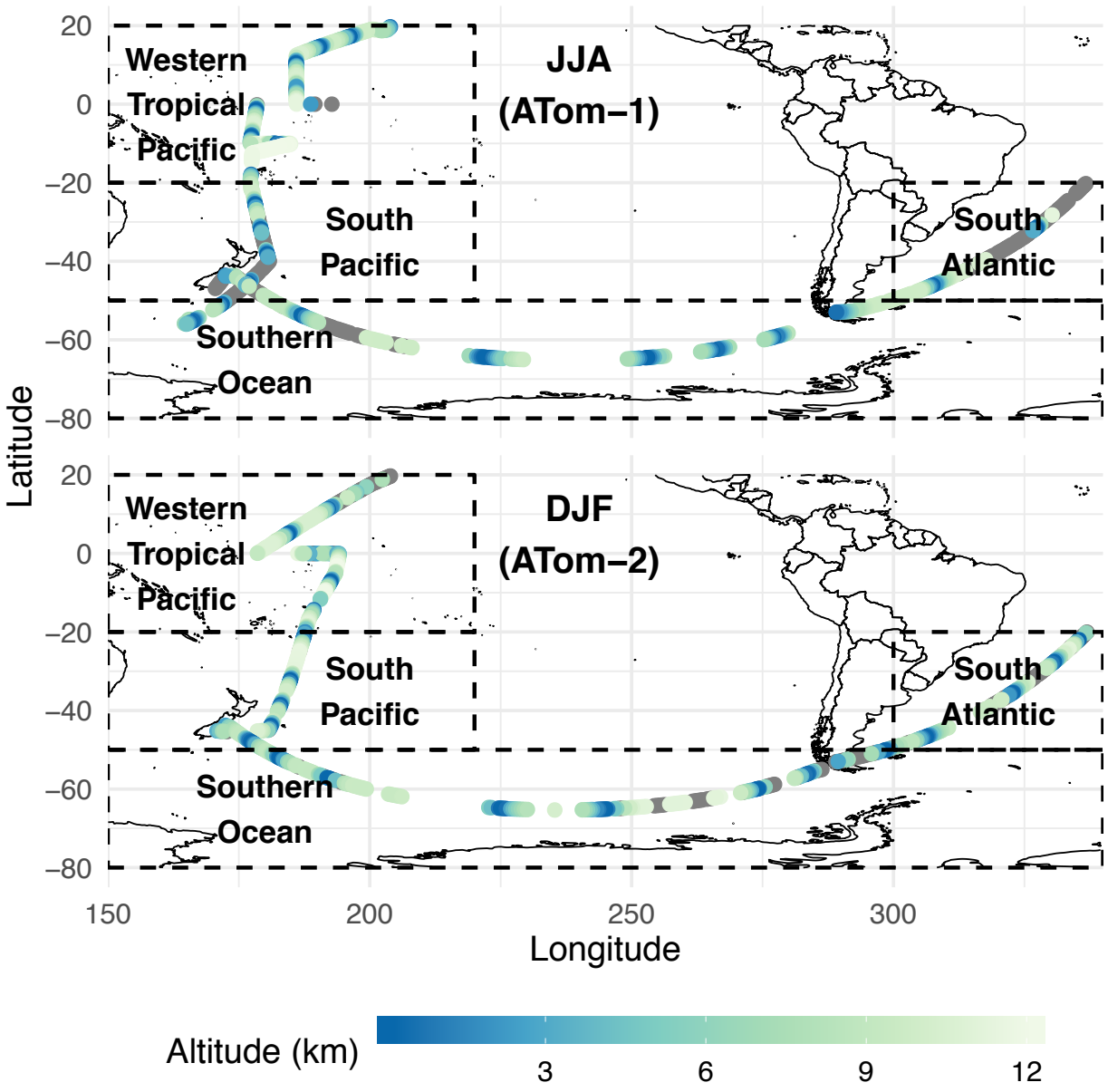

Figure 4.1 ATom-1 (Jul-Aug) and ATom-2 (Jan-Feb) sampling locations. Grey data points are classified as anthropogenically influenced, and not included in our analysis. The colored points are at or below CO background as defined in the text and are classified as clean marine airmasses (see text). The color scale shows the aircraft altitude. Data has been grouped into four coherent regions: Western Tropical Pacific, South Pacific, Southern Ocean, and South Atlantic.

4.2.2. Flux Calculations

We use a simplified two-layer model developed by Liss & Slater (1974) to calculate the air-sea exchange of MEK. This model, used in many air-sea flux schemes (Fischer et al., 2012; Johnson, 2010; Wang et al., 2019), parameterizes the flux of a gas into or out of the ocean based

on windspeeds and concentration gradients. We supplement the original two-layer model with updated air (Johnson, 2010) and water (Nightingale et al., 2000) transfer velocities. The necessary variables for this parameterization were from *in situ* ATom observations taken at less than 200 m above sea level (temperature, pressure, atmospheric MEK mixing ratios, windspeed), non-ATom observations (oceanic MEK mixing ratios, discussed below), and satellite observations (sea surface temperature, salinity). Sea surface temperature (SST) for the ATom-1 and ATom-2 time periods are from the Moderate Resolution Imaging Spectroradiometer (MODIS)-Aqua L3 11 micron SST product (NASA Ocean Biology Processing Group, 2015); salinity is from the Aquarius rain-corrected monthly sea surface salinity product for the relevant months in 2014 (the last year available from Aquarius) (JPL, 2015). We also re-ran the model using a regional mean surface windspeed from the Modern-Era Retrospective analysis for Research and Applications version 2 (MERRA-2) reanalysis (Gelaro et al., 2017) over the same time period, with similar results. All calculation inputs are included in appendix C (Table C1).

4.3. Results

4.3.1. Multi-basin evidence for an oceanic MEK source

Figure 4.2 presents vertical profiles of MEK over the remote ocean regions sampled by the ATom missions. The data are presented in 1 km altitude bins, and further classified by meteorological season. We define meteorological winter as December-February in the Northern Hemisphere and June-August in the Southern Hemisphere, while meteorological summer is the reverse. In the equatorial regions, this classification becomes less meaningful, but little seasonality was observed in the vertical profiles in those regions. We denote the 25th, 50th, and 75th percentile for each 1-km altitude bin and season. Solid colors denote the profile with a CO

filter applied; in dashed lines we show the same statistics calculated using all of the data. In taking this approach, we assume that there is some atmospheric background profile, through which more polluted coherent air masses advect. By filtering out the polluted air signal and averaging across the region, we hope to visualize a profile that reflects only the regional emissions.

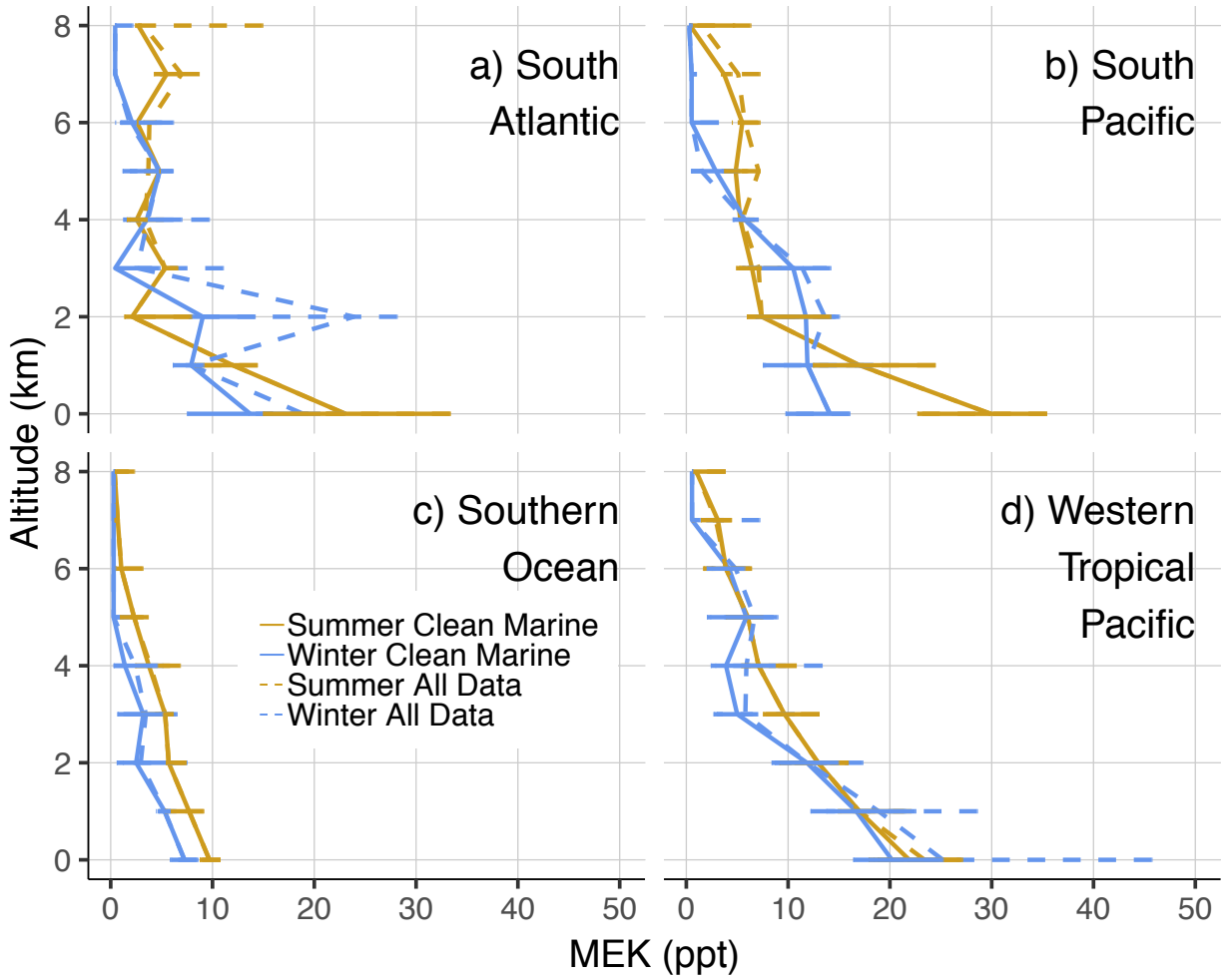

Figure 4.2 MEK observations from ATom-1 and ATom-2 in the a) South Atlantic, b) South Pacific, c) Southern Ocean, and d) Western Tropical Pacific in 1 km altitude bins. Vertical lines connect the median value for each binned vertical km, and horizontal bars show the spread of the 25th and 75th percentiles. Blue lines summarize data from the meteorological winter (January-

February in the Northern Hemisphere, July-August in the Southern Hemisphere) and orange lines summarize data from meteorological summer. The solid lines show the data from the clean marine airmasses, where CO mixing ratios are at or below the regional background (as described text). Dashed lines present the same analysis using all available MEK data. Sample sizes at each vertical level, region, and season are included in appendix C (Figure C1).

The vertical distribution of MEK over the remote oceans is consistent with a source at the surface and a sink aloft. The consistent profile shape is present during both summer and winter in all regions including the Southern Ocean. Except in the tropics, the summer surface enhancement is generally larger than the winter surface enhancement. The South Pacific and Southern Ocean summer surface enhancements are larger than their winter counterparts. The highest median MEK surface mixing ratios were encountered in the South Pacific, while the highest extremes in the unfiltered data were measured in the Western Tropical Pacific; in the filtered data, both maxima were in the South Pacific. The similarity in shapes between the filtered (i.e., clean marine) and full-data vertical profiles in the middle and lower troposphere strengthens the evidence for an oceanic source; it also means that our analysis is not sensitive to the choice of background CO mixing ratio(s). The only major feature removed by filtering for CO occurs in the mid to lower troposphere during the South Atlantic winter is the MEK spike at 2 km in the full-data profile. Examination of other fire tracer mixing ratios observed with TOGA (HCN, CH_3CN) suggests that the source of this MEK enhancement was biomass burning. Additional examination of the n-butane and i-pentane abundances measured by WAS over the study region shows that concentrations of these species are either negligible or too small to explain the observed MEK signal; they also have the opposite seasonality (i.e., concentrations are larger in the winter than the summer). We thus do not believe that the observed MEK profile can be explained by a terrestrial or otherwise anthropogenic source. Sample sizes for each vertical level, region, and season are included in appendix C (Figure C1).

4.3.2. Possible sources of oceanic MEK

We suggest that there are at least two potential oceanic sources of MEK, (1) Phytoplankton in the remote oceans and (2) another chemical or photochemical process in the surface ocean. If MEK were produced mostly by phytoplankton, we would expect to observe a correlation between the abundance of MEK and tracers for oceanic production. We calculated correlations between MEK and four OVOCs with documented ocean sources: methyl nitrate, acetone, acetaldehyde, and DMS. The atmospheric lifetimes of these species to chemical loss (primarily oxidation by OH and photodissociation) vary. The global mean lifetimes of methyl nitrate, acetone, and acetaldehyde, respectively, are 26 days (Fisher et al., 2018), 19 days (Brewer et al., 2017), and 20 hours (Millet et al., 2010); the mean atmospheric lifetime of DMS is 1-2 days (Kloster et al., 2006; Marandino, 2005). These lifetimes bracket the lifetime of MEK of 5-6 days to chemical loss at an OH concentration ~1.5×10^6 cm^{-3} (Jordan et al., 2009; Yañez-Serrano et al., 2016). Figure 4.3 presents the correlation between the MEK and these species in clean marine air below 1 km in each of the regions in Figure 4.1. Sample sizes are limited to 20 and 37 in the Western Tropical Pacific and Southern Ocean and to 25 and 14 in the South Atlantic and South Pacific respectively. To ensure the maximum reliability in the statistics, this analysis does not discriminate between seasons – all clean marine data are combined in this analysis regardless of season. The one exception is the acetaldehyde-MEK correlation, which shows dramatic differences between seasons. Scatterplots showing the complete dataset summarized in Figure 4.3 are included in appendix C (Figures S2-S5).

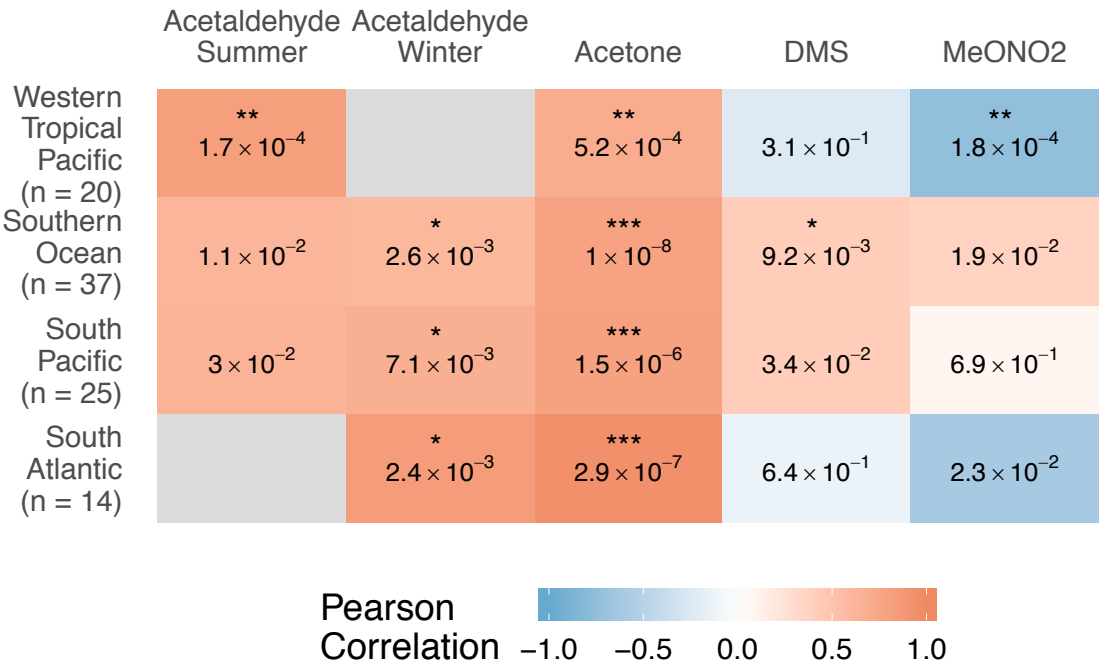

Figure 4.3. Pearson correlation coefficients between individual near-surface (<1 km) profile-averaged ATom observations of MEK and various species in clean marine air by region. Total sample *n* is shown on the y-axis for each region. Tiles are colored by the sign of the Pearson correlation coefficient in that region. Grey tiles indicate that the sample size is too small for correlation to be meaningful ($n < 10$). The p-value is shown on each tile, along with stars showing the relative p-value magnitudes in each region: one star corresponds to a p-value between $1x10^{-3}$-$1x10^{-2}$, two stars $1x10^{-3}$-$1x10^{-4}$, and three stars $p <= 1x10^{-4}$. Acetaldehyde has been separated into winter and summer correlations because the distributions differ between seasons in all regions, which is not true for the other three species shown; as such, the *n* values given for each region refer to the total sample size of winter and summer combined.

Figure 4.3 shows that MEK and acetone are well-correlated across ocean basins, while the other species show more heterogeneity in the relationships to MEK in this dataset. Correlation coefficients between acetone and MEK range from 0.72-0.95, three of which have p-values $\leq$ $1.5x10^{-6}$. This robust correlation in clean marine air across ocean regions suggests that acetone and MEK share an oceanic source. This source is sufficiently large that observed mixing ratios of MEK are around 10% of that of acetone in the remote marine boundary layer. Given the

disparity in lifetime between these two compounds, the flux of MEK out of the surface layer must be greater than 10% of that of acetone. Acetaldehyde and MEK are also positively correlated, but less strongly than acetone and MEK. Unlike in the MEK-acetone case, the correlations between MEK and acetaldehyde differ seasonally. For this reason, we present the seasonal correlations for acetaldehyde in each region and season in which sample sizes were sufficiently large. A possible explanation for this correlation is that the photooxidation of MEK can produce acetaldehyde (Calvert et al., 2011), and so we might expect the two species to appear correlated due to causation, even absent a common source. To examine this possibility, we used a back trajectory analysis (Bowman, 1993; Bowman & Carrie, 2002) to estimate the mean time that a sampled air mass had been in contact with the oceanic boundary layer. The specifics of this procedure, and the results of the modeling, are included in appendix C (Figure C6). In all locations and seasons studied, the median air mass sampled had been in the boundary layer for less than five days. Given the relatively long atmospheric lifetime of MEK, the correlations observed are still likely to represent a common source rather than the atmospheric production of acetaldehyde from MEK. In the Western Tropical Pacific and South Pacific during summer, a small number of air masses sampled were within the boundary layer for between 12-15 days. Therefore, it is possible that the particularly strong correlation shown between MEK and acetaldehyde in the Western Tropical Pacific summer might be the result MEK photooxidation; in light of the similar correlations shown in other regions, we still believe that the weight of evidence rests on the side of a common oceanic source for the two species. Methyl nitrate shows a strong negative correlation with MEK in the Western Tropical Pacific. This may simply be an artifact of the greater variability of methyl nitrate in these regions (mixing ratios range from 4-88 ppt for methyl nitrate and 5-39 ppt for MEK), but the robustness of the negative

correlation observed does suggest the possibility of some real and unexplained inverse relationship between MEK and methyl nitrate emissions. In our analysis, DMS is mostly uncorrelated with MEK, with the sole exception being a weak positive correlation observed in the South Pacific ($r = 0.47$, $p = 0.02$). This correlation may simply reflect the summertime increases in both MEK and DMS in the region (See Figure C3 in appendix C) and the near-zero DMS values observed during winter. Because the rate of reaction with OH is ~10x slower for MEK than DMS (Burkholder et al., 2015) and our back-trajectory modeling shows that most airmasses sampled had been in contact with the oceanic boundary layer for more than a day (the mean lifetime of DMS; see Figure C6 in appendix C), we cannot rule out the possibility that MEK and DMS were co-emitted in these regions and over time the co-emitted DMS reacted away and was not observed by our study. However, given that acetaldehyde did show a correlation with MEK despite having a similar atmospheric lifetime to DMS, we believe that the emissions of DMS and MEK are unlikely to be correlated. Given the observed connections between the decline of phytoplankton blooms and acetone emissions (Sinha et al., 2007), it is possible that a time-lagged correlation between MEK and DMS might exist; however the temporal resolution of our data does not allow the analysis necessary to observe such a connection. These results are insensitive to the choice of background CO. Based on this analysis, our observed correlations between MEK and acetone as well as those between MEK and acetaldehyde, are robust and consistent with the three species sharing similar oceanic sources.

We are only aware of a two papers detailing observations of MEK in seawater, which give wildly divergent results. In one case, the samples were taken in Australian coral reefs (Swan et al., 2016). Observed concentrations of MEK in seawater range from 102-119 nM. Swan et al. (2016) documented similar seawater acetone concentrations (74-183 nM), which are an order of

magnitude higher than the range of previously recorded open ocean mixed layer acetone concentrations (Brewer et al., 2017; Fischer et al., 2012), and roughly 2-4 times as high as the highest previous measurements in the open ocean (Tanimoto et al., 2014). Since acetone concentrations are observed to be lower in the pelagic environment than in coral reef seawater, we assume that open-ocean MEK concentrations are also much lower than those observed by Swan et al. (2016). Therefore, we treat their observation as an upper limit for our model calculations. In the other set of observations, taken over the South China Sea and Sulu Sea in November 2011, the median oceanic MEK concentration observed was 0.88 nM (Schlundt et al., 2017). Although it should not be surprising that the chemical environment differs between a coral reef and a pelagic environment, it is not known why these observed values are so different from those seen by Swan et al. (2016); there is clearly significant variability in oceanic MEK concentrations.

The air-sea exchange of MEK can also be represented using a flux model (Section 4.2.2). When we estimate the flux of MEK using realistic ocean conditions with seawater MEK concentrations two orders of magnitude lower than those observed by Swan et al. (2016), the model produces a net positive flux of MEK in all seasons and regions examined. For all regions and both seasons, the ocean does not uptake MEK until the seawater concentration of MEK falls below 1 nM (~10 nmol mol^{-1}). These model results are presented in greater detail in appendix C (Figure C7), and agree with prior models of MEK air-sea exchange (Schlundt et al., 2017).

While seawater MEK concentrations are as of now mostly unknown, existing measurements suggest that MEK shares a similar oceanic abundance to acetone. The lowest acetone observed in the surface ocean ranges from 2-5 nM, as summarized by Brewer et al. (2017). Our calculations suggest that ocean regions shown in Figure 4.1 likely serve as a net source of MEK to the

atmosphere. For comparison purposes, a 3 nM average seawater MEK concentration in the Southern Ocean implies a ~0.5 Tg annual source from that region.

4.4. Conclusions

Using data from clean marine air masses sampled in the ATom-1 and ATom-2 field campaigns, we provide evidence that the ocean is a source of MEK to the atmosphere. Outside the tropics, this source is more pronounced during summer than winter; less seasonality is observed in the tropics. MEK in the regions we examined is sometimes weakly correlated with DMS – a reliable tracer of marine biological activity. Ocean-produced MEK is strongly correlated with acetone and slightly less strongly correlated with acetaldehyde, which suggests the three species could share similar sources. Acetone and MEK have similar abundances in the only existing measurements of both species in seawater, providing additional evidence of a similar source, and even a small concentration of MEK in surface seawaters results in a flux of MEK out of the surface waters.

ATom observations suggest that MEK's flux out of the ocean is >10% of that of acetone. As MEK oxidation is a source of acetaldehyde in the troposphere, this oceanic MEK might serve as a source of acetaldehyde in regions where current sources fail to explain observations (Wang et al., 2019; Wolfe et al., 2019). Quantification of the sources and sinks of MEK in the oceans is needed to improve our understanding of MEK and its implications for global oxidation capacity.

Chapter References

Apel, E. C., Hornbrook, R. S., Hills, A. J., Blake, N. J., Barth, M. C., Weinheimer, A., et al. (2015). Upper tropospheric ozone production from lightning NOx-impacted convection: Smoke ingestion case study from the DC3 campaign. *Journal of Geophysical Research: Atmospheres*, *120*(6), 2505–2523. https://doi.org/10.1002/2014JD022121

Barletta, B., Nissenson, P., Meinardi, S., Dabdub, D., Sherwood Rowland, F., VanCuren, R. A., et al. (2011). HFC-152a and HFC-134a emission estimates and characterization of CFCs, CFC replacements, and other halogenated solvents measured during the 2008 ARCTAS campaign (CARB phase) over the South Coast Air Basin of California. *Atmospheric Chemistry and Physics*, *11*(6), 2655–2669. https://doi.org/10.5194/acp-11-2655-2011

Brewer, J. F., Bishop, M., Kelp, M., Keller, C., Ravishankara, A. R., & Fischer, E. V. (2017). A sensitivity analysis of key factors in the modeled global acetone budget. *Journal of Geophysical Research*.

Burkholder, J. B., Sander, S. P., Abbatt, J., Barker, J. R., Huie, R. E., Kolb, C. E., et al. (2015). Chemical Kinetics and Photochemical Data for Use in Atmospheric Studies. In *JPL Publication 15-10* (Vol. 18). Pasadena: Jet Propulsion Laboratory.

Calvert, J. G., Mellouki, A., Orlando, J. J., Pilling, M. J., & Wallington, T. J. (2011). *The Mechanisms of Atmospheric Oxidation of the Oxygenates*. New York: Oxford University Press.

Colman, J. J., Swanson, A. L., Meinardi, S., Sive, B. C., Blake, D. R., & Rowland, F. S. (2001). Description of the Analysis of a Wide Range of Volatile Organic Compounds in Whole Air Samples Collected during PEM-Tropics A and B. *Analytical Chemistry*, *73*(15), 3723–3731. https://doi.org/10.1021/ac010027g

Dixon, J. L., Beale, R., & Nightingale, P. D. (2013). Production of methanol, acetaldehyde, and acetone in the Atlantic Ocean. *Geophysical Research Letters*, *40*(17), 4700–4705. https://doi.org/10.1002/grl.50922

Dixon, J. L., Beale, R., Sargeant, S. L., Tarran, G. A., & Nightingale, P. D. (2014). Microbial acetone oxidation in coastal seawater. *Frontiers in Microbiology*, *5*. https://doi.org/10.3389/fmicb.2014.00243

Fischer, E. V., Jacob, D. J., Millet, D. B., Yantosca, R. M., & Mao, J. (2012). The role of the ocean in the global atmospheric budget of acetone. *Geophysical Research Letters*, *39*(1), n/a-n/a. https://doi.org/10.1029/2011gl050086

Fisher, J. A., Atlas, E. L., Barletta, B., Meinardi, S., Blake, D. R., Thompson, C. R., et al. (2018). Methyl, Ethyl, and Propyl Nitrates: Global Distribution and Impacts on Reactive Nitrogen in Remote Marine Environments. *Journal of Geophysical Research: Atmospheres*, *123*(21), 12,429-12,451. https://doi.org/10.1029/2018JD029046

Gelaro, R., McCarty, W., Suárez, M. J., Todling, R., Molod, A., Takacs, L., et al. (2017). The Modern-Era Retrospective Analysis for Research and Applications, Version 2 (MERRA-2). *Journal of Climate*, *30*(14), 5419–5454. https://doi.org/10.1175/JCLI-D-16-0758.1

Hodnebrog, Ø., Dalsøren, S. B., & Myhre, G. (2018). Lifetimes, direct and indirect radiative forcing, and global warming potentials of ethane (C_2H_6), propane (C_3H_8), and butane (C_4H_{10}). *Atmospheric Science Letters*, *19*(2), e804. https://doi.org/10.1002/asl.804

Johnson, M. T. (2010). A numerical scheme to calculate temperature and salinity dependent air-water transfer velocities for any gas. *Ocean Science*, *6*(4), 913–932. https://doi.org/10.5194/os-6-913-2010

Jordan, C., Fitz, E., Hagan, T., Sive, B., Frinak, E., Haase, K., et al. (2009). Long-term study of VOCs measured with PTR-MS at a rural site in New Hampshire with urban influences. *Atmos. Chem. Phys.*, 21.

JPL. (2015). Aquarius CAP Level 3 Sea Surface Salinity Rain Corrected Standard Mapped Image Monthly Data V4.0. NASA Physical Oceanography DAAC. https://doi.org/10.5067/AQR40-3QMCS

Keiber, R. J., Zhou, X., & Mopper, K. (1990). Formation of carbonyl compounds from UV-induced photodegradation of humic substances in natural waters: fate of riverine carbon in the sea. *Limnol. Oceanogr.*, *35*(7), 1503–1515.

Kloster, S., Feichter, J., Maier-Reimer, E., Six, K. D., Stier, P., & Wetzel, P. (2006). DMS cycle in the marine ocean-atmosphere system – a global model study, 23.

Lee, B. H., Munger, J. W., Wofsy, S. C., & Goldstein, A. H. (2006). Anthropogenic emissions of nonmethane hydrocarbons in the northeastern United States: Measured seasonal variations from 1992–1996 and 1999–2001. *Journal of Geophysical Research*, *111*(D20). https://doi.org/10.1029/2005JD006172

Liss, P., & Slater, P. G. (1974). Flux of Gases across the Air-Sea Interface. *Nature*, *247*, 181–184.

Marandino, C. A. (2005). Oceanic uptake and the global atmospheric acetone budget. *Geophysical Research Letters*, *32*(15). https://doi.org/10.1029/2005gl023285

Millet, D. B., Guenther, A., Siegel, D. A., Nelson, N. B., Singh, H. B., de Gouw, J. A., et al. (2010). Global atmospheric budget of acetaldehyde: 3-D model analysis and constraints from in-situ and satellite observations. *Atmos. Chem. Phys.*, 21.

Moore, R. M., & Blough, N. V. (2002). A marine source of methyl nitrate. *Geophysical Research Letters*, *29*(15), 27-1-27–4. https://doi.org/10.1029/2002GL014989

NASA Ocean Biology Processing Group. (2015). MODIS-Aqua Level 2 Ocean Color Data Version 2014 [Data set]. NASA Ocean Biology DAAC. https://doi.org/10.5067/AQUA/MODIS_OC.2014.0

Nemecek-Marshall, M., Wojciechowski, C., Kuzma, J., Silver, G. M., & Fall, R. (1995). Marine Vibrio Species Produce the Volatile Organic Compound Acetone. *Applied and Environmental Microbiology*, *61*(1), 44–47.

Nevitt, G. A., Veit, R. R., & Kareiva, P. (1995). Dimethyl sulphide as a foraging cue for Antarctic Procellariiform seabirds. *Nature*, *376*(6542), 680–682. https://doi.org/10.1038/376680ao

Nightingale, P. D., Malin, G., Law, C. S., Watson, A. J., Liss, P. S., Liddicoat, M. I., et al. (2000). In situ evaluation of air-sea gas exchange parameterizations using novel conservative and volatile tracers. *Global Biogeochemical Cycles*, *14*(1), 373–387. https://doi.org/10.1029/1999gb900091

Rossabi, S., & Helmig, D. (2018). Changes in Atmospheric Butanes and Pentanes and Their Isomeric Ratios in the Continental United States. *Journal of Geophysical Research: Atmospheres*, *123*(7), 3772–3790. https://doi.org/10.1002/2017JD027709

Santoni, G. W., Daube, B. C., Kort, E. A., Jiménez, R., Park, S., Pittman, J. V., et al. (2014). Evaluation of the Airborne Quantum Cascade Laser Spectrometer (QCLS) measurements of the carbon and greenhouse gas suite – CO_2, CH_4, N_2O, and CO – during the CalNex and HIPPO campaigns. *Atmospheric Measurement Techniques Discussions*, *6*(6), 9689–9734. https://doi.org/10.5194/amtd-6-9689-2013

Schlundt, C., Tegtmeier, S., Lennartz, S. T., Bracher, A., Cheah, W., Krüger, K., et al. (2017). Oxygenated volatile organic carbon in the western Pacific convective center: ocean cycling, air–sea gas exchange and atmospheric transport. *Atmospheric Chemistry and Physics*, *17*(17), 10837–10854. https://doi.org/10.5194/acp-17-10837-2017

Sinha, V., Williams, J., Meyerhofer, M., Riebesell, U., Paulino, A. I., & Larsen, A. (2007). Air-Sea Fluxes of methanol, acetone, acetaldehyde, isoprene, and DMS from a Norwegian fjord following a phytoplankton bloom in a mesocosm experiment. *Atmospheric Chemistry and Physics*, *7*, 739–755.

Swan, H. B., Crough, R. W., Vaattovaara, P., Jones, G. B., Deschaseaux, E. S. M., Eyre, B. D., et al. (2016). Dimethyl sulfide and other biogenic volatile organic compound emissions from branching coral and reef seawater: potential sources of secondary aerosol over the Great Barrier Reef. *Journal of Atmospheric Chemistry*, *73*(3), 303–328. https://doi.org/10.1007/s10874-016-9327-7

Tanimoto, H., Kameyama, S., Omori, Y., Inomata, S., & Tsunogai, U. (2014). High-Resolution Measurement of Volatile Organic Compounds Dissolved in Seawater Using Equilibrator Inlet-Proton Transfer Reaction-Mass Spectrometry (EI-PTR-MS), 89–115. https://doi.org/10.5047/w-pass.a02.001

Wang, S., Hornbrook, R. S., Hills, A., Emmons, L. K., Tilmes, S., Lamarque, J.-F., et al. (2019). Atmospheric Acetaldehyde: Importance of Air-Sea Exchange and a Missing Source in the Remote Troposphere. *Geophysical Research Letters*. https://doi.org/10.1029/2019GL082034

Wolfe, G. M., Nicely, J. M., Clair, J. M. S., Hanisco, T. F., Liao, J., Oman, L. D., et al. (2019). Mapping hydroxyl variability throughout the global remote troposphere via synthesis of airborne and satellite formaldehyde observations. *Proceedings of the National Academy of Sciences*, *116*(23), 11171–11180. https://doi.org/10.1073/pnas.1821661116

Yañez-Serrano, A. M., Nolscher, A. C., Bourtsoukidis, E., Derstroff, B., Zanoni, N., Gros, V., et al. (2016). Atmospheric mixing ratios of methyl ethyl ketone (2-butanone) in tropical, boreal, temperate, and marine environments. *Atmos. Chem. Phys.*, *16*, 10965–10984. https://doi.org/10.5194/acp-16-10965-2016

Yang, M., Beale, R., Liss, P., Johnson, M., Blomquist, B., & Nightingale, P. (2014). Air–sea fluxes of oxygenated volatile organic compounds across the Atlantic Ocean. *Atmospheric Chemistry and Physics*, *14*(14), 7499–7517. https://doi.org/10.5194/acp-14-7499-2014

Yang, M., Bell, T. G., Blomquist, B. W., Fairall, C. W., Brooks, I. M., & Nightingale, P. D. (2016). Air-sea transfer of gas phase controlled compounds. *IOP Conference Series: Earth and Environmental Science*, *35*, 012011. https://doi.org/10.1088/1755-1315/35/1/012011

Yu, F., & Luo, G. (2010). Oceanic Dimethyl Sulfide Emission and New Particle Formation around the Coast of Antarctica: A Modeling Study of Seasonal Variations and Comparison with Measurements. *Atmosphere*, *1*(1), 34–50. https://doi.org/10.3390/atmos1010034

Zhou, X., & Mopper, K. (1997). Photochemical production of low-molecular-weight-carbonyl compounds in seawater and surface microlayer and their air-sea exchange. *Marine Chemistry*, *56*, 201–213.

CHAPTER 5: GLOBAL ATMOSPHERIC BUDGET AND IMPORTANCE OF METHYL ETHYL KETONE (MEK): CHEMICAL TRANSPORT ANALYSIS AND CONSTRAINTS FROM IN-SITU AIRCRAFT OBSERVATIONS

5.1. Chapter Introduction

In this chapter, we present an analysis of the sources and sinks of MEK in the troposphere. Our analysis includes four direct sources and one indirect sources of MEK: (1) direct emission from the biosphere (Jordan et al., 2009; Yañez-Serrano et al., 2016); (2) direct anthropogenic emissions (EMEP, 2015; Hoesly et al., 2018; U. S. EPA, 2013); (3) biomass burning (Akagi et al., 2011; Andreae, 2019); and (4) oceanic emissions (see Chapter 4). It also includes one indirect sources of MEK via secondarily production from the atmospheric oxidation of predominantly anthropogenically emitted alkanes, most importantly *n*-butane and to a lesser extent *i*-pentane and longer alkanes (Jenkin et al., 1997). Sinks for MEK in our simulation are to photolysis (IUPAC, 2005), oxidation by OH, NO_3, and Cl (Calvert et al., 2011), uptake to the ocean (see Chapter 4), and dry deposition (Jordan et al., 2009; Talbot, 2005). We compare our modeled MEK mixing ratios to a suite of aircraft and surface observations and evaluate model performance.

5.2. Methods

5.2.1. Model Framework

We simulate the sources, sinks, and global tropospheric distribution of MEK using the detailed atmospheric oxidation scheme in the GEOS-Chem global 3-D Chemical Transport model (version 12.0.0, www.geos-chem.org; Bey et al., 2001). We have improved the representation of several processes within the model in order to explicitly include the emissions of MEK and its atmospheric fate, and these updates are explained in the following sub-sections.

The GEOS-Chem simulations presented here use GEOS-FP assimilated meteorological data provided by the Global Modeling and Assimilation Office (GMAO) at the NASA Goddard Space Flight Center. This data is produced on a 1/4° × 5/16° grid, with time resolution of 1 hour averages for surface fluxes and 3 hour averages for upper air tendencies (GMAO, 2013). We regrid this data to a horizontal resolution of 2° × 2.5° with 47 hybrid pressure-sigma vertical levels up to 0.66 hPa, 15-minute transportation timesteps, and 30-minute chemistry timesteps. These simulations also use the GEOS-Chem *Tropchem* scheme, which explicitly represents tropospheric chemistry while parameterizing the stratosphere. We use two different sets of simulations: 1) a one-year simulation of 2016 conditions; and 2) two-month simulations covering each of the four two-month ATom studies (July-August 2016, January-February 2017, September-October 2017, and April-May 2018). Each simulation is initiated using a one-year model spin-up.

5.2.1.1. Secondary Chemical Production of MEK

In the default chemistry scheme included in GEOS-Chem 12.0.0, MEK is not treated as an independent species; rather, it has been used up to this point as a lumped stand-in for >3 carbon ketones, referred to hereafter as 'pseudo-MEK' (Paulot, Crounse, Kjaergaard, Kroll, et al., 2009; Paulot, Crounse, Kjaergaard, Kürten, et al., 2009). This choice was made due to computational limitations, but it has major implications for diagnosing the actual source of MEK because pseudo-MEK includes a secondary chemical source from the atmospheric oxidation of isoprene and various monoterpenes. These reactions are unlikely to occur in an oxidizing medium such as the troposphere, and indeed no mechanistic pathways have been proposed for

production of MEK from atmospheric oxidation of isoprene, α- or β-pinene, or methyl butenol oxidation (Rollins et al., 2009; Singh et al., 2004; Yañez-Serrano et al., 2016).

To better represent explicit MEK chemistry, we follow the example of Goliff et al. (2013) and split the lumped pseudo-MEK species into two different model species: an explicit MEK and a $>C_4$ ketone tracer (KET). KET is photolyzed in the same way as MEK but is otherwise handled identical to the previously existing pseudo-MEK. This speciation necessitates changes to both the production (discussed here) and removal (discussed below in Section 5.2.1.2) of MEK in GEOS-Chem. In the MEK production scheme in GEOS-Chem 12.0.0, the reaction intermediate lumping scheme implemented in the Caltech Isoprene scheme (Paulot, Crounse, Kjaergaard, Kroll, et al., 2009; Paulot, Crounse, Kjaergaard, Kürten, et al., 2009) meant that alkane, isoprene, and monoterpene chemical schemes all fed into common RO_2 pools. We separate these schemes entirely, creating two separate RO_2 reaction families: one from biogenic VOCs (isoprene and the terpenes) and one from anthropogenic alkanes.

We further parse out the alkane species in order to better represent their emissions and subsequent contribution to MEK. In GEOS-Chem 12.0.0, $> C_3$ alkanes are treated as a single lumped species (ALK4) with 4.3 carbon atoms, which has several reactions in its oxidation scheme that produce pseudo-MEK at yields between 19-30%. The emissions and reaction rate coefficients of this higher-alkane species are treated in the model as a weighted average of butane, pentane, and larger alkanes. This alkane lumping scheme (hereafter referred to as 'The ALK4 scheme') is computationally cheaper than a fully speciated alkane representation and has a long history in atmospheric modeling (Lurmann et al., 1986), but it does not accurately represent the production of MEK because butanes and pentanes are both commonly emitted as multiple isomers each with different oxidative pathways in the atmosphere. Butane can be

emitted in both *i* and *n* configurations, and only the latter is capable of oxidizing to form MEK. Similarly, of the pentanes, only *i*-pentane can form MEK upon oxidation, while the analogous oxidation of *n*-pentane forms larger ketones such as 2 or 3-pentanone. We therefore speciate the original > C_3 alkane species in GEOS-Chem into five different compounds: *i* and *n*-butane, *i* and *n*-pentane, and a > C_6 tracer (ALK6). Each of these five compounds now has its own oxidation mechanism in our version of GEOS-Chem, with unique alkyl nitrate, peroxide, and RO_2 daughter reactions. This alkane scheme is referred to as 'the ALK6 scheme' in this paper. In the ALK6 scheme, MEK yields are distinct for each >C_3 alkane represented. For *n*-butane, all yields are unchanged from those in the ALK4 scheme. In the case of *i*-pentane and the >C_4 alkane species, 10% of the prior pseudo-MEK yield is now treated as explicitly MEK and the remaining 90% is lumped into our new >C_4 ketone species (KET), as both *i*-pentane and various higher alkanes (*e.g.* 1-methyl-pentane) are capable of producing both ketones, but they are much more likely to produce other heavier ketones (Saunders et al., 2003). Neither remaining branch (*i*-butane and *n*-pentane) is capable of oxidizing to produce MEK in the atmosphere, and so the net MEK yeilds are also changed. In the *i*-butane reactions, 50% of the prior pseudo-MEK yields are now acetone and 50% are treated as acetaldehyde, while in the *n*-pentane case 100% of the prior pseudo-MEK yields are now treated as >C_4 ketone species.

All reaction rate coefficients except those dealing with the direct oxidation of MEK are the same as the previous lumped version despite this speciation. We recognize the fundamental non-physicality of this choice, but we make it in the interest of keeping the updated model as simple and consistent as possible in its non-MEK chemistry. Future work is required to more accurately represent this speciated ALK6 scheme but is beyond the scope this thesis. The kpp equation file containing the updated mechanism is included in appendix D (Code D1), and the required

relevant reaction rate expressions can be found by downloading 12.0.0 of GEOS-Chem (www.geos-chem.org).

5.2.1.2. MEK Oxidation Pathways

In GEOS-Chem 12.0.0, MEK is lost to reaction with NO_3 and OH radicals. MEK can also be photolyzed; this process and its representation is discussed in Section 5.2.1.3 below. MEK in GEOS-Chem 12.0.0 is not lost to reaction with Cl, though the reaction does occur in laboratory studies (Atkinson et al., 2006; Kaiser et al., 2009; Zhao et al., 2008). The reaction with NO_3 is a minor sink, with a rate constant of 8.0×10^{-16} cm^3 $molecule^{-1}$ s^{-1}. Temperature dependent reaction rate coefficients for the OH and Cl pathways from GEOS-Chem and comparable literature parameterizations (Atkinson et al., 2006, 2006; Calvert et al., 2011; Carr et al., 2008; IUPAC, 2009; Jiménez et al., 2005; Kaiser et al., 2009; Le Calvé et al., 1998; Wallington & Kurylo, 1987; Zhao et al., 2008) are provided in Figure D1. Relative to literature values, the rate coefficients of MEK reaction with the OH radical in GEOS-Chem 12.0.0 (1.3×10^{-12} $e^{(-25/T)}$ cm^3 $molecule^{-1}$ s^{-1}) are generally higher than those in the literature for this carbonyl, which reflects the lumped nature of the $>C_3$ ketone (called MEK in the release version of the model and called pseudo-MEK here). As we differentiate between MEK and $>C_4$ ketones, we adopt the IUPAC recommendation of 1.5×10^{-12} $e^{(-90/T)}$ cm^3 $molecule^{-1}$ s^{-1} (Atkinson et al., 2006; IUPAC, 2009) for the reaction of OH with MEK. This change decreases the MEK-hydroxyl rate coefficient by ~7% at 300 K and ~17% at 200 K. The reaction rate coefficient for pseudo-MEK remains in GEOS-Chem and now represents the rate coefficient for oxidation of the new $> C_4$ ketone lumped species.

We also implement the reaction of MEK with the Cl atom, building upon the halogen chemistry scheme already incorporated into GEOS-Chem 12.0.0 (Sherwen et al., 2016). As shown in Figure D1, the rate coefficient for the reaction of MEK and Cl can vary by as much as a factor of two, depending upon the parameterization chosen. The most recent study of this reaction by Kaiser et al. (2009) suggests that this rate coefficient should be $k = 4.0 \times 10^{-11}$ cm^3 $molecule^{-1}$ s^{-1}, independent of temperature; however, this study only recommends the use of its parameterization down to temperatures of 297 K (Calvert et al., 2011; Kaiser et al., 2009). Instead, we rely on the IUPAC recommendation of 3.05×10^{-11} $e^{(80/T)}$ cm^3 $molecule^{-1}$ s^{-1}, which predates the publication of the Kaiser et al. (2009) data, but is recommended for temperatures from 200-450 K (Atkinson et al., 2008; Calvert et al., 2011).

5.2.1.3. MEK Photolysis

GEOS-Chem uses a customized implementation of the FAST-JX scheme (Wild et al., 2000) to efficiently estimate tropospheric photolysis. In this scheme, quantum yields and cross-sections are pre-computed offline for a set combination of pressure and temperature levels across 18 wavelength bins covering 177-850 nm and then interpolated to the relevant pressure levels (Eastham et al., 2014; Wild et al., 2000). In GEOS-Chem 12.0.0, IUPAC recommended quantum yields and cross-sections for MEK were used (IUPAC, 2013). However, the IUPAC recommended cross-sections do not include temperature dependence, and the quantum yields do not include a wavelength dependence and are measured only at 68 and 1000 hPa. We make use of the models derived in Chapter 3 to represent the absorption cross-sections across a range of atmospherically relevant temperatures. Two separate parameterizations of MEK quantum yields are currently treated as possible: either an inverse-linear interpolation of the IUPAC

recommended quantum yields without wavelength dependence (Raber & Moortgat, 1987) or a Stern-Volmer parameterization (Romero et al., 2005) with both wavelength and pressure dependence. When compared to the original parameterization of MEK photolysis in idealized conditions (i.e., IUPAC recommended cross-sections and quantum yields), implementing the temperature-dependent cross-sections and the IUPAC quantum yields results in no difference at the surface and a ~25% decrease in J-values at 15 km, while implementing the temperature-dependent cross-sections and available Stern-Volmer quantum yield fit results in an ~8-10% decrease in J-values across all altitudes relative to the IUPAC recommendations (Brewer et al., 2019). In this work, we use the latter implementation – temperature dependent cross-sections and Stern-Volmer quantum yields (Brewer et al., 2019; Romero et al., 2005) – and see the expected average ~8-10% decrease in MEK J-values across all altitudes relative to GEOS-Chem 12.0.0.

5.2.1.4. Anthropogenic Emissions

Both MEK and its alkane precursors have significant anthropogenic emissions. MEK can be emitted from solvent evaporation (Legreid et al., 2007) and combustion exhaust (Bon et al., 2011; Brito et al., 2015; Liu et al., 2015; Verschueren, 1983). MEK's precursor alkanes, most importantly *n*-butane, can be emitted either through leaks in petroleum and natural gas production and use, as well as from transportation and other combustion sources (Fraser et al., 1998; Gilman et al., 2013; Rossabi & Helmig, 2018). In GEOS-Chem, these emissions are processed using the Harvard Emissions Component software (HEMCO; Keller et al., 2014). In GEOS-Chem 12.0.0, HEMCO represents anthropogenic emissions using a global database – the Community Emissions Database (CEDS; Hoesly et al., 2018) – as a universal base case, expected to be overwritten in regions where more specific emissions inventories have been

developed. For all VOC emissions except the $>C_3$ alkanes, we overwrite CEDS with a series of local emissions inventories where appropriate: Asia (MIX; Li et al., 2015), the United States (2011 NEI; U. S. EPA, 2013), Europe (EMEP; EMEP, 2015; Vestreng & Klein, 2002), and Africa (DICE; Marais & Wiedinmyer, 2016). However, because these region-specific emissions inventories have not been processed for GEOS-Chem to reflect a speciated alkane mechanism, we do not include the alkane emissions from them in our model runs and instead rely solely on CEDS for anthropogenic alkane emissions.

CEDS, as processed in GEOS-Chem, represents $>C_3$ alkane species as three species: butane, pentane, and $>C_5$ alkanes (Hoesly et al., 2018). CEDS emissions are further broken down according to emissions category: for alkanes, the six relevant categories are (a) agricultural (non-burning); (b) energy transformation & extraction; (c) industrial combustion & processes; (d) surface transportation; (e) solvents; and (f) waste disposal & handling (Keller et al., 2014). Because *i/n*-butane and pentane ratios vary widely by emissions source, we take the emissions of butane and pentane from these CEDS categories and further parse them into isomers by source type. We represent *i/n* ratios for surface transportation based on studies of traffic in tunnels (Fraser et al., 1998), energy transformation and extraction based on studies of the oil and natural gas industries (Gilman et al., 2013), and all other categories based on an average of compiled *i/n* ratios from cities across the U.S. (Rossabi & Helmig, 2018). The speciation ratios used in our code are included in Table D1.

5.2.1.5. Biogenic Emissions

Biogenic VOC emissions in GEOS-Chem are calculated using the Model of Emissions of Gases and Aerosols from Nature (MEGAN) v2.1 as a function of meteorological conditions,

leaf-area index, and land cover parameters (Guenther et al., 2012). In MEGAN, emissions of MEK are estimated to be extremely small, and are not represented in GEOS-Chem. However, numerous other studies have shown biogenic emissions of MEK, often correlated with isoprene emissions (Alwe et al., 2019; Cappellin et al., 2017; Jordan et al., 2009; Millet et al., 2018; Yañez-Serrano et al., 2016; Yáñez-Serrano et al., 2015). The specific biogenic source of this MEK is not certain, but the correlation observed between MEK and isoprene emissions, and specifically the correlation observed between MVK uptake by leaves and MEK emissions suggests the possibility that MEK is produced via the in-leaf detoxification of MVK via reduction to MEK by an enone reductase enzyme (Cappellin et al., 2017). Multiple studies have shown similar enzymatic behavior in yeast, cyanobacteria, and plant cells (Kermogard et al., 1998; Shimoda et al., 2005; Wanner & Tressl, 1998). Other mechanisms may also be possible, as many plants emit OVOCs as a byproduct of plant wounding (Fall, 1999; de Gouw et al., 1999). As such, we include a biogenic source of MEK in GEOS-Chem pegged to the emissions of isoprene from MEGAN to be 0.5% of that for isoprene emission. This value is similar to that reported from multiple sites (Alwe et al., 2019; Cappellin et al., 2017; Millet et al., 2018), though this simplification likely does not capture the true complexity of MEK emission from the biosphere but is assumed to be adequate for our calculations.

5.2.1.6. Biomass Burning

Both MEK and its precursor alkanes are known to be emitted by biomass burning (Akagi et al., 2011; Singh et al., 2004). These emissions are handled in GEOS-Chem using the Global Fire Emissions Database (GFED) version 4. The GFED4 emissions use estimates of burned area and mass of fuel burned (Giglio et al., 2013; Randerson et al., 2012; Werf et al., 2017), in

conjunction with emission factors for different species based on fuel type (Akagi et al., 2011; Andreae, 2019). The emissions factors used in the current implementation are summarized in Table D2 in appendix D. In certain cases, no emission factor data is present in either source, and the necessary assumptions and assumed values are specified in Table D2.

5.2.1.7. Air-Sea Exchange

In Chapter 4, we identify that MEK has an oceanic source correlated with both the emissions of acetaldehyde and acetone (Brewer et al., 2020). The magnitude of this flux in is >10% of that of acetone over the remote oceans (Brewer et al., 2020). Because both acetaldehyde and acetone are known to be produced by the photolysis of Chromophoric Dissolved Organic Matter (CDOM) in seawater (Dixon et al., 2013; Kieber et al., 1990; X. Zhou & Mopper, 1997), we represent oceanic MEK concentrations as a function of CDOM in the same manner as acetaldehyde (Millet et al., 2010). We normalize the acetaldehyde distribution by its maximum value, then multiply that value by the maximum oceanic observation of MEK, 120 nM (Swan et al., 2016). In this manner, we found our *a priori* oceanic MEK estimate. We then performed a rudimentary sensitivity analysis, using model runs with parameterized oceanic concentrations 0.5, 0.1, 0.05, and 0.01 times this maximum. We compared our modeled atmospheric mixing ratios to those observed in the lower troposphere by the Atmospheric Tomography experiment (ATom; see Section 5.2.2.2) and calculated mean bias terms for each model run. Based on this analysis, we modify this oceanic max value to an *a posteriori* value of 60 nM, scaled as acetaldehyde (Millet et al., 2010). We thus derive a mean oceanic MEK concentration of 0.76 nM across the entire ocean; this derived value is very similar to the pelagic MEK concentrations observed in the Sulu and South China Seas (0.88 nM; Schlundt et al., 2017). The January, April,

July, and October ocean MEK plots are shown in Figure D2 in appendix D. The flux of this species into and out of the ocean proceeds as an analogue of acetone (Fischer et al., 2012), with flux modeled using a two-layer model (Liss & Slater, 1974) with updated air (Johnson, 2010) and water (Nightingale et al., 2000) resistances. We use a Henry's Law constant of 0.18 mol m^{-3} Pa^{-1} for MEK (R. Sander, 2015; S. P. Sander et al., 2011)

5.2.1.8. Dry Deposition of MEK over Ice-Free Land

MEK has been shown in field experiments to dry deposit onto soils and plants with deposition velocities ranging from 0.34-0.5 cm s^{-1} (Jordan et al., 2009; Talbot, 2005). Dry deposition has also been shown to be an important sink for acetone (Brewer et al., 2017; Karl, 2004; Karl et al., 2005); and acetone deposition is represented in GEOS-Chem using a constant dry deposition velocity over ice free land (Brewer et al., 2017; Jacob et al., 2002). We include MEK dry deposition as an analogue of acetone dry deposition, with a deposition velocity of 0.35 cm s^{-1}, which is at the lower end of the observed velocities (Jordan et al., 2009; Talbot, 2005). We do not include the possibility of MEK wet deposition, as this process is not included in the GEOS-Chem acetone simulation and MEK has a Henry's Law constant ~1/3 smaller than acetone (R. Sander, 2015).

5.2.2. Observations

In this work, we make use of a data from thirteen flight campaigns, with the earliest data from the 2006 Intercontinental Chemical Transport Experiment Phase B (INTEX-B) campaign and the latest from the 2018 fourth phase of the Atmospheric Tomography Mission (ATom-4). In

order to preserve a consistent record across this long time period, we use data primarily from a single instrument, the Trace Organic Gas Analyzer (TOGA).

5.2.2.1. The Trace Organic Gas Analyzer (TOGA)

TOGA is a combination fast online mass spectrometry and gas chromatography instrument (Apel et al., 2015). TOGA has been deployed on many field campaigns in the last 15 years, and it is used to measure a wide range of VOCs including non-methane hydrocarbons (NMHCs) and oxygenated VOCs (OVOCs) in the C_3-C_{10} range (Apel et al., 2015; Wang et al., 2019). TOGA has a sample collection time of 35 s, for a total sample processing time of 2 minutes (Apel et al., 2015). Although historically TOGA has shown some issues measuring acetone and acetaldehyde at mixing ratios at or near the LLOD, this has been improved in more recent implementations of the instrument and has never been observed to impact observations of MEK (Apel, 2003; Apel et al., 2015; Brewer et al., 2020; Wang et al., 2019). The lower limit of detection (LLOD) of TOGA varies by compound and campaign. Values below the LLOD are dynamically assigned a value between 0 and the LLOD as a linear function of how many LLOD-flagged values are recorded on a given flight, as described in Chapter 4.

5.2.2.2. The Atmospheric Tomography (ATom) Experiment

In this work, we compare aircraft observations from the NASA ATom field campaigns to GEOS-Chem simulations co-sampled in space and time. The ATom missions sampled both the Atlantic and Pacific oceans from 83° N to 87° S in July-August of 2016, January-February of 2017, October-November of 2017, and again in April-May of 2018. All four campaigns used a repeating vertical profile sampling design *en route*, repeatedly climbing and descending between

the upper troposphere and near the ocean surface (~150 m). The sampling also incorporated a number of level legs in the marine boundary layer (MBL). This repeated sampling of the remote troposphere across seasons, unbiased by a focus on specific atmospheric phenoma (*e.g.* pollution or smoke plumes), makes ATom singularly well-suited to model comparison (AToM Science Team, 2017; Wofsy et al., 2018). A large number of instruments were included in the ATom payloads, including TOGA. Details regarding individual instruments may be found in the ATom ESPO repository, at https://espo.nasa.gov/atom/content/ATom.

5.2.2.3. Other Observations

In addition to the direct comparisons to the ATom campaign missions, we compare GEOS-Chem simulations to observations from a suite of fourteen additional flight campaigns. These campaigns span 2006-2016. The details of the dates, instruments, locations, and references are included below in Table 5.2. In some campaigns, MEK and acetone were measured using Proton Transfer Reaction – Mass Spectrometry (PTR-MS; de Gouw et al., 2003; Warneke et al., 2001). This technique cannot distinguish between the aldehyde and ketone form of the molecule. In these cases, we partition the observations using the observed ratios of aldehyde:ketone from the ATom TOGA measurements. Chen et al. (2019) use the same approach with TOGA data from the Front Range Air Pollution and Photochemistry Éxperiment (FRAPPÉ). In the context of a global study, we decided that the comparison to ATom was more appropriate, as the aldehyde to ketone ratios over polluted regions like the Colorado front range are different from those observed globally, especially over the oceans. Based on the TOGA observations from ATom, we used a ratio of propanal:acetone of 0.005 and a ratio of butanal:MEK of 0.3; this compares to ratios of 0.009 and 0.09 used by Chen et al. (2019), respectively. In the context of more polluted

study regions where most of the PTR-MS observations were collected, it could be argued that our use of the larger aldehyde:ketone ratios is overly conservative. However, because of the large amount of non-PTR-MS data used in our comparisons, the choice of aldehyde:ketone ratios does not change any of our conclusions and is mentioned below where appropriate.

Table 5.1 – Non-ATom MEK aircraft measurements used in this paper, by location, date, and measurement method.

ID	Campaign	Dates	Location	Method	Reference
1	ARCPAC	March-April 2008	Alaska	PTR-MS	Brock et al. (2011)
2	ARCTAS	April-July 2008	N. American Arctic	TOGA	Simpson et al. (2011)
3	CA Discover AQ	Jan-Feb 2013	Southern California	PTR-MS	Crawford & Pickering (2014)
4	CalNex	April-June 2010	Southern California	PTR-MS	Warneke et al. (2012)
5	DC3	May-June 2012	Southern Central USA	TOGA	Apel et al. (2015)
6	FRAPPE	July-August 2014	Colorado Front Range	TOGA & PTR-MS	Pfister et al. (2017)
7	INTEX-B	March-April 2006	E. Pacific	TOGA	Singh et al. (2009)
8	KORUS-AQ	April-June 2016	Republic of Korea	PTR-MS	Nault et al. (2018)
9	NEAQS	July-August 2004	New England	PTR-MS	De Gouw et al. (2003)
10	NOMADSS	June-July 2013	SE. United States	TOGA	Yuan et al. (2015)
11	SENEX	June-July 2013	SE. United States	PTR-MS	Yuan et al. (2015)
12	SONGNEX	March-April 2015	Western US	PTR-MS	Koss et al. (2017), Yuan et al. (2016)
13	TexAQS	Sept-Oct 2006	E. Texas	PTR-MS	Gilman et al. (2013)
14	TORERO	Jan-Feb 2012	Western S. America	TOGA	Zhou et al. (2014)
15	TX Discover AQ	September 2013	E. Texas	PTR-MS	Crawford & Pickering (2014)

Figure 5.1 contextualizes these observations in space. Panel a) shows the spatial extent of all the field campaigns, both globally and over North America. ATom data points are shown in blue, gridded to 4º x 4º x 3 km mean positions for display purposes; other field campaigns are numbered by the campaign ID values listed in Table 5.1 and shown as red boxes encompassing their minimum and maximum latitudes and longitudes. Note that the spatial extents of these campaigns do not imply anything about the spatial coverage over the campaign region – this is particularly relevant in the Arctic Research of the Composition of the Troposphere from Aircraft and Satellites (ARCTAS) campaign (Campaign ID = 2), which took place in the polar region and thus has a minimum longitude of 50º. In fact, these points were basically over the pole itself – the only campaign with any Asian observations is the Korea-United States Air Quality Study (KORUS-AQ; Campaign ID = 12). Panel b) shows the regions used for compositing analysis in the paper.

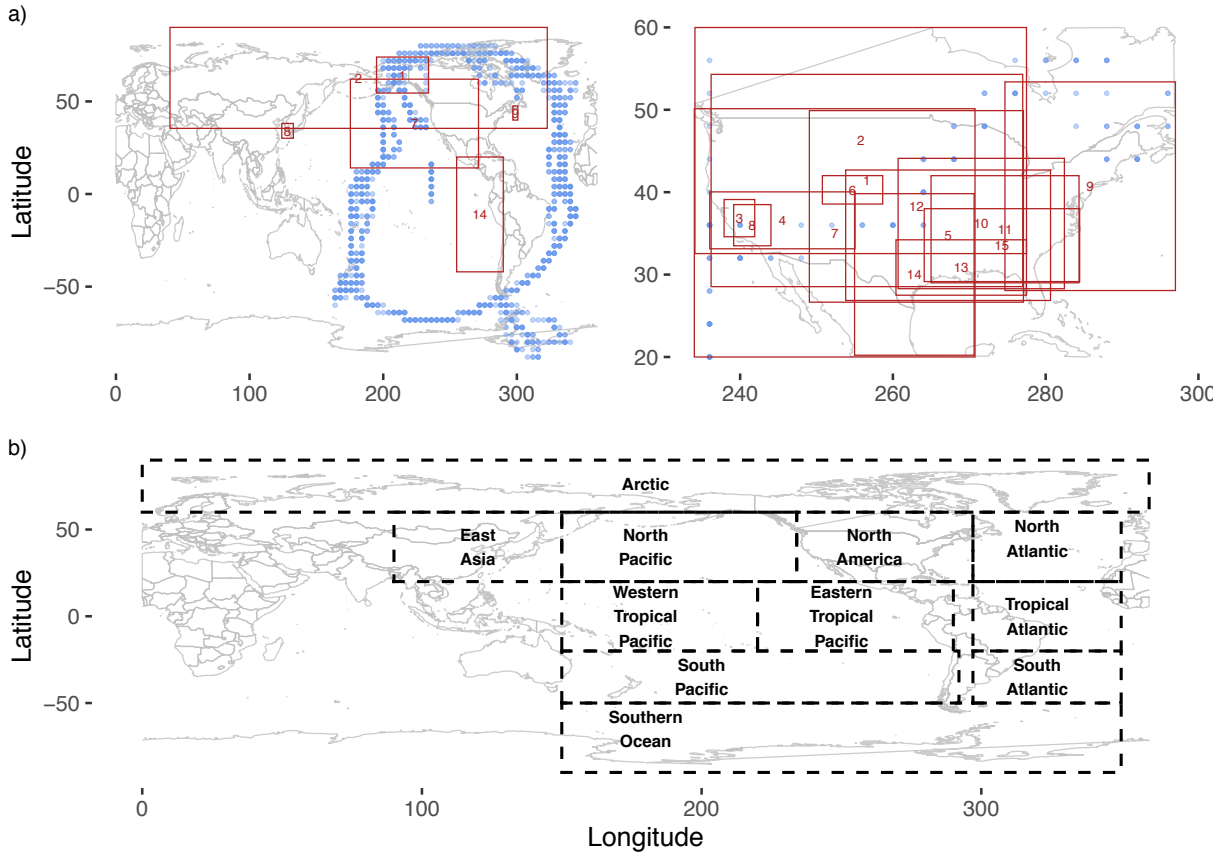

Figure 5.1 – A summary of regions and observations referenced in this paper. Panel a) shows the location of available observations from ATom and the other field campaigns referenced in Table 5.1, over both North America and the globe as a whole. Locations of observations from the ATom missions (1-4) are shown as blue points, which represent averaged 4º x 4º x 3 km positions for display purposes. The spatial extents of the non-ATom field campaigns are shown as squares denoting their range of latitudes and longitudes. Panel b) demarcates regions used for analysis in later figures.

5.3. Results

5.3.1. The Sources and Sinks of MEK in the Atmosphere

Table 5.2 summarizes the sinks and sources of MEK by hemisphere and alkane scheme. Regardless of the alkane scheme chosen, the largest source of MEK is from oceanic emissions. With a gross source of 6.3 Tg yr^{-1} against a sink of 2.3-2.6 Tg yr^{-1} (depending upon the alkane scheme used), oceanic emissions are a large net source to the atmosphere in both hemispheres. This source is slightly larger in the Northern Hemisphere than the Southern Hemisphere. This may seem surprising given the difference in sea surface area between the two hemispheres and contrasts with acetone, where 60% of the global ocean source is in the Southern Hemisphere (Brewer et al., 2017). However, this difference likely reflects the different oceanic parameterizations. While acetone is parameterized with a constant oceanic concentration at all points and seasons, our MEK parameterization has large variability between regions and seasons (see Figure D2), with much lower concentrations in wintertime in both hemispheres. ATom observations of acetone and MEK in the marine boundary layer reveal strong correlations between acetone and MEK, and these correlations suggest that oceanic MEK emissions are slightly more than 10% of the oceanic emissions of acetone (Brewer et al., 2020). This model suggests that global oceanic MEK emissions (6.3 Tg yr^{-1}) are ~12% of those of acetone (51.3 Tg yr^{-1}; Brewer et al., 2017). In the case of the ALK4 scheme, the source of MEK from alkane oxidation is of the same magnitude as the net oceanic source (3.9 Tg yr^{-1} and 3.7 Tg yr^{-1}, respectively) but more heavily weighted toward the Northern Hemisphere. In that region, it is a larger source of MEK than the net oceanic emission, although the gross oceanic source is still slightly larger. Under the ALK6 scheme, the source of MEK from alkane oxidation is much less important than the oceanic source as the MEK yield from oxidation is lower overall. The third

most important source of MEK is from the terrestrial biosphere (2.5 Tg yr^{-1}), with direct anthropogenic emissions and biomass burning much less important on the global scale.

Table 5.2. **Global and hemispheric budgets** for atmospheric MEK calculated with different alkane schemes. In the 'ALK4' scheme, the 'Oxidation of Isoalkanes' category includes the source of MEK from lumped > C_4 alkanes. In the 'ALK6' scheme, the 'Oxidation of Isoalkanes category' only includes MEK arising from the oxidation of *n*-butane, *i*-pentane, and lumped > C_6 alkanes. Units are in Tg of MEK per year. We calculate an average monthly global MEK burden ranging between 0.07 Tg (ALK6 scheme) and 0.11 Tg (ALK4 scheme). The average monthly MEK burden in the ALK4 case is 0.06 Tg and 0.05 Tg in the Northern and Southern Hemisphere, respectively.

		GEOS-Chem ALK4 Scheme			ALK6 Scheme
	Sources				
		NH	**SH**	**Global**	
Emissions	Anthropogenic	0.39	0.07	0.46	0.45
	Biomass Burning	0.48	0.32	0.80	0.80
	Terrestrial Biosphere	1.2	1.3	2.5	2.5
Atmospheric Production	Oxidation of Isoalkanes (Primarily Anthropogenic)	3.3	0.66	3.9	1.5
	Sinks				
	Oxidation by OH	3.6	1.7	5.3	3.4
	Photolysis	2.8	1.9	4.7	4.8
	Oxidation by Cl and NO_3	0.02	0.01	0.03	0.01
	Land Uptake	0.92	0.47	1.4	1.1
	Net Ocean Exchange				
	Ocean Source	3.4	2.9	6.3	6.3
	Ocean Sink	1.4	1.1	2.6	2.3
	Net Exchange	2.0	1.8	3.7	4.0

[a]Including biofuel use

Of the global sinks, photolysis and oxidation by OH are somewhat similar in importance. Which sink dominates depends upon the alkane scheme. While the magnitude of the loss to photolysis remains unchanged depending upon the scheme used, the rate of MEK oxidation by

OH changes by 1.9 Tg yr^{-1}. This shift reflects the fact that the alkane oxidation rate is higher in more polluted and radical-rich regions of the lower troposphere, leading to both a higher production rate and higher loss rate of MEK due to OH reactions. Dry deposition to the ocean and land surface are of lesser importance; deposition to the ocean is approximately twice the rate of deposition on land. Oxidation by other radicals is much less important, regardless of alkane scheme chosen. Based on the sinks summarized in Table 5.2 and the simulated monthly mean MEK burden of 0.1 Tg MEK, we estimate a mean atmospheric lifetime of ~3 days. This is a shorter atmospheric lifetime than the 5-6 days quoted in previous studies (Jordan et al., 2009; Yañez-Serrano et al., 2016) which based this calculation solely on the reaction of MEK with OH (Atkinson et al., 2006; IUPAC, 2009). Our estimate is also much shorter than the mean atmospheric lifetime of acetone (~19 days) (Brewer et al., 2017).

5.3.2. Aircraft Observations

The vertical columns profiled in the field campaigns listed in Table 5.1 show two very distinct profile types depending on location (Figure 5.2). Most of these campaigns predominantly sampled Northern Hemispheric areas that are highly anthropogenically-influenced, with the exception of the Aerosol, Radiation, and Cloud Processes affecting Arctic Climate (ARCPAC) and ARCTAS campaigns (which predominantly sampled the North American Arctic atmosphere), the ATom missions (which primarily sampled the remote marine troposphere – see section 5.2.2.2), and the Tropical Ocean tRoposophere Exchange of Reactive Halogen Species and Oxygenated VOCs (TORERO) field campaign (which sampled the marine troposphere off the Pacific coast of South America). Median MEK mixing ratios in these observations vary by 3 orders of magnitude, and the extreme values span 4 orders of magnitude from the 5th to 95th

percentile. The highest observed MEK mixing ratios in this dataset are found over Korea, where 10% of MEK mixing ratios were > 1 ppb and some observations reached as high as 10 ppb. These observations were taken using a PTR-MS and are thus subject to our choice of butanal:ketone ratio (as discussed in Section 5.2.2.3); if we instead assume the lower butanal:ketone ratio observed in polluted airmasses during the Front Range Air Pollution and Photochemistry Éxperiment (FRAPPÉ) (Chen et al., 2019), these extreme mixing ratios are in excess of 12 ppb. In this dataset, MEK is indeed the second most abundant ketone in the troposphere, occurring at a median of 22 times the abundance of methyl vinyl ketone (MVK), the third most abundant atmospheric ketone.

While there is a clear decrease in observed mixing ratios with altitude over the remote oceans in ATom data, the vertical gradients appear to be quite small over North America and East Asia (KORUS-AQ) during spring, and over North America during summer. Observations from ATom-1, 2, and 3 all show median MEK mixing ratios <1 ppt in the upper troposphere, and this corresponds to values at or below the lower limit of detection of the instruments involved. The median mixing ratio drops below 1 ppt at 7-8 km. In ATom-4, while median mixing ratios never reached this low, a clear decrease to a median mixing ratio of ~3 ppt is also seen above 8 km. TORERO and the Deep Convective Clouds and Chemistry Project (DC3) are the only other field campaigns to observe median mixing ratios below 10 ppt, and in both abundances these low were only observed above 11 km. In all other cases, mixing ratios of MEK are >10 ppt in all of the vertical column sampled. Roughly 5% of the observations in the upper troposphere are > 100 ppt. MEK does decrease with altitude in almost every case, but rarely as dramatically sampled in ATom. This implies that the sources of MEK are mostly at or near the surface. This could either imply that the increase in MEK emissions over source regions leads to an increase that carries

throughout the column, or it could be the result of the sampling design of ATom, which focused on a pre-determined flight patterns rather than following plumes.

Several datasets show more consistent abundances of MEK with altitude, in particular ARCPAC and ARCTAS, both sampled the North American Arctic. Median mixing ratios at the top of the sampled profile (7 km ARCPAC, 11 km in ARCTAS) are higher than any median values observed in any of the ATom missions: 78 ppt (7 km - ARCPAC), 41 ppt (11 km - ARCTAS). Both campaigns took place in the Boreal spring and focused on sampling wildfire smoke and other sources of pollution to the Arctic.

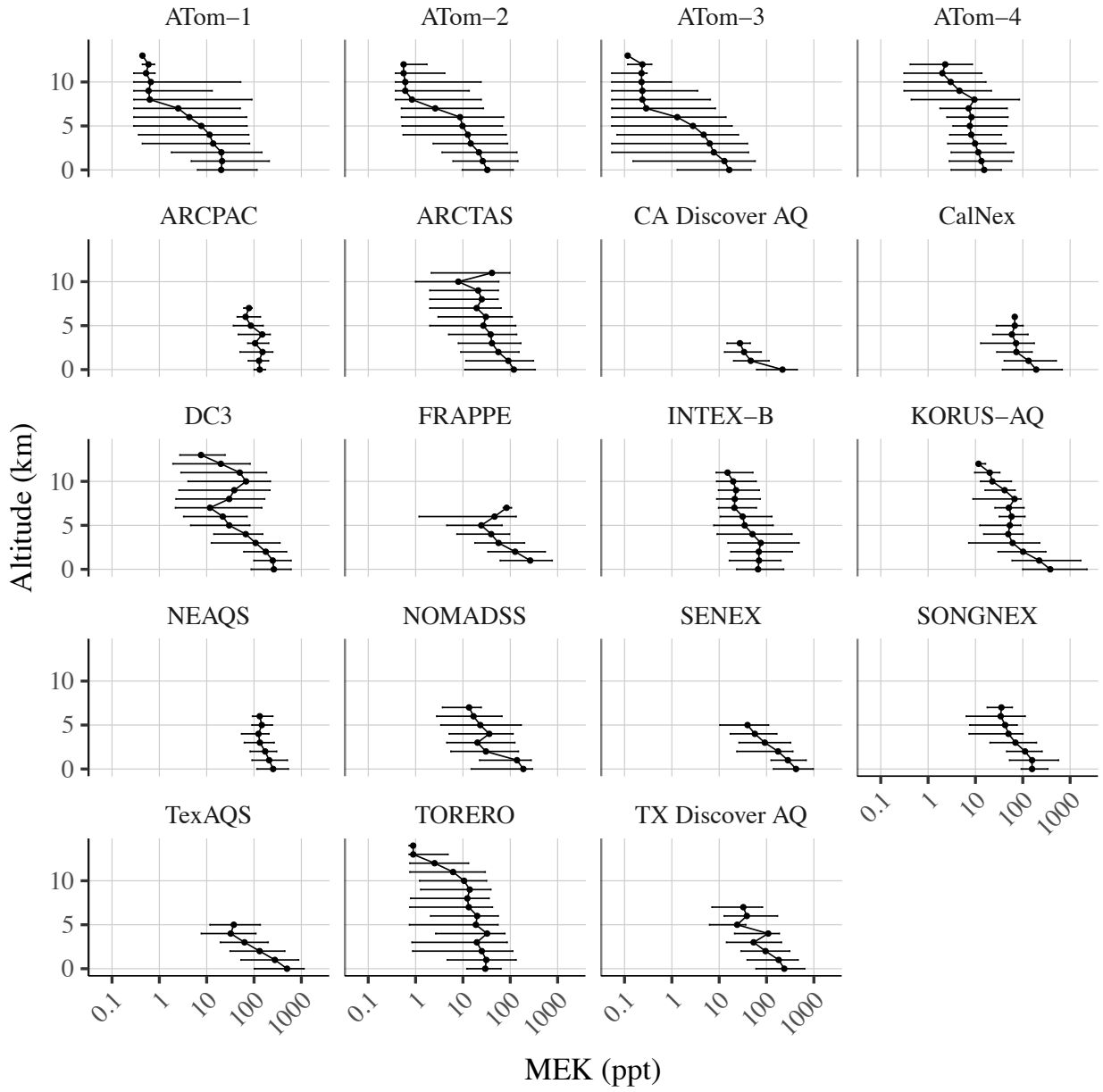

Figure 5.2 – Median mission vertical profiles of MEK (ppt), binned in 1 km vertical bins. Whiskers represent the 5th and 95th percentiles.

This observation dataset is biased spatially as we have almost no observations of MEK over half the globe. Our only observations over Asia are from the KORUS-AQ campaign, and we lack observations over Africa. This is a significant limitation of our analysis.

While many field campaigns were focused on answering specific questions about chemical processes in air pollution or fire plumes, ATom focused on a pre-planned sampling strategy rather than trying to follow plumes. To examine the impact of different sampling strategies on the distribution of MEK present in the aircraft datasets, we compare the observed carbon monoxide (CO) distributions in ATom versus non-ATom campaigns in the regions and seasons where both datasets are available, for a total of 10 comparisons. This information is summarized in Figure D3 in appendix D. In nearly all regions and seasons where both sets of data were available, ATom observed a distribution of CO mixing ratios lower than those observed in non-ATom field campaigns. In the North Pacific during spring and in the Arctic summer, this difference was relatively minor, with the peaks of the two distributions essentially co-located and only the extreme values showing differences. In the Eastern Tropical Pacific, the distribution of observed CO mixing ratios in ATom is actually slightly higher than in TORERO, which occurred in the same region. In the other seven region-season pairings (North America in all four seasons, North Pacific and North Atlantic in JJA, and Arctic in MAM) the distribution of non-ATom CO mixing ratios is essentially redshifted relative to ATom CO mixing ratios. It should be noted that these observations did not take place contemporaneously; the observations in ATom occur years and sometimes up to a decade later than those in other field campaigns in our dataset. However, these differences do highlight the fact that the ATom data generally, but not always, represents airmasses less impacted by anthropogenic emissions than the other datasets.

5.3.3. Modeled and Observed MEK Mixing Ratios

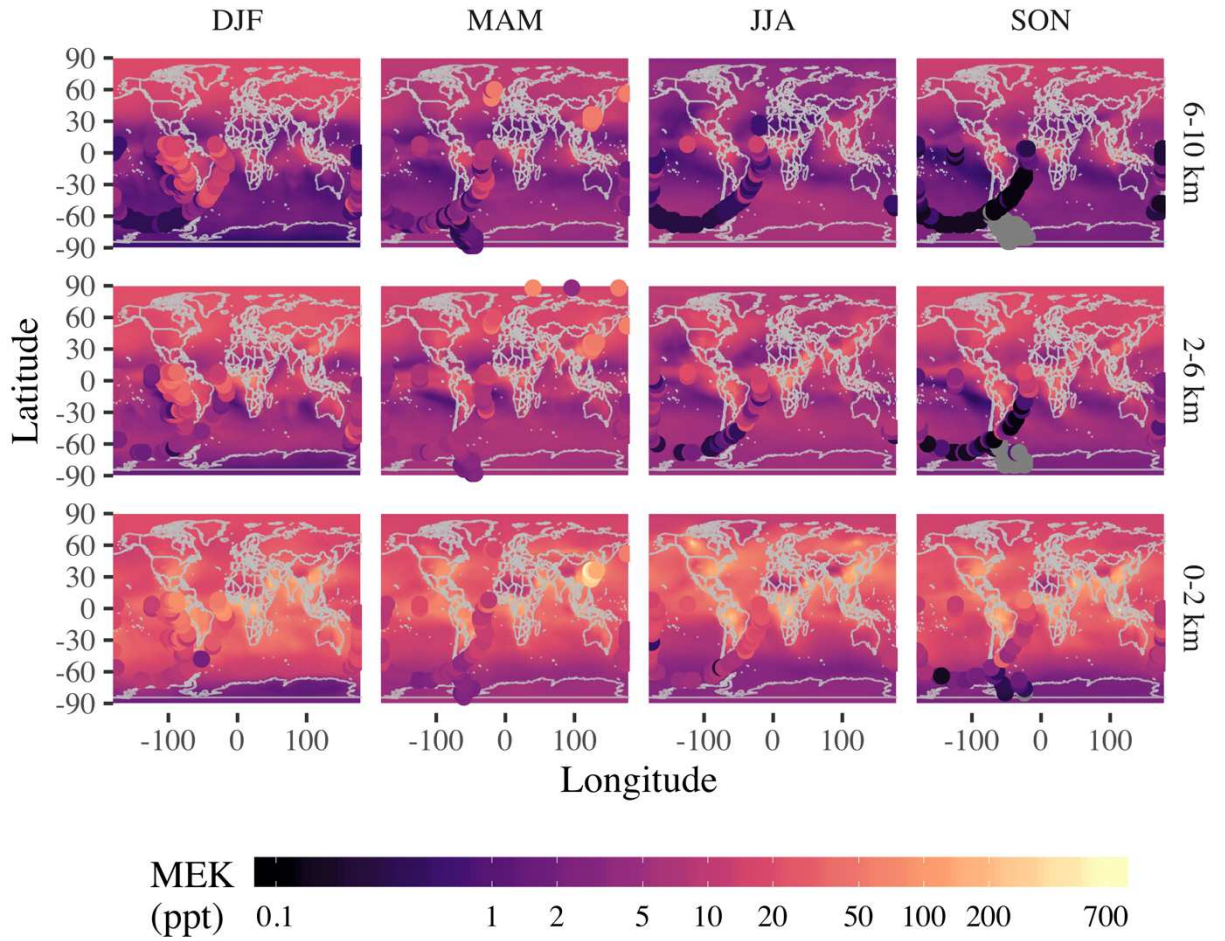

Figure 5.3. Simulated (contours) and observed (points) mixing ratios (in ppt) of atmospheric MEK for four seasons and three altitude bins. Simulated mixing ratios are for 2016, use the ALK4 alkane scheme, and are shown in solid contours. Filled circles are mean observations in different years from aircraft missions binned into 4º x 4º bins for display purposes. Table 5.1 gives the details of the aircraft campaigns. Observations from the North American region (20º - 180º W, 10º - 90º N) are plotted separately in Figure 5.4 due the density of available observations. Note that the color scale is logarithmic. Grey points are MEK mixing ratios below 0.1 ppt, the TOGA limit of detection for MEK.

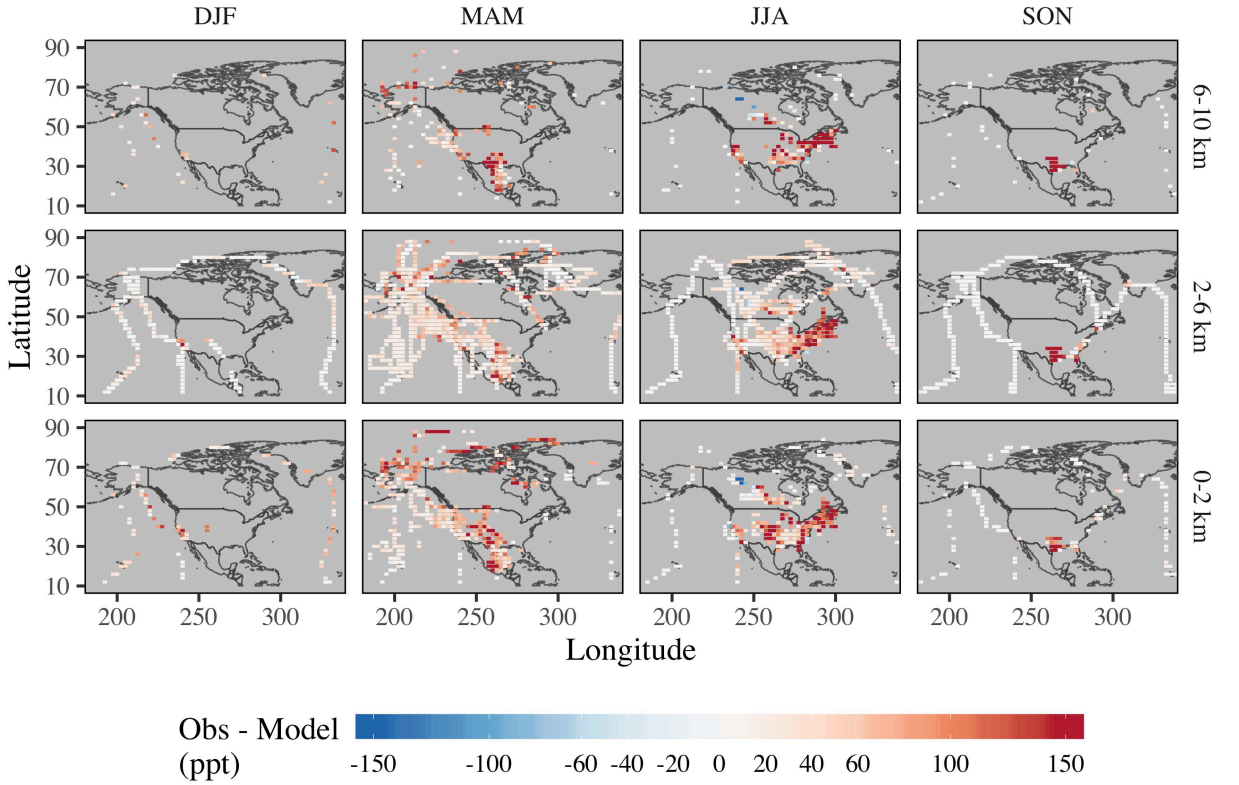

Figure 5.4. Mean difference between observed and simulated mixing ratios (in ppt) of atmospheric MEK for four seasons and three altitude bins over the North American region (20º - 180º W, 10º - 90º N). The observations are from aircraft campaigns over a range of years and are gridded to the GEOS-Chem 2º x 2.5º grid, and vertically averaged. Simulated mixing ratios are for 2016 and use the ALK4 alkane scheme. Aircraft campaign details are provided in Table 5.1.

Figures 5.3 and 5.4 show the global comparison of observed MEK with the simulated MEK mixing ratios generated using the ALK4 alkane scheme detailed in Section 5.2.1.1. Figure 5.3 shows global modeled MEK mixing ratios with observed MEK mixing ratios outside of North America overlayed as dots; Figure 5.4 shows the mean bias of North American MEK (observed – simulated MEK) in ppt, gridded to model resolution. A companion plot to Figure 5.4 that shows the fractional bias at each grid cell is included in appendix D (Figure D4). The different presentation between Figure 5.3 and 5.4 is necessary due to the density of observations over North America. Figure 5.3 shows that there is a large seasonal cycle of MEK in the Northern Hemisphere in the mid-to-upper troposphere (i.e. 2-10 km). The observations show the

highest mixing ratios over North America and Korea in summer and much higher mixing ratios in spring than other seasons over the North Pacific. Mixing ratios in the lower troposphere range over three orders of magnitude, from <1 ppt to ~600 ppt. In the middle troposphere, mixing ratios over the strongest source regions (the tropical rainforests and coastal China) reach 100s of ppt, but all other simulated values are below this level. In the upper troposphere, mixing ratios over these strong sources reach 40 ppt, but most simulated mixing ratios are <5 ppt. In the boreal winter, Arctic MEK mixing ratios in the upper troposphere are higher than at other times of year, but do not exceed 15 ppt. The highest observed mixing ratios are in the lower troposphere over Korea and are higher than any simulated MEK mixing ratios. Figure 5.4 shows that the model significantly underestimates MEK mixing ratios over the central and eastern US, especially during boreal summertime (JJA).

To statistically evaluate the performance of the two model schemes used over large spatial regions, we rely on a series of standardized model metrics calculated using paired model-observation points. These model-observation pairs are co-located in space, while all model output is taken from the appropriate monthly average in 2016. Figure 5.6 presents a summary of several standard statistical performance measures: the fraction of predictions within a factor of 2, fractional mean bias, geometric mean bias, and normalized mean square error (Chang & Hanna, 2004), the mathematical definitions of which are provided in appendix D. These metrics have a long history of use in various air quality models (e.g., Chang & Hanna, 2004; Hanna et al., 1991, 1993) and have more recently been used in GEOS-Chem evaluations of model performance relative to observations (David et al., 2019). Fractional bias is a measure of mean bias, which indicates systematic model errors that can lead to under- or over-estimation of the measured values. Values of fractional bias can range by definition from +2 (extreme underprediction) to -2

(extreme overprediction), with an ideal model having a fractional bias of 0. A model that overpredicts observations by a factor of 2 has a fractional bias of -0.67. Geometric mean bias is similar but makes use of the geometric rather than arithmetic mean to calculate bias. A geometric mean bias of 2 is equivalent to an underprediction by a factor of 2 while a value of 0.5 is equivalent to an overprediction by a factor of 2; an ideal model will have a value of 1. The comparison of the geometric and fractional mean biases is useful because the fractional mean bias, as a linear measure, may be overly influenced by rare extremes in either the observations or predictions, while the logarithmic geometric mean bias may be overly influenced by extremely low values (Chang & Hanna, 2004). Given that our dataset contains both pervasive amounts of extremely low values (at or below the lower limit of detection) as well as some rare but extremely high outlier values (~10^4 times the LLOD), it is not clear which metric will perform better, and thus we include both. Normalized mean square error (NMSE) is a measure of scatter and reflects both model and random measurement errors. An NMSE of 0.5 indicates the model is biased by a factor of 2, although this cannot be differentiated between over- or underprediction, and an ideal model would have an NMSE of 0. The last measure, the 'fraction of predictions within a factor of 2', is self-explanatory but worth including as it is both the easiest metric to understand and the least influenced by any outliers in the dataset. An ideal model would have a fraction of predictions within a factor of 2 value of 1 (*i.e.*, 100% of predictions within a factor of 2). These metrics give us a numeric means of evaluating the information summarized in Figures 5.3 and 5.4.

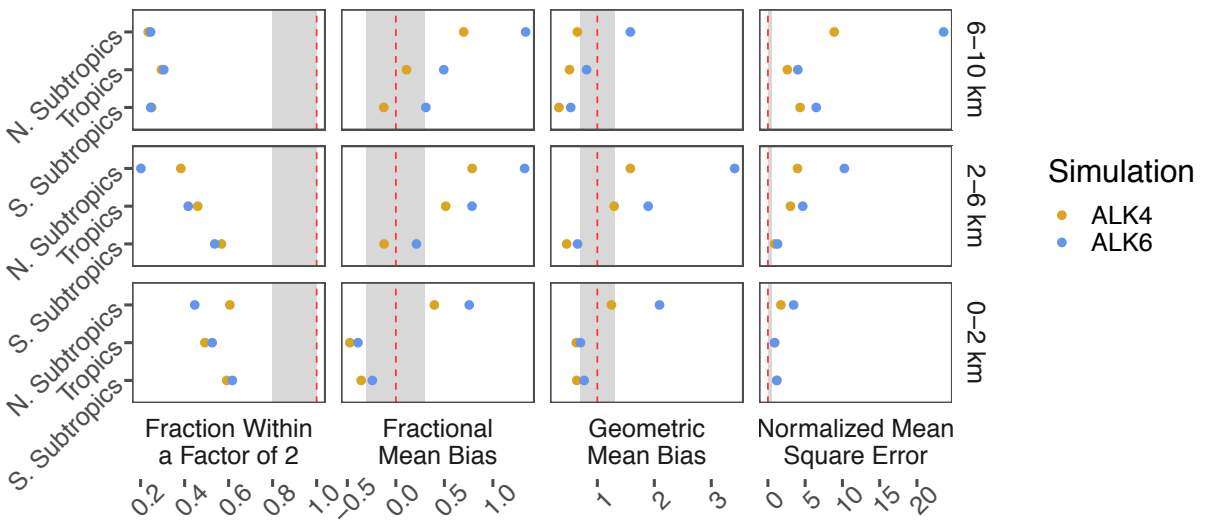

Figure 5.5. Simulation performance relative to observations for two alkane schemes, evaluated over three global region bins and three altitude bins. Perfect model performance for each statistic is shown as a dashed red line (0 for fractional mean bias and NMSE; 1 for the 'fraction [of predictions] within a factor of 2'), while values commonly used to denote 'acceptable' performance are shown as grey bars (Chang & Hanna, 2004). Model performance for the ALK4 scheme (which represents all alkanes with 4 or more carbons as a single species) is presented in gold; simulation performance for the ALK6 scheme (which represents all alkanes with 6 or more carbons as a single species and explicitly represents *i*- and *n*-butanes and pentanes) is presented in blue.

Figure 5.5 shows numerically what Figures 5.3 and 5.4 showed graphically: model performance decreases as both latitude and altitude increase, with the largest differences in all metrics occurring in the Northern Hemisphere upper troposphere. According to both bias metrics, the model overpredicts MEK in the lower troposphere in both the tropics and subtropics regardless of alkane scheme and continues to overpredict MEK throughout the southern subtropics under the ALK4 scheme. According to the Geometric Mean Bias, the model also overpredicts MEK throughout the upper troposphere except in the northern subtropics under the ALK6 scheme. The difference between the two schemes is also clearly evident in these bias metrics: in any cases of model underprediction, the ALK6 scheme performs worse (sometimes much worse); in cases of model overprediction, the difference between the two schemes is

generally small. This is likely because the model is overpredicting MEK in regions with very low mixing ratios and underpredicting in the more polluted regions (see Figures 5.3 and 5.4). However, the NMSE metrics show that the ALK6 alkane scheme routinely performs worse than ALK4, with this disparity increasing with both latitude and altitude. This is surprising, given that we believe the ALK6 scheme to be more chemically representative. It may be that our choices of MEK yield from alkane oxidation is not sufficiently high, as discussed in Section 5.2.1.1. Alternatively, it may be that the model is underestimating some source of MEK emission or secondary production.

Overall, Figure 5.5 shows a model that does not perform well relative to observations, despite our improvements. According to the criteria for model performance taken from Chang & Hanna (2004), most regions and altitudes represented are not considered acceptable by these metrics. Only a few are acceptable according to the bias metrics and none are deemed acceptable according to NMSE. Not one region-altitude combination reaches the level of acceptable in our least biased estimator, which is deemed to be 80% of predictions within a factor of 2. In fact, we do not ever do better than 60% of predictions within a factor of 2 and are closer to 30% in the critical upper troposphere.

5.3.4. Spatial Influence of Various MEK Sources

Figure 5.6 presents the spatial distribution of the sources summarized in Table 5.2 for four months (January, April, July, and October) as a percentage of total MEK. Note that Figure 5.6 does not display abundance but rather an apportionment. Despite their overall small contribution to the global source of MEK, biogenic emissions are important sources to the atmosphere over the equatorial forests in the Amazon, Congo Basin, Indonesia, and Australia in all seasons.

Forests in North America and Siberian Russia are important sources in April and especially July. Emissions from biomass burning are seasonal and have high interannual variability in some regions. While biomass burning is especially widespread in the tropics (Crutzen and Andrea, 1990), the emissions from fires in the Northern Hemisphere appear to be most important for MEK. Major regions of biomass burning in Africa in January (north of the tropical forests) and July (south of the tropical forests) do not appear to impact the distribution of MEK offshore. Our prior analyses of vertical ATom-1 and 2 profiles over the southern Atlantic and Pacific oceans support this conclusion. In Chapter 4, we showed that, with respect to MEK, biomass plumes in these regions were very distinct and constituted transient features in these regions rather than dominating the MEK source in the region (See Figure 4.3).

Alkane oxidation is the most important source of MEK in the northern sub-tropics, responsible for >40% of MEK in nearly all regions north of the Tropic of Cancer. Oceanic emissions are likely a very important source of atmospheric MEK, though the ocean is in near-equilibrium on a global scale. Outside of the alkane-influenced northern third of the atmosphere, the oceanic source of MEK is responsible for nearly all the MEK in the atmospheric column over ocean-covered regions and a non-zero fraction of MEK over continental margins. In fact, only a few regions of the atmosphere are unaffected by ocean emissions. The role of the ocean is at a minimum over regions with large biogenic emissions (e.g., the Amazon, the Congo basin, and southeast Asia) and most inland regions such as Central Asia. Even there, however, emissions from the ocean contribute to simulated MEK columns in all months except July.

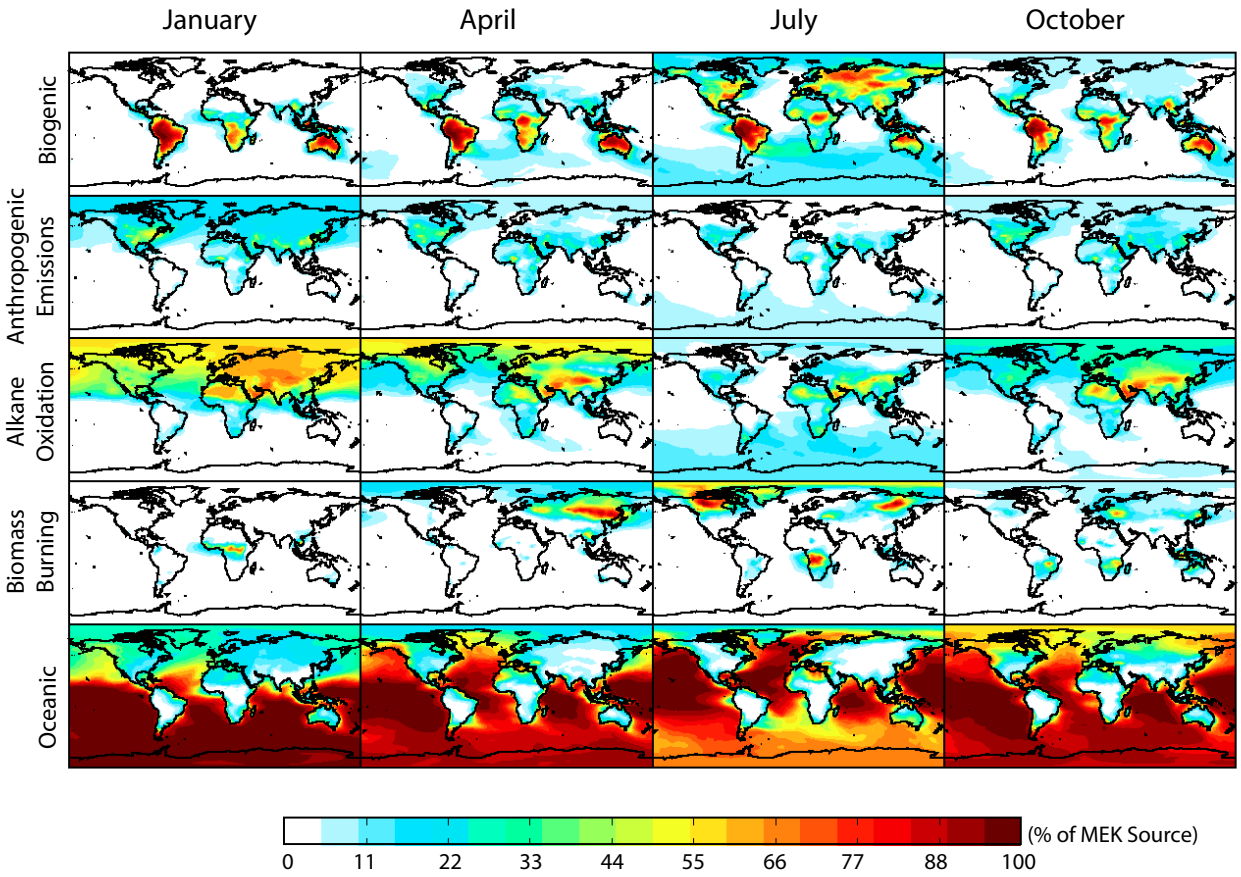

Figure 5.6. Sensitivity of MEK to different emission types. The results are shown as a relative decrease of monthly mean total MEK columns in sensitivity simulations with individual emission types shut off.

Non-oceanic sources exert their largest influence on MEK over the remote Southern Hemisphere in July. MEK in the troposphere over the oceans to the south and east of South America and Africa (and to a lesser extent Australia) is influenced by alkane oxidation, biogenic emissions, and anthropogenic emissions. Over much of this region, these sources combine to contribute ~50% of column MEK, and up to 60% in some regions. Given the large net source shown in Table 5.2, this influence should not be surprising. This source calculation is based on sources and not sinks, and the ocean is responsible for the single largest gross source of MEK (3.7 Tg/yr to 2.2 Tg/yr from alkane oxidation). Furthermore, the ocean influence shown in Figure 5.7 dominates where simulated MEK mixing ratios are very low. As shown in Figure 5.3,

simulated MEK mixing ratios over northern Siberia in January and October, the two months with the highest oceanic influence over Siberia, are generally < 15 ppt – this is effectively an artifact of the choice to use fractional contributions.

5.3.5. Alkanes in GEOS-Chem

As demonstrated in both Table 5.2 and Figure 5.6, understanding alkanes is crucial to understanding MEK in the Northern Hemisphere. Figure 5.7 shows the same metrics as Figure 5.5, but this time comparing observed >C_3 alkanes measured by TOGA (i/n-butanes, i/n-pentanes, 2- and 3-methyl pentanes, n-hexane, n-heptane, and 2,2,4-trimethyl pentane) from the ATom campaigns to GEOS-Chem. This data has been further filtered to remove any points at which all measured alkanes did not have data.

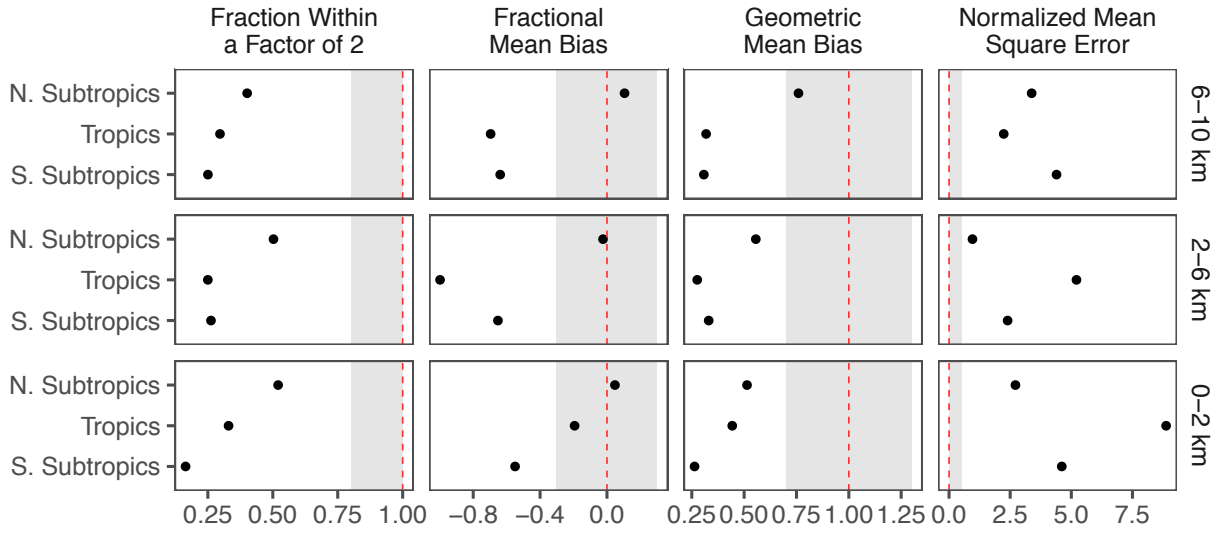

Figure 5.7. Simulation performance relative to observations of >C_3 alkanes, evaluated over three global region bins and three altitude bins. Perfect model performance for each statistic is shown as a dashed red line (0 for fractional mean bias and NMSE; 1 for geometric mean bias, and fraction [of predictions] within a factor of 2), while values commonly used to denote 'acceptable' performance are shown as grey bars (Chang & Hanna, 2004). Model performance is represented for the ALK4 scheme (which represents all alkanes with 4 or more carbons as a single species), while the corresponding >C_3 alkane measurement from ATom is the sum of the

TOGA measurements of *i/n*-butanes, *i/n*-pentanes, 2- and 3-methyl pentanes, *n*-hexane, n-heptane, and 2,2,4-trimethyl pentane.

Once again, the model does not perform well according to our criteria. The fractional mean bias is acceptable throughout the northern subtropics and at the surface in the tropics, while the geometric mean bias only deems performance in the northern upper troposphere acceptable. None of the other metrics are within the acceptable ranges, GEOS-Chem never predicts more than ~50% of the comparison points within a factor of 2. This model overprediction of $>C_3$ alkanes may explain some portion of model overestimation of MEK mixing ratios in the southern subtropics shown in Figure 5.5.

5.3.6. Comparison of MEK and Acetone in the Atmosphere

As discussed above, acetone plays an important role in both the production of oxidants and the formation of PAN-type compounds. One of the motivations behind this work was to investigate whether MEK is similarly important to either HO_x or PAN in a global or regional context. The most crucial contribution of acetone to global HO_x formation occurs in the upper troposphere, where water vapor is scarce (Neumaier et al., 2014). Both our suite of MEK observations and our updated MEK simulations suggest that MEK is much less abundant than acetone throughout the troposphere, and this is especially so in the upper troposphere. Figure 5.8 presents the quartiles of the ratio of acetone to MEK in our observation dataset by region and latitude.

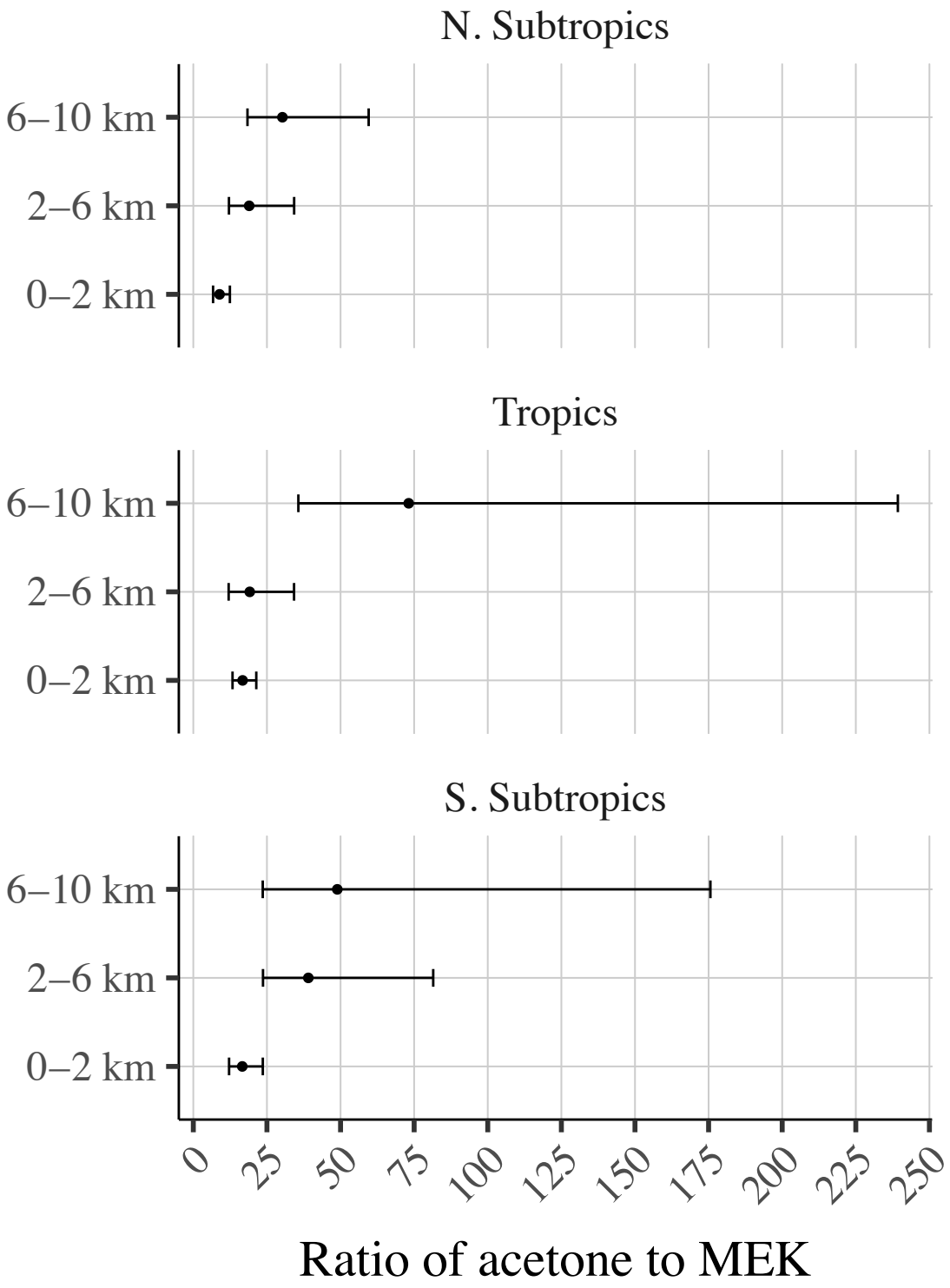

Figure 5.8. Observed median ratio of acetone to MEK, by global region and altitude. Error bars represent the 25th and 75th percentile of the data. Data are taken from a series of aircraft campaigns, detailed in Table 5.1.

The median ratio of acetone to MEK in the dataset overall is ~14:1, with a minimum median ratio of 9:1 in the boreal subtropical lower troposphere and a maximum median ratio of 73:1 in the tropical upper troposphere. Median values are reported because this dataset is heavily skewed: in the tropical upper troposphere, the 75th percentile acetone:MEK ratio is 239:1 and the 95th is >1000:1. Given the relatively short lifetime reported here (~3 days for MEK vs ~19 for acetone; Brewer et al., 2017), this is not surprising, but it does imply that it is very unlikely that MEK plays an important role in upper troposphere oxidation comparable to that of acetone.

However, abundance is not the only metric for atmospheric importance. Because MEK has a higher potential HO_x yield per molecule, and because MEK has a shorter lifetime than acetone to both photolysis and oxidation, the fluxes of MEK are also important to consider. As shown in Table 5.2, the sources of MEK globally are slightly more than 10% of that of acetone (7-8 Tg/year vs 67 Tg/year). KORUS-AQ, sampling in a highly polluted region, observed MEK mixing ratios in the 10s of ppb. In the 113 observations featuring extremely high-MEK observations (MEK > 3 ppb), the median acetone:MEK ratio was 1.4:1. Under these conditions, MEK could be regionally important to the production of both PAN and OH, with consequent implications for air quality and reactive nitrogen budgets.

5.4. Conclusions

We use a global observation dataset, updated chemical mechanisms, and an improved accounting of sinks and sources to update the simulation of MEK in GEOS-Chem. We include improved representation of MEK photolysis, oxidation, air-sea exchange, dry deposition, biogenic production, and secondary production from alkane oxidation. We then use the observations and the model together to understand the sources and sinks responsible for the

global distribution of MEK. This leads us to several conclusions, the first and most important of which is that MEK is much shorter-lived in the atmosphere than acetone, with an estimated global average residence time of ~3 days. Globally, the ocean is the largest source of MEK to the atmosphere, with secondary production from alkane oxidation playing an equally important role in the Northern Hemisphere. In agreement with our findings in Chapter 4, we find that the source of MEK from the ocean is ~12% as large as that of acetone. In both model and observation datasets, there is more MEK in the Northern Hemisphere than the Southern Hemisphere; this gradient is larger in the observed mixing ratios than in the simulated mixing ratios. The highest observed MEK mixing ratios in our dataset are found over Korea, where 10% of MEK mixing ratios were > 1 ppb and some observations reached as high as 10 ppb. In extreme observed MEK enrichment events (MEK > 3 ppb), the median acetone to MEK ratio was 1.4.

Among the many changes we made to the representation of MEK in GEOS-Chem was an updated alkane mechanism. In place of the pre-existing ALK4 mechanism in which all $>C_3$ alkanes are treated as a single species with 4.3 carbons, we created the ALK6 mechanism, which specified the chemistry of speciated C_4 and C_5 alkanes while continuing to lump $>C_5$ alkanes together. In particular, we were interested in specifying which alkane species do and do not contribute to the secondary formation of MEK in the troposphere. In general, our ALK6 mechanism leads to lower MEK mixing ratios across the northern subtropics, where alkanes are an important MEK source. Despite the increased chemical accuracy of our alkane mechanism, it generally performs worse relative to observations than does the pre-existing ALK4 mechanism. If we were to assume that the missing MEK source was from an improperly specified alkane oxidation, the most obvious explanation for this difference would be that GEOS-Chem is underestimating alkane mixing ratios and thus the higher alkane yields from the ALK4

mechanism compensate for alkane underestimation. However, our analysis shows that GEOS-Chem instead overestimates alkane mixing ratios across the troposphere relative to ATom observations and comes closest to correctly estimating alkane mixing ratios in the northern subtropics. It is possible that other sources of MEK in the northern subtropics are independently underestimated, leading to model underestimates; it is also possible that our admittedly simple ALK6 scheme is missing some crucial nuances of MEK yield and alkane loss rate. Whatever the answer, this work suggests that further study of the $>C_3$ alkane oxidation scheme in GEOS-Chem is needed. We are not the first to encounter challenges with respect to the $>C_3$ alkane scheme in GEOS-Chem: Tzompa-Sosa et al. (2019) also identify similar challenges related to the lumping of the various butane and pentane isomers in GEOS-Chem.

We are also able to use our analysis to make some conclusions about the dataset itself. When comparing ATom field campaigns to non-ATom field campaigns in regions and seasons where both datasets were available, we find that ATom generally observed lower CO and MEK mixing ratios than other campaigns. This may be the result of the different sampling schemes; while many other campaigns are designed to study a particular air quality problem or chase a particular type of plume, ATom had a repeated sampling design aimed at finding a tomography of the atmosphere as a whole. This analysis further emphasizes the need to thoughtfully combine campaign and model data. Finally, this work points to crucial deficits in our understanding of global ketone mixing ratios. More atmospheric measurements of ketones are needed, especially in central Asia and the tropics and subtropics of Southeast Asia, South America, and Africa where large ketone sources from both biogenic and biomass burning exist. We do not have observations of MEK from half of the world. Additionally, more observations of MEK in seawater would be very helpful in constraining the air-sea exchange. As of now, we rely on only

two sets of measurements, with no information on how oceanic MEK might vary in space and time. It would also be useful to know what processes control the production and loss of MEK in ocean water, which could help more firmly establish the seasonal cycle of the species.

Chapter References

Akagi, S. K., Yokelson, R. J., Wiedinmyer, C., Alvarado, M. J., Reid, J. S., Karl, T., et al. (2011). Emission factors for open and domestic biomass burning for use in atmospheric models. *Atmospheric Chemistry and Physics*, *11*(9), 4039–4072. https://doi.org/10.5194/acp-11-4039-2011

Alwe, H. D., Millet, D. B., Chen, X., Raff, J. D., Payne, Z. C., & Fledderman, K. (2019). Oxidation of Volatile Organic Compounds as the Major Source of Formic Acid in a Mixed Forest Canopy. *Geophysical Research Letters*, *46*(5), 2940–2948. https://doi.org/10.1029/2018GL081526

Andreae, M. O. (2019). Emission of trace gases and aerosols from biomass burning – an updated assessment. *Atmospheric Chemistry and Physics*, *19*(13), 8523–8546. https://doi.org/10.5194/acp-19-8523-2019

Apel, E. C. (2003). A fast-GC/MS system to measure C2to C4carbonyls and methanol aboard aircraft. *Journal of Geophysical Research*, *108*(D20). https://doi.org/10.1029/2002jd003199

Apel, E. C., Hornbrook, R. S., Hills, A. J., Blake, N. J., Barth, M. C., Weinheimer, A., et al. (2015). Upper tropospheric ozone production from lightning NOx-impacted convection: Smoke ingestion case study from the DC3 campaign. *Journal of Geophysical Research: Atmospheres*, *120*(6), 2505–2523. https://doi.org/10.1002/2014JD022121

Atkinson, R., Baulch, D. L., Cox, R. A., Crowley, J. N., Hampson, R. F., Hynes, R. G., et al. (2006). Evaluated kinetic and photochemical data for atmospheric chemistry: Volume II – gas phase reactions of organic species. *Atmospheric Chemistry and Physics*, *6*(11), 3625–4055. https://doi.org/10.5194/acp-6-3625-2006

Atkinson, R., Baulch, D. L., Cox, R. A., Crowley, J. N., Hampson, R. F., Hynes, R. G., et al. (2008). Evaluated kinetic and photochemical data for atmospheric chemistry: Volume IV – gas phase reactions of organic halogen species. *Atmos. Chem. Phys.*, 356.

AToM Science Team. (2017). AToM EVS2 airborne mission [Data set]. Earth Science Project Office, NASA Ames Research Center. https://doi.org/10.5067/Aircraft/ATom/TraceGas_Aerosol_Global_Distribution

Bon, D. M., Ulbrich, I. M., de Gouw, J. A., Warneke, C., Kuster, W. C., Alexander, M. L., et al. (2011). Measurements of volatile organic compounds at a suburban ground site (T1) in Mexico City during the MILAGRO 2006 campaign: measurement comparison, emission ratios, and source attribution. *Atmospheric Chemistry and Physics*, *11*(6), 2399–2421. https://doi.org/10.5194/acp-11-2399-2011

Brewer, J. F., Bishop, M., Kelp, M., Keller, C., Ravishankara, A. R., & Fischer, E. V. (2017). A sensitivity analysis of key factors in the modeled global acetone budget. *Journal of Geophysical Research*.

Brewer, J. F., Papanastasiou, D. K., Burkholder, J. B., Fischer, E. V., Ren, Y., Mellouki, A., & Ravishankara, A. R. (2019). Atmospheric Photolysis of Methyl Ethyl, Diethyl, and Propyl Ethyl Ketones: Temperature Dependent UV Absorption Cross Sections. *Journal of Geophysical Research: Atmospheres*. https://doi.org/10.1029/2019JD030391

Brewer, J. F., Fischer, E. V., Commane, R., Wofsy, S. C., Daube, B. C., Apel, E. C., et al. (2020). Evidence for an Oceanic Source of Methyl Ethyl Ketone to the Atmosphere. *Geophysical Research Letters*, *47*(4). https://doi.org/10.1029/2019GL086045

Brito, J., Wurm, F., Yáñez-Serrano, A. M., de Assunção, J. V., Godoy, J. M., & Artaxo, P. (2015). Vehicular Emission Ratios of VOCs in a Megacity Impacted by Extensive Ethanol Use: Results of Ambient Measurements in São Paulo, Brazil. *Environmental Science & Technology*, *49*(19), 11381–11387. https://doi.org/10.1021/acs.est.5b03281

Brock, C. A., Cozic, J., Bahreini, R., Froyd, K. D., Middlebrook, A. M., McComiskey, A., et al. (2011). Characteristics, sources, and transport of aerosols measured in spring 2008 during the aerosol, radiation, and cloud processes affecting Arctic Climate (ARCPAC) Project. *Atmospheric Chemistry and Physics*, *11*(6), 2423–2453. https://doi.org/10.5194/acp-11-2423-2011

Calvert, J. G., Mellouki, A., Orlando, J. J., Pilling, M. J., & Wallington, T. J. (2011). *The Mechanisms of Atmospheric Oxidation of the Oxygenates*. New York: Oxford University Press.

Cappellin, L., Algarra Alarcon, A., Herdlinger-Blatt, I., Sanchez, J., Biasioli, F., Martin, S. T., et al. (2017). Field observations of volatile organic compound (VOC) exchange in red oaks. *Atmospheric Chemistry and Physics*, *17*(6), 4189–4207. https://doi.org/10.5194/acp-17-4189-2017

Carr, S. A., Baeza-Romero, M. T., Blitz, M. A., Price, B. J. S., & Seakins, P. W. (2008). Ketone photolysis in the presence of oxygen: A useful source of OH for flash photolysis kinetics experiments. *International Journal of Chemical Kinetics*, *40*(8), 504–514. https://doi.org/10.1002/kin.20330

Chang, J. C., & Hanna, S. R. (2004). Air quality model performance evaluation. *Meteorology and Atmospheric Physics*, *87*(1–3). https://doi.org/10.1007/s00703-003-0070-7

Chen, X., Millet, D. B., Singh, H. B., Wisthaler, A., Apel, E. C., Atlas, E. L., et al. (2019). On the sources and sinks of atmospheric VOCs: an integrated analysis of recent aircraft campaigns over North America. *Atmospheric Chemistry and Physics*, *19*(14), 9097–9123. https://doi.org/10.5194/acp-19-9097-2019

Crawford, J. H., & Pickering, K. E. (2014). In *DISCOVER-AQ: Advancing Strategies for Air Quality Observations in the Next Decade* (pp. 4–7). Pittsburgh, PA: Air & Waste Management Association.

David, L. M., Ravishankara, A. R., Brewer, J. F., Sauvage, B., Thouret, V., Venkataramani, S., & Sinha, V. (2019). Tropospheric ozone over the Indian subcontinent from 2000 to 2015: Data set and simulation using GEOS-Chem chemical transport model. *Atmospheric Environment*, *219*, 117039. https://doi.org/10.1016/j.atmosenv.2019.117039

Dixon, J. L., Beale, R., & Nightingale, P. D. (2013). Production of methanol, acetaldehyde, and acetone in the Atlantic Ocean. *Geophysical Research Letters*, *40*(17), 4700–4705. https://doi.org/10.1002/grl.50922

Eastham, S. D., Weisenstein, D. K., & Barrett, S. R. H. (2014). Development and evaluation of the unified tropospheric–stratospheric chemistry extension (UCX) for the global chemistry-transport model GEOS-Chem. *Atmospheric Environment*, *89*, 52–63. https://doi.org/10.1016/j.atmosenv.2014.02.001

EMEP. (2015). The co-operative programme for monitoring and evaluation of the long-range transmissions of air pollutants in Europe.

Fall, R. (1999). *Biogenic emissions of volatile organic compounds from higher plants*. San Diego: Academic Press, San Diego.

Fischer, E. V., Jacob, D. J., Millet, D. B., Yantosca, R. M., & Mao, J. (2012). The role of the ocean in the global atmospheric budget of acetone. *Geophysical Research Letters*, *39*(1), n/a-n/a. https://doi.org/10.1029/2011gl050086

Fraser, M. P., Cass, G. R., & Simoneit, B. R. T. (1998). Gas-phase and particle-phase organic compounds emitted from motor vehicle traffic in a Los Angeles roadway tunnel. *Environ Sci Technol*, *32*, 2051–2060.

Giglio, L., Randerson, J. T., & van der Werf, G. R. (2013). Analysis of daily, monthly, and annual burned area using the fourth-generation global fire emissions database (GFED4). *Journal of Geophysical Research: Biogeosciences*, *118*(1), 317–328. https://doi.org/10.1002/jgrg.20042

Gilman, J. B., Lerner, B. M., Kuster, W. C., & de Gouw, J. A. (2013). Source Signature of Volatile Organic Compounds from Oil and Natural Gas Operations in Northeastern Colorado. *Environmental Science & Technology*, *47*(3), 1297–1305. https://doi.org/10.1021/es304119a

Goliff, W. S., Stockwell, W. R., & Lawson, C. V. (2013). The regional atmospheric chemistry mechanism, version 2. *Atmospheric Environment*, *68*, 174–185. https://doi.org/10.1016/j.atmosenv.2012.11.038

de Gouw, J. A., Howard, C. J., Custer, T. G., & Fall, R. (1999). Emissions of volatile organic compounds from cut grass and clover are enhanced during the drying process. *Geophysical Research Letters*, *26*(7), 811–814. https://doi.org/10.1029/1999gl900076

de Gouw, J. A., Goldan, P. D., Warneke, C., Kuster, W. C., Roberts, J. M., Marchewka, M., et al. (2003). Validation of proton transfer reaction-mass spectrometry (PTR-MS) measurements of gas-phase organic compounds in the atmosphere during the New England Air Quality Study (NEAQS) in 2002: VALIDATION OF PTR-MS DURING NEAQS. *Journal of Geophysical Research: Atmospheres*, *108*(D21). https://doi.org/10.1029/2003JD003863

Guenther, A., Jiang, X., Heald, C. L., Sakulyanontvittaya, T., Duhl, T., Emmons, L. K., & Wang, X. (2012). The Model of Emissions of Gases and Aerosols from Nature version 2.1 (MEGAN2.1): an extended and updated framework for modeling biogenic emissions. *Geoscientific Model Development*, *5*(6), 1471–1492. https://doi.org/10.5194/gmd-5-1471-2012

Hanna, S. R., Strimaitis, D. G., & Chang, J. C. (1991). *vol. I: User's guide for software for evaluating hazardous gas dispersion models; vol. II: Evaluation of commonly-used hazardous gas dispersion models; vol. III: Components of uncertainty in hazardous gas dispersion models.* (Hazard response modeling uncertainty (A quantitative method) No. A119/A120). Earth Tech, Inc.,196 Baker Avenue, Concord, MA 01742.

Hanna, S. R., Chang, J. C., Strimaitis, D. G., & Hanna, D. (1993). Hazardous gas model evaluation with field observations. *Atmospheric Environment*, *27a*(15), 2265–2285.

Hoesly, R. M., Smith, S. J., Feng, L., Klimont, Z., Janssens-Maenhout, G., Pitkanen, T., et al. (2018). Historical (1750–2014) anthropogenic emissions of reactive gases and aerosols from the Community Emissions Data System (CEDS). *Geoscientific Model Development*, *11*(1), 369–408. https://doi.org/10.5194/gmd-11-369-2018

IUPAC. (2005). *CH3C(O)C2H5.* (IUPAC Task Group on Atmospheric Chemical Kinetic Data Evaluation No. Data Sheet P8).

IUPAC. (2009). Data Sheet HOx_VOC20. Retrieved from http://iupac.pole-ether.fr/

IUPAC. (2013). *Data Sheet P7*.

Jacob, D. J., Field, B. D., Jin, E. M., Bey, I., Li, Q., Logan, J. A., & Yantosca, R. M. (2002). Atmospheric budget of acetone. *Journal of Geophysical Research*, *107*(D10). https://doi.org/10.1029/2001jd000694

Jenkin, M. E., Saunders, S. M., & Pilling, M. J. (1997). The tropospheric degradation of volatile organic compounds: a protocol for mechanism development. *Atmospheric Environment*, *31*(1), 81–104.

Jiménez, E., Ballesteros, B., Martínez, E., & Albaladejo, J. (2005). Tropospheric Reaction of OH with Selected Linear Ketones: Kinetic Studies between 228 and 405 K. *Environmental Science & Technology*, *39*(3), 814–820. https://doi.org/10.1021/es049333c

Johnson, M. T. (2010). A numerical scheme to calculate temperature and salinity dependent air-water transfer velocities for any gas. *Ocean Science*, *6*(4), 913–932. https://doi.org/10.5194/os-6-913-2010

Jordan, C., Fitz, E., Hagan, T., Sive, B., Frinak, E., Haase, K., et al. (2009). Long-term study of VOCs measured with PTR-MS at a rural site in New Hampshire with urban influences. *Atmos. Chem. Phys.*, 21.

Kaiser, E. W., Wallington, T. J., & Hurley, M. D. (2009). Products and Mechanism of the Reaction of Cl with Butanone in N2/O2 Diluent at 297-526 K. *J Phys Chem A*, *113*, 2424–2437.

Karl, T. (2004). Exchange processes of volatile organic compounds above a tropical rain forest: Implications for modeling tropospheric chemistry above dense vegetation. *Journal of Geophysical Research*, *109*(D18). https://doi.org/10.1029/2004jd004738

Karl, T., Harley, P., Guenther, A., Rasmussen, R., Baker, B., Jardine, L., & Nemitz, E. (2005). The bi-directional exchange of oxygenated VOCs between a loblolly pine (Pinus tadea) plantation and the atmosphere. *Atmospheric Chemistry and Physics*, *5*(11), 3015–3031.

Keller, C. A., Long, M. S., Yantosca, R. M., Da Silva, A. M., Pawson, S., & Jacob, D. J. (2014). HEMCO v1.0: a versatile, ESMF-compliant component for calculating emissions in atmospheric models. *Geoscientific Model Development*, *7*(4), 1409–1417. https://doi.org/10.5194/gmd-7-1409-2014

Kermogard, A., Renard, M. F., Veschambre, H., Courtois, D., & Petiard, V. (1998). Reduction of alpha, beta-unsaturated ketones by plant suspension cultures. *Phytochemistry*, *27*(n), 407–409. https://doi.org/10.1016/0031-9422(88)83108-X

Kieber, R. J., Zhou, X., & Mopper, K. (1990). Formation of carbonyl compounds from UV-induced photodegradation of humic substances in natural waters: fate of riverine carbon in the sea. *Limnol. Oceanogr.*, *35*(7), 1503–1515.

Koss, A., Yuan, B., Warneke, C., Gilman, J. B., Lerner, B. M., Veres, P. R., et al. (2017). Observations of VOC emissions and photochemical products over US oil- and gas-producing regions using high-resolution H3O+ CIMS (PTR-ToF-MS). *Atmospheric Measurement Techniques*, *10*(8), 2941–2968. https://doi.org/10.5194/amt-10-2941-2017

Le Calvé, S., Hitier, D., Le Bras, G., & Mellouki, A. (1998). Kinetic Studies of OH Reactions with a Series of Ketones. *Journal of Physical Chemistry*, *102*(24), 4579–4584.

Legreid, G., Lööv, J. B., Staehelin, J., Hueglin, C., Hill, M., Buchmann, B., et al. (2007). Oxygenated volatile organic compounds (OVOCs) at an urban background site in Zürich (Europe): Seasonal variation and source allocation. *Atmospheric Environment*, *41*(38), 8409–8423. https://doi.org/10.1016/j.atmosenv.2007.07.026

Li, M., Q. Zhang, J. Kurokawa, J. H. Woo, K. B. He, Z. Lu, et al. (2015). MIX: a mosaic Asian anthropogenic emission inventory for the MICS-Asia and the HTAP projects. *Atmos.*

Chem. Phys. Discuss., *15*(23), 34813–34869. https://doi.org/10.5194/acpd-15-34813-2015

Liss, P., & Slater, P. G. (1974). Flux of Gases across the Air-Sea Interface. *Nature*, *247*, 181–184.

Liu, Y., Yuan, B., Li, X., Shao, M., Lu, S., Li, Y., et al. (2015). Impact of pollution controls in Beijing on atmospheric oxygenated volatile organic compounds (OVOCs) during the 2008 Olympic Games: observation and modeling implications. *Atmospheric Chemistry and Physics*, *15*(6), 3045–3062. https://doi.org/10.5194/acp-15-3045-2015

Lurmann, F. W., Lloyd, A. C., & Atkinson, R. (1986). A chemical mechanism for use in long-range transport/acid deposition computer modeling. *Journal of Geophysical Research: Atmospheres*, *91*(D10), 10905–10936. https://doi.org/10.1029/JD091iD10p10905

Marais, E. A., & Wiedinmyer, C. (2016). Air Quality Impact of Diffuse and Inefficient Combustion Emissions in Africa (DICE-Africa). *Environmental Science & Technology*, *50*(19), 10739–10745. https://doi.org/10.1021/acs.est.6b02602

Millet, D. B., Guenther, A., Siegel, D. A., Nelson, N. B., Singh, H. B., de Gouw, J. A., et al. (2010). Global atmospheric budget of acetaldehyde: 3-D model analysis and constraints from in-situ and satellite observations. *Atmos. Chem. Phys.*, 21.

Millet, D. B., Alwe, H. D., Chen, X., Deventer, M. J., Griffis, T. J., Holzinger, R., et al. (2018). Bidirectional Ecosystem–Atmosphere Fluxes of Volatile Organic Compounds Across the Mass Spectrum: How Many Matter? *ACS Earth and Space Chemistry*, *2*(8), 764–777. https://doi.org/10.1021/acsearthspacechem.8b00061

Nault, B. A., Campuzano-Jost, P., Day, D. A., Schroder, J. C., Anderson, B., Beyersdorf, A. J., et al. (2018). Secondary organic aerosol production from local emissions dominates the organic aerosol budget over Seoul, South Korea, during KORUS-AQ. *Atmospheric Chemistry and Physics*, *18*(24), 17769–17800. https://doi.org/10.5194/acp-18-17769-2018

Nightingale, P. D., Malin, G., Law, C. S., Watson, A. J., Liss, P. S., Liddicoat, M. I., et al. (2000). In situ evaluation of air-sea gas exchange parameterizations using novel conservative and volatile tracers. *Global Biogeochemical Cycles*, *14*(1), 373–387. https://doi.org/10.1029/1999gb900091

Paulot, F., Crounse, J. D., Kjaergaard, H. G., Kroll, J. H., Seinfeld, J. H., & Wennberg, P. O. (2009). Isoprene photooxidation: new insights into the production of acids and organic nitrates. *Atmospheric Chemistry and Physics*, *9*(4), 1479–1501. https://doi.org/10.5194/acp-9-1479-2009

Paulot, F., Crounse, J. D., Kjaergaard, H. G., Kürten, A., Clair, J. M. S., Seinfeld, J. H., & Wennberg, P. O. (2009). Unexpected Epoxide Formation in the Gas-Phase Photooxidation of Isoprene. *Science*, *325*(5941), 730–733. https://doi.org/10.1126/science.1172910

Pfister, G. G., Reddy, P. J., Barth, M. C., Flocke, F. F., Fried, A., Herndon, S. C., et al. (2017). Using Observations and Source-Specific Model Tracers to Characterize Pollutant Transport During FRAPPÉ and DISCOVER-AQ: Pollutant Transport During FRAPPE/DAQ. *Journal of Geophysical Research: Atmospheres*, *122*(19), 10,510-10,538. https://doi.org/10.1002/2017JD027257

Raber, W. H., & Moortgat, G. K. (1987). Photooxidation of Selected Carbonyl Compounds in Air: Methyl Ethyl Ketone, Methyl Vinyl Ketone, Methacrolein and Methylglyoxal. In J.

Barker (Ed.), *Progress and Problems in Atmospheric Chemistry*. Singapore: World Scientific Publishing.

Randerson, J. T., Chen, Y., Werf, G. R. van der, Rogers, B. M., & Morton, D. C. (2012). Global burned area and biomass burning emissions from small fires, *Journal of Geophysical Research: Biogeosciences*. Retrieved from https://agupubs.onlinelibrary.wiley.com/doi/full/10.1029/2012JG002128

Rollins, A. W., Kiendler-Scharr, A., Fry, J. L., Brauers, T., Brown, S. S., Dorn, H.-P., et al. (2009). Isoprene oxidation by nitrate radical: alkyl nitrate and secondary organic aerosol yields. *Atmos. Chem. Phys.*, *9*(18), 6685–6703.

Romero, M. T. B., Blitz, M. A., Heard, D. E., Pilling, M. J., Price, B., Seakins, P. W., & Wang, L. (2005). Photolysis of methylethyl, diethyl and methylvinyl ketones and their role in the atmospheric HOx budget. *Faraday Discussions*, *130*, 73. https://doi.org/10.1039/b419160a

Rossabi, S., & Helmig, D. (2018). Changes in Atmospheric Butanes and Pentanes and Their Isomeric Ratios in the Continental United States. *Journal of Geophysical Research: Atmospheres*, *123*(7), 3772–3790. https://doi.org/10.1002/2017JD027709

Sander, R. (2015). Compilation of Henry's law constants (version 4.0) for water as solvent. *Atmospheric Chemistry and Physics*, *15*(8), 4399–4981. https://doi.org/10.5194/acp-15-4399-2015

Sander, S. P., Abbatt, J., Barker, J. R., Burkholder, J. B., Friedl, R. R., Golden, D. M., & et al. (2011). *Chemical Kinetics and Photochemical Data for Use in Atmospheric Studies, Evaluation Number 17.* Pasadena, CA. Retrieved from http://jpldataeval.jpl.nasa.gov/

Saunders, S. M., Jenkin, M. E., Derwent, R. G., & Pilling, M. J. (2003). Protocol for the development of the Master Chemical Mechanism, MCM v3 (Part A): tropospheric degradation of non-aromatic volatile organic compounds. *Atmos. Chem. Phys.*, 20.

Schlundt, C., Tegtmeier, S., Lennartz, S. T., Bracher, A., Cheah, W., Krüger, K., et al. (2017). Oxygenated volatile organic carbon in the western Pacific convective center: ocean cycling, air–sea gas exchange and atmospheric transport. *Atmospheric Chemistry and Physics*, *17*(17), 10837–10854. https://doi.org/10.5194/acp-17-10837-2017

Sherwen, T., Schmidt, J. A., Evans, M. J., Carpenter, L. J., Großmann, K., Eastham, S. D., et al. (2016). Global impacts of tropospheric halogens (Cl, Br, I) on oxidants and composition in GEOS-Chem. *Atmospheric Chemistry and Physics*, *16*(18), 12239–12271. https://doi.org/10.5194/acp-16-12239-2016

Shimoda, K., Kubota, N., Hamada, H., Yamane, S., & Hirata, T. (2005). Asymmetric Transformation of Enones with Synechococcus sp. PCC 7942. *ChemInform*, *36*(15). https://doi.org/10.1002/chin.200515035

Simpson, I. J., Akagi, S. K., Barletta, B., Blake, N. J., Choi, Y., Diskin, G. S., et al. (2011). Boreal forest fire emissions in fresh Canadian smoke plumes: C1-C10 volatile organic compounds (VOCs), CO2, CO, NO2, NO, HCN and CH3CN. *Atmospheric Chemistry and Physics*, *11*(13), 6445–6463. https://doi.org/10.5194/acp-11-6445-2011

Singh, H. B., Salas, L. J., Chatfield, R. B., Czech, E., Fried, A., Walega, J., et al. (2004). Analysis of the atmospheric distribution, sources, and sinks of oxygenated volatile organic chemicals based on measurements over the Pacific during TRACE-P. *Journal of Geophysical Research*, *109*(D15). https://doi.org/10.1029/2003jd003883

Singh, H. B., Brune, W. H., Crawford, J. H., Flocke, F., & Jacob, D. (2009). Chemistry and transport of pollution over the Gulf of Mexico and the Pacific: spring 2006 INTEX-B campaign overview and first results. *Atmospheric Chemistry and Physics*, *9*, 2301–2318.

Swan, H. B., Crough, R. W., Vaattovaara, P., Jones, G. B., Deschaseaux, E. S. M., Eyre, B. D., et al. (2016). Dimethyl sulfide and other biogenic volatile organic compound emissions from branching coral and reef seawater: potential sources of secondary aerosol over the Great Barrier Reef. *Journal of Atmospheric Chemistry*, *73*(3), 303–328. https://doi.org/10.1007/s10874-016-9327-7

Talbot, R. (2005). Diurnal characteristics of surface level O $_3$ and other important trace gases in New England. *Journal of Geophysical Research*, *110*(D9). https://doi.org/10.1029/2004JD005449

Tzompa-Sosa, Z. A., Henderson, B. H., Keller, C. A., Travis, K., Mahieu, E., Franco, B., et al. (2019). Atmospheric Implications of Large C2-C5 Alkane Emissions From the U.S. Oil and Gas Industry. *Journal of Geophysical Research: Atmospheres*, *124*(2), 1148–1169. https://doi.org/10.1029/2018JD028955

U. S. EPA. (2013). *National Emissions Inventory 2011*. (U. S. EPA, Trans.).

Verschueren, K. (1983). Methyl Ethyl Ketone. In *Handbook of Environmental Data on Organic Chemicals* (pp. 850–852). Van Nostrand Reinhold Co.

Vestreng, V., & Klein, H. (2002). *Emissions Data Reported to UN-ECE/EMEP: Quality assurance and trend analysis & presentation of WebDab*. Oslo, Norway: Norwegian Meteorological Institute.

Wallington, T. J., & Kurylo, M. J. (1987). Flash photolysis resonance fluorescence investigation of the gas-phase reactions of hydroxyl radicals with a series of aliphatic ketones over the temperature range 240-440 K. *The Journal of Physical Chemistry*, *91*(19), 5050–5054. https://doi.org/10.1021/j100303a033

Wang, S., Hornbrook, R. S., Hills, A., Emmons, L. K., Tilmes, S., Lamarque, J.-F., et al. (2019). Atmospheric Acetaldehyde: Importance of Air-Sea Exchange and a Missing Source in the Remote Troposphere. *Geophysical Research Letters*. https://doi.org/10.1029/2019GL082034

Wanner, P., & Tressl, R. (1998). Purification and characterization of two enone reductases from Saccharomyces cerevisiae. *European Journal of Biochemistry*, *255*(1), 271–278. https://doi.org/10.1046/j.1432-1327.1998.2550271.x

Warneke, C., van der Veen, C., Luxembourg, S., de Gouw, J. A., & Kok, A. (2001). Measurements of benzene and toluene in ambient air using proton-transfer-reaction mass spectrometry: calibration, humidity dependence, and field intercomparison. *International Journal of Mass Spectrometry*, *207*(3), 167–182. https://doi.org/10.1016/S1387-3806(01)00366-9

Warneke, C., de Gouw, J. A., Holloway, J. S., Peischl, J., Ryerson, T. B., Atlas, E., et al. (2012). Multiyear trends in volatile organic compounds in Los Angeles, California: Five decades of decreasing emissions: TRENDS IN VOCS IN LOS ANGELES. *Journal of Geophysical Research: Atmospheres*, *117*(D21), n/a-n/a. https://doi.org/10.1029/2012JD017899

Werf, G. R. van der, Randerson, J. T., Giglio, L., Leeuwen, T. T. van, Chen, Y., Rogers, B. M., et al. (2017). Global fire emissions estimates during 1997–2016. *Earth System Science Data*, *9*(2), 697–720. https://doi.org/10.5194/essd-9-697-2017

Wild, O., Zhu, X., & Prather, M. J. (2000). Fast-J: Accurate simulaton of in- and below-cloud photolysis in tropospheric chemical models. *Journal of Atmospheric Chemistry*, *37*(3), 245–282. https://doi.org/10.1023/a:1006415919030

Wofsy, S. C., AFSHAR, S., ALLEN, H. M., APEL, E., ASHER, E. C., BARLETTA, B., et al. (2018). ATom: Merged Atmospheric Chemistry, Trace Gases, and Aerosols. ORNL Distributed Active Archive Center. https://doi.org/10.3334/ORNLDAAC/1581

Yáñez-Serrano, A. M., Nölscher, A. C., Williams, J., Wolff, S., Alves, E., Martins, G. A., et al. (2015). Diel and seasonal changes of biogenic volatile organic compounds within and above an Amazonian rainforest. *Atmospheric Chemistry and Physics*, *15*(6), 3359–3378. https://doi.org/10.5194/acp-15-3359-2015

Yañez-Serrano, A. M., Nolscher, A. C., Bourtsoukidis, E., Derstroff, B., Zanoni, N., Gros, V., et al. (2016). Atmospheric mixing ratios of methyl ethyl ketone (2-butanone) in tropical, boreal, temperate, and marine environments. *Atmos. Chem. Phys.*, *16*, 10965–10984. https://doi.org/10.5194/acp-16-10965-2016

Yuan, B., Kaser, L., Karl, T., Graus, M., Peischl, J., Campos, T. L., et al. (2015). Airborne flux measurements of methane and volatile organic compounds over the Haynesville and Marcellus shale gas production regions: AIRBORNE EDDY COVARIANCE FLUX. *Journal of Geophysical Research: Atmospheres*, *120*(12), 6271–6289. https://doi.org/10.1002/2015JD023242

Yuan, B., Koss, A., Warneke, C., Gilman, J. B., Lerner, B. M., Stark, H., & de Gouw, J. A. (2016). A high-resolution time-of-flight chemical ionization mass spectrometer utilizing hydronium ions (H_3O^+ ToF-CIMS) for measurements of volatile organic compounds in the atmosphere. *Atmospheric Measurement Techniques*, *9*(6), 2735–2752. https://doi.org/10.5194/amt-9-2735-2016

Zhao, Z., Huskey, D. T., Nicovich, J. M., & Wine, P. H. (2008). Temperature-dependent kinetics study of the gas-phase reactions of atomic chlorine with acetone, 2-butanone, and 3-pentanone. *International Journal of Chemical Kinetics*, *40*(5), 259–267. https://doi.org/10.1002/kin.20321

Zhou, S., Gonzalez, L., Leithead, A., Finewax, Z., Thalman, R., Vlasenko, A., et al. (2014). Formation of gas-phase carbonyls from heterogeneous oxidation of polyunsaturated fatty acids at the air–water interface and of the sea surface microlayer. *Atmospheric Chemistry and Physics*, *14*(3), 1371–1384. https://doi.org/10.5194/acp-14-1371-2014

Zhou, X., & Mopper, K. (1997). Photochemical production of low-molecular-weight-carbonyl compounds in seawater and surface microlayer and their air-sea exchange. *Marine Chemistry*, *56*, 201–213.

CHAPTER 6: CONCLUSIONS

6.1. Chapter Introduction

This thesis explains the results of studies regarding four aspects of ketones in the troposphere. The conclusion of each of the four studies are given here.

6.2. Summary of Chapter 2

Chapter 2 discussions an analysis of the sensitivities of the global budget of acetone to uncertainties in the natural sources of that compound. This analysis was performed using the Morris Method, a computationally efficient way to perform a comprehensive sensitivity analysis on large models. In our global acetone budget, the most important net sources of acetone are the direct emissions of acetone from the terrestrial biosphere (37.1 Tg/year), and the oxidation of alkanes (18.3 Tg/year). The most important net sinks are the oxidation of acetone by OH (25.6 Tg/year) and the photolysis of acetone (21.0 Tg/year). The ocean is both the largest gross source (51.8 Tg/year) and gross sink (59.2 Tg/year) of acetone to the atmosphere, but on net, we still find that the ocean is a relatively small net sink of acetone (7.5 Tg/year). In general, the size of the uncertainty of a given factor in the acetone budget is not a predictor of the overall model uncertainty attributable to that factor. Of the factor uncertainties tested, the uncertainty in the direct biogenic emission of acetone, though less uncertain than other factors tested, was the most consequential globally. Monoterpene emissions from the biosphere in MEGAN are 150% more uncertain than acetone emissions, but this greater uncertainty range is far less consequential to the simulated global atmospheric burden than the smaller uncertainty range in acetone emissions; similarly, despite the simplicity of the dry deposition parameterization in GEOS-Chem, the

model is far less sensitive to the dry deposition velocity chosen than it is to the uncertainties in photolysis rate or biogenic emission. Therefore, establishing a more certain direct biogenic emission estimates and quantifying the photolysis rates should be of high priority for improving the acetone budget.

We further show that sensitivity in the acetone budget varies by region and season. The uncertainty in ocean acetone concentrations is more important for understanding acetone abundances in the Southern Hemisphere relative to the Northern Hemisphere because of the differences in land area between hemispheres, and it is important in both extra-tropical winters. Not including a representation of ocean exchange of acetone will incorrectly simulate atmospheric acetone abundances, particularly in the Southern Hemisphere, and improving representation of oceanic acetone would have the greatest impact in this region. Conversely, the uncertainty in dry deposition velocity is more consequential for a simulation of the Northern Hemisphere than the Southern Hemisphere, and improvements in the representation of dry deposition may be more important for resolving disagreements in measured and modeled abundances over this area. Finally, the modeled global budget is sensitive to the representation of acetone photolysis frequency, especially in the crucial mid-to-upper troposphere region where acetone is considered to be most important for producing HO_x.

6.3. Summary of Chapter 3

We present new laboratory measurements of MEK and DEK absorption cross sections at temperatures between 242 K - 320 K and of PEK at 298 K between 200 and 335 nm. We use these measured values to understand the role of photolysis in the tropospheric chemistry of these compounds. We further show that the measured cross sections are robustly represented by a

physically-based two-state model. While we do not have data to assess the accuracy of the model at temperatures below 242 K, this model can be extrapolated to temperatures lower than those measured to provide empirical, numerically stable, and physically reasonable ketone cross sections at all tropospherically relevant temperatures. We further show that this same model also allows us to simulate the temperature dependence of acetone UV absorption cross sections and we suggest that an analogous treatment works for PEK.

For MEK, DEK, and PEK, the inclusion of temperature dependence leads to a decrease in photolysis rate coefficients of up to 25%, when compared to photolysis rate coefficients derived using available room temperature literature recommendations. This decrease is largest in the upper troposphere (Figures 3.6 and 3.7), where ketone photolysis is thought to be most important to global oxidation potential. Finally, we provide a set of calculated J values for easy comparison at both 1 nm and wide-binned resolutions and produce first-order estimates of photolysis rates in the troposphere. We also provide the code necessary to extend and modify this work as needed in future applications. This work better quantifies the photochemical losses of ketones in the troposphere.

6.4. Summary of Chapter 4

Using data from clean marine air masses sampled in the ATom-1 and ATom-2 field campaigns, we provide evidence that the ocean is a source of MEK to the atmosphere. Outside the tropics, this source is more pronounced during summer than winter; less seasonality is observed in the tropics. MEK in the regions we examined is not correlated with DMS – a reliable tracer of marine biological activity. MEK in the marine boundary layer is correlated with acetone and slightly less strongly correlated with acetaldehyde, which suggests the three species

could share similar sources. Acetone and MEK have similar abundances in the only existing measurements of both species in seawater, providing additional evidence of a similar source, and even a small concentration of MEK in surface seawaters can provide a flux of MEK out of the ocean that can account for the observations.

ATom observations suggest that MEK's flux out of the ocean is >10% of that of acetone. As MEK oxidation is a source of acetaldehyde in the troposphere, this oceanic MEK might serve as a source of acetaldehyde and help better account for the observed abundances (Wang et al., 2019; Wolfe et al., 2019). Quantification of the sources and sinks of MEK in the oceans is needed to improve understanding of MEK and its implications for global oxidation capacity.

6.5. Summary of Chapter 5

We present several important updates to GEOS-Chem necessary to simulate atmospheric abundances of MEK, including improved representation of MEK photolysis, oxidation, air-sea exchange, dry deposition, biogenic production, and secondary production from alkane oxidation. We then use a suite of aircraft observations and the model together to understand the sources and sinks responsible for the global distribution of MEK. We show that MEK has a shorter mean residence time in the atmosphere of ~3 days, shorter than previously believed. The addition of an ocean source proves to be important to understanding the global budget of the species, as our research suggests that the ocean is the largest source of MEK to the atmosphere. Even accounting for the fact that the ocean is also a sink of MEK, we find that the ocean is a net source of MEK to the atmosphere of roughly the same magnitude as the atmospheric oxidation of alkanes. This secondary production is the other most important source of MEK to the atmosphere, and is mostly important in the Northern Hemisphere, especially in the boreal

subtropics. In agreement with our findings in Chapter 4, we find that the source of MEK from the ocean is ~12% as large as that of acetone.

The sources of MEK show pronounced seasonal and regional differences – in the Southern Hemisphere, the oceanic and biogenic sources dominate while in the Northern Hemisphere both direct emission and secondary production from the alkanes are more important, especially in the fall and winter. The current version of the model underestimates MEK abundances in the upper troposphere in the Northern Hemisphere during boreal spring and summer, especially over Asia and North America. It also underestimates MEK abundances over the Pacific in the lower and mid troposphere, which may be linked to the under-predictions of MEK abundances over Asia. In particular, our analysis of the KORUS-AQ aircraft dataset over Korea shows that MEK mixing ratios in this region are much higher than elsewhere, with 10% of MEK mixing ratios > 1 ppb with some observations as high as 10 ppb. Maximum simulated mixing ratios are < ~600 ppt over the same region. More aircraft observations are necessary in this region to understand the sources of MEK and whether the KORUS-AQ sampling period is representative.

In the observations summarized in Chapter 5, the median ratio of acetone to MEK is ~14:1, with a minimum median ratio of 9:1 in the in the boreal subtropical lower troposphere and a maximum median ratio of 73:1 in the tropical upper troposphere. These ratios are heavily skewed: in the tropical upper troposphere, where acetone is most important to OH production, the 75th percentile acetone:MEK ratio is 239:1 and the 95th percentile is >1000:1. This is not surprising given the short lifetime reported here, but it does imply that MEK is much less important to global OH production than acetone. However, mixing ratio is not the only thing that matters. MEK has a shorter lifetime than acetone to both photolysis and oxidation, and so the

fluxes of MEK are also important to consider. The gross sources of MEK globally are slightly more than 10% of that of acetone (14 Tg/year vs 119 Tg/year). We thus infer that MEK is not as important to global HO_x production as acetone.

6.6. Additional Needs

The studies discussed in this thesis have improved our understanding of the ketones in the troposphere. They also identify some important gaps in our knowledge which need to be addressed in order to more fully understand the importance of ketones to atmospheric chemistry. For both acetone and MEK, the atmospheric chemistry community needs to reduce uncertainty in the processes that lead to a biogenic source of each compound in different ecosystems around the globe. A move towards a more processed-based understanding of dry deposition of both MEK and acetone could also be important, especially in the Northern Hemisphere. Given the strong hemispheric gradient, short lifetime, and observed regional mega-enrichments of MEK, this improvement could be even more important for the global budget of that species. Processed-based understanding of the sources and sinks of ketones in the ocean mixed layer is essential to predictions of where and why the ocean serves as either a source or a sink. While we show that the ocean tends a net source globally, the location and magnitude of individual fluxes matters for regional or even global atmospheric chemistry.

Additionally, more atmospheric measurements of ketones are needed, especially in the tropics and subtropics of Southeast Asia, South America, and Africa where large ketone sources from both biogenic and biomass burning exist. While additional observations of both acetone and MEK are clearly of highest importance here, it would also be helpful to gain some additional measurements of larger ketones in the atmosphere, especially over the oceans. Given the strong

correlation and presumably linked sources of MEK and acetone from the ocean mixed layer, it would not be surprising to find that the ocean is also a source of larger ketones to the atmosphere. While it would make sense that these larger ketones might have lower mixing ratios than MEK, their higher reactivity would mean that they might contribute to either PAN-type compound formation or the formation of other atmospherically relevant species such as acetaldehyde and CH_2O. Furthermore, if such a common source was established, the atmospheric chemistry community might be better able to understand the mechanisms responsible.

The biggest two recommendations for future work are specific processes for the production and loss of MEK. Significant uncertainty remains in the quantum yields of MEK (more so than for acetone), which limits our ability to make strong conclusions about the role of this species in atmospheric oxidation. IUPAC's recommended quantum yields are sparse – they consist of two measurements at 1000 hPa and 68 hPa, without any wavelength dependence information (IUPAC, 2005). While a Stern-Volmer parameterization of these quantum yields does exist (Romero et al., 2005), IUPAC does not recommend its use. This is a major shortcoming in the literature, which leaves significant uncertainties in one of MEK's most consequential sinks. Further quantification of the photolysis quantum yields as a function of pressure and temperature is needed.

A more sophisticated treatment of alkane oxidation in global models is also needed. While in this work we speciate the $>C_3$ alkane species into *i/n* butanes and pentanes in addition to a $>C_5$ alkane tracer, this speciation was done solely with an eye on the MEK yields, and inherited both reaction rates and product yields from the prior lumped-alkane scheme in GEOS-Chem. As shown in Chapter 5, our relatively simplistic attempts to more accurately represent this mechanism did not result in a more accurate MEK simulation, but we nonetheless believe some

improvement to be warranted, especially over highly polluted regions. Improving the representation of the $>C_3$ alkanes as individual species and isomers with distinct oxidation pathways would have other benefits in future atmospheric chemistry simulations both O_3 and PAN production as well (Tzompa-Sosa et al., 2019). The development of a more rigorous and chemically based alkane scheme should be a priority for future work in ketone chemistry.

Chapter References

Bey, I., Jacob, D. J., Yantosca, R. M., Logan, J. A., Field, B. D., Fiore, A. M., et al. (2001). Global Modeling of tropospheric chemistry with assimilated meteorology: Model description and evaluation. *Journal of Geophysical Research*, *106*(D19), 23073–23095.

Brewer, J. F., Papanastasiou, D. K., Burkholder, J. B., Fischer, E. V., Ren, Y., Mellouki, A., & Ravishankara, A. R. (2019). Atmospheric Photolysis of Methyl Ethyl, Diethyl, and Propyl Ethyl Ketones: Temperature Dependent UV Absorption Cross Sections. *Journal of Geophysical Research: Atmospheres*. https://doi.org/10.1029/2019JD030391

IUPAC. (2005). *CH3C(O)C2H5.* (IUPAC Task Group on Atmospheric Chemical Kinetic Data Evaluation No. Data Sheet P8).

Lurmann, F. W., Lloyd, A. C., & Atkinson, R. (1986). A chemical mechanism for use in long-range transport/acid deposition computer modeling. *Journal of Geophysical Research: Atmospheres*, *91*(D10), 10905–10936. https://doi.org/10.1029/JD091iD10p10905

Romero, M. T. B., Blitz, M. A., Heard, D. E., Pilling, M. J., Price, B., Seakins, P. W., & Wang, L. (2005). Photolysis of methylethyl, diethyl and methylvinyl ketones and their role in the atmospheric HOx budget. *Faraday Discussions*, *130*, 73. https://doi.org/10.1039/b419160a

Tzompa-Sosa, Z. A., Henderson, B. H., Keller, C. A., Travis, K., Mahieu, E., Franco, B., et al. (2019). Atmospheric Implications of Large C2-C5 Alkane Emissions From the U.S. Oil and Gas Industry. *Journal of Geophysical Research: Atmospheres*, *124*(2), 1148–1169. https://doi.org/10.1029/2018JD028955

Wang, S., Hornbrook, R. S., Hills, A., Emmons, L. K., Tilmes, S., Lamarque, J.-F., et al. (2019). Atmospheric Acetaldehyde: Importance of Air-Sea Exchange and a Missing Source in the Remote Troposphere. *Geophysical Research Letters*. https://doi.org/10.1029/2019GL082034

Wolfe, G. M., Nicely, J. M., Clair, J. M. S., Hanisco, T. F., Liao, J., Oman, L. D., et al. (2019). Mapping hydroxyl variability throughout the global remote troposphere via synthesis of airborne and satellite formaldehyde observations. *Proceedings of the National Academy of Sciences*, *116*(23), 11171–11180. https://doi.org/10.1073/pnas.1821661116

APPENDIX A

Contents of this file

Figures A1 to A2
Table A1

Introduction

The figures included in this supplement detail the comparison between the modeled mixing ratios found using GEOS-Chem v10 for 2006 at 4° × 5° resolution and a suite of aircraft missions, ship cruises, and surface sites *[J. A. de Gouw et al.*, 2001; 2006; *Hornbrook et al.*, 2011; *Jacob et al.*, 1996; *Lelieveld et al.*, 2002; *Lewis et al.*, 2005; *Mao et al.*, 2006; *Marandino et al.*, 2005; *Murphy et al.*, 2010; *Singh et al.*, 2009; 2001; 1994; 2004; 2000; *Warneke and de Gouw*, 2001; *Williams et al.*, 2004]. Data for aircraft missions have been averaged over regionally coherent regions as in *Jacob et al.* [2002] with the addition of more recent missions. Data from ship cruises are primarily the averages reported in the literature.

The table included in this supplement details the differences in the global annual acetone budgets between the two largest resolutions of GEOS-Chem v10 (4° × 5° and 2° × 2.5° resolution). The values found do not depend upon the resolution used.

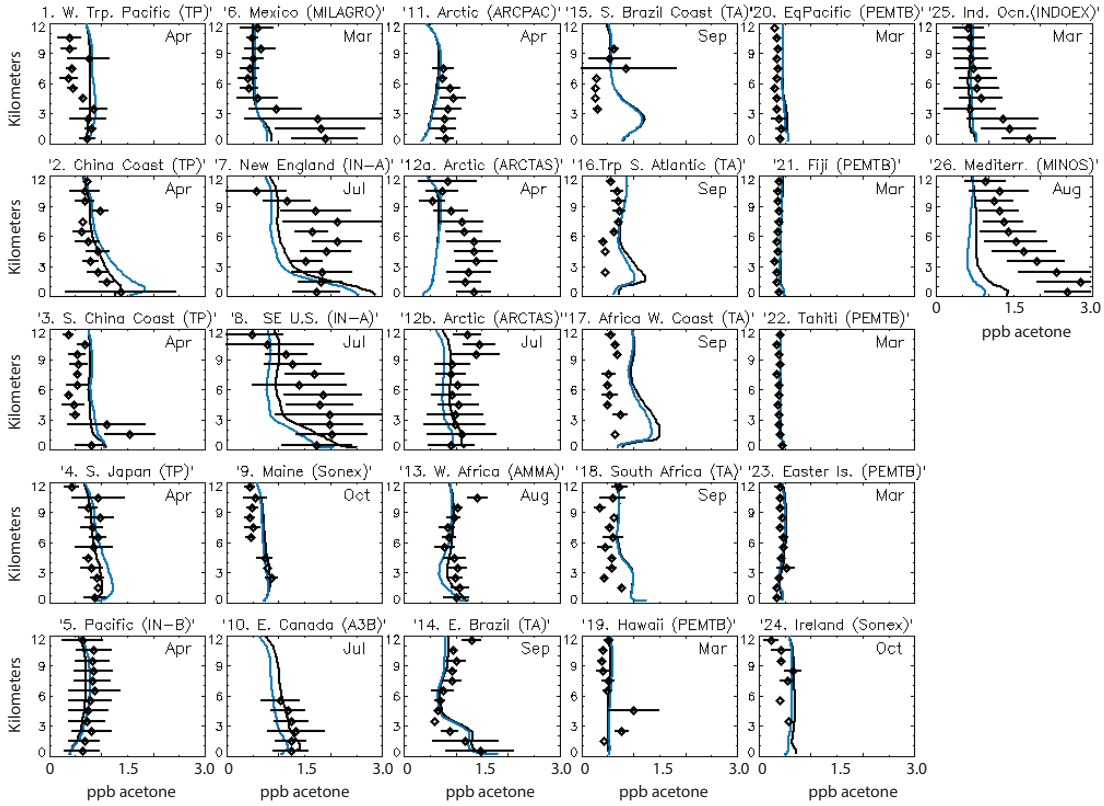

Figure A1. Model output from GEOS-Chem v10 (Black lines), v9 (Blue lines), and a suite of aircraft missions, ship cruises, and surface sites (dots with error bars) [*J. A. de Gouw et al.*, 2001; 2006; *Hornbrook et al.*, 2011; *Jacob et al.*, 1996; *Lelieveld et al.*, 2002; *Lewis et al.*, 2005; *Mao et al.*, 2006; *Marandino et al.*, 2005; *Murphy et al.*, 2010; *H. B. Singh et al.*, 2009; 2001; 1994; 2004; 2000; *Warneke and de Gouw*, 2001; *Williams et al.*, 2004]. Average model bias is -0.12 ppb acetone for v10, -0.14 ppb acetone for v9.

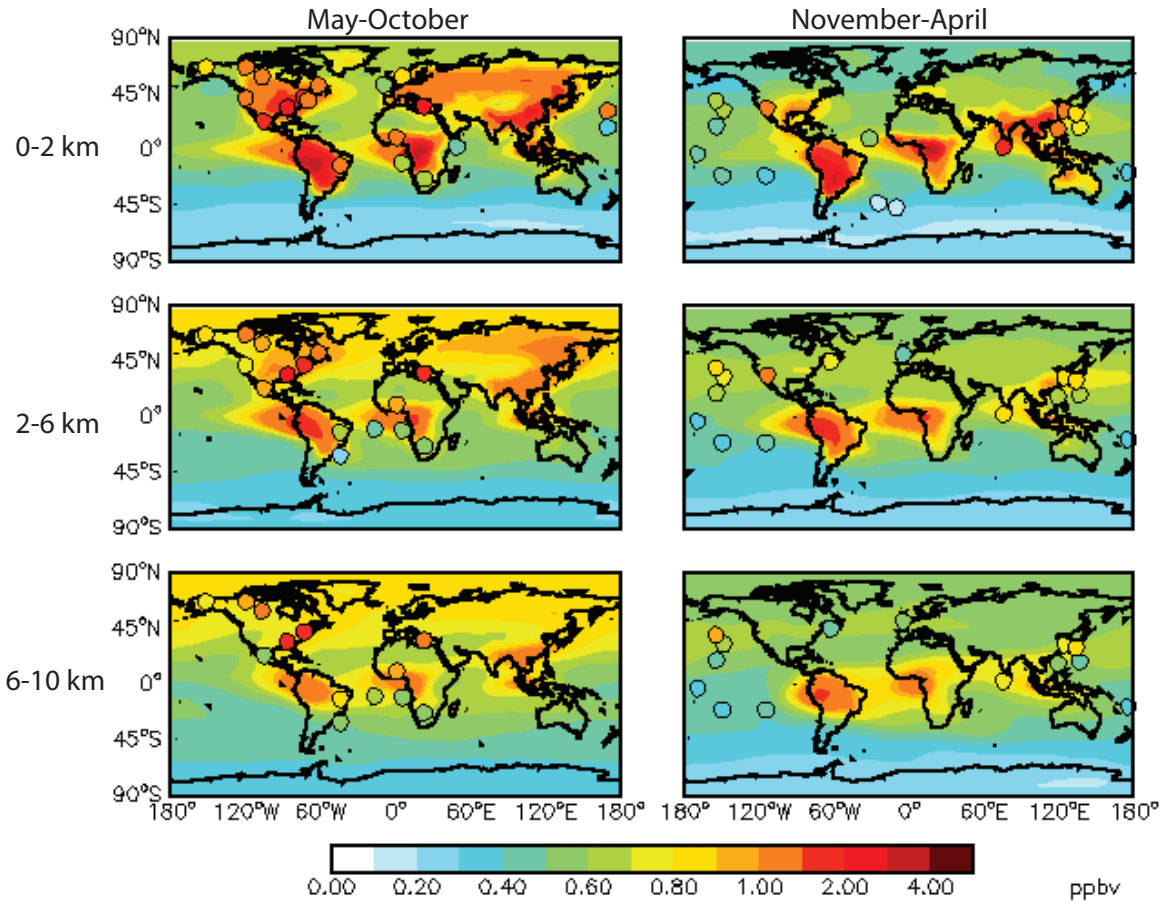

Figure A2. Simulated and observed acetone mixing ratios for three altitude bins and two seasons. Simulated mixing ratios are for 2006 and are shown as solid contours. Filled circles are vertically binned mean observations in different years from a suite of aircraft missions, ship cruises, and surface sites [*J. A. de Gouw et al.*, 2001; 2006; *Hornbrook et al.*, 2011; *Jacob et al.*, 1996; *Lelieveld et al.*, 2002; *Lewis et al.*, 2005; *Mao et al.*, 2006; *Marandino et al.*, 2005; *Murphy et al.*, 2010; *H. B. Singh et al.*, 2009; 2001; 1994; 2004; 2000; *Warneke and de Gouw*, 2001; *Williams et al.*, 2004].

		4°×5°		2°×2.5°
Emissions	Anthropogenic	3.6[a]		3.5
	Biomass Burning	2.6		2.5
	Terrestrial Biosphere	37.1		37.9
Atmospheric Production	Oxidation of Isoalkanes (Primarily Anthropogenic)	18.3		18.2
	Oxidation of Biogenic VOCs	5.8		6.0
	Oxidation by OH	25.6		26.0
	Photolysis	21.0		22.2
	Land Uptake	12.4		12.0
	Ocean Source	51.8		53.4
	Ocean Sink	59.2		60.2
	Net Exchange	-7.5		-6.8

Table A1. Global budgets for the 4° × 5° and 2° × 2.5° resolution of GEOS-Chem v10. The 'Oxidation of Isoalkanes' category includes the source of acetone from both propane and lumped alkanes with 4 or more carbon atoms. Units are in Tg of acetone.

APPENDIX B

Contents of this file

Figures B1 to B4

Additional Supporting Information

Tables B1-B4 can be found in CSV form in the supplemental materials to Brewer et al. (2019), doi: 10.1029/2019JD030391

Table B1 – This table presents the cross section and error at every wavelength, temperature, and species measured in this paper in csv format. Data is recorded as NA if the uncertainty was greater than 10% of the measured value.

Table B2 – This table tabulates the calculated values for $\boldsymbol{\sigma}_0(\lambda)$ and $\boldsymbol{\sigma}_1(\lambda)$ for acetone, MEK, DEK, and PEK at wavelengths from 230-335. These values can be used to generate cross sections for each species at tropospherically-relevant temperatures using equations 2-5 from the paper. Table S2 also makes use of the errors reported in Table S1 to calculate a lower and upper bound for each $\boldsymbol{\sigma}_0(\lambda)$ and $\boldsymbol{\sigma}_1(\lambda)$, which can then be used to bound the uncertainty of the model output. The models presented in this table were parameterized with a $\Delta E = 1720$ cm^{-1}. Note that $\boldsymbol{\sigma}_1(\lambda)$ is <0 for wavelengths less than ~260 nm. We do not mean to imply that the cross section is actually "negative" over this region, as that would not be a physically meaningful concept. These values, which are mostly near-zero, purely reflect the numerical solution to the QR decomposition algorithm, and do not impact the utility of the model.

Table B3 – This table provides the vertical column values of pressure (hPa), temperature (K), and OH (molecules/cm^3) that are used in the paper to calculate Figure 6 and S4. Concentrations of OH were from (Spivakovsky et al., 2000) that does not include any HO_x produced from the oxidation of MEK, DEK, or PEK; temperature and pressure profiles from a 2007-2017 average of monthly NCAR NCEP reanalysis data (Kalnay et al., 1996).

Table B4 – This table provides the quantum yields and cross-sections binned for use in the Fast-J model, according to the bin limits provided by Wild et al. (2000). Temperature and pressure values used are included in the table; the temperatures used were 220 K, 272 K, and 285 K, which were paired with pressures of 177 hPa, 566 hPa, and 999 hPa. These values were taken from a 2007-2017 average of monthly NCAR NCEP reanalysis data (Kalnay et al., 1996), and are the same as those currently used in the default GEOS-Chem Fast-JX implementation for the interpolation of MEK.

Brewer_JValue_Subroutines_Code_S1.R – This R script includes a series of subroutines built in R, requiring the use of R 3.5 or greater as well as the use of the "tidyverse" and "fuzzyjoin" packages. The subroutines included in this code can be used to perform the following operations:

1. Use the models provided in Table B2 to output a cross-section for MEK, DEK, PEK, or Acetone at any atmospherically relevant temperature, as described in the main body of the paper.
2. Calculate the quantum yields used in Figure 3.6 for MEK (Romero et al., 2005; IUPAC, 2005), DEK (Romero et al., 2005), and PEK (assumed to be unity due to lack of data) at any single pressure and temperature.
3. Bin any QY, $\boldsymbol{\sigma}$, or actinic flux spectrum according to binning schemes such as Fast-J (Wild et al., 2000). The expected structure for the bin data is included in the code file, but must include columnar variables name "Bin_Number" (a label for each bin), "Lambda_Start" (the lower limit of the wavelength bin), and "Lambda_End" (the upper limit of the wavelength bin). Additional variables (such as "Effective Lambda") may be included in the bin data and will be inherited by the final function output, but these three are required.

Brewer_JValue_Example_Code_S2.R – This R script contains example code showing the usage of the subroutines in **Brewer_JValue_Subroutines_Code_S1.R**. This is included for ease of code implementation. To use this code, Table B2 will either need to be in the working directory or the address of that csv file will need to be updated in the code.

Introduction

This appendix contains four figures. All are based primarily on the cross section data presented in the main body of the paper. Figure B1 is a ratio of the magnitude of the uncertainty of each measured cross section to the measured cross section itself. Figure B2 shows the results of fitting a two-state model parameterized using wavenumbers ranging from 1-2000 cm^{-1} against two separate metrics of fit: the mean absolute error in percent, and the number of negative values produced by the algorithmic solution to the system of equations. Figure B3 shows model outputs at temperatures outside the measured range, and demonstrates that the model is numerically stable. Finally, Figure B4 replicates Figure 3.6 in the paper with a cloud layer added to the TUV model.

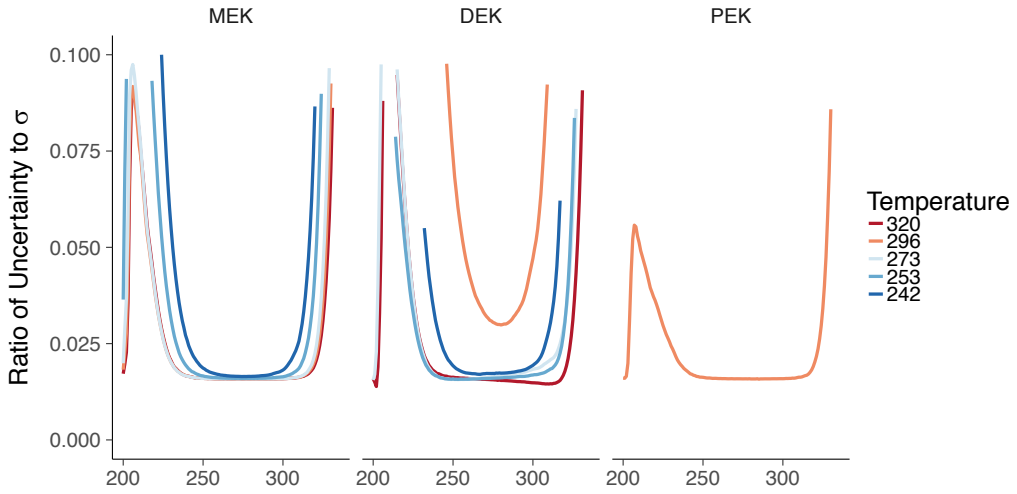

Figure B1– Ratio of uncertainty to measured spectra at each wavelength for all measured absorption spectra at all temperatures.

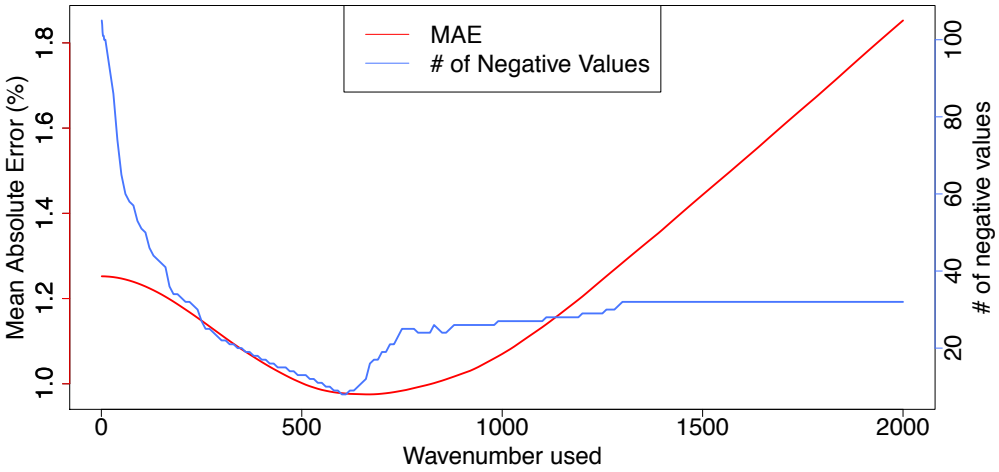

Figure B2 – Mean absolute model fit error for MEK, compared over all temperatures measured and all wavelengths from 230-330 nm as a function of wavenumber used to parameterize the model (in red, left axis), and total number of negative values observed over the same comparison parameters as a function of wavenumber used to parameterize the model (in blue, right axis). MAE is minimized at wavenumber 680 cm^{-1}, and the number of negative values is minimized at wavenumber 600 cm^{-1}.

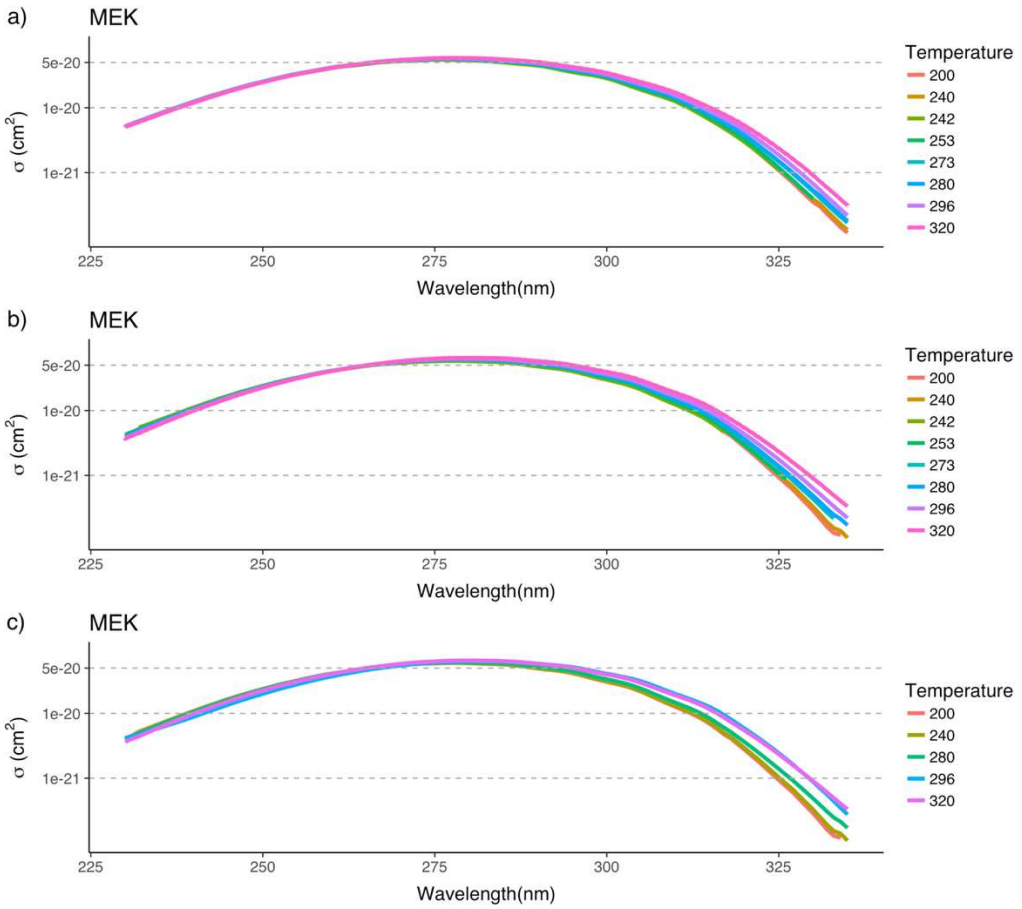

Figure B3 – This plot shows modeled absorption spectra at temperatures measured in this work as well as at temperatures outside the range of our measurements. For MEK and DEK, the spectra at 200 K, 240 K, and 280 K are purely model derived while all other spectra are measured. For PEK, only 296 K was measured and all other spectra are model-derived. This figure shows that the model continues to perform in basically expected ways even outside its parameterized temperature range.

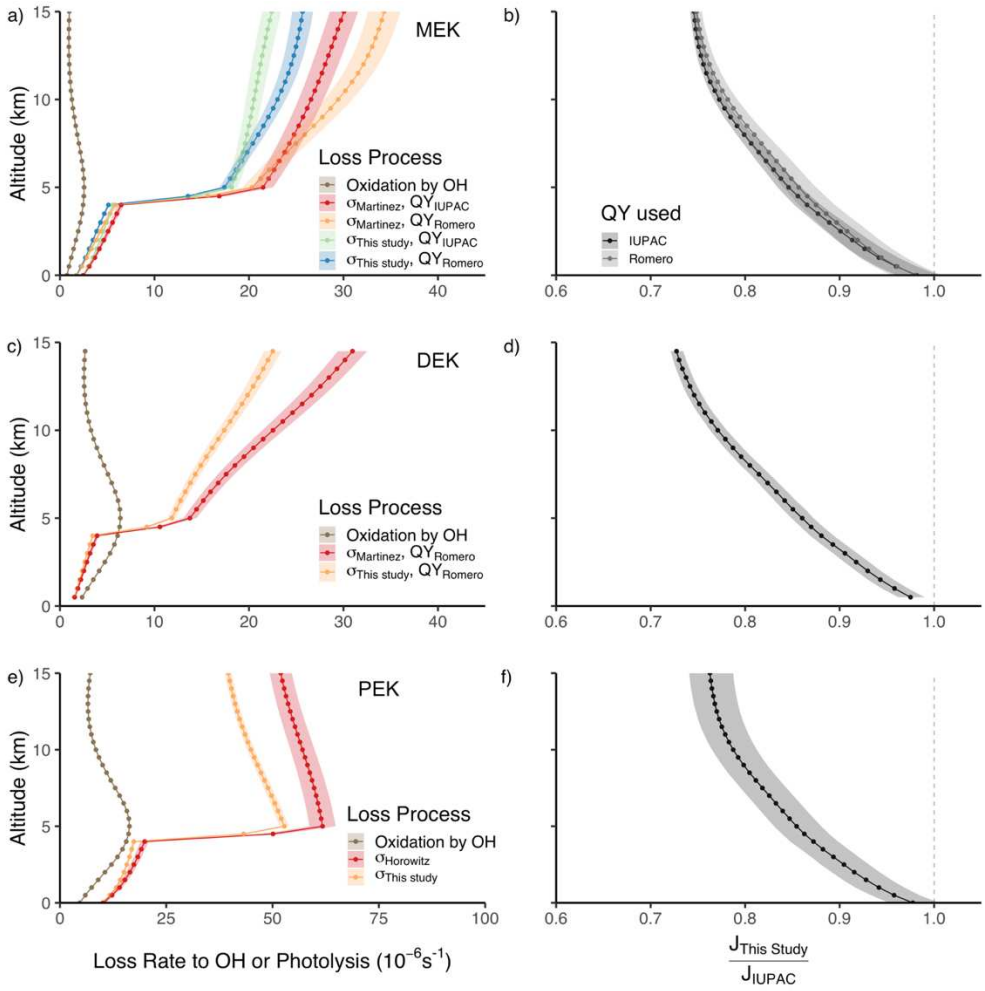

Figure B4 - a) shows photolytic and oxidative loss rate constants for MEK in April at the Equator with 50% cloud cover, in 10^6 s^{-1}. This is a replication of Figure 3.6 from the main body of the paper. MEK J-values are calculated using two different absorption cross-sections and two different quantum yield possibilities. Quantum yields used are a reciprocal-linear interpolation of the IUPAC recommendations and a Stern-Volmer parameterization from Romero et al. (2005). Cross sections used are those measured in this paper and the current IUPAC recommendation. Figures c) and e) show DEK and PEK J-values in the same conditions and units. These J-values are also calculated using two different absorption cross-sections but using only one quantum yield, those of Romero et al. (2005) for DEK and an assumed quantum yield of 0.5 for PEK, as no IUPAC recommendation exists for either and no studies of PEK quantum yields have been made. J-value uncertainties in a), c), and e) reflect only the uncertainties in cross-sections and not those in the various quantum yields used. b) displays the ratio between the J-Values calculated with our cross-sections and those calculated with the IUPAC recommendations for each quantum yield used. Shaded area in this plot is the ratio between the upper (and lower) bounds of this study's calculated J-values to the upper (and lower) bounds of the J-values calculated according IUPAC cross-sections. d) and f) show the same ratio, calculated this time for DEK and PEK, which each use only one quantum yield.

Code B1. Code_Main_Body.R

```
library(tidyverse)
source("Supplemental_Subroutines.R")

models <- read_csv("SI_Table_2.csv")
Use.Temperature <- 287 # Example temperature, in K

# Sample structure for FJX_bins
FJX_bins <- structure(
  list(
    Bin_Number = c(1, 2, 3, 4, 5, 6, 7),
    Lambda_Start = c(289, 298.25, 307.45, 312.45, 320.3, 345, 412.45),
    Lambda_End = c(298.25, 307.45, 312.45, 320.3, 345, 412.45, 850),
    Effective_Lambda = c(294, 303, 210, 316, 333, 380, 574)
  ),
  class = c("spec_tbl_df", "tbl_df",
            "tbl", "data.frame"),
  row.names = c(NA,-7L),
  spec = structure(list(
    cols = list(
      Bin_Number = structure(list(), class = c("collector_double", "collector")),
      Lambda_Start = structure(list(), class = c("collector_double", "collector")),
      Lambda_End = structure(list(), class = c("collector_double", "collector")),
      Effective_Lambda = structure(list(), class = c("collector_double", "collector"))
    ),
    default = structure(list(), class = c("collector_guess", "collector")),
    skip = 1
  ), class = "col_spec")
)


MEK.QY <- Calculate.QY(SpeciesName = "MEK", lambda = seq(230, 335, 1),
                       Pressure = 1000, Temperature = Use.Temperature, Use.Romero = T)
MEK.Sigma <- run.model.forward(SpeciesName = "MEK", TK = Use.Temperature, mod
= models)

MEK.data <- full_join(MEK.Sigma, MEK.QY) %>%
  select(-Temp, -Source)

FJX_MEK <- Bin_for_J_Processing(MEK.data, FJX_bins)
```

Code B2. Code_Subroutines.R

```
library(tidyverse)
library(fuzzyjoin)

run.model.forward <- function(SpeciesName, TK, mod, wn.in = 1715){
  # This function takes a Species name (either "MEK", "DEK", "PEK", or "Acetone",
  # A temperature, a set of Sigma-0 and Sigma-1 (with their uncertainties), and a
wavenumber.
  # it then runs the model forward and returns a modeled spectrum at the input
Temperature
  # This is as per Nicovich and Wine 1988

  if(!(SpeciesName %in% mod$SPP)){
    #print("Whoops wrong name, try again")
    stop("Whoops wrong name, try again")
  }

  model.subset <- filter(mod, SPP == SpeciesName)

  # If using this subroutine with the sigmas provided in Table S2, wn.in should be left as
1715 cm-1
  # (currently the default value)
  Q <- Calc.Q(TK, wn.in)
  X0 <- 1/Q #
  X1 <- 1-X0 # Calculate the partitions

  sigma.calc <- X0*model.subset$Sigma0 + X1*model.subset$Sigma1     # Sigma
  sigma.UB <- X0*model.subset$Sigma0_UB + X1*model.subset$Sigma1_UB # Upper
bound for uncertainty
  sigma.LB <- X0*model.subset$Sigma0_LB + X1*model.subset$Sigma1_LB # Lower
bound for uncertainty
  sig.out <- tibble(model.subset$Wavelength, sigma.calc, sigma.UB, sigma.LB, TK,
"Modeled")
  colnames(sig.out) <- c("Wavelength", "Sigma", "SigmaUB", "SigmaLB", "Temp",
"Source")
  sig.out <- type_convert(sig.out)
  return(sig.out)
}

Calc.Q <- function(TK, wn = 1715){
  # fed a C=O vibration wavenumber in per-cm and an array of Temperatures in K
  # Function calculates and returns Q partitioning term, as per Nicovich and Wine 1988
  # 1705-1725 is the wavenumber of stretch energy for an aliphatic ketone C=O bond

  # If using this subroutine with the sigmas provided in Table S2, wn.in should be left as
1715 cm-1
```

```
  # (currently the default value)

  # Declare constants
  h <- 6.63e-34 # Planck's Constant (J-s)
  c <- 3e8 # speed of light (m/s)
  cm.per.m <- 100 # cm/m
  Av <- 6.022E23 # molecules/mol
  R <- 8.314/Av # [J/(K-mol)]/[molecules/mol] => J/K

  # First, put E in useful units using Planck's Equation
  lambda <- (1/wn)/cm.per.m # lambda in m
  nu <- c/lambda # frequency in 1/s
  E <- h*nu # Energy in J

  # Now calculate Q as per Nicovich and Wine (1988)
  Q <- 1. + exp(-E/(R*TK))
  return(Q)
}

Calculate.QY <- function(SpeciesName, lambda = seq(220, 335, 1), Pressure,
Temperature, Use.Romero = T){
  # This function calculates the quantum yields used in Brewer et al. (2019)
  # over a given set of wavelengths (lambda). The default for Lambda is 1 nm increments
from 220-335

  # It is fed a species name (either "MEK", "DEK", or "PEK"),
  # an array of wavelengths at which to calculate the quantum yields,
  # and a single Pressure (hpa) and Temperature (K) value at which to do the calculations.

  # In the special case of MEK, where multiple different QY suggestions exist,
  # the Use.Romero flag tells the subroutine whether to use the Romero et al. (2005) or
IUPAC QY values
  # The function default is to use the Romero values.

  if(length(Pressure) > 1 | length(Temperature) > 1){
    # Verify that only one temperature and Pressure were entered
    print("Woah this function only runs for 1 P-T value pair right now!")
    break()
  }
  if(SpeciesName == "PEK"){
    # For PEK, QY = 1 at all points
    QY <- Assumed_QY_PEK(lambda)
  } else if(SpeciesName == "DEK"){
    # For DEK, use Romero et al. (2005)
    QY <- Romero_QY_DEK(Temperature, Pressure, lambda)
  } else if(SpeciesName == "MEK" & Use.Romero == T){
```

```
  # For MEK, use either Romero et al. (2005)...
  QY <- Romero_QY_MEK(Temperature, Pressure, lambda)
 } else if(SpeciesName == "MEK" & Use.Romero == F){
  # Or an interpolation of the values reported in the IUPAC Data Sheet (P8, 2005)
  QY <- IUPAC_MEK_QY_model(Pressure, lambda)
 } else {
  # Catch error of wrong species name
  print("Oh no something is wrong. Did you type the wrong species name?")
  break()
 }
 QY <- rename(QY, Wavelength = lambda)
 return(QY)
}

Romero_QY_DEK <- function(Temp, p, lambda){ # This QY has a temperature AND a
Pressure dependence
 # Calculates the DEK QY according to Romero et al. (2005)
 # T in K
 # M in molecules/cm3, but p is hPa
 R <- 8.314E6*(1/100)*(1/6.022E23) # Gas constant in (hPa-cm3)/(K-molecules)
 # M = p/(R-T) according to Ideal Gas Law
 M <- p/(R*Temp) # molecules/cm3


 const_df <- structure(list(DEK = structure(c(1L, 2L, 4L, 5L, 3L),
                        .Label = c("a1","a12", "a13", "a2", "a22"), class = "factor"),
                        Value = c(1.06e-18, 0.00103, 3.13, 5.36e-07, 30000),
                        MOE = c(1.5e-19, 0.00017, 2.26, 4.64e-07, 0),
                        Tdep = c(-5.43, -0.985, -19.3, -10.2, -0.064),
                        Tdep.MOE = c(1.68, 0.92, 86, 13.4, 0)),
                   .Names = c("DEK", "Value", "MOE", "Tdep", "Tdep.MOE"),
                   class = "data.frame",
                   row.names = c(NA, -5L))

 a <- const_df$Value * (Temp/295)^-const_df$Tdep

 A1 <- a[1]*exp(-a[2]*(((1E7)/lambda)-30488))
 A2 <- a[3]*exp(-a[4]*(((1E7)/lambda)-a[5])^2)
 QY <- round(1./(1+A1*M+A2), digits = 4)
 out.df <- tibble(lambda, QY)
 return(out.df)
}

Assumed_QY_PEK <- function(lambda){ # assume a unitary PEK quantum yield
 QY <- 1
 out.df <- tibble(lambda, QY)
```

```
  return(out.df)
}

Romero_QY_MEK <- function(Temp, p, lambda){
  # Calculates the MEK QY according to Romero et al. (2005)

  # This QY has a temperature AND a Pressure dependence
  # T in K
  # M in molecules/cm3, but p is hPa
  R <- 8.314E6*(1/100)*(1/6.022E23) # Gas constant in (hPa-cm3)/(K-molecules)
  # M = p/(R-T) according to Ideal Gas Law
  M <- p/(R*Temp) # molecules/cm3

  # The following lines reconstruct the data structure needed to calculate the Quantum
Yield
  const_df <- structure(list(MEK = structure(c(1L, 2L, 4L, 5L, 3L),
                             .Label = c("a1", "a12", "a13", "a2", "a22"), class = "factor"),
                             Value = c(2.53e-19, 0.00055, 0.103, 1.95e-09, 30006),
                             MOE = c(3e-20, 6e-05, 0.025, 1.64e-09, 0),
                             Tdep = c(-5.03, -0.382, -12.4, -19.46, -0.064),
                             Tdep.MOE = c(1.4, 1.06, 0.98, 2.96, 0)),
                        .Names = c("MEK", "Value", "MOE", "Tdep", "Tdep.MOE"),
                        class = "data.frame", row.names = c(NA, -5L))

  a <- const_df$Value * (Temp/295)^-const_df$Tdep

  A1 <- a[1]*exp(-a[2]*(((1E7)/lambda)-30488))
  A2 <- a[3]*exp(-a[4]*(((1E7)/lambda)-a[5])^2)
  QY <- round(1./(1+A1*M+A2), digits = 4)
  out.df <- tibble(lambda, QY)
  return(out.df)
}

IUPAC_MEK_QY_model <- function(p, lambda){
  # p is in hpa
  # according to IUPAC MEK Fact Sheet (P8, 2005), no other QY measurements exist,
  # so we will do an inverse linear interpolation
  Prange <- c(1000, 68) # these are the observations given in the IUPAC MEK fact sheet
(P8, 2005)
  QYrange <- 1/c(0.34, 0.89) # these values are only valid from 275-380, but we will use
them

  QY_model <- lm(QYrange ~ Prange)
  interp.inverse.QY <- QY_model$coefficients[1] + QY_model$coefficients[2]*p
  QY <- 1/interp.inverse.QY
  out.df <- tibble(lambda, QY)
```

```
  return(out.df)
}

library(tidyverse)
library(fuzzyjoin)

# Sample structure for FJX_bins
FJX_bins <- structure(
  list(
    Bin_Number = c(1, 2, 3, 4, 5, 6, 7),
    Lambda_Start = c(289, 298.25, 307.45, 312.45, 320.3, 345, 412.45),
    Lambda_End = c(298.25, 307.45, 312.45, 320.3, 345, 412.45, 850),
    Effective_Lambda = c(294, 303, 210, 316, 333, 380, 574)
  ),
  class = c("spec_tbl_df", "tbl_df",
            "tbl", "data.frame"),
  row.names = c(NA,-7L),
  spec = structure(list(
    cols = list(
      Bin_Number = structure(list(), class = c("collector_double", "collector")),
      Lambda_Start = structure(list(), class = c("collector_double", "collector")),
      Lambda_End = structure(list(), class = c("collector_double", "collector")),
      Effective_Lambda = structure(list(), class = c("collector_double", "collector"))
    ),
    default = structure(list(), class = c("collector_guess", "collector")),
    skip = 1
  ), class = "col_spec")
)

Bin_for_J_Processing <- function(spectrum, bin_df = FJX_bins){
  # this function will bin the cross-sections and quantum yields into bins appropriate for
use
  # in standard CTMs, such as Fast-J or Fast-TUV

  # It takes as input: 1) either a quantum yield or cross section (spectrum), and
  # 2) a dataframe detailing the start and end of each bin as well as the bin number.
  # Other values can be added on to this dataframe and will be preserved, but
  # Lambda_Start, Lambda_End, and Bin_Number are required columns.

  # An example is provided here: the 7 bins from Fast-J (Wild et al., 2000)

  # This code does all the work:
  output.df <- spectrum %>%
    #First, filter to remove any wavelengths outside the overall bin space
    filter(Wavelength >= min(bin_df$Lambda_Start) & Wavelength <=
max(bin_df$Lambda_End)) %>%
```

```
    # Assign bin numbers by according to the Start and End wavelengths
    interval_left_join(., bin_df,
                       by = c('Wavelength' = 'Lambda_Start', 'Wavelength' = 'Lambda_End'))
%>%
    # Remove unneeded columns
    select(-Lambda_Start, -Lambda_End, -Wavelength) %>%
    # group by bin number
    group_by(Bin_Number) %>%
    # collapse on bin number, taking the mean at each variable
    summarise_each(list(mean)) %>%
    # Add back in the original dataframe, in order to make sure all bins are accounted for
    full_join(., bin_df)

  # Finally, replace all NA values with 0
  output.df[is.na(output.df)] <- 0

  return(output.df)
}
```

Sources

Kalnay, E., Kanamitsu, M., Kistler, R., Collins, W. J., Deaven, D., Gandin, L., et al. (1996). The NCEP/NCAR 40-year Reanalysis Project. *Bulletin of the American Meteorological Society, 77*(3), 437-472. http://journals.ametsoc.org/doi/abs/10.1175/1520-0477(1996)077%3C0437:TNYRP%3E2.0.CO;2

Spivakovsky, C. M., Logan, J. A., Montzka, S. A., Balkanski, Y. J., Foreman-Fowler, M., Jones, D. B. A., et al. (2000). Three-dimensional climatological distribution of tropospheric OH: Update and evaluation. *Journal of Geophysical Research: Atmospheres, 105*(D7), 8931-8980.

APPENDIX C

Contents of this file

Figures C1 to C7
Table C1

Introduction

This supporting information helps make the case for the oceanic source of methyl ethyl ketone (MEK) to the atmosphere. Figure C1 supplements Figure 4.2 from the paper by detailing the sample sizes used to calculate the median MEK concentation at each altitude; Figures C2-C5 supplement Figure 4.3, by showing the actual plot of MEK vs VOC concentrations for the species examined. All of these figures are all made directly from the ATom data, as discussed in the paper. Figure C6 shows the residence time analysis that supplements Figure 4.3 and allows us to examine whether MEK and acetaldehyde are correlated simply because the latter is an oxidation product of the former. Finally, Table C1 includes all of the specifics of the box modeling simulation of air-sea trace gas exchange which produced the findings detailed in Figure C7.

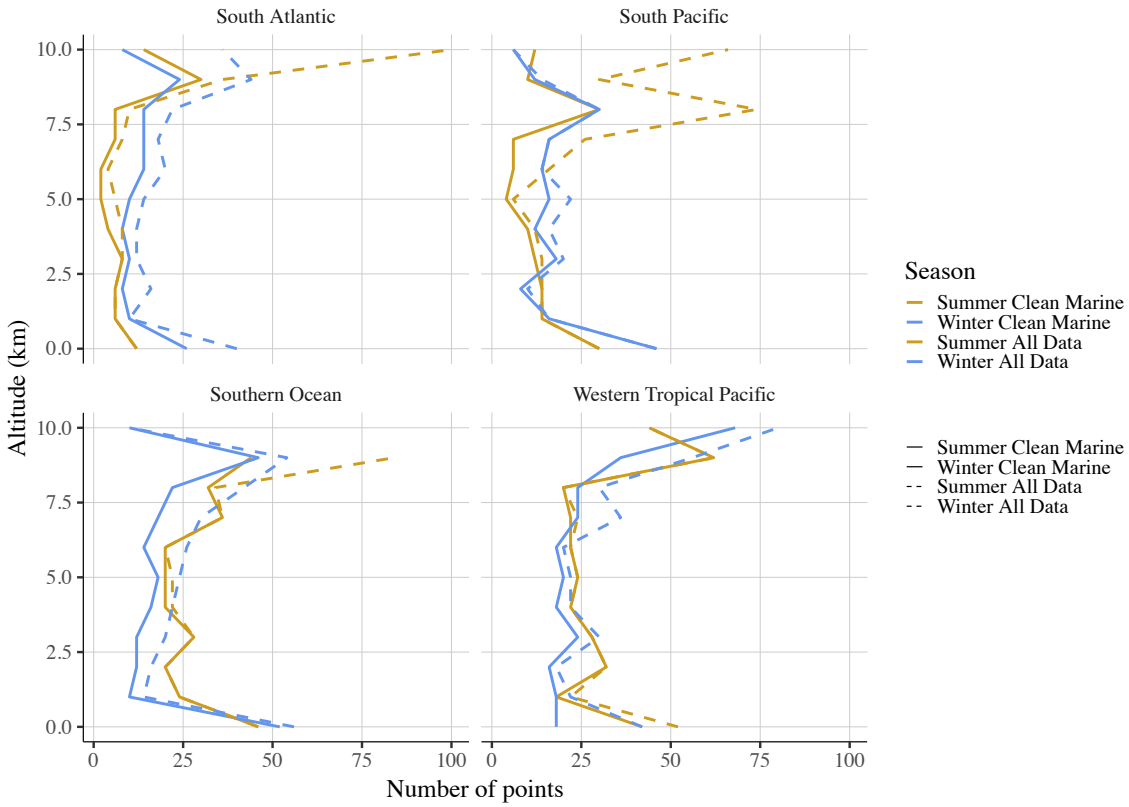

Figure C1. MEK sample sizes from ATom-1 and ATom-2 in the South Atlantic, South Pacific, Southern Ocean, and Western Tropical Pacific in 1-km altitude bins. Blue lines

summarize observations numbers from the meteorological winter (January-February in the Northern Hemisphere, July-August in the Southern Hemisphere) and orange lines summarize data from meteorological summer. The solid lines show the sample sizes from the clean marine air masses, where CO mixing ratios are at or below the regional background (see text). Dashed lines present the same information using all available MEK data.

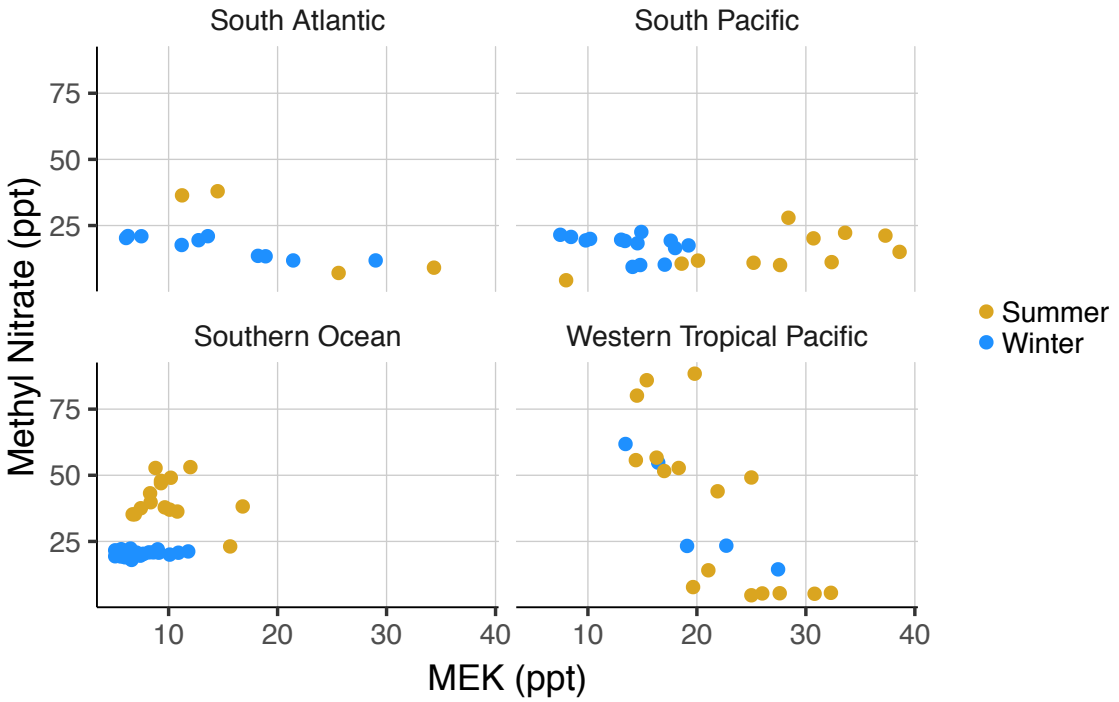

Figure C2. Surface (<1 km) mean MEK and methyl nitrate mixing ratios (ppt) observed in clean marine air masses during ATom-1 and ATom-2 in the South Atlantic, South Pacific, Southern Ocean, and Western Tropical Pacific. Blue points are observations numbers from the meteorological winter (January-February in the Northern Hemisphere, July-August in the Southern Hemisphere) and orange points are from meteorological summer.

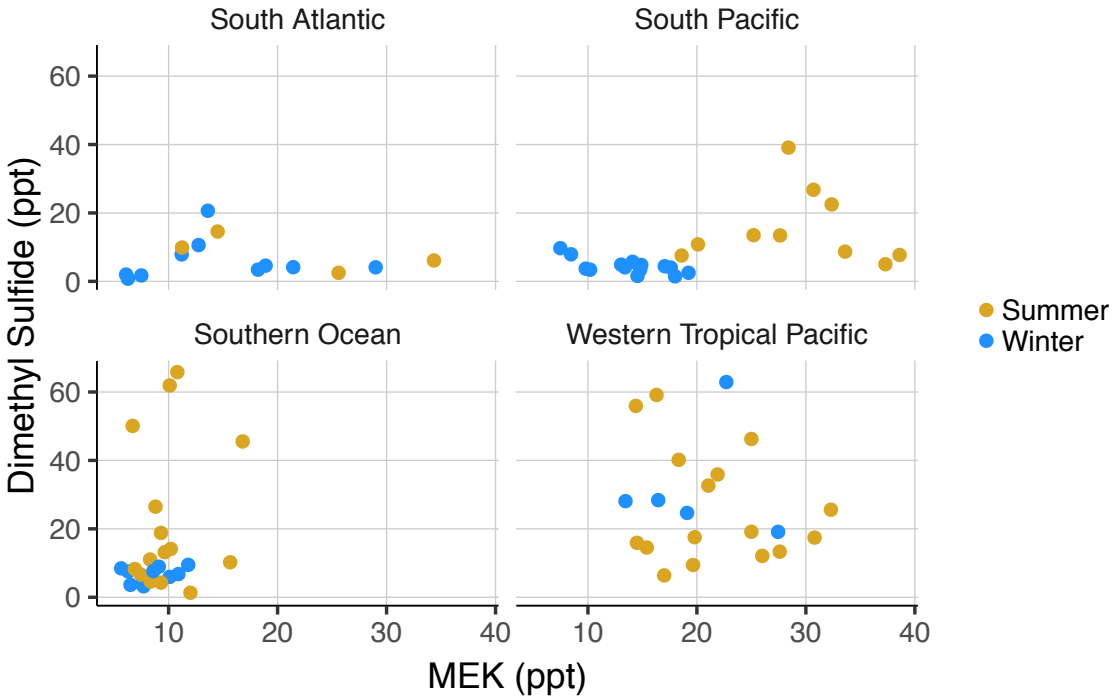

Figure C3. Surface (<1 km) mean MEK and DMS mixing ratios (ppt) observed in clean marine air masses during ATom-1 and ATom-2 in the South Atlantic, South Pacific, Southern Ocean, and Western Tropical Pacific. Blue points are observations numbers from the meteorological winter (January-February in the Northern Hemisphere, July-August in the Southern Hemisphere) and orange points are from meteorological summer.

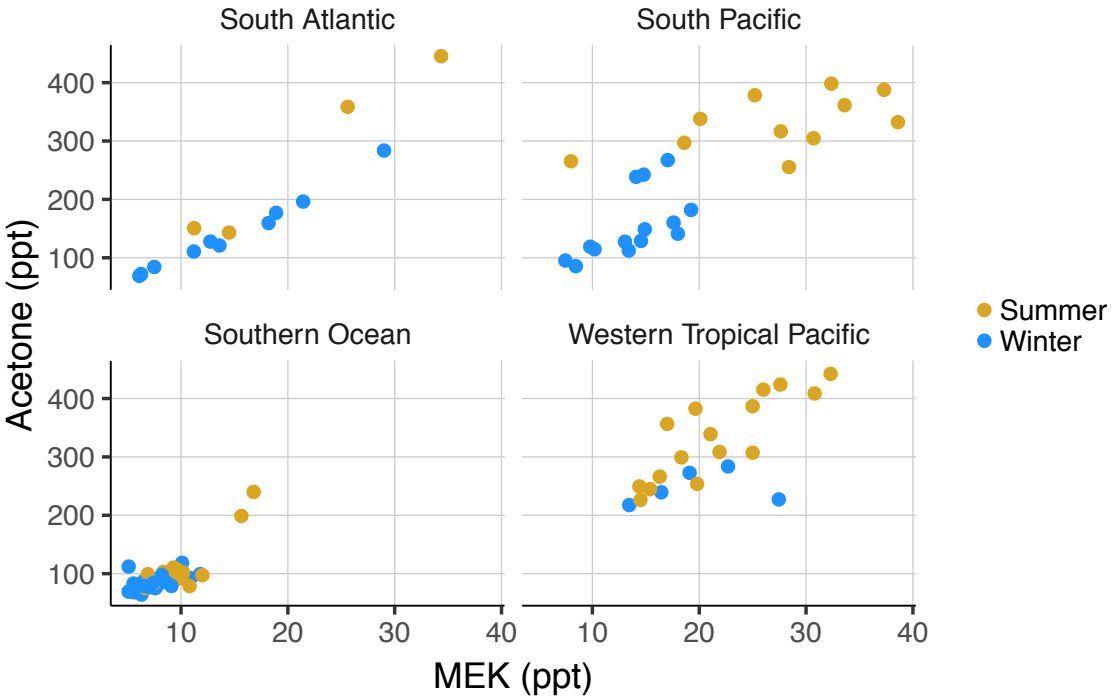

Figure C4. Surface (<1 km) mean MEK and acetone mixing ratios (ppt), as in Figure C2.

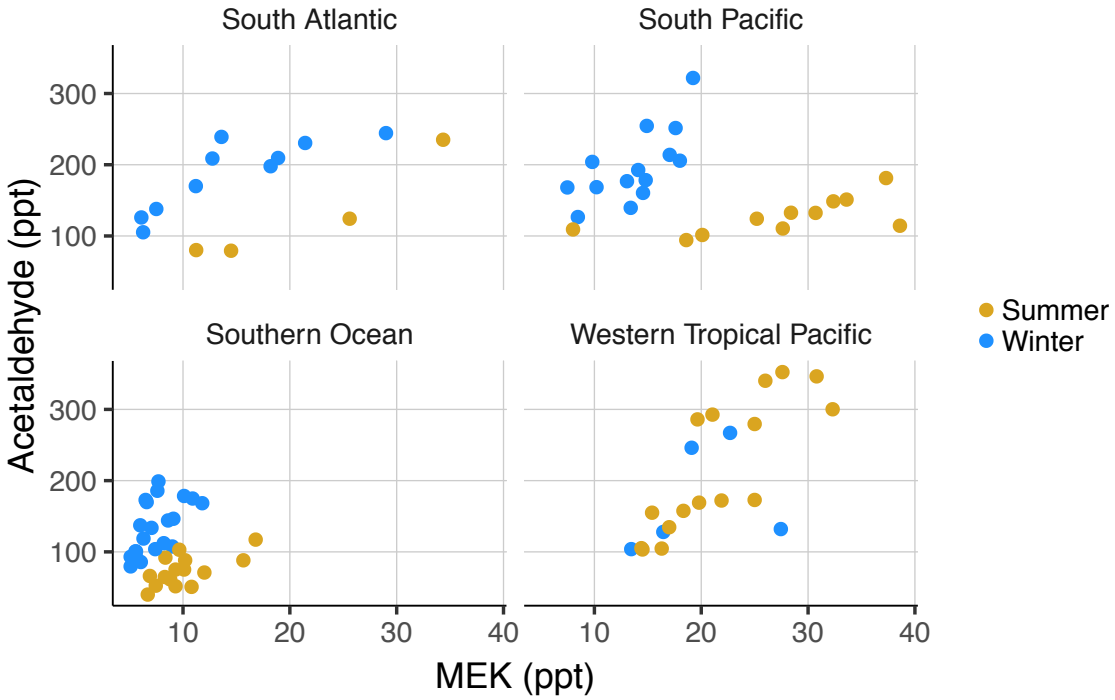

Figure C5. Surface (<1 km) mean MEK and acetaldehyde mixing ratios (ppt) as in Figure C2.

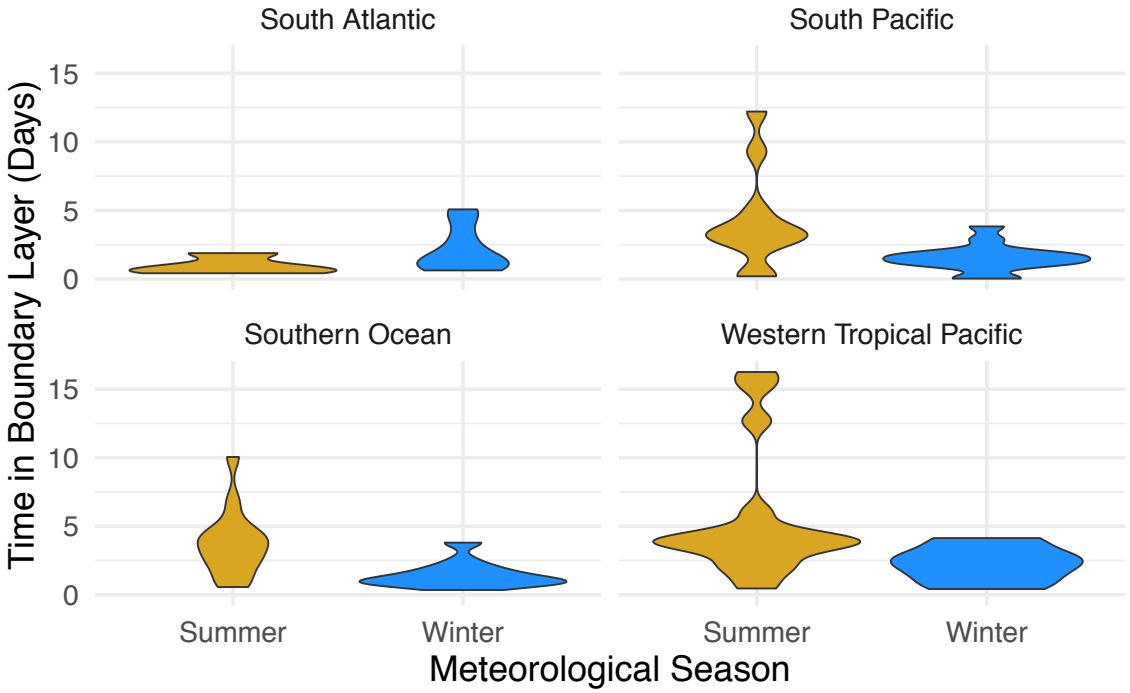

Figure C6. Probability distribution functions of the mean time in days that each sampled air mass spent in the marine boundary layer, organized by meteorological season and region. This figure was calculated based on back trajectories from the Traj3D model (Bowman, 1993; Bowman & Carrie, 2002) run with National Centers for Environmental Predictions (NCEP) Global Forecast System (GFS) 0.5°x0.5° resolution meteorology (https://www.ncdc.noaa.gov/data-access/model-data/model-datasets/global-forcast-system-gfs). A cluster of 245 trajectories was initialized along the flight track each minute and run backwards for 14 days. Time in the boundary layer was defined based on the position of each trajectory compared to the height of the local marine boundary layer, and the time elapsed since last entry into the boundary layer was recorded. The mean time in the boundary layer for every flight minute was calculated from the average boundary layer times of the trajectory cluster and combined into profile averages in the same way as the recorded instrumental readings from TOGA and WAS (see Sections 4.2.1 and 4.3.2 in the paper).

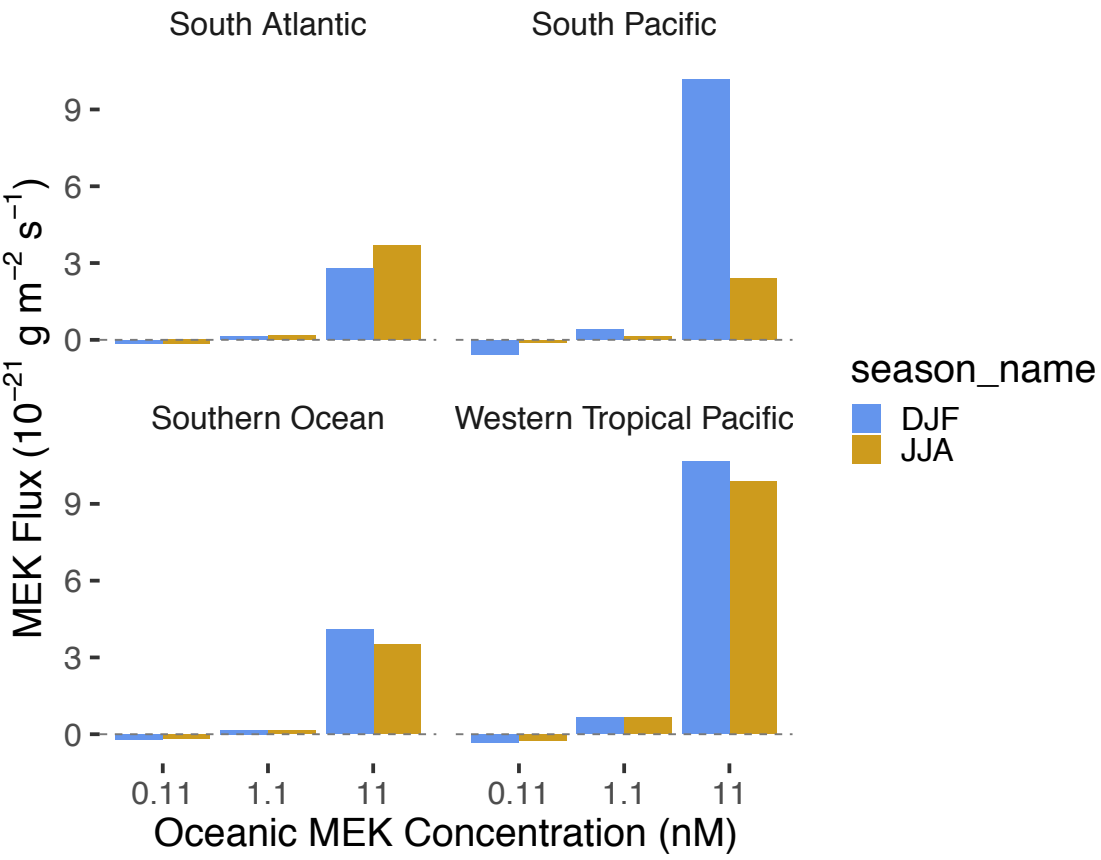

Figure C7. MEK Flux (10^{-21} g m^{-2} s^{-1}) as a function of oceanic MEK concentration (nM). Data used in this calculation are detailed in Table C1.

Table C1. Data used to calculate air-sea fluxes of MEK.

Ocean Region	Season	Observed Air Temperature (C)[a]	Pressure (hPa)[a]	Observed Windspeed (m/s)[a]	MERRA Windspeed (m/s)[b]	MEK (ppt)[a]	SST (C)[c]	Sal-inity (psu)[d]
South Atlantic	DJF	18.3	1004.3	4.4	7.5	25.1 ± 13.4	26	31
South Atlantic	JJA	13.6	990.5	6.4	10.0	16.9 ± 8.7	18	33
South Pacific	DJF	19.9	993.6	10.8	7.0	29.5 ± 6.4	24	31
South Pacific	JJA	10.5	998.6	5.1	10.0	12.7 ± 3.7	18	33
Southern Ocean	DJF	4.4	965.0	10.1	13.0	11.5 ± 4.9	3	29
Southern Ocean	JJA	-0.9	983.8	11.2	12.0	7.6 ± 1.1	3	31
Western Tropical Pacific	DJF	25.9	989.8	9.1	7.0	26.7 ± 11.7	28	30
Western Tropical Pacific	JJA	26.2	991.2	8.5	7.0	23.4 ± 4.8	30	29

[a]*in situ* ATom observations from below 200 meters ASL averaged over the regions of interest.

[b]Regional mean surface windspeed from the Modern-Era Retrospective analysis for Research and Applications version 2 (MERRA-2) reanalysis (Gelaro et al., 2017) during ATom-1 and 2.

[c]Moderate Resolution Imaging Spectroradiometer (MODIS)-Aqua L3 11 micron SST product (NASA Ocean Biology Processing Group, 2015)

[d]Aquarius rain-corrected monthly sea surface salinity product for the relevant months in 2014 (the last year available from Aquarius) (JPL, 2015).

APPENDIX D

Contents of this file

Figures D1-D4
Tables D1 and D2
Code D1

Additional Supporting Information

Figures D1 and D2 and Tables D1 and D2 detail the model inputs used in the analysis contained in Chapter 5. Figure D3 shows the difference between ATom and non-ATom carbon monoxide distributions by region and season, as discussed in Section 5.3.2. Figure D4 is a companion figure to Figure 5.4: where Figure 5.4 shows the mean difference between observed and simulated mixing ratios of MEK over North America, Figure D4 shows the fractional mean bias of the same data. The attached code (Code D1) is the modified chemistry file from GEOS-Chem discussed in Section 5.2.1. The code is built using the KPP equation solver and is based off the GEOS-Chem *Tropchem* scheme. The files to build and run the mechanism and solve for the rate coefficients can be downloaded at www.geos-chem.org. This chemical mechanism was built off GEOS-Chem v12.0.0 and should be built with that version of the model.

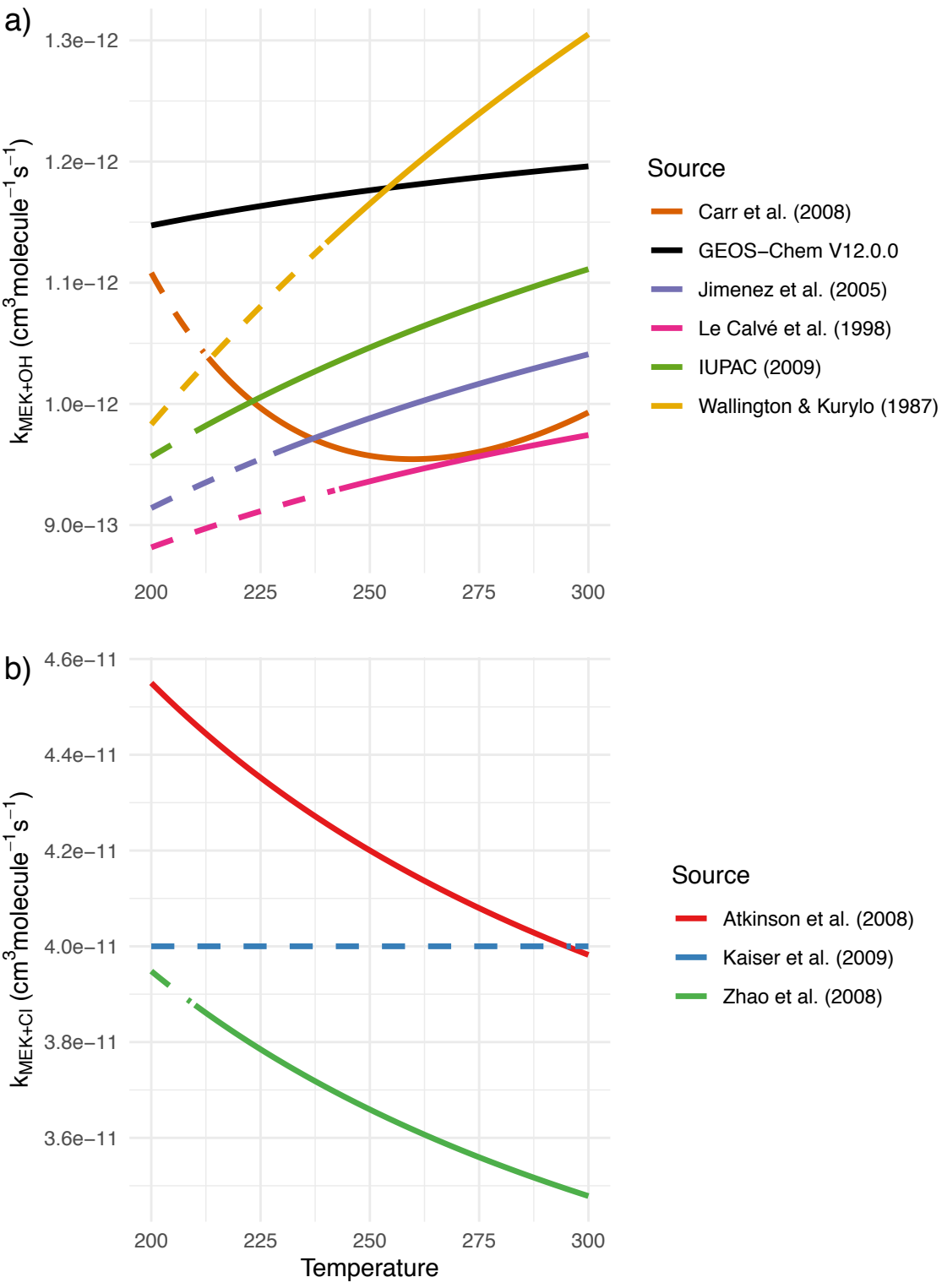

Figure D1. Comparisons of rate coefficient parameterizations for the reaction of MEK with the a) OH and b) Cl radicals. Solid lines represent parameterizations over the temperature ranges for which they are reported, while dashed lines are the same parameterizations extended beyond the measured ranges but across the temperature range of the troposphere.

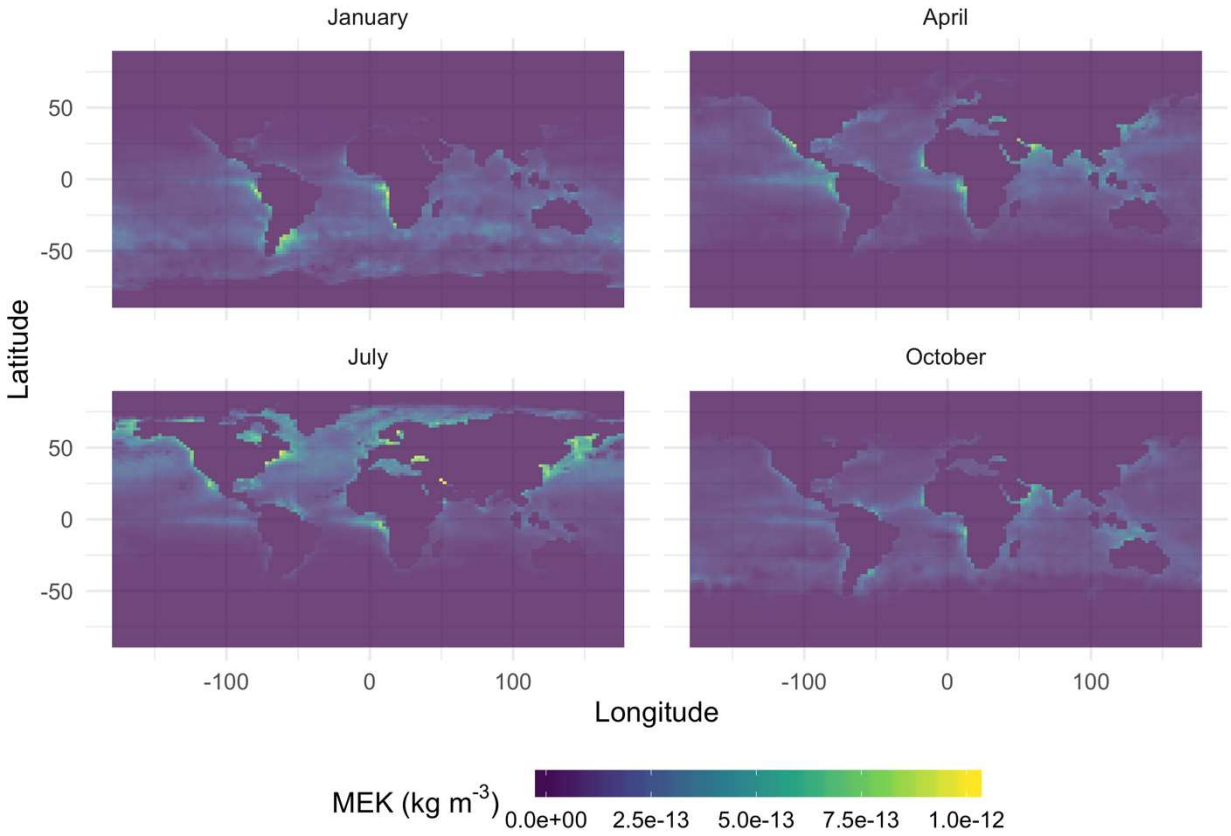

Figure D2. Parameterized monthly MEK seawater concentrations in units of kg m^{-3} for four months.

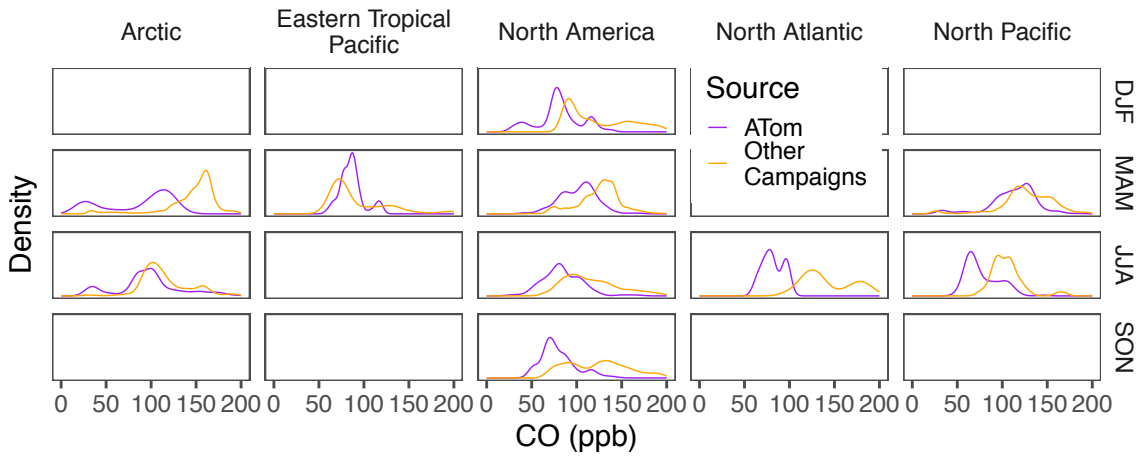

Figure D3. Histograms of CO in ATom (purple) vs non-ATom (orange) field campaigns by region and season. The units of the y-axis are density; the values have been normalized by sample size and are comparable to one another, but the exact numbers are therefore not meaningful and so have not been included here.

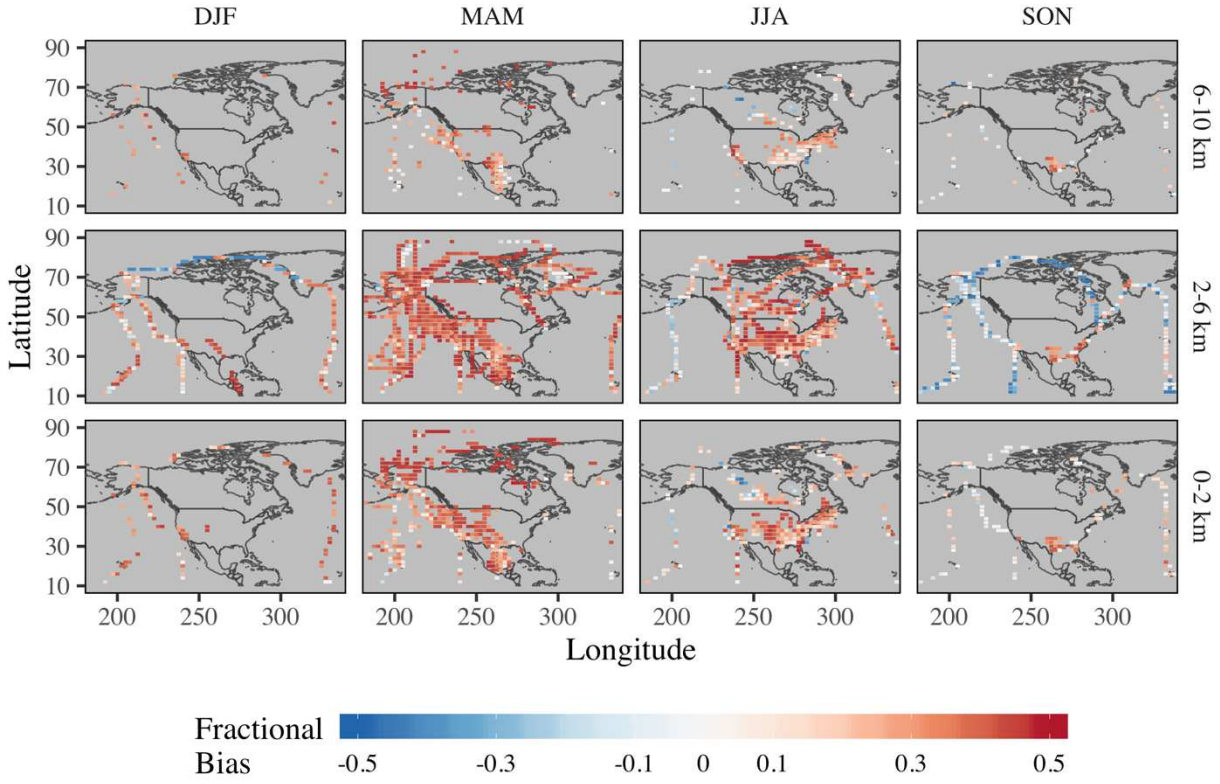

Figure D4. Fractional bias calculated between observed and simulated mixing ratios (in ppt) of atmospheric MEK for four seasons and three altitude bins over the North American region (20º - 180º W, 10º - 90º N). The observations are from aircraft campaigns over a range of years and are gridded to the GEOS-Chem 2º x 2.5º grid, and vertically averaged. Simulated mixing ratios are for 2016 and use the ALK4 alkane scheme. Aircraft campaign details are provided in Table 2.

Table D1. Speciation ratios of *i*-butane/*n*-butane and *i*-pentane/*n*-pentane used to speciate >C_3 alkane emissions by sector.

Study	Sector	i/n-butane ratio	i/n-pentane ratio
Gilman et al., 2013	Oil & Natural Gas	0.43	0.89
Fraser et al., 1998	Transportation	0.10	2.45
Rossabi & Helmig, 2017	Others	0.52	1.81

Table D2. Emissions factors used in the implementation of GFED into GEOS-Chem in units of kg C per kg fuel burned. Unless otherwise noted, all emission factors are taken from Akagi et al. (2011). These data were supplemented with values from Andreae (2019) and from the pre-existing GEOS-Chem implementation where necessary.

Emission Factor	i-Butane	n-Butane	i-Pentane	n-Pentane	n-Hexane	MEK
Agriculture Waste	2.5×10^{-5}	7.2×10^{-5}	2.0×10^{-5}	2.5×10^{-5}	[a]3.2×10^{-5}	[a]5.8×10^{-4}
Deforestation	1.4×10^{-5}	4.0×10^{-5}	7.4×10^{-6}	5.6×10^{-6}	[b]3.2×10^{-5}	9.4×10^{-4}
Boreal Forest	4.2×10^{-5}	1.2×10^{-4}	3.8×10^{-5}	8.5×10^{-5}	5.5×10^{-5}	2.2×10^{-4}
Peat	[a]9.0×10^{-5}	[a]3.2×10^{-5}	[a]1.23×10^{-4}	[a]2.4×10^{-5}	[a]1.4×10^{-4}	[a]3.4×10^{-4}
Savanna	4.3×10^{-6}	1.6×10^{-5}	2.2×10^{-6}	3.2×10^{-6}	1.3×10^{-5}	[a]1.3×10^{-4}
Temperate Forest	[a]3.1×10^{-5}	[a]8.0×10^{-5}	[a]1.7×10^{-5}	[a]3.4×10^{-5}	[a]3.2×10^{-5}	[c]2.2×10^{-4}

[a]Emission factors from Andreae (2019)
[b]Assume the same emission factor for n-hexane from agricultural waste burning, from Andreae (2019)
[c]Emission factor for MEK from Boreal Forest used to represent Temperate Forest (Akagi et al., 2011)

Code D1

```
{ Custom.eqn

-------------------------------------------------------------------------------
DESCRIPTION
-------------------------------------------------------------------------------

GEOS-Chem KPP tropchem chemistry file containing species and equations for
the NOx-Ox-HC-Aer-Br-Cl-I mechanism applied from the surface to the tropopause.

================================================================================
==========
FILE HISTORY
================================================================================
==========

v11-01g (Sep 2016)
----------------------

 (1) Initial version for FlexChem (MSL,MJE,MPS,EWL)

v11-02a (Mar 2017)
----------------------

 (1) Update rate constants based on JPL 15-10 (MJE,BHH)
    - See wiki.geos-chem.org/Updates_in_JPL_Publication_15-10
 (2) Fix ALK4 lumping issue in R4O2 + NO reaction (BHH)
 (3) PAN chemistry updates (EVF)
    - Added several new NMVOCs. The extended mechanism includes ethanol,
      benzene, toluene and ethylbenzene (lumped), xylenes and trimethyl
      benzenes (lumped), and monoterpenes (lumped).
    - Treatment of monoterpene oxidation is adopted from theRACM2 chemical
      mechanism (Goliff et al., 2013), lumping terpenes with one double bond
      (alpha-pinene, beta-pinene, sabinene, delta-3-carene) into one proxy.

v11-02c (Jul 2017)
----------------------

 (1) Add isoprene SOA updates from Marais2016 (EAM,MPS)
 (2) Update isoprene and monoterpene chemistry (KRT,JAF,CCM,EAM,KHB,RHS)
     - Based on Travis2016, Fisher2016, ChanMiller2017, Marais2016
     - Add Bates2014 epoxide scheme
     - Update isoprene nitrate chemistry following Lee2014
```

- Add Muller2014 fast photolysis of carbonyl nitrates
- Add HNO2 chemistry from Lee2014
- Updated product yields and rx rate for RIO2+RIO2 (Xie2013)

(3) Add fixes for carbon-creating reactions (SAS,BHH,MJE)

v11-02d (Sep 2017)
---

(1) Add halogen chemistry from Sherwen2016b/Sherwen2017 (TS,JAS,SDE,LZHU)
(2) Add HOBr + S(IV) from Chen2017 (QJC)

==========
DEVELOPERS (alphabetical order; add your name!)
==========

BHH : Barron Henderson; barronh@gmail.com
CCM : Christopher Chan Miller; cmiller@fas.harvard.edu
DBM : Dylan Millet dbm@umn.edu
EAM : Eloise Marais; e.a.marais@bham.ac.uk
ECB : Ellie Browne eleanor.browne@colorado.edu
EVF : Emily Fischer; evf@rams.colostate.edu
EWL : Lizzie Lundgren; elundgren@seas.harvard.edu
FP : Fabien Paulot; fabien.paulot@noaa.gov
HOTP: Havala Pye; pye.havala@epa.gov
JAF : Jenny Fisher; jennyf@uow.edu.au
JAS : Johan Schmidt; johanalbrechtschmidt@gmail.com
JMAO: Jingqiu Mao; jmao2@alaska.edu
JPP : Justin Parrella; justin.parrella@gmail.com
KHB : Kelvin Bates; kelvin@caltech.edu
KRT : Katie Travis; ktravis@fas.harvard.edu
LZHU: Lei Zhu; leizhu@fas.harvard.edu
MJE : Mat Evans; mat.evans@york.ac.uk
MPS : Melissa Sulprizio; mpayer@seas.harvard.edu
MSL : Mike Long; mlong@seas.harvard.edu
QJC : Qianjie Chen; chenqjie@uw.edu
RHS : Rebecca Schwantes; rschwant@caltech.edu
SAS : Sarah Safieddine; sarahsaf@mit.edu
SDE : Sebastian Eastham; seastham@seas.harvard.edu
TMS : Tomas Sherwen; tomas.sherwen@york.ac.uk
JFB : Jared Brewer jfbrewer@colostate.edu

==========
REFERENCES (alphabetical order)

==========
* Atkinson2003: Atkinson and Arey, Chem. Rev., doi:10.1021/cr0206420, 2003.
* Bates2014: Bates et al., J. Phys. Chem A, 118, doi:10.1021/jp4107958, 2014.
* Browne2011: Browne et al., Atmos. Chem. Phys., doi:10.5194/acp-11-4209-2011, 2011.
* Browne2014: Browne et al., Atmos. Chem. Phys., doi:10.5194/acp-14-1225-2014, 2014.
* Chen2017: Chen et al., Geophys. Res. Lett., doi:10.1002/2017GL073812, 2017.
* Crounse2012: Crounse et al., J. Phys. Chem. A, doi:10.1021/jp211560u, 2012.
* Eastham2014: Eastham et al., Atmos. Env., doi:10.1016/j.atmosenv.2014.02.001, 2014.
* Fischer2014: Fischer et al., Atmos. Chem. Phys., doi:10.5194/acp-14-2679-2014, 2014.
* Fisher2016: Fisher et al., Atmos. Chem. Phys., doi:10.5194/acp-16-5969-2016, 2016.
* Fry2014: Fry et al. Environ. Sci. Technol., doi:10.1021/es502204x, 2014.
* Gill2002: Gill and Hites, J. Phys. Chem. A, doi:10.1021/jp013532, 2002.
* Goliff2013: Goliff et al., Atmos. Environ., doi:10.1016/j.atmosenv.2012.11.038, 2013.
* Jacobs2014: Jacobs et al., Atmos. Chem. Phys., doi:10.5194/acp-14-8933-2014, 2014.
* Jenkin2015: Jenkin et al., Atmos. Chem. Phys., doi:10.5194/acp-15-11433-2015, 2015.
* JPL 10-6: JPL Publication 10-6, https://jpldataeval.jpl.nasa.gov/previous_evaluations.html, 2011.
* JPL 15-10: JPL Publication 15-10, https://jpldataeval.jpl.nasa.gov, 2015.
* Lee2014: Lee et al., J. Phys. Chem. A, doi:10.1021/jp4107603, 2014.
* Marais2016: Marais et al., Atmos. Chem. Phys, doi:10.5194/acp-16-1603-2016, 2016.
* Miller2017: Miller et al., Atmos. Chem. Phys. Discuss., doi:10.5194/acp-2016-1042, 2017.
* Millet2015: Millet et al., Atmos. Chem. Phys., doi:10.5194/acp-15-6283-2015, 2015.
* Muller2014: Muller et al., Atmos. Chem. Phys., doi:10.5194/acp-14-2497-2014, 2014.
* Parrella2012: Parrella et al. Atmos. Chem. Phys, doi:10.5194/acp-12-6723-2012, 2012.
* Paulot2009: Paulot et al., Atmos. Chem. Phys., doi:10.5194/acp-9-1479-2009, 2009a and Paulot et al., Science, doi:10.1126/science.1172910, 2009b.
* Peeters2010: Peeters and Muller, Phys. Chem. Chem. Phys., doi:10.1039/C0CP00811G, 2010.
* Peeters2014: Peeters et al., J. Phys. Chem. A, doi:10.1021/jp5033146, 2014.
* Pye2010: Pye et al., Atmos. Chem. Phys., doi:10.5194/acp-10-11261-2010, 2010.
* Roberts1992: Roberts and Bertman, Int. J. Chem. Kinet., doi:10.1002/kin.550240307, 1992.
* Sherwen2016b: Sherwen et al., Atmos. Chem. Phys., doi:10.5194/acp-16-12239-2016, 2016b.
* Sherwen2017: Sherwen et al., Faraday Discuss., doi:10.1039/C7FD00026J, 2017.
* StClair2016: St. Clair et al., J. Phys. Chem. A, doi:10.1021/acs.jpca.5b065322016, 2016.
* Travis2016: Travis et al., Atmos. Chem. Phys., doi:10.5194/acp-16-13561-2016, 2016.
* Wolfe2012: Wolfe et al., Phys. Chem. Chem. Phys., doi: 10.1039/C2CP40388A, 2012.
* Xie2013: Xie et al., Atmos. Chem. Phys., doi:10.5194/acp-13-8439-2013, 2013.

==========
NOTES
==========

Comment format is
Species - Molecular formula; full name

```
 Equations - Date modified; Reference; Developer initials
}

#include atoms

#DEFVAR

A3O2       = IGNORE; {CH3CH2CH2OO; Primary RO2 from C3H8}
ACET       = IGNORE; {CH3C(O)CH3; Acetone}
ACTA       = IGNORE; {CH3C(O)OH; Acetic acid}
AERI       = IGNORE; {I; Dissolved iodine}
ALD2       = IGNORE; {CH3CHO; Acetaldehyde}
ALK6       = IGNORE; {>= C6 alkanes}    {SPECIATING ALK4 - JFB 11/20/19}
IBUT       = IGNORE; {C4H10; i-BUTANE}  {SPECIATING ALK4 - JFB 11/20/19}
NBUT       = IGNORE; {C4H10; n-BUTANE}  {SPECIATING ALK4 - JFB 11/20/19}
IPENT      = IGNORE; {C5H12; i-PENTANE} {SPECIATING ALK4 - JFB 11/20/19}
NPENT      = IGNORE; {C5H12; n-PENTANE} {SPECIATING ALK4 - JFB 11/20/19}
ATO2       = IGNORE; {CH3C(O)CH2O2; RO2 from acetone}
ATOOH      = IGNORE; {CH3C(O)CH2OOH; ATO2 peroxide}
B3O2       = IGNORE; {CH3CH(OO)CH3; Secondary RO2 from C3H8}
BENZ       = IGNORE; {C6H6; Benzene}
Br         = IGNORE; {Br; Atomic bromine}
Br2        = IGNORE; {Br2; Molecular bromine}
BrCl       = IGNORE; {BrCl; Bromine chloride}
BrO        = IGNORE; {BrO; Bromine monoxide}
BRO2       = IGNORE; {C6H5O2 ; Peroxy radical from BENZ oxidation}
BrNO2      = IGNORE; {BrNO2; Nitryl bromide}
BrNO3      = IGNORE; {BrNO3; Bromine nitrate}
BrSALA     = IGNORE; {Br; Fine sea salt bromine}
BrSALC     = IGNORE; {Br; Course sea salt bromine}
C2H4       = IGNORE; {C2H4; Ethylene}
C2H6       = IGNORE; {C2H6; Ethane}
C3H8       = IGNORE; {C3H8; Propane}
CH2Br2     = IGNORE; {CH3Br2; Dibromomethane}
CH2Cl2     = IGNORE; {CH2Cl2; Dichloromethane}
CH2I2      = IGNORE; {CH2I2; Diiodomethane}
CH2ICl     = IGNORE; {CH2ICl; Chloroiodomethane}
CH2IBr     = IGNORE; {CH2IBr; Bromoiodomethane}
CH2O       = IGNORE; {CH2O; Formaldehyde}
CH2OO      = IGNORE; {CH2OO; Criegee intermediate}
CH3Br      = IGNORE; {CH3Br; Methyl bromide}
CH3CHOO    = IGNORE; {CH3CHOO; Criegee intermediate}
CH3Cl      = IGNORE; {CH3Cl; Chloromethane}
CH3I       = IGNORE; {CH3I; Methyl iodide}
CHBr3      = IGNORE; {CHBr3; Tribromethane}
CHCl3      = IGNORE; {CHCl3; Chloroform}
```

```
Cl        = IGNORE; {Cl; Atomic chlorine}
Cl2       = IGNORE; {Cl2; Molecular chlorine}
Cl2O2     = IGNORE; {Cl2O2; Dichlorine dioxide}
ClNO2     = IGNORE; {ClNO2; Nitryl chloride}
ClNO3     = IGNORE; {ClONO2; Chlorine nitrate}
ClO       = IGNORE; {ClO; Chlorine monoxide}
ClOO      = IGNORE; {ClOO; Chlorine dioxide}
CO        = IGNORE; {CO; Carbon monoxide}
CO2       = IGNORE; {CO2; Carbon dioxide}
DHDN      = IGNORE; {C5H10O8N2; C5 dihydroxydinitrate}
DHDC      = IGNORE; {C5H8O6; Dihydroxyperoxide dicarbonyl}
DHMOB     = IGNORE; {HOCH2C(CH3)(OH)C(=O)CHO; See Paulot et al., ACP, 2009}
DHPCARP   = IGNORE; {C5H9O7; Dihydroxy a-formyl peroxy radical}
DIBOO     = IGNORE; {Dibble peroxy radical}
DMS       = IGNORE; {(CH3)2S; Dimethylsulfide}
EOH       = IGNORE; {C2H5OH; Ethanol}
ETHLN     = IGNORE; {CHOCH2ONO2; Ethanal nitrate}
ETO2      = IGNORE; {CH3CH2OO; Ethylperoxy radical}
ETP       = IGNORE; {CH3CH2OOH; Ethylhydroperoxide}
GAOO      = IGNORE; {Criegee intermediate}
GLYC      = IGNORE; {HOCH2CHO; Glycoaldehyde}
GLYX      = IGNORE; {CHOCHO; Glyoxal}
H2O2      = IGNORE; {H2O2; Hydrogen peroxide}
HAC       = IGNORE; {HOCH2C(O)CH3; Hydroxyacetone}
HBr       = IGNORE; {HBr; Hypobromic acid}
HC187     = IGNORE; {Epoxide oxidation product m/z 187-189}
HC5       = IGNORE; {HOCH2CH=C(CH3)CHO; Hydroxycarbonyl with 5C}
HC5OO     = IGNORE; {Peroxy radical from HC5}
HCl       = IGNORE; {HCl; Hydrochloric acid}
HCOOH     = IGNORE; {HCOOH; Formic acid}
HI        = IGNORE; {HI; Hydrogen iodide}
HNO2      = IGNORE; {HONO; Nitrous acid}
HNO3      = IGNORE; {HNO3; Nitric acid}
HNO4      = IGNORE; {HNO4; Pernitric acid}
HO2       = IGNORE; {HO2; Hydroperoxyl radical}
HOBr      = IGNORE; {HOBr; Hypobromous acid}
HOCl      = IGNORE; {HOCl; Hypochlorous acid}
HOI       = IGNORE; {HOI; Hypoiodous acid}
HONIT     = IGNORE; {2nd gen monoterpene organic nitrate}
HPALD     = IGNORE; {C5H8O3; Hydroperoxyaldehydes}
HPC52O2   = IGNORE; {OOCC(C(C=O)O)(O[O])C}
I         = IGNORE; {I; Atmoic iodine}
I2        = IGNORE; {I2; Molecular iodine}
I2O2      = IGNORE; {I2O2; Diiodine dioxide}
I2O3      = IGNORE; {I2O3; Diiodine trioxide}
I2O4      = IGNORE; {I2O4; Diiodine tetraoxide}
```

IAP = IGNORE; {HOCH2C(CH3)(OOH)CH(OH)CHO; Peroxide from IAO2}
IBr = IGNORE; {IBr; Iodine monobromide}
ICl = IGNORE; {ICl; Iodine monochloride}
IEPOXA = IGNORE; {C5H10O3; trans-Beta isoprene epoxydiol}
IEPOXB = IGNORE; {C5H10O3; cis-Beta isoprene epoxydiol}
IEPOXD = IGNORE; {C5H10O3; Delta isoprene epoxydiol}
IEPOXOO = IGNORE; {RO2 from IEPOX}
IMAE = IGNORE; {C4H6O3; C4 epoxide from oxidation of NPMN}
IMAO3 = IGNORE; {CH2=C(CH3)C(O)OO; Isoprene peroxyacyl from MVK and MACR}
INDIOL = IGNORE; {Generic aerosol phase organonitrate hydrolysis product}
INO2 = IGNORE; {O2NOCH2C(OO)(CH3)CH=CH2; RP2 from IEPOX}
INPN = IGNORE; {O2NOCH2C(OOH)(CH3)CH=CH2; Peroxide from INO2}
INO = IGNORE; {INO; Nitrosyl iodide}
IO = IGNORE; {IO; Iodine monoxide}
IONO = IGNORE; {IONO; Nitryl iodide}
IONO2 = IGNORE; {IONO2; Iodine nitrate}
IONITA = IGNORE; {Aerosol-phase organic nitrate from isoprene precursors}
IPMN = IGNORE; {CH2=C(CH3)C(O)OONO2; Isoprene peroxymethacryloyl nitrate}
IR4N1 = IGNORE; {RO2 from R4N2 from isoprene} {2018/07/16; Speciating C5 Ketone; JFB}
IR4N2 = IGNORE; {RO2NO; >= C4 alkylnitrates from isoprene} {2018/07/16; Speciating C5 Ketone; JFB}
IR4O2 = IGNORE; {RO2 from ALK4 vis Isoprene oxidation} {2018/07/16; Speciating C5 Ketone; JFB}
IR4P = IGNORE; {CH3CH2CH2CH2OOH; Peroxide from R4O2 from Isoprene} {2018/07/16; Speciating C5 Ketone; JFB}
ISALA = IGNORE; {I; Fine sea salt iodine}
ISALC = IGNORE; {I; Coarse sea salt iodine}
ISN1 = IGNORE; {C5H8NO4; Nighttime isoprene nitrate}
ISN1OA = IGNORE; {C5H10O8N2; Aerosol-phase second generation hydroxynitrates formed from ISOP+NO3 pathway}
ISN1OG = IGNORE; {C5H10O8N2; Gas-phase second generation hydroxynitrates formed from ISOP+NO3 pathway}
ISNOOA = IGNORE; {Peroxy radical from ISN1}
ISNOOB = IGNORE; {Peroxy radical from ISN1}
ISNOHOO = IGNORE; {Peroxy radical from ISN1}
ISNP = IGNORE; {HOCH2C(OOH)(CH3)CH(ONO2)CH2OH; Isoprene nitrate}
ISOP = IGNORE; {CH2=C(CH3)CH=CH2; Isoprene}
ISOPNB = IGNORE; {C5H9NO4; Isoprene nitrate Beta}
ISOPNBO2 = IGNORE; {Product of ISOPNB+OH}
ISOPND = IGNORE; {C5H9NO4; Isoprene nitrate Delta}
ISOPNDO2 = IGNORE; {Product of ISOPND+OH}
KET = IGNORE; {RC(O)R; >C4 Ketones} {2018/07/16; Speciating C5 Ketone; JFB}
KETO2 = IGNORE; {RO2 from >C4 ketones} {2018/07/16; Speciating C5 Ketone; JFB}
KO2 = IGNORE; {RO2 from MEK} {2018/07/16; Speciating C5 Ketone; JFB}
LBRO2H = IGNORE; {Dummy spc to track oxidation of BRO2 by HO2}

LBRO2N = IGNORE; {Dummy spc to track oxidation of BRO2 by NO}
LIMO = IGNORE; {C10H16; Limonene}
LIMO2 = IGNORE; {RO2 from LIMO}
LISOPOH = IGNORE; {Dummy spc to track loss of ISOP from rxn with OH}
LISOPNO3 = IGNORE; {Dummy spc to track loss of ISOP from rxn with NO3}
LTRO2H = IGNORE; {Dummy spc to track oxidation of TRO2 by HO2}
LTRO2N = IGNORE; {Dummy spc to track oxidation of TRO2 by NO}
LVOC = IGNORE; {C5H14O5; Gas-phase low-volatility non-IEPOX product of ISOPOOH (RIP) oxidation}
LVOCOA = IGNORE; {C5H14O5; Aerosol-phase low-volatility non-IEPOX product of ISOPOOH (RIP) oxidation}
LXRO2H = IGNORE; {Dummy spc to track oxidation of XRO2 by HO2}
LXRO2N = IGNORE; {Dummy spc to track oxidation of XRO2 by NO}
MACR = IGNORE; {CH2=C(CH3)CHO; Methacrolein}
MACRN = IGNORE; {HOCH2C(ONO2)(CH3)CHO; Nitrate from MACR}
MACRNO2 = IGNORE; {Product of MACRN+OH}
MACROO = IGNORE; {Criegee intermediate}
MAN2 = IGNORE; {HOCH2C(ONO2)(CH3)CHO; RO2 from MACR+NO3}
MAOP = IGNORE; {CH2=C(CH3)C(O)OOH; Peroxide from NMAO3}
MAOPO2 = IGNORE; {CH2OH-CHOO*CH3C(O)OOH; Peroxy radical from MAOP}
MAP = IGNORE; {CH3C(O)OOH; Peroxyacetic acid}
MBO = IGNORE; {Criegee intermediate}
MBOOO = IGNORE; {Criegee intermediate}
MCO3 = IGNORE; {CH3C(O)O; Peroxyacetyl radical}
MEK = IGNORE; {C2H5C(O)CH3; Methyl ethyl ketone} {2018/07/16; Speciating C5 Ketone; JFB}
MEKX = IGNORE; {MEK+Cl Reaction tracer}{2018/12/19, JFB}
MEKY = IGNORE; {MEK+OH Reaction tracer}{2018/12/19, JFB}
MEKZ = IGNORE; {MEK+hv Photolysis tracer}{2018/12/19, JFB}
MGLOO = IGNORE; {Criegee intermediate}
MGLY = IGNORE; {CH3COCHO; Methylglyoxal}
MGLYOO = IGNORE; {Criegee intermediate}
MOBA = IGNORE; {HOC(=O)C(CH3)=CHCHO; 5C acid from isoprene}
MOBAOO = IGNORE; {RO2 from MOBA}
MO2 = IGNORE; {CH3O2; Methylperoxy radical}
MONITA = IGNORE; {Aerosol-phase organic nitrate from monoterpene precursors}
MONITS = IGNORE; {Saturated 1st gen monoterpene organic nitrate}
MONITU = IGNORE; {Unsaturated 1st gen monoterpene organic nitrate}
MP = IGNORE; {CH3OOH; Methylhydroperoxide}
MPN = IGNORE; {CH3O2NO2; Methyl peroxy nitrate}
MRO2 = IGNORE; {HOCH2C(OO)(CH3)CHO; RO2 from MACR+OH}
MRP = IGNORE; {HOCH2C(OOH)(CH3)CHO; Peroxide from MRO2}
MSA = IGNORE; {CH4SO3; Methanesulfonic acid}
MTPA = IGNORE; {Lumped monoterpenes: a-pinene, b-pinene, sabinene, carene}
MTPO = IGNORE; {Other monoterpenes: Terpinene, terpinolene, myrcene, ocimene, other monoterpenes}

MVK = IGNORE; {CH2=CHC(=O)CH3; Methyl vinyl ketone}
MVKN = IGNORE; {HOCH2CH(ONO2)C(=O)CH3; Nitrate from MVK}
MVKOO = IGNORE; {Criegee intermediate}
N2O5 = IGNORE; {N2O5; Dinitrogen pentoxide}
NMAO3 = IGNORE; {CH2=C(CH3)C(O)OO; Non-isoprene peroxyacyl from MVK and MACR}
NO = IGNORE; {NO; Nitric oxide}
NO2 = IGNORE; {NO2; Nitrogen dioxide}
NO3 = IGNORE; {NO3; Nitrate radical}
NPMN = IGNORE; {CH2=C(CH3)C(O)OONO2; Non-isoprene peroxymethacryloyl nitrate}
O1D = IGNORE; {O(1D); Excited atomic oxygen}
O3 = IGNORE; {O3; Ozone}
OClO = IGNORE; {OClO; Chlorine dioxide}
OH = IGNORE; {OH; Hydroxyl radical}
OIO = IGNORE; {OIO; Iodine dioxide}
OLND = IGNORE; {Monoterpene-derived NO3-alkene adduct}
OLNN = IGNORE; {Monoterpene-derived NO3 adduct}
ONIT = IGNORE; {Organic nitrate}
PAN = IGNORE; {CH3C(O)OONO2; Peroxyacetylnitrate}
PIO2 = IGNORE; {RO2 from MTPA}
PIP = IGNORE; {Peroxides from MTPA}
PMNN = IGNORE; {Product of PMNO2+NO}
PMNO2 = IGNORE; {Product of NPMN+OH}
PO2 = IGNORE; {HOCH2CH(OO)CH3; RO2 from isoprene}
PP = IGNORE; {HOCH2CH(OOH)CH3; Peroxide from PO2}
PPN = IGNORE; {CH3CH2C(O)OONO2; Peroxypropionylnitrate}
PRN1 = IGNORE; {O2NOCH2CH(OO)CH3; RO2 from propene + NO3}
PRPE = IGNORE; {C3H6; >= C3 alkenes}
PRPN = IGNORE; {O2NOCH2CH(OOH)CH3; Peroxide from PRN1}
PROPNN = IGNORE; {CH3C(=O)CH2ONO2; Propanone nitrate}
PYAC = IGNORE; {CH3COCOOH; Pyruvic acid}
R6N1 = IGNORE; {RO2 from R6N2} {SPECIATING ALK4 - JFB 11/20/19}
R6N2 = IGNORE; {RO2NO; >= C4 alkylnitrates} {SPECIATING ALK4 - JFB 11/20/19}
R6O2 = IGNORE; {RO2 from ALK6} {SPECIATING ALK4 - JFB 11/20/19}
R6P = IGNORE; {CH3CH2CH2CH2OOH; Peroxide from R6O2}{SPECIATING ALK4 - JFB 11/20/19}
IBN1 = IGNORE; {RO2 from IBN2} {SPECIATING ALK4 - JFB 11/20/19}
IBN2 = IGNORE; {IBUTO2NO; i-BUTANE Akylnitrates} {SPECIATING ALK4 - JFB 11/20/19}
IBO2 = IGNORE; {RO2 from IBUT} {SPECIATING ALK4 - JFB 11/20/19}
IBP = IGNORE; {CH3CH2CH2CH2OOH; Peroxide from IBO2}{SPECIATING ALK4 - JFB 11/20/19}
NBN1 = IGNORE; {RO2 from NBN2} {SPECIATING ALK4 - JFB 11/20/19}
NBN2 = IGNORE; {RO2NO; n-BUTANE alkylnitrates} {SPECIATING ALK4 - JFB 11/20/19}

```
NBO2      = IGNORE; {RO2 from n-BUTANE}                {SPECIATING ALK4 - JFB
11/20/19}
NBP       = IGNORE; {CH3CH2CH2CH2OOH; Peroxide from NBO2}{SPECIATING ALK4 -
JFB 11/20/19}
IPN1      = IGNORE; {RO2 from IPN2}                    {SPECIATING ALK4 - JFB 11/20/19}
IPN2      = IGNORE; {RO2NO; i-PENTANE alkylnitrates}     {SPECIATING ALK4 - JFB
11/20/19}
IPO2      = IGNORE; {RO2 from IPENT}                   {SPECIATING ALK4 - JFB 11/20/19}
IPP       = IGNORE; {CH3CH2CH2CH2OOH; Peroxide from ipO2}{SPECIATING ALK4 -
JFB 11/20/19}
NPN1      = IGNORE; {RO2 from NPN2}                    {SPECIATING ALK4 - JFB 11/20/19}
NPN2      = IGNORE; {RO2NO; n-PENTANE alkylnitrates}     {SPECIATING ALK4 - JFB
11/20/19}
NPO2      = IGNORE; {RO2 from NPENT}                   {SPECIATING ALK4 - JFB 11/20/19}
NPP       = IGNORE; {CH3CH2CH2CH2OOH; Peroxide from NPO2}
RA3P      = IGNORE; {CH3CH2CH2OOH; Peroxide from A3O2}
RB3P      = IGNORE; {CH3CH(OOH)CH3; Peroxide from B3O2}
RCHO      = IGNORE; {CH3CH2CHO; >= C3 aldehydes}
RCO3      = IGNORE; {CH3CH2C(O)OO; Peroxypropionyl radical}
RIO2      = IGNORE; {HOCH2C(OO)(CH3)CH=CH2; RO2 from isoprene, aka ISOPO2}
RIPA      = IGNORE; {HOCH2C(OOH)(CH3)CH=CH2; 1,2-ISOPOOH}
RIPB      = IGNORE; {HOCH2C(OOH)(CH3)CH=CH2; 4,3-ISOPOOH}
RIPD      = IGNORE; {HOCH2C(OOH)(CH3)CH=CH2; d(1,4 and 4,1)-ISOPOOH}
ROH       = IGNORE; {C3H7OH; > C2 alcohols}
RP        = IGNORE; {CH3CH2C(O)OOH; Peroxide from RCO3}
SO2       = IGNORE; {SO2; Sulfur dioxide}
SO4       = IGNORE; {SO4; Sulfate}
SO4H1     = IGNORE; {SO4; Sulfate produced by HOBr}
SO4H2     = IGNORE; {SO4; Sulfate produced by HOBr}
SOAGX     = IGNORE; {CHOCHO; Aerosol-phase glyoxal}
SOAIE     = IGNORE; {C5H10O3; Aerosol-phase IEPOX}
SOAME     = IGNORE; {C4H6O3; Aerosol-phase IMAE}
SOAMG     = IGNORE; {CH3COCHO; Aerosol-phase methylglyoxal}
TOLU      = IGNORE; {C7H8; Toluene}
TRO2      = IGNORE; {Peroxy radical from TOLU oxidation}
VRO2      = IGNORE; {HOCH2CH(OO)C(O)CH3; RO2 from MVK+OH}
VRP       = IGNORE; {HOCH2CH(OOH)C(O)CH3; Peroxide from VRO2}
XYLE      = IGNORE; {C8H10; Xylene}
XRO2      = IGNORE; {Peroxy radical from XYLE oxidation}

#DEFFIX

CH4       = IGNORE; {CH4; Methane}
H         = IGNORE; {H; Atomic hydrogen}
H2        = IGNORE; {H2; Molecular hydrogen}
H2O       = IGNORE; {H2O; Water vapor}
```

```
MNO3      = IGNORE; {CH3ONO2; Methylnitrate}
MOH       = IGNORE; {CH3OH; Methanol}
N2        = IGNORE; {N2; Molecular nitrogen}
NH2       = IGNORE; {NH2; Ammonia radical}
NH3       = IGNORE; {NH3; Ammonia}
O         = IGNORE; {O(3P); Ground state atomic oxygen}
O2        = IGNORE; {O2; Molecular oxygen}
RCOOH     = IGNORE; {C2H5C(O)OH; > C2 organic acids}

#EQUATIONS
//
// Gas-phase reactions
//
O3 + NO = NO2 + O2 :                    GCARR(3.00E-12, 0.0E+00, -1500.0);
O3 + OH = HO2 + O2 :                    GCARR(1.70E-12, 0.0E+00, -940.0);
O3 + HO2 = OH + O2 + O2 :               GCARR(1.00E-14, 0.0E+00, -490.0);
O3 + NO2 = O2 + NO3 :                   GCARR(1.20E-13, 0.0E+00, -2450.0);
O3 + MO2 = CH2O + HO2 + O2 :            GCARR(2.90E-16, 0.0E+00, -1000.0);
{2014/02/03; Eastham2014; SDE}
OH + OH = H2O + O3 :                    GCARR(1.80E-12, 0.0E+00, 0.0);
OH + OH {+M} = H2O2 :                   GCJPLPR(6.90E-31, 1.0E+00, 0.0, 2.6E-11, 0.0, 0.0,
0.6, 0.0, 0.0);
OH + HO2 = H2O + O2 :                   GCARR(4.80E-11, 0.0E+00, 250.0);
OH + H2O2 = H2O + HO2 :                 GCARR(1.80E-12, 0.0E+00, 0.0);
HO2 + NO = OH + NO2 :                   GCARR(3.30E-12, 0.0E+00, 270.0);     {2013/02/12;
JPL 10-6; BHH,JMAO,EAM}
HO2 + HO2 = H2O2 + O2 :                 GC_HO2NO3(3.00E-13, 0.0E+00, 460.0, 2.1E-33, 0.0,
920.0); {2014/02/03; Eastham2014; SDE}
OH + H2 = H2O + HO2 :                   GCARR(2.80E-12, 0.0E+00, -1800.0);
OH + CO = HO2 + CO2 :                   GC_OHCO(1.50E-13, 0.0E+00, 0.0);     {2017/02/22;
JPL 15-10; BHH,MJE}
OH + CH4 = MO2 + H2O :                  GCARR(2.45E-12, 0.0E+00, -1775.0);
MO2 + NO = CH2O + HO2 + NO2 :           GCARR(2.80E-12, 0.0E+00, 300.0);
MO2 + HO2 = MP + O2 :                   GCARR(4.10E-13, 0.0E+00, 750.0);
MO2 + MO2 = MOH + CH2O + O2 :           GC_TBRANCH(9.50E-14, 0.0E+00, 390.0,
2.62E1, 0.0, -1130.0);
MO2 + MO2 = 2.000CH2O + 2.000HO2 :      GC_TBRANCH(9.50E-14, 0.0E+00, 390.0,
4.E-2, 0.0, 1130.0);
MP + OH = MO2 + H2O :                   GCARR(2.66E-12, 0.0E+00, 200.0);
MP + OH = CH2O + OH + H2O :             GCARR(1.14E-12, 0.0E+00, 200.0);
ATOOH + OH = ATO2 + H2O :               GCARR(2.66E-12, 0.0E+00, 200.0);
{2013/03/22; Paulot2009; FP,EAM,JMAO,MJE}
ATOOH + OH = MGLY + OH + H2O :          GCARR(1.14E-12, 0.0E+00, 200.0);
{2013/03/22; Paulot2009; FP,EAM,JMAO,MJE}
CH2O + OH = CO + HO2 + H2O :            GCARR(5.50E-12, 0.0E+00, 125.0);
```

```
NO2 + OH {+M} = HNO3 {+M} :              GCJPLPR(1.80E-30, 3.0E+00, 0.0, 2.8E-11, 0.0,
0.0, 0.6, 0.0, 0.0);
HNO3 + OH = H2O + NO3 :                  GC_OHHNO3(2.41E-14, 0.0E+00, 460.0, 2.69E-17,
0.E0, 2199., 6.51E-34, 0.E0, 1335.0);
NO + OH {+M} = HNO2 {+M} :               GCJPLPR(7.00E-31, 2.6E+00, 0.0, 3.60E-11, 0.1,
0.0, 0.6, 0.0, 0.0);
HNO2 + OH = H2O + NO2 :                  GCARR(1.80E-11, 0.0E+00, -390.0);
HO2 + NO2 {+M} = HNO4 {+M} :             GCJPLPR(1.90E-31, 3.4E+00, 0.0, 4.0e-12, 0.3,
0.0, 0.6, 0.0, 0.0); {2017/02/22; JPL 15-10; BHH,MJE}
HNO4 {+M} = HO2 + NO2 :                  GCJPLPR(9.05E-05, 3.4E+00, -10900.0, 1.90E15,
0.3, -10900.0, 0.6, 0.0, 0.0); {2017/02/22; JPL 15-10; BHH,MJE}
HNO4 + OH = H2O + NO2 + O2 :             GCARR(1.30E-12, 0.0E+00, 380.0);
HO2 + NO3 = OH + NO2 + O2 :              GCARR(3.50E-12, 0.0E+00, 0.0);
NO + NO3 = 2.000NO2 :                    GCARR(1.50E-11, 0.0E+00, 170.0);
OH + NO3 = HO2 + NO2 :                   GCARR(2.20E-11, 0.0E+00, 0.0);
NO2 + NO3 {+M} = N2O5 {+M} :             GCJPLPR(2.40E-30, 3.0E+00, 0.0, 1.6E-12, -0.1,
0.0, 0.6, 0.0, 0.0 ); {2017/02/22; JPL 15-10; BHH,MJE}
N2O5 {+M} = NO2 + NO3 :                  GCJPLPR(4.14E-04, 3.0E+00, -10840.0, 2.76E14, -
0.1, -10840.0, 0.6, 0.0, 0.0 ); {2017/02/22; JPL 15-10; BHH,MJE}
HCOOH + OH = H2O + CO2 + HO2 :           GCARR(4.00E-13, 0.0E+00, 0.0);
{2013/03/22; Paulot2009; FP,EAM,JMAO,MJE}
MOH + OH = HO2 + CH2O :                  GCARR(2.90E-12, 0.0E+00, -345.0);
NO2 + NO3 = NO + NO2 + O2 :              GCARR(4.50E-14, 0.0E+00, -1260.0);
NO3 + CH2O = HNO3 + HO2 + CO :           GCARR(5.80E-16, 0.0E+00, 0.0);
ALD2 + OH = 0.950MCO3 + 0.050CH2O +
 0.050CO + 0.050HO2 + H2O :              GCARR(4.63E-12, 0.0E+00, 350.0);    {2014/02/03;
Eastham2014; SDE}
ALD2 + NO3 = HNO3 + MCO3 :               GCARR(1.40E-12, 0.0E+00, -1900.0);
MCO3 + NO2 {+M} = PAN :                  GCJPLPR(9.70E-29, 5.6E+00, 0.0, 9.3E-12, 1.5E0,
0.0, 0.6, 0.0, 0.0); {JPL Eval 17}
PAN = MCO3 + NO2 :                       GCJPLEQ(9.30E-29, 0.0E+00, 14000.0, 9.7E-29, 5.6E0,
0.0, 9.3E-12, 1.5E0, 0., 0.6, 0., 0.);
MCO3 + NO = MO2 + NO2 + CO2 :            GCARR(8.10E-12, 0.0E+00, 270.0);
C2H6 + OH = ETO2 + H2O :                 GCARR(7.66E-12, 0.0E+00, -1020.0);   {2013/02/12;
JPL 10-6; BHH,JMAO,EAM}
ETO2 + NO = ALD2 + NO2 + HO2 :           GCARR(2.60E-12, 0.0E+00, 365.0);
C3H8 + OH = B3O2 :                       GC_TBRANCH(7.60E-12, 0.0E+00, -585.0, 5.87E0,
0.64E0, -816.0);
C3H8 + OH = A3O2 :                       GC_TBRANCH(7.60E-12, 0.0E+00, -585.0, 1.7E-1, -
0.64E0, 816.0);
A3O2 + NO = NO2 + HO2 + RCHO :           GCARR(2.90E-12, 0.0E+00, 350.0);
PO2 + NO = NO2 + HO2 + CH2O + ALD2 :     GCARR(2.70E-12, 0.0E+00, 350.0);
ALK6 + OH = R6O2 :                       GCARR(9.10E-12, 0.0E+00, -405.0);
R6O2 + NO = NO2 + 0.320ACET + 0.019MEK +
 0.190MO2 + 0.270HO2 + 0.320ALD2 +
 0.140RCHO + 0.050A3O2 + 0.180B3O2 +
```

```
 0.320ETO2 + 0.171KET :                    GC_RO2NO('B', 2.70E-12, 0.0E+00, 350.0, 4.5E0, 0.0,
0.0); {2017/02/23; ALK6 lumping fix; BHH}
R6O2 + NO = R6N2 :                        GC_RO2NO('A', 2.70E-12, 0.0E+00, 350.0, 4.5E0, 0.0,
0.0);
R6N1 + NO = 2.000NO2 + 0.570RCHO +
 0.860ALD2 + 0.570CH2O :                   GCARR(2.70E-12, 0.0E+00, 350.0);     {2017/07/27;
Fix C creation; SAS,BHH,MJE}
IBUT + OH = IBO2 :                        GCARR(9.10E-12, 0.0E+00, -405.0);      {2019/11/21;
Speciate Alk4; JFB}
IBO2 + NO = NO2 + 0.415ACET +
 0.190MO2 + 0.270HO2 + 0.415ALD2 +
 0.140RCHO + 0.050A3O2 + 0.180B3O2 +
 0.320ETO2 :                               GC_RO2NO('B', 2.70E-12, 0.0E+00, 350.0, 4.5E0, 0.0, 0.0);
{2017/02/23; ALK4 lumping fix; BHH} {2019/11/21; Speciate Alk4; JFB}
IBO2 + NO = IBN2 :                        GC_RO2NO('A', 2.70E-12, 0.0E+00, 350.0, 4.5E0, 0.0,
0.0); {2019/11/21; Speciate Alk4; JFB}
IBN1 + NO = 2.000NO2 + 0.570RCHO +
 0.860ALD2 + 0.570CH2O :                   GCARR(2.70E-12, 0.0E+00, 350.0);     {2017/07/27;
Fix C creation; SAS,BHH,MJE}       {2019/11/21; Speciate Alk4; JFB}
NBUT + OH = NBO2 :                        GCARR(9.10E-12, 0.0E+00, -405.0);      {2019/11/21;
Speciate Alk4; JFB}
NBO2 + NO = NO2 + 0.320ACET + 0.190MEK +
 0.190MO2 + 0.270HO2 + 0.320ALD2 +
 0.140RCHO + 0.050A3O2 + 0.180B3O2 +
 0.320ETO2 :                               GC_RO2NO('B', 2.70E-12, 0.0E+00, 350.0, 4.5E0, 0.0, 0.0);
{2017/02/23; ALK4 lumping fix; BHH} {2019/11/21; Speciate Alk4; JFB}
NBO2 + NO = NBN2 :                        GC_RO2NO('A', 2.70E-12, 0.0E+00, 350.0, 4.5E0, 0.0,
0.0); {2019/11/21; Speciate Alk4; JFB}
NBN1 + NO = 2.000NO2 + 0.570RCHO +
 0.860ALD2 + 0.570CH2O :                   GCARR(2.70E-12, 0.0E+00, 350.0);     {2017/07/27;
Fix C creation; SAS,BHH,MJE}       {2019/11/21; Speciate Alk4; JFB}
IPENT + OH = IPO2 :                       GCARR(9.10E-12, 0.0E+00, -405.0);      {2019/11/21;
Speciate Alk4; JFB}
IPO2 + NO = NO2 + 0.320ACET + 0.019MEK +
 0.190MO2 + 0.270HO2 + 0.320ALD2 +
 0.140RCHO + 0.050A3O2 + 0.180B3O2 +
 0.320ETO2 + 0.171KET :                    GC_RO2NO('B', 2.70E-12, 0.0E+00, 350.0, 4.5E0, 0.0,
0.0); {2017/02/23; ALK4 lumping fix; BHH} {2019/11/21; Speciate Alk4; JFB}
IPO2 + NO = IPN2 :                        GC_RO2NO('A', 2.70E-12, 0.0E+00, 350.0, 4.5E0, 0.0,
0.0); {2019/11/21; Speciate Alk4; JFB}
IPN1 + NO = 2.000NO2 + 0.570RCHO +
 0.860ALD2 + 0.570CH2O :                   GCARR(2.70E-12, 0.0E+00, 350.0);     {2017/07/27;
Fix C creation; SAS,BHH,MJE}       {2019/11/21; Speciate Alk4; JFB}
NPENT + OH = NPO2 :                       GCARR(9.10E-12, 0.0E+00, -405.0);      {2019/11/21;
Speciate Alk4; JFB}
NPO2 + NO = NO2 + 0.320ACET + 0.190KET +
```

```
 0.190MO2 + 0.270HO2 + 0.320ALD2 +
 0.140RCHO + 0.050A3O2 + 0.180B3O2 +
 0.320ETO2 :                    GC_RO2NO('B', 2.70E-12, 0.0E+00, 350.0, 4.5E0, 0.0, 0.0);
{2017/02/23; ALK4 lumping fix; BHH} {2019/11/21; Speciate Alk4; JFB}
NPO2 + NO = NPN2 :              GC_RO2NO('A', 2.70E-12, 0.0E+00, 350.0, 4.5E0, 0.0,
0.0); {2019/11/21; Speciate Alk4; JFB}
NPN1 + NO = 2.000NO2 + 0.570RCHO +
 0.860ALD2 + 0.570CH2O :        GCARR(2.70E-12, 0.0E+00, 350.0);    {2017/07/27;
Fix C creation; SAS,BHH,MJE}    {2019/11/21; Speciate Alk4; JFB}
IR4O2 + NO = NO2 + 0.320ACET + 0.190KET +
 0.190MO2 + 0.270HO2 + 0.320ALD2 +
 0.140RCHO + 0.050A3O2 + 0.180B3O2 +
 0.320ETO2 :                    GC_RO2NO('B', 2.70E-12, 0.0E+00, 350.0, 4.5E0, 0.0, 0.0);
{2017/02/23; ALK6 lumping fix; BHH} {2018/07/16; Speciating C5 Ketone; JFB}
IR4O2 + NO = IR4N2 :            GC_RO2NO('A', 2.70E-12, 0.0E+00, 350.0, 4.5E0, 0.0,
0.0); {2018/07/16; Speciating C5 Ketone; JFB}
IR4N1 + NO = 2.000NO2 + 0.570RCHO +
 0.860ALD2 + 0.570CH2O :        GCARR(2.70E-12, 0.0E+00, 350.0);    {2017/07/27;
Fix C creation; SAS,BHH,MJE} {2018/07/16; Speciating C5 Ketone; JFB}
ATO2 + NO = NO2 + CH2O + MCO3 :     GCARR(2.80E-12, 0.0E+00, 300.0);
{2017/07/27; Fix C creation; SAS,BHH,MJE}
KO2 + NO = 0.930NO2 + 0.930ALD2 +
 0.930MCO3 + 0.070IR4N2 :       GCARR(2.70E-12, 0.0E+00, 350.0);
KETO2 + NO = 0.77HO2 + 0.23MCO3 +
 NO2 + 0.46ALD2 + 0.54MGLY :        GCARR(2.70E-12, 0.0E+00, 350.0);
{2018/07/16; Speciating C5 Ketone; JFB}
RIO2 + NO = 0.910NO2 + 0.820HO2 +
 0.820CH2O + 0.476MVK + 0.344MACR +
 0.058HC5 + 0.030DIBOO + 0.009ISOPND +
 0.081ISOPNB :                  GCARR(2.70E-12, 0.0E+00, 350.0);    {2017/07/14;
Fisher2016; KRT,JAF,CCM,EAM,KHB,RHS}
RIO2 = 0.500HPALD + 0.500DHPCARP :  GCARR(4.07E+08, 0.0E+00, -7694.0);
{2017/07/14; Peeters2014; KRT,JAF,CCM,EAM,KHB,RHS}
VRO2 + NO = 0.880NO2 + 0.350HO2 +
 0.350CH2O + 0.530MCO3 + 0.530GLYC +
 0.350MGLY + 0.120MVKN :        GCARR(2.70E-12, 0.0E+00, 350.0);    {2013/03/22;
Paulot2009; FP,EAM,JMAO,MJE}
MRO2 + NO = 0.850NO2 + 0.850HO2 +
 0.122MGLY + 0.728HAC + 0.728CO +
 0.122CH2O + 0.150MACRN :       GCARR(2.70E-12, 0.0E+00, 350.0);    {2013/03/22;
Paulot2009; FP,EAM,JMAO,MJE}
MRO2 = CO + HAC + OH :          GCARR(2.90E+07, 0.0E+00, -5297.0);
{2013/03/22; Paulot2009; FP,EAM,JMAO,MJE}
MAN2 + NO = 1.500NO2 + 0.500CH2O +
 0.500MGLY + 0.500PROPNN + 0.500CO +
```

0.500OH : GCARR(2.70E-12, 0.0E+00, 350.0); {2013/03/22;
Paulot2009; FP,EAM,JMAO,MJE}
B3O2 + NO = NO2 + HO2 + ACET : GCARR(2.70E-12, 0.0E+00, 350.0);
INO2 + NO = 1.300NO2 + 0.800HO2 +
0.700ISN1 + 0.230HC5 + 0.035MACR +
0.070CH2O + 0.035MVK : GCARR(2.70E-12, 0.0E+00, 350.0); {2013/03/22;
Paulot2009; FP,EAM,JMAO,MJE}
INO2 + NO3 = 1.300NO2 + 0.800HO2 +
0.700ISN1 + 0.230HC5 + 0.035MACR +
0.070CH2O + 0.035MVK : GCARR(2.30E-12, 0.0E+00, 0.0); {2013/03/22;
Paulot2009; FP,EAM,JMAO,MJE}
ISN1 + NO3 = 0.600ISNOOA + 0.400ISNOOB +
0.600HNO3 : GCARR(3.15E-13, 0.0E+00, -448.0); {2013/03/22;
Paulot2009; FP,EAM,JMAO,MJE}
ISNOOA + NO3 = NO2 + 0.960PROPNN + CO +
HO2 + 0.040ISN1OG : GCARR(4.00E-12, 0.0E+00, 0.0); {2017/07/14;
Fisher2016; KRT,JAF,CCM,EAM,KHB,RHS}
ISNOOA + NO = NO2 + 0.960PROPNN + CO +
HO2 + 0.040ISN1OG : GCARR(6.70E-12, 0.0E+00, 340.0); {2017/07/14;
Fisher2016; KRT,JAF,CCM,EAM,KHB,RHS}
ISNOOA + NO2 {+M} = 0.960IPMN +
0.040ISN1OG : GCJPLPR(9.00E-28, 8.9E+00, 0.0, 7.7E-12, 0.2, 0.0, 0.6,
0.0, 0.0); {2017/06/14; Marais2016; EAM}
ISNOOA + HO2 = 0.750RP + 0.250RCOOH +
0.250O3 + 0.960NO2 + 0.040ISN1OG : GCARR(5.20E-13, 0.0E+00, 980.0);
{2017/07/14; Fisher2016; KRT,JAF,CCM,EAM,KHB,RHS}
ISNOOB + NO3 = 0.940PROPNN + GLYX +
2.000NO2 + 0.040ISN1OG : GCARR(2.30E-12, 0.0E+00, 0.0); {2017/07/14;
Fisher2016; KRT,JAF,CCM,EAM,KHB,RHS}
ISNOOB + NO = 0.900PROPNN + 0.940GLYX +
1.880NO2 + 0.040ISN1OG : GCARR(2.60E-12, 0.0E+00, 380.0); {2017/07/14;
Fisher2016; KRT,JAF,CCM,EAM,KHB,RHS}
ISNOOB + HO2 = 0.960INPN + 0.040ISN1OG : GCARR(2.06E-13, 0.0E+00, 1300.0);
{2017/07/14; Fisher2016; KRT,JAF,CCM,EAM,KHB,RHS}
ISNOOB + MO2 = 0.660PROPNN + 0.700GLYX +
0.700NO2 + 0.750CH2O + 0.250MOH +
0.500HO2 + 0.040ISN1OG : GCARR(2.00E-13, 0.0E+00, 0.0); {2017/07/14;
Fisher2016; KRT,JAF,CCM,EAM,KHB,RHS}
ISN1 + O3 = 0.300PROPNN + 0.700GLYX +
0.700NO2 + 0.250CH2O + 0.250MOH +
0.500HO2 + 0.500CH2O : GCARR(4.15E-15, 0.0E+00, -1520.0); {2017/07/14;
Fisher2016; KRT,JAF,CCM,EAM,KHB,RHS}
ISN1 + OH = 0.345ISNOOA + 0.655ISNOHOO : GCARR(7.48E-12, 0.0E+00, 410.0);
{2013/03/22; Paulot2009; FP,EAM,JMAO,MJE}
ISNOHOO + NO = 0.894PROPNN + 0.934HO2 +

0.919GLYX + 0.0400ISN1OG : GCARR(2.60E-12, 0.0E+00, 380.0); {2017/07/14; Fisher2016; KRT,JAF,CCM,EAM,KHB,RHS}
ISNOHOO + HO2 = 0.960INPN + 0.040ISN1OG : GCARR(2.06E-13, 0.0E+00, 1300.0); {2017/07/14; Fisher2016; KRT,JAF,CCM,EAM,KHB,RHS}
ISNOHOO + MO2 = 0.660PROPNN + 0.700GLYX +
1.200HO2 + 0.750CH2O + 0.250MOH +
0.040ISN1OG : GCARR(2.06E-13, 0.0E+00, 0.0); {2017/07/14; Fisher2016; KRT,JAF,CCM,EAM,KHB,RHS}
INO2 + INO2 = 0.300NO2 + 0.800HO2 +
0.700ISN1 + 0.230HC5 + 0.035MACR +
0.070CH2O + 0.035MVK + 0.500ISN1 +
0.500ISOPND : GCARR(1.20E-12, 0.0E+00, 0.0); {2013/03/22; Paulot2009; FP,EAM,JMAO,MJE}
PRN1 + NO = 2.000NO2 + CH2O + ALD2 : GCARR(2.70E-12, 0.0E+00, 350.0);
ALK6 + NO3 = HNO3 + R6O2 : GCARR(2.80E-12, 0.0E+00, -3280.0);
R6N2 + OH = R6N1 + H2O : GCARR(1.60E-12, 0.0E+00, 0.0);
IBUT + NO3 = HNO3 + IBO2 : GCARR(2.80E-12, 0.0E+00, -3280.0); {2019/11/21; Speciate Alk4; JFB}
IBN2 + OH = IBN1 + H2O : GCARR(1.60E-12, 0.0E+00, 0.0); {2019/11/21; Speciate Alk4; JFB}
NBUT + NO3 = HNO3 + NBO2 : GCARR(2.80E-12, 0.0E+00, -3280.0); {2019/11/21; Speciate Alk4; JFB}
NBN2 + OH = NBN1 + H2O : GCARR(1.60E-12, 0.0E+00, 0.0); {2019/11/21; Speciate Alk4; JFB}
IPENT + NO3 = HNO3 + IPO2 : GCARR(2.80E-12, 0.0E+00, -3280.0); {2019/11/21; Speciate Alk4; JFB}
IPN2 + OH = IPN1 + H2O : GCARR(1.60E-12, 0.0E+00, 0.0); {2019/11/21; Speciate Alk4; JFB}
NPENT + NO3 = HNO3 + NPO2 : GCARR(2.80E-12, 0.0E+00, -3280.0); {2019/11/21; Speciate Alk4; JFB}
NPN2 + OH = NPN1 + H2O : GCARR(1.60E-12, 0.0E+00, 0.0); {2019/11/21; Speciate Alk4; JFB}
IR4N2 + OH = IR4N1 + H2O : GCARR(1.60E-12, 0.0E+00, 0.0); {2018/07/16; Speciating C5 Ketone; JFB}
ACTA + OH = MO2 + CO2 + H2O : GCARR(3.15E-14, 0.0E+00, 920.0); {2013/02/12; JPL 10-6; BHH,JMAO,EAM}
OH + RCHO = RCO3 + H2O : GCARR(6.00E-12, 0.0E+00, 410.0);
RCO3 + NO2 {+M} = PPN : GCJPLPR(9.00E-28, 8.9E+00, 0.0, 7.7E-12, 0.2, 0.0, 0.6, 0.0, 0.0); {JPL Eval 17}
PPN = RCO3 + NO2 : GCJPLEQ(9.00E-29, 0.0E+00, 14000.0, 9.00E-28, 8.9E0, 0.0, 7.7E-12, 0.2, 0., 0.6, 0., 0.);
IMAO3 + NO2 {+M} = IPMN : GCJPLPR(9.00E-28, 8.9E+00, 0.0, 7.7E-12, 0.2, 0.0, 0.6, 0.0, 0.0); {2017/06/14; Marais2016; EAM}
NMAO3 + NO2 {+M} = NPMN : GCJPLPR(9.00E-28, 8.9E+00, 0.0, 7.7E-12, 0.2, 0.0, 0.6, 0.0, 0.0); {2017/06/14; Marais2016; EAM}

IPMN = IMAO3 + NO2 : GCJPLEQ(9.00E-29, 0.0E+00, 14000.0, 9.00E-28, 8.9E0, 0.0, 7.7E-12, 0.2, 0., 0.6, 0., 0.); {2017/06/14; Marais2016; EAM}
NPMN = NMAO3 + NO2 : GCJPLEQ(9.00E-29, 0.0E+00, 14000.0, 9.00E-28, 8.9E0, 0.0, 7.7E-12, 0.2, 0., 0.6, 0., 0.); {2017/06/14; Marais2016; EAM}
RCO3 + NO = NO2 + ETO2 : GCARR(6.70E-12, 0.0E+00, 340.0);
NMAO3 + NO = NO2 + 0.500CH2O + 0.500CO + CO2 + 0.500MO2 + 0.500MCO3 : GCARR(6.70E-12, 0.0E+00, 340.0); {2013/03/22; Paulot2009; FP,EAM,JMAO,MJE}
RCHO + NO3 = HNO3 + RCO3 : GCARR(6.50E-15, 0.0E+00, 0.0);
ACET + OH = ATO2 + H2O : 1.33E-13+3.82E-11*exp(-2000.0_dp/TEMP); {JPL Eval 17, p1-62-D31; EVF}
A3O2 + MO2 = HO2 + 0.750CH2O + 0.750RCHO + 0.250MOH + 0.250ROH : GCARR(5.92E-13, 0.0E+00, 0.0);
PO2 + MO2 = HO2 + 0.500ALD2 + 1.250CH2O + 0.160HAC + 0.090RCHO + 0.250MOH + 0.250ROH : GCARR(5.92E-13, 0.0E+00, 0.0);
R6O2 + HO2 = R6P : GCARR(7.40E-13, 0.0E+00, 700.0); {2019/11/21; Speciate Alk4; JFB}
IBO2 + HO2 = IBP : GCARR(7.40E-13, 0.0E+00, 700.0); {2019/11/21; Speciate Alk4; JFB}
NBO2 + HO2 = NBP : GCARR(7.40E-13, 0.0E+00, 700.0); {2019/11/21; Speciate Alk4; JFB}
IPO2 + HO2 = IPP : GCARR(7.40E-13, 0.0E+00, 700.0); {2019/11/21; Speciate Alk4; JFB}
NPO2 + HO2 = NPP : GCARR(7.40E-13, 0.0E+00, 700.0); {2019/11/21; Speciate Alk4; JFB}
IR4O2 + HO2 = IR4P : GCARR(7.40E-13, 0.0E+00, 700.0); {2018/07/16; Speciating C5 Ketone; JFB}
R6N1 + HO2 = R6N2 : GCARR(7.40E-13, 0.0E+00, 700.0); {2019/11/21; Speciate Alk4; JFB}
IBN1 + HO2 = IBN2 : GCARR(7.40E-13, 0.0E+00, 700.0); {2019/11/21; Speciate Alk4; JFB}
NBN1 + HO2 = NBN2 : GCARR(7.40E-13, 0.0E+00, 700.0); {2019/11/21; Speciate Alk4; JFB}
IPN1 + HO2 = IPN2 : GCARR(7.40E-13, 0.0E+00, 700.0); {2019/11/21; Speciate Alk4; JFB}
NPN1 + HO2 = NPN2 : GCARR(7.40E-13, 0.0E+00, 700.0); {2019/11/21; Speciate Alk4; JFB}
IR4N1 + HO2 = IR4N2: GCARR(7.40E-13, 0.0E+00, 700.0); {2018/07/16; Speciating C5 Ketone; JFB}
ATO2 + HO2 = 0.150MCO3 + 0.150OH + 0.150CH2O + 0.850ATOOH : GCARR(8.60E-13, 0.0E+00, 700.0); {2013/03/22; Paulot2009; FP,EAM,JMAO,MJE}
KO2 + HO2 = 0.150OH + 0.150ALD2 + 0.150MCO3 + 0.850ATOOH : GC_RO2HO2(2.91E-13, 0.0E+00, 1300.0, 4.0, 0.0, 0.0); {2013/03/22; Paulot2009; FP,EAM,JMAO,MJE}

KETO2 + HO2 = 0.150OH + 0.150ALD2 +
0.150MCO3 + 0.850ATOOH : GC_RO2HO2(2.91E-13, 0.0E+00, 1300.0, 4.0, 0.0, 0.0); {2013/03/22; Paulot2009; FP,EAM,JMAO,MJE} {2018/07/16; Speciating C5 Ketone; JFB}
RIO2 + HO2 = 0.628RIPA + 0.272RIPB +
0.037RIPD + 0.063OH + 0.063CH2O +
0.063HO2 + 0.038MVK + 0.025MACR : GCARR(2.06E-13, 0.0E+00, 1300.0); {2017/07/14; StClair2016; KRT,JAF,CCM,EAM,KHB,RHS}
VRO2 + HO2 = 0.100VRP + 0.680OH +
0.578GLYC + 0.578MCO3 + 0.187KET +
0.102HO2 + 0.102CH2O + 0.102MGLY +
0.033RCHO : GC_RO2HO2(2.91E-13, 0.0E+00, 1300.0, 4.0, 0.0, 0.0); {2013/03/22; Paulot2009; FP,EAM,JMAO,MJE} {2018/07/16; Speciating C5 Ketone; JFB}
MRO2 + HO2 = MRP : GC_RO2HO2(2.91E-13, 0.0E+00, 1300.0, 4.0, 0.0, 0.0); {2013/03/22; Paulot2009; FP,EAM,JMAO,MJE}
MAN2 + HO2 = 0.075PROPNN + 0.075CO +
0.075HO2 + 0.075MGLY + 0.075CH2O +
0.075NO2 + 0.150OH + 0.850MAOP + 0.85NO2 : GC_RO2HO2(2.91E-13, 0.0E+00, 1300.0, 4.0, 0.0, 0.0); {2017/07/27; Fix C creation; SAS,BHH,MJE}
B3O2 + HO2 = RB3P : GC_RO2HO2(2.91E-13, 0.0E+00, 1300.0, 3.0, 0.0, 0.0); {2013/03/22; Paulot2009; FP,EAM,JMAO,MJE}
INO2 + HO2 = INPN : GC_RO2HO2(2.91E-13, 0.0E+00, 1300.0, 5.0, 0.0, 0.0); {2013/03/22; Paulot2009; FP,EAM,JMAO,MJE}
PRN1 + HO2 = PRPN : GC_RO2HO2(2.91E-13, 0.0E+00, 1300.0, 3.0, 0.0, 0.0); {2013/03/22; Paulot2009; FP,EAM,JMAO,MJE}
MEK + OH = KO2 + H2O + MEKY : GCARR(1.50E-12, 0.0E+00, -90.0);
MEK + Cl = KO2 + HCl + MEKX : GCARR(3.05E-11, 0.0E+00, 80.0); {2019/12/17; Explicit MEK Chemistry; JFB}
KET + OH = KETO2 + H2O : GCARR(1.30E-12, 0.0E+00, -25.0); {2018/07/16; Speciating C5 Ketone; JFB}
MO2 + ETO2 = 0.750CH2O + 0.750ALD2 + HO2 +
0.250MOH + 0.250EOH : GCARR(3.00E-13, 0.0E+00, 0.0);
MEK + NO3 = HNO3 + KO2 : GCARR(8.00E-16, 0.0E+00, 0.0);
KET + NO3 = HNO3 + KETO2 : GCARR(8.00E-16, 0.0E+00, 0.0); {2018/07/16; Speciating C5 Ketone; JFB}
R6O2 + MO2 = 0.160ACET + 0.035MEK +
0.090MO2 + 0.140HO2 + 0.160ALD2 +
0.070RCHO + 0.030A3O2 + 0.090B3O2 +
0.160ETO2 + 0.315KET + 0.750CH2O +
0.250MOH + 0.250ROH + 0.500HO2 : GCARR(8.37E-14, 0.0E+00, 0.0); {2019/11/21; Speciate Alk4; JFB}
IBO2 + MO2 = 0.335ACET +
0.090MO2 + 0.140HO2 + 0.335ALD2 +
0.070RCHO + 0.030A3O2 + 0.090B3O2 +
0.160ETO2 + 0.750CH2O +

0.250MOH + 0.250ROH + 0.500HO2 : GCARR(8.37E-14, 0.0E+00, 0.0); {2019/11/21; Speciate Alk4; JFB}

NBO2 + MO2 = 0.160ACET + 0.100MEK +
0.090MO2 + 0.140HO2 + 0.160ALD2 +
0.070RCHO + 0.030A3O2 + 0.090B3O2 +
0.160ETO2 + 0.250MEK + 0.750CH2O +
0.250MOH + 0.250ROH + 0.500HO2 : GCARR(8.37E-14, 0.0E+00, 0.0); {2019/11/21; Speciate Alk4; JFB}

IPO2 + MO2 = 0.160ACET + 0.035MEK +
0.090MO2 + 0.140HO2 + 0.160ALD2 +
0.070RCHO + 0.030A3O2 + 0.090B3O2 +
0.160ETO2 + 0.315KET + 0.750CH2O +
0.250MOH + 0.250ROH + 0.500HO2 : GCARR(8.37E-14, 0.0E+00, 0.0); {2019/11/21; Speciate Alk4; JFB}

NPO2 + MO2 = 0.160ACET + 0.350KET +
0.090MO2 + 0.140HO2 + 0.160ALD2 +
0.070RCHO + 0.030A3O2 + 0.090B3O2 +
0.160ETO2 + 0.750CH2O +
0.250MOH + 0.250ROH + 0.500HO2 : GCARR(8.37E-14, 0.0E+00, 0.0); {2019/11/21; Speciate Alk4; JFB}

IR4O2 + MO2 = 0.160ACET + 0.100KET +
0.090MO2 + 0.140HO2 + 0.160ALD2 +
0.070RCHO + 0.030A3O2 + 0.090B3O2 +
0.160ETO2 + 0.250KET + 0.750CH2O +
0.250MOH + 0.250ROH + 0.500HO2 : GCARR(8.37E-14, 0.0E+00, 0.0); {2018/07/16; Speciating C5 Ketone; JFB}

R6N1 + MO2 = NO2 + 0.200CH2O + 0.380ALD2 +
0.290RCHO + 0.150R6O2 + 0.250RCHO +
0.750CH2O + 0.250MOH + 0.250ROH +
0.500HO2 : GCARR(8.37E-14, 0.0E+00, 0.0); {2019/11/21; Speciate Alk4; JFB}

IBN1 + MO2 = NO2 + 0.200CH2O + 0.380ALD2 +
0.290RCHO + 0.150IBO2 + 0.250RCHO +
0.750CH2O + 0.250MOH + 0.250ROH +
0.500HO2 : GCARR(8.37E-14, 0.0E+00, 0.0); {2019/11/21; Speciate Alk4; JFB}

NBN1 + MO2 = NO2 + 0.200CH2O + 0.380ALD2 +
0.290RCHO + 0.150NBO2 + 0.250RCHO +
0.750CH2O + 0.250MOH + 0.250ROH +
0.500HO2 : GCARR(8.37E-14, 0.0E+00, 0.0); {2019/11/21; Speciate Alk4; JFB}

IPN1 + MO2 = NO2 + 0.200CH2O + 0.380ALD2 +
0.290RCHO + 0.150IPO2 + 0.250RCHO +
0.750CH2O + 0.250MOH + 0.250ROH +
0.500HO2 : GCARR(8.37E-14, 0.0E+00, 0.0); {2019/11/21; Speciate Alk4; JFB}

NPN1 + MO2 = NO2 + 0.200CH2O + 0.380ALD2 +
0.290RCHO + 0.150NPO2 + 0.250RCHO +
0.750CH2O + 0.250MOH + 0.250ROH +
0.500HO2 : GCARR(8.37E-14, 0.0E+00, 0.0); {2019/11/21; Speciate Alk4; JFB}
IR4N1 + MO2 = NO2 + 0.200CH2O + 0.380ALD2 +
0.290RCHO + 0.150IR4O2 + 0.250RCHO +
0.750CH2O + 0.250MOH + 0.250ROH +
0.500HO2 : GCARR(8.37E-14, 0.0E+00, 0.0); {2018/07/16; Speciating C5 Ketone; JFB}
ATO2 + MO2 = 0.300HO2 + 0.300CH2O +
0.300MCO3 + 0.200HAC + 0.200CH2O +
0.500MGLY + 0.500MOH : GCARR(7.50E-13, 0.0E+00, 500.0);
KETO2 + MO2 = 0.500ALD2 + 0.500MCO3 +
0.250KET + 0.750CH2O + 0.250MOH +
0.250ROH + 0.500HO2 : GCARR(8.37E-14, 0.0E+00, 0.0); {2018/07/16; Speciating C5 Ketone; JFB}
KO2 + MO2 = 0.500ALD2 + 0.500MCO3 +
0.250KET + 0.750CH2O + 0.250MOH +
0.250ROH + 0.500HO2 : GCARR(8.37E-14, 0.0E+00, 0.0); {2018/07/16; Speciating C5 Ketone; JFB}
RIO2 + MO2 = 1.100HO2 + 1.220CH2O +
0.280MVK + 0.180MACR + 0.300HC5 +
0.240MOH + 0.240ROH : GCARR(8.37E-14, 0.0E+00, 0.0); {2013/03/22; Paulot2009; FP,EAM,JMAO,MJE}
RIO2 + RIO2 = 0.910HO2 + 0.750CH2O +
0.450MVK + 0.290MACR + 0.090DIBOO +
1.110HC5 + 0.290CO : GCARR(2.30E-12, 0.0E+00, 0.0); {2017/07/14; Xie2013; KRT,JAF,CCM,EAM,KHB,RHS}
HC5OO + MO2 = 0.500HO2 + 0.330CO +
0.090H2 + 0.180HAC + 0.130GLYC +
0.290MGLY + 0.250KET + 0.950CH2O +
0.250MOH + 0.250ROH + 0.500HO2 : GCARR(8.37E-14, 0.0E+00, 0.0); {2013/03/22; Paulot2009; FP,EAM,JMAO,MJE}
VRO2 + MO2 = 0.140HO2 + 0.140CH2O +
0.360MCO3 + 0.360GLYC + 0.140MGLY +
0.250KET + 0.750CH2O + 0.250MOH +
0.250ROH + 0.500HO2 : GCARR(8.37E-14, 0.0E+00, 0.0); {2018/07/16; Speciating C5 Ketone; JFB}
MRO2 + MO2 = 0.595HAC + 0.255MGLY +
0.595CO + 1.255CH2O + 1.700HO2 + 0.150ROH : GCARR(8.37E-14, 0.0E+00, 0.0); {2013/03/22; Paulot2009; FP,EAM,JMAO,MJE}
MAN2 + MO2 = 0.375PROPNN + 0.375CO +
0.375HO2 + 0.375MGLY + 0.375CH2O +
0.375NO2 + 0.250CH2O + 0.250IR4N2 : GCARR(8.37E-14, 0.0E+00, 0.0); {2013/03/22; Paulot2009; FP,EAM,JMAO,MJE} {2018/07/16; Speciating C5 Ketone; JFB}

```
B3O2 + MO2 = 0.500HO2 + 0.500ACET +
 0.250ACET + 0.750CH2O + 0.250MOH +
 0.250ROH + 0.500HO2 :                GCARR(8.37E-14, 0.0E+00, 0.0);
INO2 + MO2 = 0.150NO2 + 0.400HO2 +
 0.350ISN1 + 0.035CH2O + 0.018MACR +
 0.018MVK + 0.115HC5 + 0.250ISN1 +
 0.250ISOPND + 0.500CH2O + 0.500HO2 +
 0.250CH2O + 0.250MOH :               GCARR(1.30E-12, 0.0E+00, 0.0);      {2013/03/22;
Paulot2009; FP,EAM,JMAO,MJE}
PRN1 + MO2 = NO2 + 0.500CH2O + 0.500ALD2 +
 0.250RCHO + 0.750CH2O + 0.250MOH +
 0.250ROH + 0.500HO2 :                GCARR(8.37E-14, 0.0E+00, 0.0);
EOH + OH = HO2 + ALD2 :               GCARR(3.35E-12, 0.0E+00, 0.0);      {2013/02/12;
JPL 10-6; BHH,JMAO,EAM}
ROH + OH = HO2 + RCHO :               GCARR(4.60E-12, 0.0E+00, 70.0);
ETO2 + ETO2 = 2.000ALD2 + 2.000HO2 :  GCARR(4.10E-14, 0.0E+00, 0.0);
ETO2 + ETO2 = EOH + ALD2 :            GCARR(2.70E-14, 0.0E+00, 0.0);
HO2 + ETO2 = ETP :                    GCARR(7.40E-13, 0.0E+00, 700.0);
A3O2 + HO2 = RA3P :                   GC_RO2HO2(2.91E-13, 0.0E+00, 1300.0, 3.0, 0.0, 0.0);
{2013/03/22; Paulot2009; FP,EAM,JMAO,MJE}
PO2 + HO2 = PP :                      GC_RO2HO2(2.91E-13, 0.0E+00, 1300.0, 3.0, 0.0, 0.0);
{2013/03/22; Paulot2009; FP,EAM,JMAO,MJE}
HO2 + MCO3 = 0.410MAP + 0.150ACTA +
 0.150O3 + 0.440OH + 0.440MO2 :       GCARR(5.20E-13, 0.0E+00, 980.0);
{2013/03/22; Paulot2009; FP,EAM,JMAO,MJE}
RCO3 + HO2 = 0.410RP + 0.150RCOOH +
 0.150O3 + 0.440OH + 0.440ETO2 :      GCARR(4.30E-13, 0.0E+00, 1040.0);
{2013/03/22; Paulot2009; FP,EAM,JMAO,MJE}
NMAO3 + HO2 = 0.440OH + 0.150O3 +
 0.590CH2O + 0.390MO2 + 0.410MAOP +
 0.390CO :                            GCARR(4.30E-13, 0.0E+00, 1040.0);   {2013/03/22;
Paulot2009; FP,EAM,JMAO,MJE}
PRPE + OH {+M} = PO2 :                GCJPLPR(4.60E-27, 4.0E+00, 0.0, 2.6E-11, 1.3, 0.0,
0.5, 0.0, 0.0); {2017/02/22; JPL 15-10; BHH,MJE}
PRPE + O3 = 0.500ALD2 + 0.500CH2O +
 0.120CH3CHOO + 0.100CH4 + 0.120CH2OO +
 0.280MO2 + 0.560CO + 0.280HO2 + 0.360OH :   GCARR(5.50E-15, 0.0E+00, -1880.0);
{2015/09/25; Millet2015; DBM,EAM}
NPMN + OH = HAC + CO + NO2 :          GCARR(2.90E-11, 0.0E+00, 0.0);
{2013/03/22; Paulot2009; FP,EAM,JMAO,MJE}
IPMN + OH = 0.030HAC + 0.030CO +
 0.810NO3 + 0.781IMAE + 0.190PAN +
 0.190CH2O + 0.190HO2 :               GCARR(3.00E-11, 0.0E+00, 0.0);      {2017/06/14;
Marais2016; EAM}
NPMN + O3 = CH2O + MCO3 + NO3 :       GCARR(8.20E-18, 0.0E+00, 0.0);
{2015/07/06; Bug fix (v11-02b); DBM}
```

IMAE + OH = OH : GCARR(3.48E-12, 0.0E+00, 0.0); {2017/06/14; Marais2016; EAM}
GLYC + OH = 0.732CH2O + 0.361CO2 +
0.505CO + 0.227OH + 0.773HO2 +
0.134GLYX + 0.134HCOOH : GC_GLYCOHA(8.00E-12, 0.0E+00, 0.0); {2013/03/22; Paulot2009; FP,EAM,JMAO,MJE}
GLYC + OH = HCOOH + OH + CO : GC_GLYCOHB(8.00E-12, 0.0E+00, 0.0); {2013/03/22; Paulot2009; FP,EAM,JMAO,MJE}
PRPE + NO3 = PRN1 : GCARR(4.59E-13, 0.0E+00, -1156.0);
GLYX + OH = HO2 + 2.000CO : GCARR(3.10E-12, 0.0E+00, 340.0); {2013/03/22; Paulot2009; FP,EAM,JMAO,MJE}
MGLY + OH = MCO3 + CO : GCARR(1.50E-11, 0.0E+00, 0.0);
GLYX + NO3 = HNO3 + HO2 + 2.000CO : GC_GLYXNO3(1.40E-12, 0.0E+00, -1860.0);
MGLY + NO3 = HNO3 + CO + MCO3 : GCARR(3.36E-12, 0.0E+00, -1860.0); {2013/03/22; Paulot2009; FP,EAM,JMAO,MJE}
ISOP + OH = RIO2 + LISOPOH : GCARR(3.00E-11, 0.0E+00, 360.0); {2017/02/22; JPL 15-10; BHH,MJE}
MVK + OH = VRO2 : GCARR(2.70E-12, 0.0E+00, 580.0); {2017/02/22; JPL 15-10; BHH,MJE}
MACR + OH = 0.530IMAO3 + 0.470MRO2 : GCARR(9.60E-12, 0.0E+00, 360.0); {2017/02/22; JPL 15-10; BHH,MJE}
HAC + OH = MGLY + HO2 : GC_HACOHA(2.15E-12, 0.0E+00, 305.0); {2013/03/22; Paulot2009; FP,EAM,JMAO,MJE}
HAC + OH = 0.500HCOOH + OH + 0.500ACTA +
0.500CO2 + 0.500CO + 0.500MO2 : GC_HACOHB(2.15E-12, 0.0E+00, 305.0); {2013/03/22; Paulot2009; FP,EAM,JMAO,MJE}
MCO3 + A3O2 = MO2 + RCHO + HO2 : GCARR(1.68E-12, 0.0E+00, 500.0);
MCO3 + PO2 = MO2 + ALD2 + CH2O + HO2 : GCARR(1.68E-12, 0.0E+00, 500.0);
MCO3 + A3O2 = ACTA + RCHO : GCARR(1.87E-13, 0.0E+00, 500.0);
MCO3 + PO2 = ACTA + 0.350RCHO + 0.650HAC : GCARR(1.87E-13, 0.0E+00, 500.0);
ISOP + O3 = 0.200MVK + 0.300MACR +
0.456CH2O + 0.110CH2OO + 0.495CO +
0.044MVKOO + 0.105MCO3 + 0.237HO2 +
0.243OH + 0.102PRPE + 0.051MO2 +
0.044MACROO + 0.054VRO2 : GCARR(1.00E-14, 0.0E+00, -1970.0); {2017/06/14; Marais2016; EAM}
MVK + O3 = 0.360OH + 0.280HO2 + 0.560CO +
0.120MGLOO + 0.100ALD2 + 0.500MGLY +
0.600CH2O + 0.280MCO3 + 0.120CH2OO : GCARR(8.5E-16, 0.0E+00, -1520.0); {2017/02/22; JPL 15-10; BHH,MJE}
MACR + O3 = 0.239OH + 0.141HO2 + 0.625CO +
0.326CH2OO + 0.880MGLY + 0.120CH2O +
0.022MGLYOO + 0.098MCO3 : GCARR(1.50E-15, 0.0E+00, -2110.0); {2017/06/14; Marais2016; EAM}

ISOP + NO3 = INO2 + LISOPNO3 : GCARR(3.50E-12, 0.0E+00, -450.0);
{2017/02/22; JPL 15-10; BHH,MJE}
MACR + NO3 = MAN2 : GCARR(3.40E-15, 0.0E+00, 0.0); {2017/02/22;
JPL 15-10; BHH,MJE}
MACR + NO3 = 0.500IMAO3 + 0.500HNO3 +
0.500MRO2 + 0.500HO2 + 0.500CO +
0.500MAOP : GCARR(1.50E-12, 0.0E+00, -1815.0); {2017/06/14;
Marais2016; EAM}
RCO3 + MO2 = CH2O + HO2 + ETO2 : GCARR(1.68E-12, 0.0E+00, 500.0);
NMAO3 + MO2 = CH2O + HO2 + CH2O + MCO3 : GCARR(1.68E-12, 0.0E+00, 500.0);
RCO3 + MO2 = RCOOH + CH2O : GCARR(1.87E-13, 0.0E+00, 500.0);
NMAO3 + MO2 = RCOOH + CH2O : GCARR(1.87E-13, 0.0E+00, 500.0);
{2013/03/22; Paulot2009; FP,EAM,JMAO,MJE}
INPN + OH = OH + NO2 + KET : GCARR(1.90E-11, 0.0E+00, 390.0);
{2013/03/22; Paulot2009; FP,EAM,JMAO,MJE}
INPN + OH = 0.360INO2 + 0.640IR4N2 +
0.640OH : GCARR(5.18E-12, 0.0E+00, 200.0); {2013/03/22;
Paulot2009; FP,EAM,JMAO,MJE} {2018/07/16; Speciating C5 Ketone; JFB}
PRPN + OH = 0.209PRN1 + 0.791OH +
0.791PROPNN : GCARR(8.78E-12, 0.0E+00, 200.0); {2013/03/22;
Paulot2009; FP,EAM,JMAO,MJE}
ETP + OH = 0.640OH + 0.360ETO2 + 0.640ALD2 : GCARR(5.18E-12, 0.0E+00, 200.0);
{2013/03/22; Paulot2009; FP,EAM,JMAO,MJE}
RA3P + OH = 0.640OH + 0.360A3O2 +
0.640RCHO : GCARR(5.18E-12, 0.0E+00, 200.0); {2013/03/22;
Paulot2009; FP,EAM,JMAO,MJE}
RB3P + OH = 0.791OH + 0.209B3O2 +
0.791ACET : GCARR(8.78E-12, 0.0E+00, 200.0); {2013/03/22;
Paulot2009; FP,EAM,JMAO,MJE}
R6P + OH = 0.791OH + 0.209R6O2 + 0.791RCHO : GCARR(8.78E-12, 0.0E+00, 200.0);
{2013/03/22; Paulot2009; FP,EAM,JMAO,MJE} {2019/11/21; Speciate Alk4; JFB}
IBP + OH = 0.791OH + 0.209IBO2 + 0.791RCHO : GCARR(8.78E-12, 0.0E+00, 200.0);
{2013/03/22; Paulot2009; FP,EAM,JMAO,MJE} {2019/11/21; Speciate Alk4; JFB}
NBP + OH = 0.791OH + 0.209NBO2 + 0.791RCHO : GCARR(8.78E-12, 0.0E+00, 200.0);
{2013/03/22; Paulot2009; FP,EAM,JMAO,MJE} {2019/11/21; Speciate Alk4; JFB}
IPP + OH = 0.791OH + 0.209IPO2 + 0.791RCHO : GCARR(8.78E-12, 0.0E+00, 200.0);
{2013/03/22; Paulot2009; FP,EAM,JMAO,MJE} {2019/11/21; Speciate Alk4; JFB}
NPP + OH = 0.791OH + 0.209NPO2 + 0.791RCHO : GCARR(8.78E-12, 0.0E+00, 200.0);
{2013/03/22; Paulot2009; FP,EAM,JMAO,MJE} {2019/11/21; Speciate Alk4; JFB}
IR4P + OH = 0.791OH + 0.209IR4O2 +
0.791RCHO : GCARR(8.78E-12, 0.0E+00, 200.0); {2013/03/22;
Paulot2009; FP,EAM,JMAO,MJE} {2018/07/16; Speciating C5 Ketone; JFB}
RP + OH = RCO3 : GCARR(6.13E-13, 0.0E+00, 200.0); {2013/03/22;
Paulot2009; FP,EAM,JMAO,MJE}
PP + OH = 0.791OH + 0.209PO2 + 0.791HAC : GCARR(8.78E-12, 0.0E+00, 200.0);
{2013/03/22; Paulot2009; FP,EAM,JMAO,MJE}

RIPA + OH = 0.750RIO2 + 0.243HC5 +
0.125OH + 0.125H2O + 0.007LVOC : GCARR(6.13E-12, 0.0E+00, 200.0);
{2017/07/14; StClair2016,Marais2016; KRT,JAF,CCM,EAM,KHB,RHS}
RIPB + OH = 0.480RIO2 + 0.513HC5 +
0.260OH + 0.260H2O + 0.007LVOC : GCARR(4.14E-12, 0.0E+00, 200.0);
{2017/07/14; StClair2016,Marais2016; KRT,JAF,CCM,EAM,KHB,RHS}
RIPD + OH = 0.250RIO2 + 0.743HC5 +
0.375OH + 0.375H2O + 0.007LVOC : GCARR(5.11E-12, 0.0E+00, 200.0);
{2017/07/14; StClair2016,Marais2016; KRT,JAF,CCM,EAM,KHB,RHS}
RIPA + OH = 0.850OH + 0.578IEPOXA +
0.272IEPOXB + 0.143HC5OO + 0.007LVOC : GCARR(1.70E-11, 0.0E+00, 390.0);
{2017/07/14; StClair2016,Marais2016; KRT,JAF,CCM,EAM,KHB,RHS}
RIPB + OH = OH + 0.680IEPOXA + 0.320IEPOXB : GCARR(2.97E-11, 0.0E+00, 390.0);
{2017/07/14; StClair2016; KRT,JAF,CCM,EAM,KHB,RHS}
RIPD + OH = 0.500OH + 0.500IEPOXD +
0.493HC5OO + 0.007LVOC : GCARR(2.92E-11, 0.0E+00, 390.0); {2017/07/14;
StClair2016,Marais2016; KRT,JAF,CCM,EAM,KHB,RHS}
LVOC + OH = OH : GCARR(4.82E-11, 0.0E+00, -400.0); {2017/06/14;
Marais2016; EAM}
IEPOXA + OH = IEPOXOO : GCARR(3.73E-11, 0.0E+00, -400.0);
{2017/07/14; Bates2014; KRT,JAF,CCM,EAM,KHB,RHS}
IEPOXB + OH = IEPOXOO : GCARR(5.79E-11, 0.0E+00, -400.0);
{2017/07/14; Bates2014; KRT,JAF,CCM,EAM,KHB,RHS}
IEPOXD + OH = IEPOXOO : GCARR(3.20E-11, 0.0E+00, -400.0);
{2017/07/14; Bates2014; KRT,JAF,CCM,EAM,KHB,RHS}
IEPOXOO + HO2 = 0.085HAC + 0.025GLYC +
0.085GLYX + 0.085MGLY + 1.125OH +
0.825HO2 + 1.100CO2 + 0.375CH2O +
0.278HCOOH + 0.600CO + 0.440HC187 +
0.072CO2 : GCARR(2.06E-13, 0.0E+00, 1300.0); {2017/07/14;
Bates2014; KRT,JAF,CCM,EAM,KHB,RHS}
IEPOXOO + NO = 0.117HAC + 0.088GLYC +
0.088GLYX + 0.088MGLY + 0.125OH +
0.825HO2 + 0.800CO2 + 0.375CH2O +
0.142HCOOH + 0.678CO + NO2 + 0.473HC187 +
0.058CO2 : GCARR(2.70E-12, 0.0E+00, 350.0); {2017/07/14;
Bates2014; KRT,JAF,CCM,EAM,KHB,RHS}
IAP + OH = 0.654OH + 0.654DHMOB +
0.346HC5OO : GCARR(5.31E-12, 0.0E+00, 200.0); {2013/03/22;
Paulot2009; FP,EAM,JMAO,MJE}
VRP + OH = 0.791OH + 0.791KET + 0.209VRO2 : GCARR(8.78E-12, 0.0E+00, 200.0);
{2013/03/22; Paulot2009; FP,EAM,JMAO,MJE} {2018/07/16; Speciating C5 Ketone; JFB}
MRP + OH = MRO2 : GCARR(1.84E-12, 0.0E+00, 200.0); {2013/03/22;
Paulot2009; FP,EAM,JMAO,MJE}
MRP + OH = CO2 + HAC + OH : GCARR(4.40E-12, 0.0E+00, 380.0);
{2013/03/22; Paulot2009; FP,EAM,JMAO,MJE}

MAOP + OH = NMAO3 : GCARR(6.13E-13, 0.0E+00, 200.0); {2013/03/22; Paulot2009; FP,EAM,JMAO,MJE}
MAOP + OH = MAOPO2 : GCARR(3.60E-12, 0.0E+00, 380.0); {2013/03/22; Paulot2009; FP,EAM,JMAO,MJE}
MCO3 + MAOPO2 = HAC + 2.000CO2 + OH + MO2 : GCARR(1.68E-12, 0.0E+00, 500.0); {2013/03/22; Paulot2009; FP,EAM,JMAO,MJE}
MCO3 + MAOPO2 = ACTA + KET : GCARR(1.87E-13, 0.0E+00, 500.0); {2013/03/22; Paulot2009; FP,EAM,JMAO,MJE} {2018/07/16; Speciating C5 Ketone; JFB}
MAOPO2 + MO2 = 0.700HAC + 0.700CO2 +
0.700OH + CH2O + 0.700HO2 + 0.300ROH : GCARR(8.37E-14, 0.0E+00, 0.0); {2013/03/22; Paulot2009; FP,EAM,JMAO,MJE}
MAOPO2 + MAOPO2 = 2.000HAC + 2.000CO2 +
2.000OH : GCARR(8.37E-14, 0.0E+00, 0.0); {2013/03/22; Paulot2009; FP,EAM,JMAO,MJE}
MAOPO2 + HO2 = HAC + CO2 + 2.000OH : GC_RO2HO2(2.91E-13, 0.0E+00, 1300.0, 4.0, 0.0, 0.0); {2013/03/22; Paulot2009; FP,EAM,JMAO,MJE}
MAOPO2 + NO = HAC + CO2 + OH + NO2 : GC_RO2NO('B', 2.70E-12, 0.0E+00, 350.0, 4.0, 0.0, 0.0); {2013/03/22; Paulot2009; FP,EAM,JMAO,MJE}
MAOPO2 + NO = HNO3 : GC_RO2NO('A', 2.70E-12, 0.0E+00, 350.0, 4.0, 0.0, 0.0); {2013/03/22; Paulot2009; FP,EAM,JMAO,MJE}
OH + MAP = MCO3 : GCARR(6.13E-13, 0.0E+00, 200.0); {2013/03/22; Paulot2009; FP,EAM,JMAO,MJE}
C2H6 + NO3 = ETO2 + HNO3 : GCARR(1.40E-18, 0.0E+00, 0.0); {2013/03/22; Paulot2009; FP,EAM,JMAO,MJE}
HC5 + O3 = 0.500GLYC + 0.500MGLY +
0.055MGLYOO + 0.890CO + 0.445MCO3 +
0.055GAOO + 0.445HO2 + 0.445CH2O +
0.890OH : GCARR(6.16E-15, 0.0E+00, -1814.0); {2015/09/25; Millet2015; DBM,EAM}
MCO3 + MCO3 = 2.000MO2 : GCARR(2.50E-12, 0.0E+00, 500.0);
MCO3 + MO2 = CH2O + MO2 + HO2 : GCARR(1.80E-12, 0.0E+00, 500.0);
MCO3 + MO2 = ACTA + CH2O : GCARR(2.00E-13, 0.0E+00, 500.0);
R6O2 + MCO3 = MO2 + 0.320ACET + 0.019MEK +
0.270HO2 + 0.320ALD2 + 0.130RCHO +
0.050A3O2 + 0.180B3O2 + 0.320ETO2 +
0.171KET: GCARR(1.68E-12, 0.0E+00, 500.0); {2013/03/22; Paulot2009; FP,EAM,JMAO,MJE} {2019/11/21; Speciate Alk4; JFB}
IBO2 + MCO3 = MO2 + 0.415ACET +
0.270HO2 + 0.415ALD2 + 0.130RCHO +
0.050A3O2 + 0.180B3O2 + 0.320ETO2 : GCARR(1.68E-12, 0.0E+00, 500.0); {2013/03/22; Paulot2009; FP,EAM,JMAO,MJE} {2019/11/21; Speciate Alk4; JFB}
NBO2 + MCO3 = MO2 + 0.320ACET + 0.190MEK +
0.270HO2 + 0.320ALD2 + 0.130RCHO +
0.050A3O2 + 0.180B3O2 + 0.320ETO2 : GCARR(1.68E-12, 0.0E+00, 500.0); {2013/03/22; Paulot2009; FP,EAM,JMAO,MJE} {2019/11/21; Speciate Alk4; JFB}
IPO2 + MCO3 = MO2 + 0.320ACET + 0.019MEK +

0.270HO2 + 0.320ALD2 + 0.130RCHO +
0.050A3O2 + 0.180B3O2 + 0.320ETO2 +
0.171KET : GCARR(1.68E-12, 0.0E+00, 500.0); {2013/03/22;
Paulot2009; FP,EAM,JMAO,MJE} {2019/11/21; Speciate Alk4; JFB}
NPO2 + MCO3 = MO2 + 0.320ACET + 0.190KET +
0.270HO2 + 0.320ALD2 + 0.130RCHO +
0.050A3O2 + 0.180B3O2 + 0.320ETO2 : GCARR(1.68E-12, 0.0E+00, 500.0);
{2013/03/22; Paulot2009; FP,EAM,JMAO,MJE} {2019/11/21; Speciate Alk4; JFB}
IR4O2 + MCO3 = MO2 + 0.320ACET + 0.190KET +
0.270HO2 + 0.320ALD2 + 0.130RCHO +
0.050A3O2 + 0.180B3O2 + 0.320ETO2 : GCARR(1.68E-12, 0.0E+00, 500.0);
{2013/03/22; Paulot2009; FP,EAM,JMAO,MJE} {2018/07/16; Speciating C5 Ketone; JFB}
ATO2 + MCO3 = MO2 + MCO3 + CH2O : GCARR(1.68E-12, 0.0E+00, 500.0);
{2013/03/22; Paulot2009; FP,EAM,JMAO,MJE}
KO2 + MCO3 = MO2 + ALD2 + MCO3 : GCARR(1.68E-12, 0.0E+00, 500.0);
KETO2 + MCO3 = MO2 + ALD2 + MCO3 : GCARR(1.68E-12, 0.0E+00, 500.0);
RIO2 + MCO3 = 0.887HO2 + 0.747CH2O +
0.453MVK + 0.294MACR + 0.140HC5 +
0.113DIBOO + CO2 + MO2 : GCARR(1.68E-12, 0.0E+00, 500.0); {2013/03/22;
Paulot2009; FP,EAM,JMAO,MJE}
HC5OO + MCO3 = 0.216GLYX + 0.234MGLY +
0.234GLYC + 0.216HAC + 0.290DHMOB +
0.170MOBA + 0.090RCHO + HO2 + 0.090CO +
MO2 : GCARR(1.68E-12, 0.0E+00, 500.0); {2013/03/22;
Paulot2009; FP,EAM,JMAO,MJE}
VRO2 + MCO3 = 0.400HO2 + 0.400CH2O +
0.600MCO3 + 0.600GLYC + 0.400MGLY + MO2 : GCARR(1.68E-12, 0.0E+00, 500.0);
{2013/03/22; Paulot2009; FP,EAM,JMAO,MJE}
MRO2 + MCO3 = 0.850HO2 + 0.143MGLY +
0.857HAC + 0.857CO + 0.143CH2O + MO2 : GCARR(1.68E-12, 0.0E+00, 500.0);
{2013/03/22; Paulot2009; FP,EAM,JMAO,MJE}
B3O2 + MCO3 = MO2 + HO2 + ACET : GCARR(1.68E-12, 0.0E+00, 500.0);
R6N1 + MCO3 = MO2 + NO2 + 0.390CH2O +
0.750ALD2 + 0.570RCHO + 0.300R6O2 : GCARR(1.68E-12, 0.0E+00, 500.0);
{2019/11/21; Speciate Alk4; JFB}
IBN1 + MCO3 = MO2 + NO2 + 0.390CH2O +
0.750ALD2 + 0.570RCHO + 0.300IBO2 : GCARR(1.68E-12, 0.0E+00, 500.0);
{2019/11/21; Speciate Alk4; JFB}
NBN1 + MCO3 = MO2 + NO2 + 0.390CH2O +
0.750ALD2 + 0.570RCHO + 0.300NBO2 : GCARR(1.68E-12, 0.0E+00, 500.0);
{2019/11/21; Speciate Alk4; JFB}
IPN1 + MCO3 = MO2 + NO2 + 0.390CH2O +
0.750ALD2 + 0.570RCHO + 0.300IPO2 : GCARR(1.68E-12, 0.0E+00, 500.0);
{2019/11/21; Speciate Alk4; JFB}
NPN1 + MCO3 = MO2 + NO2 + 0.390CH2O +

0.750ALD2 + 0.570RCHO + 0.300NPO2 : GCARR(1.68E-12, 0.0E+00, 500.0);
{2019/11/21; Speciate Alk4; JFB}
IR4N1 + MCO3 = MO2 + NO2 + 0.390CH2O +
0.750ALD2 + 0.570RCHO + 0.300IR4O2 : GCARR(1.68E-12, 0.0E+00, 500.0);
{2018/07/16; Speciating C5 Ketone; JFB}
MAN2 + MCO3 = 0.500PROPNN + 0.500CO +
0.500HO2 + 0.500MGLY + 0.500CH2O +
0.500NO2 + CO2 + MO2 : GCARR(1.68E-12, 0.0E+00, 500.0); {2013/03/22;
Paulot2009; FP,EAM,JMAO,MJE}
INO2 + MCO3 = MO2 + 0.700ISN1 + 0.800HO2 +
0.035MVK + 0.035MACR + 0.070CH2O +
0.300NO2 + 0.230HC5 : GCARR(1.68E-12, 0.0E+00, 500.0); {2013/03/22;
Paulot2009; FP,EAM,JMAO,MJE}
PRN1 + MCO3 = MO2 + NO2 + CH2O + ALD2 : GCARR(1.68E-12, 0.0E+00, 500.0);
R6O2 + MCO3 = 0.100MEK + ACTA + 0.900KET : GCARR(1.87E-13, 0.0E+00, 500.0);
{2019/11/21; Speciate Alk4; JFB}
IBO2 + MCO3 = 0.500ACET + 0.500ALD2 +
ACTA : GCARR(1.87E-13, 0.0E+00, 500.0); {2019/11/21; Speciate
Alk4; JFB}
NBO2 + MCO3 = MEK + ACTA : GCARR(1.87E-13, 0.0E+00, 500.0);
{2019/11/21; Speciate Alk4; JFB}
IPO2 + MCO3 = 0.100MEK + 0.900KET + ACTA : GCARR(1.87E-13, 0.0E+00, 500.0);
{2019/11/21; Speciate Alk4; JFB}
NPO2 + MCO3 = KET + ACTA : GCARR(1.87E-13, 0.0E+00, 500.0); {2019/11/21;
Speciate Alk4; JFB}
IR4O2 + MCO3 = KET + ACTA : GCARR(1.87E-13, 0.0E+00, 500.0);
{2018/07/16; Speciating C5 Ketone; JFB}
ATO2 + MCO3 = MGLY + ACTA : GCARR(1.87E-13, 0.0E+00, 500.0);
{2017/07/27; Fix C creation; SAS,BHH,MJE}
KETO2 + MCO3 = KET + ACTA : GCARR(1.87E-13, 0.0E+00, 500.0);
{2018/07/16; Speciating C5 Ketone; JFB}
RIO2 + MCO3 = KET + ACTA : GCARR(1.87E-13, 0.0E+00, 500.0);
{2018/07/16; Speciating C5 Ketone; JFB}
HC5OO + MCO3 = KET + ACTA : GCARR(1.87E-13, 0.0E+00, 500.0);
{2013/03/22; Paulot2009; FP,EAM,JMAO,MJE} {2018/07/16; Speciating C5 Ketone; JFB}
VRO2 + MCO3 = KET + ACTA : GCARR(1.87E-13, 0.0E+00, 500.0);
{2018/07/16; Speciating C5 Ketone; JFB}
MRO2 + MCO3 = KET + ACTA : GCARR(1.87E-13, 0.0E+00, 500.0);
{2018/07/16; Speciating C5 Ketone; JFB}
R6N1 + MCO3 = RCHO + ACTA + NO2 : GCARR(1.87E-13, 0.0E+00, 500.0);
{2019/11/21; Speciate Alk4; JFB}
IBN1 + MCO3 = RCHO + ACTA + NO2 : GCARR(1.87E-13, 0.0E+00, 500.0);
{2019/11/21; Speciate Alk4; JFB}
NBN1 + MCO3 = RCHO + ACTA + NO2 : GCARR(1.87E-13, 0.0E+00, 500.0);
{2019/11/21; Speciate Alk4; JFB}

IPN1 + MCO3 = RCHO + ACTA + NO2 : GCARR(1.87E-13, 0.0E+00, 500.0);
{2019/11/21; Speciate Alk4; JFB}
NPN1 + MCO3 = RCHO + ACTA + NO2 : GCARR(1.87E-13, 0.0E+00, 500.0);
{2019/11/21; Speciate Alk4; JFB}
IR4N1 + MCO3 = RCHO + ACTA + NO2 : GCARR(1.87E-13, 0.0E+00, 500.0);
{2018/07/16; Speciating C5 Ketone; JFB}
MAN2 + MCO3 = RCHO + ACTA + NO2 : GCARR(1.87E-13, 0.0E+00, 500.0);
INO2 + MCO3 = RCHO + ACTA + NO2 : GCARR(1.87E-13, 0.0E+00, 500.0);
PRN1 + MCO3 = RCHO + ACTA + NO2 : GCARR(1.87E-13, 0.0E+00, 500.0);
B3O2 + MCO3 = ACET + ACTA : GCARR(1.87E-13, 0.0E+00, 500.0);
MCO3 + ETO2 = MO2 + ALD2 + HO2 : GCARR(1.68E-12, 0.0E+00, 500.0);
MCO3 + ETO2 = ACTA + ALD2 : GCARR(1.87E-13, 0.0E+00, 500.0);
RCO3 + MCO3 = MO2 + ETO2 : GCARR(2.50E-12, 0.0E+00, 500.0);
NMAO3 + MCO3 = MO2 + CH2O + MCO3 : GCARR(2.50E-12, 0.0E+00, 500.0);
NO3 + NO3 = 2.000NO2 + O2 : GCARR(8.50E-13, 0.0E+00, -2450.0);
MO2 + NO2 {+M} = MPN {+M} : GCJPLPR(1.00E-30, 4.8E+00, 0.0, 7.2E-12,
2.1E0, 0.0, 0.6, 0.0, 0.0); {2012/02/12; Browne2011; ECB}
MPN {+M} = MO2 + NO2 : GCJPLPR(1.05E-02, 4.8E+00, -11234.0, 7.58E16,
2.1E0, -11234.0, 0.6, 0.0, 0.0); {2012/02/12; Browne2011; ECB}
ISOPNB + O3 = 0.050HO2 + 0.110MVKN +
0.320MACRN + 0.160HCOOH + 0.050OH +
0.620CH2O + 0.360CO2 + 0.210CO +
0.060PROPNN + 0.360PROPNN + 0.100MVKN +
0.410HNO3 : GCARR(3.70E-19, 0.0E+00, 0.0); {2017/07/14; Lee2014;
KRT,JAF,CCM,EAM,KHB,RHS}
ISOPND + O3 = 0.060NO2 + 0.240PROPNN +
0.260ETHLN + 0.370OH + 0.240GLYC +
0.260HAC + 0.630CO2 + 0.240MOH +
0.09EOH + 0.200CH2O + 0.100MCO3 +
0.060GLYX + 0.160HAC + 0.140PROPNN +
0.300HNO3 : GCARR(2.90E-17, 0.0E+00, 0.0); {2017/07/14; Lee2014;
KRT,JAF,CCM,EAM,KHB,RHS}
DMS + OH = SO2 + MO2 + CH2O : GCARR(1.20E-11, 0.0E+00, -280.0);
DMS + OH = 0.750SO2 + 0.250MSA + MO2 : GC_DMSOH(8.20E-39, 0.0E+00, 5376.0,
1.05E-5, 0.0, 3644.0);
DMS + NO3 = SO2 + HNO3 + MO2 + CH2O : GCARR(1.90E-13, 0.0E+00, 530.0);
SO2 + OH {+M} = SO4 + HO2 : GCJPLPR(3.30E-31, 4.3E+00, 0.0, 1.6E-12, 0.0,
0.0, 0.6, 0.0, 0.0);
Br + O3 = BrO + O2 : GCARR(1.60E-11, 0.0E+00, -780.0); {2012/06/07;
Parrella2012; JPP}
BrO + HO2 = HOBr + O2 : GCARR(4.50E-12, 0.0E+00, 460.0); {2012/06/07;
Parrella2012; JPP}
Br + HO2 = HBr + O2 : GCARR(4.80E-12, 0.0E+00, -310.0); {2012/06/07;
Parrella2012; JPP}
HBr + OH = Br + H2O : GCARR(5.50E-12, 0.0E+00, 200.0); {2012/06/07;
Parrella2012; JPP}

BrO + BrO = 2.000Br + O2 : GCARR(2.40E-12, 0.0E+00, 40.0); {2012/06/07; Parrella2012; JPP}
BrO + BrO = Br2 + O2 : GCARR(2.80E-14, 0.0E+00, 860.0); {2012/06/07; Parrella2012; JPP}
BrO + NO = Br + NO2 : GCARR(8.80E-12, 0.0E+00, 260.0); {2012/06/07; Parrella2012; JPP}
Br + BrNO3 = Br2 + NO3 : GCARR(4.90E-11, 0.0E+00, 0.0); {2012/06/07; Parrella2012; JPP}
Br2 + OH = HOBr + Br : GCARR(2.10E-11, 0.0E+00, 240.0); {2012/06/07; Parrella2012; JPP}
BrO + OH = Br + HO2 : GCARR(1.70E-11, 0.0E+00, 250.0); {2012/06/07; Parrella2012; JPP}
Br + NO3 = BrO + NO2 : GCARR(1.60E-11, 0.0E+00, 0.0); {2012/06/07; Parrella2012; JPP}
Br + CH2O = HBr + HO2 + CO : GCARR(1.70E-11, 0.0E+00, -800.0); {2012/06/07; Parrella2012; JPP}
Br + ALD2 = HBr + MCO3 : GCARR(1.80E-11, 0.0E+00, -460.0); {2017/07/27; Parrella2012,Fix C creation; SAS,BHH,MJE}
Br + ACET = HBr + ATO2 : GCARR(1.66E-10, 0.0E+00, -7000.0); {2017/07/27; Parrella2012,Fix C creation; SAS,BHH,MJE}
Br + C2H6 = HBr + ETO2 : GCARR(2.36E-10, 0.0E+00, -6411.0); {2017/07/27; Parrella2012,Fix C creation; SAS,BHH,MJE}
Br + C3H8 = HBr + A3O2 : GCARR(8.77E-11, 0.0E+00, -4330.0); {2017/07/27; Parrella2012,Fix C creation; SAS,BHH,MJE}
Br + NO2 {+M} = BrNO2 {+M} : GCJPLPR(4.20E-31, 2.4E+00, 0.0, 2.7E-11, 0.0, 0.0, 0.6, 0.0, 0.0); {2012/06/07; Parrella2012; JPP}
BrO + NO2 {+M} = BrNO3 {+M} : GCJPLPR(5.40E-31, 3.1E+00, 0.0, 6.5E-12, 2.9, 0.0, 0.6, 0.0, 0.0); {2017/02/22; JPL 15-10; BHH,MJE}
CHBr3 + OH = 3.000Br : GCARR(9.00E-13, 0.0E+00, -360.0); {2017/02/22; JPL 15-10; BHH,MJE}
CH2Br2 + OH = 2.000Br : GCARR(2.00E-12, 0.0E+00, -840.0); {2012/06/07; Parrella2012; JPP}
CH3Br + OH = Br + H2O + HO2 : GCARR(1.42E-12, 0.0E+00, -1150.0); {2017/03/08; JPL 15-10; TS,BHH,MJE}
OH + Cl2 = HOCl + Cl : GCARR(2.60E-12, 0.0E+00, -1100.0); {2014/02/03; Eastham2014; SDE}
MO2 + ClO = ClOO + HO2 + CH2O : GCARR(1.80E-11, 0.0E+00, -600.0); {2017/03/20; JPL 15-10; TS,BHH,MJE}
OH + ClO = HO2 + Cl : GCARR(7.40E-12, 0.0E+00, 270.0); {2014/02/03; Eastham2014; SDE}
OH + ClO = HCl + O2 : GCARR(6.00E-13, 0.0E+00, 230.0); {2014/02/03; Eastham2014; SDE}
OH + OClO = HOCl + O2 : GCARR(1.40E-12, 0.0E+00, 600.0); {2017/02/22; JPL 15-10; BHH,MJE}
OH + Cl2O2 = HOCl + ClOO : GCARR(6.00E-13, 0.0E+00, 670.0); {2014/02/03; Eastham2014; SDE}

OH + HCl = H2O + Cl : GCARR(1.80E-12, 0.0E+00, -250.0); {2014/02/03; Eastham2014; SDE}
OH + HOCl = H2O + ClO : GCARR(3.00E-12, 0.0E+00, -500.0); {2014/02/03; Eastham2014; SDE}
OH + ClNO2 = HOCl + NO2 : GCARR(2.40E-12, 0.0E+00, -1250.0); {2014/02/03; Eastham2014; SDE}
OH + ClNO3 = HOCl + NO3 : GCARR(1.20E-12, 0.0E+00, -330.0); {2014/02/03; Eastham2014; SDE}
OH + CH3Cl = Cl + HO2 + H2O : GCARR(1.96E-12, 0.0E+00, -1200.0); {2017/02/22; JPL 15-10; BHH,MJE}
OH + CH2Cl2 = 2.000Cl + HO2 : GCARR(2.61E-12, 0.0E+00, -944.0); {2017/09/22; Sherwen2016b;TS,JAS,SDE}
OH + CHCl3 = 3.000Cl + HO2 : GCARR(4.69E-12, 0.0E+00, -1134.0); {2017/09/22; Sherwen2016b;TS,JAS,SDE}
CH4 + Cl = HCl + MO2 : GCARR(7.10E-12, 0.0E+00, -1270.0); {2017/03/08; JPL 15-10; TS,BHH,MJE}
CH2O + Cl = CO + HCl + HO2 : GCARR(7.32E-11, 0.0E+00, -30.0); {2017/09/22; Sherwen2016b; TS,JAS,SDE}
Cl + O3 = ClO + O2 : GCARR(2.30E-11, 0.0E+00, -200.0); {2014/02/03; Eastham2014; SDE}
Cl + H2O2 = HO2 + HCl : GCARR(1.10E-11, 0.0E+00, -980.0); {2014/02/03; Eastham2014; SDE}
Cl + HO2 = O2 + HCl : GCARR(1.40E-11, 0.0E+00, 270.0); {2014/02/03; Eastham2014; SDE}
Cl + HO2 = OH + ClO : GCARR(3.60E-11, 0.0E+00, -375.0); {2014/02/03; Eastham2014; SDE}
ClO + HO2 = O2 + HOCl : GCARR(2.60E-12, 0.0E+00, 290.0); {2014/02/03; Eastham2014; SDE}
ClO + NO = Cl + NO2 : GCARR(6.40E-12, 0.0E+00, 290.0); {2014/02/03; Eastham2014; SDE}
ClO + NO2 {+M} = ClNO3 {+M} : GCJPLPR(1.80E-31, 3.4E+00, 0.0, 1.50E-11, 1.9E0, 0.0, 0.6, 0.0, 0.0); {2014/02/03; Eastham2014; SDE}
ClO + ClO = Cl2 + O2 : GCARR(1.00E-12, 0.0E+00, -1590.0); {2014/02/03; Eastham2014; SDE}
ClO + ClO = Cl + ClOO : GCARR(3.00E-11, 0.0E+00, -2450.0); {2014/02/03; Eastham2014; SDE}
ClO + ClO = OClO + Cl : GCARR(3.50E-13, 0.0E+00, -1370.0); {2014/02/03; Eastham2014; SDE}
Cl {+M} = ClOO {+M} : GCJPLPR(2.20E-33, 3.1E+00, 0.0, 1.8E-10, 0.0, 0.0, 0.6, 0.0, 0.0); {2014/02/03; Eastham2014; SDE}
ClOO {+M} = Cl + O2 {+M} : GCJPLPR(3.33E-09, 3.1E+00, -2502.0, 2.73E+14, 0.0, -2502.0, 0.6, 0.0, 0.0); {2014/02/03; Eastham2014; SDE}
ClO + ClO {+M} = Cl2O2 {+M} : GCJPLPR(1.90E-32, 3.6E+00, 0.0, 3.7E-12, 1.6, 0.0, 0.6, 0.0, 0.0); {2017/02/22; JPL 15-10; BHH,MJE}
Cl2O2 {+M} = 2.000ClO {+M} : GCJPLPR(9.30E-06, 4.5E+00, -8649.0, 1.74E+15, 2.0E0, -8649.0, 0.6, 0.0, 0.0);

ClOO + Cl = Cl2 + O2 : GCARR(2.30E-10, 0.0E+00, 0.0); {2014/02/03; Eastham2014; SDE}
ClOO + Cl = 2.000ClO : GCARR(1.20E-11, 0.0E+00, 0.0); {2014/02/03; Eastham2014; SDE}
ClO + BrO = Br + OClO : GCARR(9.50E-13, 0.0E+00, 550.0); {2014/02/03; Eastham2014; SDE}
ClO + BrO = Br + ClOO : GCARR(2.30E-12, 0.0E+00, 260.0); {2014/02/03; Eastham2014; SDE}
ClO + BrO = BrCl + O2 : GCARR(4.10E-13, 0.0E+00, 290.0); {2014/02/03; Eastham2014; SDE}
ClNO3 + Cl = Cl2 + NO3 : GCARR(6.50E-12, 0.0E+00, 135.0); {2014/02/03; Eastham2014; SDE}
CH3Cl + Cl = CO + 2.000HCl + HO2 : GCARR(2.17E-11, 0.0E+00, -1130.0); {2014/02/03; Eastham2014; SDE}
CH2Cl2 + Cl = CO + HCl + 2.000Cl + HO2 : GCARR(1.24E-12, 0.0E+00, -1070.0); {2017/09/22; Sherwen2016b;TS,JAS,SDE}
CHCl3 + Cl = CO + HCl + 3.000Cl + HO2 : GCARR(3.77E-12, 0.0E+00, -1011.0); {2017/09/22; Sherwen2016b;TS,JAS,SDE}
Cl + HCOOH = HCl + CO2 + H2O : GCARR(2.00E-13, 0.0E+00, 0.0); {2017/09/22; Sherwen2016b;TS,JAS,SDE}
Cl + MO2 = ClO + CH2O + HO2 : GCARR(1.60E-10, 0.0E+00, 0.0); {2017/09/22; Sherwen2016b;TS,JAS,SDE}
Cl + MP = HCl + MO2 : GCARR(5.7E-11, 0.0E+00, 0.0); {2017/09/22; Sherwen2016b;TS,JAS,SDE}
Cl + C2H6 = HCl + ETO2 : GCARR(7.2E-11, 0.0E+00, -70.0); {2017/09/22; Sherwen2016b;TS,JAS,SDE}
Cl + ETO2 = ClO + HO2 + ALD2 : GCARR(7.4E-11, 0.0E+00, 0.0); {2017/09/22; Sherwen2016b;TS,JAS,SDE}
Cl + MOH = HCl + CH2O + HO2 : GCARR(5.5E-11, 0.0E+00, 0.0); {2017/09/22; Sherwen2016b;TS,JAS,SDE}
Cl + EOH = HCl + ALD2 : GCARR(9.6E-11, 0.0E+00, 0.0); {2017/09/22; Sherwen2016b;TS,JAS,SDE}
Cl + ACTA = HCl + MO2 + CO2 : GCARR(2.8E-14, 0.0E+00, 0.0); {2017/09/22; Sherwen2016b;TS,JAS,SDE}
Cl + C3H8 = HCl + B3O2 : GCARR(6.54E-11, 0.0E+00, 60.0); {2017/09/22; Sherwen2016b;TS,JAS,SDE}
Cl + C3H8 = HCl + A3O2 : GCARR(8.12E-11, 0.0E+00, -90.0); {2017/09/22; Sherwen2016b;TS,JAS,SDE}
Cl + ACET = HCl + ATO2 : GCARR(7.70E-11, 0.0E+00, -1000.0); {2017/09/22; Sherwen2016b;TS,JAS,SDE}
Cl + ISOP = HCl + RIO2 : GCARR(7.60E-11, 0.0E+00, 500.0); {2017/09/22; Sherwen2016b;TS,JAS,SDE}
Cl + ALK6 = HCl + R6O2 : GCARR(2.05E-10, 0.0E+00, 0.0); {2017/09/22; Sherwen2016b;TS,JAS,SDE} {2019/11/21; Speciate Alk4; JFB}
Cl + IBUT = HCl + IBO2 : GCARR(2.05E-10, 0.0E+00, 0.0); {2017/09/22; Sherwen2016b;TS,JAS,SDE} {2019/11/21; Speciate Alk4; JFB}

Cl + NBUT = HCl + NBO2 : GCARR(2.05E-10, 0.0E+00, 0.0); {2017/09/22; Sherwen2016b;TS,JAS,SDE} {2019/11/21; Speciate Alk4; JFB}
Cl + IPENT = HCl + IPO2 : GCARR(2.05E-10, 0.0E+00, 0.0); {2017/09/22; Sherwen2016b;TS,JAS,SDE} {2019/11/21; Speciate Alk4; JFB}
Cl + NPENT = HCl + NPO2 : GCARR(2.05E-10, 0.0E+00, 0.0); {2017/09/22; Sherwen2016b;TS,JAS,SDE} {2019/11/21; Speciate Alk4; JFB}
Cl + PRPE {+M} = HCl + PO2 {+M} : GCJPLPR(4.00E-28, 0.0E+00, 0.0, 2.8E-10, 0.0E0, 0.0, 0.6, 0.0, 0.0); {2017/09/22; Sherwen2016b;TS,JAS,SDE}
Br + PRPE = HBr + PO2 : GCARR(3.60E-12, 0.0E+00, 0.0); {2017/09/22; Sherwen2016b;TS,JAS,SDE}
I + NO {+M} = INO {+M} : GCJPLPR(1.80E-32, 1.0E+00, 0.0, 1.77E-11, 0.0, 0.0, 0.6, 0.0, 0.0); {2017/09/22; Sherwen2016b;TS,JAS,SDE}
INO + INO = I2 + 2.000NO : GCARR(8.40E-11, 0.0E+00, -2620.0); {2017/09/22; Sherwen2016b;TS,JAS,SDE}
I + NO2 {+M} = IONO {+M} : GCJPLPR(3.00E-31, 1.0E+00, 0.0, 6.6E-11, 0.0, 0.0, 0.63, 0.0, 0.0); {2017/09/22; Sherwen2016b;TS,JAS,SDE}
IONO {+M} = I + NO2 {+M} : GCARR(9.94E+17, 0.0E+00, -11859.0); {2017/09/22; Sherwen2016b;TS,JAS,SDE}
IONO + IONO = I2 + 2.000NO2 : GCARR(2.90E-11, 0.0E+00, -2600.0); {2017/09/22; Sherwen2016b;TS,JAS,SDE}
I2 + NO3 = I + IONO2 : GCARR(1.50E-12, 0.0E+00, 0.0); {2017/09/22; Sherwen2016b;TS,JAS,SDE}
IO + NO2 {+M} = IONO2 {+M} : GCJPLPR(7.50E-31, 3.5E+00, 0.0, 7.6E-12, 1.5E0, 0.0, 0.6, 0.0, 0.0); {2017/09/22; Sherwen2016b;TS,JAS,SDE}
IONO2 {+M} = IO + NO2 {+M} : GCARR(2.10E+15, 0.0E+00, -13670.0); {2017/09/22; Sherwen2016b;TS,JAS,SDE}
IONO2 + I = I2 + NO3 : GCARR(9.10E-11, 0.0E+00, -146.0); {2017/09/22; Sherwen2016b;TS,JAS,SDE}
I + BrO = IO + Br : GCARR(1.20E-11, 0.0E+00, 0.0); {2017/09/22; Sherwen2016b;TS,JAS,SDE}
IO + BrO = Br + I + O2 : GCARR(3.00E-12, 0.0E+00, 510.0); {2017/09/22; Sherwen2016b;TS,JAS,SDE}
IO + BrO = Br + OIO : GCARR(1.20E-11, 0.0E+00, 510.0); {2017/09/22; Sherwen2016b;TS,JAS,SDE}
IO + OIO {+M} = I2O3 {+M} : GCARR(1.00E-10, 0.0E+00, 0.0); {2017/09/22; Sherwen2016b;TS,JAS,SDE}
OIO + OIO = I2O4 : GCARR(1.50E-10, 0.0E+00, 0.0); {2017/09/22; Sherwen2016b;TS,JAS,SDE}
I2O4 {+M} = 2.000OIO {+M} : GCARR(3.80E-02, 0.0E+00, 0.0); {2017/09/22; Sherwen2016b;TS,JAS,SDE}
OIO + NO = IO + NO2 : GCARR(1.10E-12, 0.0E+00, 542.0); {2017/09/22; Sherwen2016b;TS,JAS,SDE}
IO + ClO = I + OClO : GCARR(5.10E-12, 0.0E+00, 280.0); {2017/09/22; Sherwen2016b;TS,JAS,SDE}
IO + ClO = I + Cl + O2 : GCARR(2.81E-12, 0.0E+00, 280.0); {2017/09/22; Sherwen2016b;TS,JAS,SDE}

IO + ClO = ICl + O2 : GCARR(1.02E-12, 0.0E+00, 280.0); {2017/09/22; Sherwen2016b;TS,JAS,SDE}
I + O3 = IO + O2 : GCARR(2.30E-11, 0.0E+00, -870.0); {2017/09/22; Sherwen2016b;TS,JAS,SDE}
I + HO2 = HI + O2 : GCARR(1.50E-11, 0.0E+00, -1090.0); {2017/09/22; Sherwen2016b;TS,JAS,SDE}
I2 + OH = HOI + I : GCARR(1.80E-10, 0.0E+00, 0.0); {2017/09/22; Sherwen2016b;TS,JAS,SDE}
HI + OH = I + H2O : GCARR(3.00E-11, 0.0E+00, 0.0); {2017/09/22; Sherwen2016b;TS,JAS,SDE}
HOI + OH = IO + H2O : GCARR(5.00E-12, 0.0E+00, 0.0); {2017/09/22; Sherwen2016b;TS,JAS,SDE}
IO + HO2 = HOI + O2 : GCARR(1.30E-11, 0.0E+00, 570.0); {2017/09/22; Sherwen2016b;TS,JAS,SDE}
IO + NO = I + NO2 : GCARR(9.10E-12, 0.0E+00, 240.0); {2017/09/22; Sherwen2016b;TS,JAS,SDE}
IO + IO = I + OIO : GCARR(6.00E-12, 0.0E+00, 500.0); {2017/09/22; Sherwen2016b;TS,JAS,SDE}
IO + IO {+M} = I2O2 {+M} : GCARR(9.00E-12, 0.0E+00, 500.0); {2017/09/22; Sherwen2016b;TS,JAS,SDE}
I2O2 {+M} = 2.000IO {+M} : GCARR(1.00E+12, 0.0E+00, -9770.0); {2017/09/22; Sherwen2016b;TS,JAS,SDE}
I2O2 {+M} = OIO + I {+M} : GCARR(2.50E+14, 0.0E+00, -9770.0); {2017/09/22; Sherwen2016b;TS,JAS,SDE}
CH3I + OH = H2O + I + MO2 : GCARR(2.90E-12, 0.0E+00, -1100.0); {2017/09/22; Sherwen2016b;TS,JAS,SDE}
HC5 + OH = HC5OO : GCARR(3.35E-11, 0.0E+00, 380.0); {2013/03/22; Paulot2009; FP,EAM,JMAO,MJE}
HC5OO + NO = NO2 + 0.216GLYX + 0.234MGLY +
0.234GLYC + 0.216HAC + 0.290DHMOB +
0.170MOBA + 0.090RCHO + HO2 + 0.090CO : GC_RO2NO('B', 2.70E-12, 0.0E+00, 350.0, 5.0, 0.0, 0.0); {2013/03/22; Paulot2009; FP,EAM,JMAO,MJE}
HC5OO + NO = HNO3 : GC_RO2NO('A', 2.70E-12, 0.0E+00, 350.0, 5.0, 0.0, 0.0); {2013/03/22; Paulot2009; FP,EAM,JMAO,MJE}
HC5OO + HO2 = 0.100IAP + 0.900OH +
0.900MGLY + 0.900GLYC + 0.900HO2 : GC_RO2HO2(2.91E-13, 0.0E+00, 1300.0, 5.0, 0.0, 0.0); {2013/03/22; Paulot2009; FP,EAM,JMAO,MJE}
ISOPND + OH = 0.100IEPOXD +
0.900ISOPNDO2 + 0.100NO2 : GCARR(1.20E-11, 0.0E+00, 652.0); {2017/07/14; Jacobs2014,Lee2014; KRT,JAF,CCM,EAM,KHB,RHS}
ISOPNB + OH = 0.900ISOPNBO2 +
0.067IEPOXA + 0.033IEPOXB + 0.100NO2 : GCARR(2.40E-12, 0.0E+00, 745.0); {2017/07/14; Jacobs2014,Lee2014; KRT,JAF,CCM,EAM,KHB,RHS}
ISOPNDO2 + NO = 0.019MACRN + 0.057HCOOH +
0.270HAC + 0.210ETHLN + 0.150CH2O +
0.790NO2 + 0.300GLYC + 0.300PROPNN +

0.610HO2 + 0.270DHDN + 0.075MVKN +
0.057ISOPNDO2 : GCARR(2.40E-12, 0.0E+00, 360.0); {2017/07/14;
Lee2014; KRT,JAF,CCM,EAM,KHB,RHS}
ISOPNDO2 + HO2 = 0.010MACRN + 0.200HAC +
0.200ETHLN + 0.070CH2O + 0.230GLYC +
0.230PROPNN + 0.500HO2 + 0.500OH +
0.060MVKN + 0.500ISNP : GCARR(8.70E-14, 0.0E+00, 1650.0); {2017/07/14;
Lee2014; KRT,JAF,CCM,EAM,KHB,RHS}
ISOPNBO2 + NO = 0.090GLYC + 0.090HAC +
0.700CH2O + 0.880NO2 + 0.440MACRN +
0.690HO2 + 0.260MVKN + 0.210DHDN : GCARR(2.40E-12, 0.0E+00, 360.0);
{2017/07/14; Lee2014; KRT,JAF,CCM,EAM,KHB,RHS}
ISOPNBO2 + HO2 = 0.060GLYC + 0.060HAC +
0.440CH2O + 0.280MACRN + 0.160MVKN +
0.060NO2 + 0.440HO2 + 0.500OH + 0.510ISNP : GCARR(8.70E-14, 0.0E+00, 1650.0);
{2017/07/14; Lee2014; KRT,JAF,CCM,EAM,KHB,RHS}
ISNP + OH = 0.612OH + 0.612IR4N1 +
0.193ISOPNBO2 + 0.193ISOPNDO2 : GCARR(4.75E-12, 0.0E+00, 200.0);
{2013/03/22; Paulot2009; FP,EAM,JMAO,MJE} {2018/07/16; Speciating C5 Ketone; JFB}
MVKN + OH = 0.650HCOOH + NO3 + 0.650MGLY +
0.350CH2O + 0.350PYAC : GCARR(4.40E-13, 0.0E+00, 380.0); {2017/06/15,
Marais2016, EAM}
MACRN + OH = MACRNO2 : GCARR(8.79E-13, 0.0E+00, 380.0);
{2017/06/15, Marais2016, EAM}
MACRNO2 + NO = 0.080ACTA + 0.080CH2O +
0.150NO3 + 0.070HCOOH + 0.070MGLY +
0.850HAC + 0.850NO2 + 0.930CO2 + NO2 : GCARR(2.70E-12, 0.0E+00, 350.0);
{2013/03/22; Paulot2009; FP,EAM,JMAO,MJE}
MACRNO2 + HO2 = 0.080ACTA + 0.080CH2O +
0.150NO3 + 0.070HCOOH + 0.070MGLY +
0.850HAC + 0.850NO2 + 0.930CO2 + OH : GC_RO2HO2(2.91E-13, 0.0E+00, 1300.0, 4.0,
0.0, 0.0); {2013/03/22; Paulot2009; FP,EAM,JMAO,MJE}
MACRNO2 + NO2 {+M} = PMNN : GCJPLPR(9.00E-28, 8.9E+00, 0.0, 7.7E-12,
0.2, 0.0, 0.6, 0.0, 0.0); {2013/03/22; Paulot2009; FP,EAM,JMAO,MJE}
PMNN = MACRNO2 + NO2 : GCJPLEQ(9.00E-29, 0.0E+00, 14000.0, 9.00E-28,
8.9E0, 0.0, 7.7E-12, 0.2, 0., 0.6, 0., 0.); {2013/03/22; Paulot2009; FP,EAM,JMAO,MJE}
DHMOB + OH = 1.500CO + HO2 + 0.500HAC +
0.500KET : GCARR(2.52E-12, 0.0E+00, 410.0); {2013/03/22;
Paulot2009; FP,EAM,JMAO,MJE} {2018/07/16; Speciating C5 Ketone; JFB}
DIBOO + NO = HO2 + NO2 + 0.520GLYC +
0.520MGLY + 0.480HAC + 0.480GLYX : GC_RO2NO('B', 2.70E-12, 0.0E+00, 350.0,
5.0, 0.0, 0.0); {2013/03/22; Paulot2009; FP,EAM,JMAO,MJE}
DIBOO + NO = HNO3 : GC_RO2NO('A', 2.70E-12, 0.0E+00, 350.0, 5.0, 0.0,
0.0); {2013/03/22; Paulot2009; FP,EAM,JMAO,MJE}
DIBOO + HO2 = 0.150HO2 + 0.150OH +
0.078GLYC + 0.078MGLY + 0.072HAC +

0.072GLYX + 0.850IR4P : GC_RO2HO2(2.91E-13, 0.0E+00, 1300.0, 5.0, 0.0, 0.0); {2013/03/22; Paulot2009; FP,EAM,JMAO,MJE} {2018/07/16; Speciating C5 Ketone; JFB}
MOBA + OH = MOBAOO : GCARR(2.79E-11, 0.0E+00, 380.0);
MOBAOO + NO = RCHO + CO2 + HO2 + NO2 : GC_RO2NO('B', 2.70E-12, 0.0E+00, 350.0, 5.0, 0.0, 0.0); {2013/03/22; Paulot2009; FP,EAM,JMAO,MJE}
MOBAOO + NO = HNO3 : GC_RO2NO('A', 2.70E-12, 0.0E+00, 350.0, 5.0, 0.0, 0.0); {2013/03/22; Paulot2009; FP,EAM,JMAO,MJE}
MOBAOO + HO2 = 0.500OH + 0.500HO2 + 0.500RCHO + 0.500CO2 + 0.500IR4P : GC_RO2HO2(2.91E-13, 0.0E+00, 1300.0, 4.0, 0.0, 0.0); {2013/03/22; Paulot2009; FP,EAM,JMAO,MJE} {2018/07/16; Speciating C5 Ketone; JFB}
MOBA + O3 = OH + HO2 + CO2 + KET : GCARR(2.00E-17, 0.0E+00, 0.0); {2013/03/22; Paulot2009; FP,EAM,JMAO,MJE}
ETHLN + OH = CH2O + CO2 + NO2 : GCARR(2.40E-12, 0.0E+00, 0.0); {2017/06/15, Marais2016, EAM}
PROPNN + OH = NO2 + MGLY : GCARR(6.70E-13, 0.0E+00, 0.0); {2017/07/14; MCMv3.3; KRT,JAF,CCM,EAM,KHB,RHS}
CH2OO + NO = CH2O + NO2 : GCARR(1.00E-14, 0.0E+00, 0.0); {2015/09/25; Millet2015; DBM,EAM}
CH2OO + NO2 = CH2O + NO3 : GCARR(1.00E-15, 0.0E+00, 0.0); {2015/09/25; Millet2015; DBM,EAM}
CH2OO + SO2 = CH2O + SO4 : GCARR(7.00E-14, 0.0E+00, 0.0); {2015/09/25; Millet2015; DBM,EAM}
CH2OO + H2O = CH2O + H2O2 : GCARR(6.00E-18, 0.0E+00, 0.0); {2015/09/25; Millet2015; DBM,EAM}
CH2OO + H2O = HCOOH : GCARR(1.00E-17, 0.0E+00, 0.0); {2015/09/25; Millet2015; DBM,EAM}
MACROO + CO = MACR : GCARR(1.20E-15, 0.0E+00, 0.0); {2015/09/25; Millet2015; DBM,EAM}
MACROO + NO = MACR + NO2 : GCARR(1.00E-14, 0.0E+00, 0.0); {2015/09/25; Millet2015; DBM,EAM}
MACROO + NO2 = MACR + NO3 : GCARR(1.00E-15, 0.0E+00, 0.0); {2015/09/25; Millet2015; DBM,EAM}
MACROO + SO2 = MACR + SO4 : GCARR(7.00E-14, 0.0E+00, 0.0); {2015/09/25; Millet2015; DBM,EAM}
MACROO + H2O = MRP : GCARR(1.00E-17, 0.0E+00, 0.0); {2015/09/25; Millet2015; DBM,EAM}
MACROO + H2O = MACR + H2O2 : GCARR(6.00E-18, 0.0E+00, 0.0); {2015/09/25; Millet2015; DBM,EAM}
MVKOO + CO = MVK : GCARR(1.20E-15, 0.0E+00, 0.0); {2015/09/25; Millet2015; DBM,EAM}
MVKOO + NO = MVK + NO2 : GCARR(1.00E-14, 0.0E+00, 0.0); {2015/09/25; Millet2015; DBM,EAM}
MVKOO + NO2 = MVK + NO3 : GCARR(1.00E-15, 0.0E+00, 0.0); {2015/09/25; Millet2015; DBM,EAM}

MVKOO + SO2 = MVK + SO4 : GCARR(7.00E-14, 0.0E+00, 0.0);
{2015/09/25; Millet2015; DBM,EAM}
MVKOO + H2O = MVK + H2O2 : GCARR(6.00E-18, 0.0E+00, 0.0);
{2015/09/25; Millet2015; DBM,EAM}
MGLYOO + CO = MGLY : GCARR(1.20E-15, 0.0E+00, 0.0); {2015/09/25;
Millet2015; DBM,EAM}
MGLYOO + NO = MGLY + NO2 : GCARR(1.00E-14, 0.0E+00, 0.0);
{2015/09/25; Millet2015; DBM,EAM}
MGLYOO + NO2 = MGLY + NO3 : GCARR(1.00E-15, 0.0E+00, 0.0);
{2015/09/25; Millet2015; DBM,EAM}
MGLYOO + SO2 = MGLY + SO4 : GCARR(7.00E-14, 0.0E+00, 0.0);
{2015/09/25; Millet2015; DBM,EAM}
MGLYOO + H2O = MGLY + H2O2 : GCARR(6.00E-18, 0.0E+00, 0.0);
{2015/09/25; Millet2015; DBM,EAM}
MGLOO + CO = MGLY : GCARR(1.20E-15, 0.0E+00, 0.0); {2015/09/25;
Millet2015; DBM,EAM}
MGLOO + NO = MGLY + NO2 : GCARR(1.00E-14, 0.0E+00, 0.0);
{2015/09/25; Millet2015; DBM,EAM}
MGLOO + NO2 = MGLY + NO3 : GCARR(1.00E-15, 0.0E+00, 0.0);
{2015/09/25; Millet2015; DBM,EAM}
MGLOO + SO2 = MGLY + SO4 : GCARR(7.00E-14, 0.0E+00, 0.0);
{2015/09/25; Millet2015; DBM,EAM}
MGLOO + H2O = MCO3 + MO2 : GCARR(1.00E-17, 0.0E+00, 0.0);
{2015/09/25; Millet2015; DBM,EAM}
MGLOO + H2O = MGLY + H2O2 : GCARR(6.00E-18, 0.0E+00, 0.0);
{2015/09/25; Millet2015; DBM,EAM}
CH3CHOO + CO = ALD2 : GCARR(1.20E-15, 0.0E+00, 0.0); {2015/09/25;
Millet2015; DBM,EAM}
CH3CHOO + NO = ALD2 + NO2 : GCARR(1.00E-14, 0.0E+00, 0.0);
{2015/09/25; Millet2015; DBM,EAM}
CH3CHOO + NO2 = ALD2 + NO3 : GCARR(1.00E-15, 0.0E+00, 0.0);
{2015/09/25; Millet2015; DBM,EAM}
CH3CHOO + SO2 = ALD2 + SO4 : GCARR(7.00E-14, 0.0E+00, 0.0);
{2015/09/25; Millet2015; DBM,EAM}
CH3CHOO + H2O = ALD2 + H2O2 : GCARR(6.00E-18, 0.0E+00, 0.0);
{2015/09/25; Millet2015; DBM,EAM}
CH3CHOO + H2O = ACTA : GCARR(1.00E-17, 0.0E+00, 0.0); {2015/09/25;
Millet2015; DBM,EAM}
GAOO + CO = GLYC : GCARR(1.20E-15, 0.0E+00, 0.0); {2015/09/25;
Millet2015; DBM,EAM}
GAOO + NO = GLYC + NO2 : GCARR(1.00E-14, 0.0E+00, 0.0); {2015/09/25;
Millet2015; DBM,EAM}
GAOO + NO2 = GLYC + NO3 : GCARR(1.00E-15, 0.0E+00, 0.0);
{2015/09/25; Millet2015; DBM,EAM}
GAOO + SO2 = GLYC + SO4 : GCARR(7.00E-14, 0.0E+00, 0.0); {2015/09/25;
Millet2015; DBM,EAM}

```
GAOO + H2O = GLYC + H2O2 :                GCARR(6.00E-18, 0.0E+00, 0.0);
{2015/09/25; Millet2015; DBM,EAM}
GAOO + H2O = HAC :                        GCARR(1.00E-17, 0.0E+00, 0.0);       {2015/09/25;
Millet2015; DBM,EAM}
BENZ + OH = BRO2 + 1.920CH2O + 0.252GLYX +
 OH :                                     GCARR(2.33E-12, 0.0E+00, -193.0);    {2017/03/23; Fischer2014
; EVF}
TOLU + OH = TRO2 + 1.920CH2O + 0.260GLYX +
 0.215MGLY + OH :                         GCARR(1.81E-12, 0.0E+00, 338.0);     {2017/03/23;
Fischer2014 ; EVF}
XYLE + OH = XRO2 + 1.920CH2O + 0.268GLYX +
 0.463MGLY + OH :                         GCARR(2.31E-11, 0.0E+00, 0.0);       {2017/03/23;
Fischer2014 ; EVF}
XYLE + NO3 = CO2 :                        GCARR(2.60E-16, 0.0E+00, 0.0);
BRO2 + HO2 = LBRO2H :                      GCARR(1.40E-12, 0.0E+00, 700.0);
BRO2 + NO = LBRO2N :                       GCARR(2.60E-12, 0.0E+00, 350.0);
TRO2 + HO2 = LTRO2H :                      GCARR(1.40E-12, 0.0E+00, 700.0);
TRO2 + NO = LTRO2N :                       GCARR(2.60E-12, 0.0E+00, 350.0);
XRO2 + HO2 = LXRO2H :                      GCARR(1.40E-12, 0.0E+00, 700.0);
XRO2 + NO = LXRO2N :                       GCARR(2.60E-12, 0.0E+00, 350.0);
MTPA + OH = PIO2 :                        GCARR(1.21E-11, 0.0E+00, 440.0);     {2017/03/23;
IUPAC2010; EVF}
MTPO + OH = PIO2 :                        GCARR(1.21E-11, 0.0E+00, 440.0);     {2017/03/23;
IUPAC2010; EVF}
PIO2 + NO = 0.820HO2 + 0.820NO2 +
 0.230CH2O + 0.430RCHO + 0.110ACET +
 0.440KET + 0.070HCOOH + 0.120MONITS +
 0.060MONITU :                            GCARR(4.00E-12, 0.0E+00, 0.0);       {2017/07/14;
Browne2014; KRT,JAF,CCM,EAM,KHB,RHS} {2018/07/16; Speciating C5 Ketone; JFB}
PIO2 + HO2 = PIP :                        GCARR(1.50E-11, 0.0E+00, 0.0);       {2017/03/23;
Roberts1992; EVF}
PIO2 + MO2 = HO2 + 0.750CH2O + 0.250MOH +
 0.250ROH + 0.750RCHO + 0.750KET :        GCARR(3.56E-14, 0.0E+00, 708.0);
{2017/07/14; Roberts1992; KRT,JAF,CCM,EAM,KHB,RHS} {2018/07/16; Speciating C5
Ketone; JFB}
PIO2 + MCO3 = 0.500HO2 + 0.500MO2 + RCHO +
 KET + RCOOH :                            GCARR(7.40E-13, 0.0E+00, 765.0);     {2017/03/23;
Roberts1992; EVF} {2018/07/16; Speciating C5 Ketone; JFB}
PIO2 + NO3 = HO2 + NO2 + RCHO + KET :     GCARR(1.20E-12, 0.0E+00, 0.0);
{2017/03/23; Roberts1992; EVF} {2018/07/16; Speciating C5 Ketone; JFB}
MTPA + O3 = 0.850OH + 0.100HO2 +
 0.620KETO2 + 0.140CO + 0.020H2O2 +
 0.650RCHO + 0.530KET :                   GCARR(5.00E-16, 0.0E+00, -530.0);    {2017/07/14;
Atkinson2003; KRT,JAF,CCM,EAM,KHB,RHS} {2018/07/16; Speciating C5 Ketone; JFB}
MTPO + O3 = 0.850OH + 0.100HO2 +
 0.620KETO2 + 0.140CO + 0.020H2O2 +
```

0.650RCHO + 0.530KET : GCARR(5.00E-16, 0.0E+00, -530.0); {2017/07/14; Atkinson2003; KRT,JAF,CCM,EAM,KHB,RHS} {2018/07/16; Speciating C5 Ketone; JFB}
MTPA + NO3 = 0.100OLNN + 0.900OLND : GCARR(8.33E-13, 0.0E+00, 490.0); {2017/07/14; Fisher2016; KRT,JAF,CCM,EAM,KHB,RHS}
MTPO + NO3 = 0.100OLNN + 0.900OLND : GCARR(8.33E-13, 0.0E+00, 490.0); {2017/07/14; Fisher2016; KRT,JAF,CCM,EAM,KHB,RHS}
LIMO + OH = LIMO2 : GCARR(4.20E-11, 0.0E+00, 401.0); {2017/07/14; Gill2002; KRT,JAF,CCM,EAM,KHB,RHS}
LIMO + O3 = 0.850OH + 0.100HO2 +
0.160ETO2 + 0.420KETO2 + 0.020H2O2 +
0.140CO + 0.460PRPE + 0.040CH2O +
0.790MACR + 0.010HCOOH + 0.070RCOOH : GCARR(2.95E-15, 0.0E+00, -783.0); {2017/07/14; Atkinson2003; KRT,JAF,CCM,EAM,KHB,RHS} {2018/07/16; Speciating C5 Ketone; JFB}
LIMO + NO3 = 0.500OLNN + 0.500OLND : GCARR(1.22E-11, 0.0E+00, 0.0); {2017/07/14; Fry2014,Atkinson2003; KRT,JAF,CCM,EAM,KHB,RHS}
LIMO2 + NO = 0.686HO2 + 0.780NO2 +
0.220MONITU + 0.289PRPE + 0.231CH2O +
0.491RCHO + 0.058HAC + 0.289KET : GCARR(4.00E-12, 0.0E+00, 0.0); {2017/07/14; Browne2014,Roberts1992; KRT,JAF,CCM,EAM,KHB,RHS} {2018/07/16; Speciating C5 Ketone; JFB}
LIMO2 + HO2 = PIP : GCARR(1.50E-11, 0.0E+00, 0.0); {2017/07/14; Roberts1992; KRT,JAF,CCM,EAM,KHB,RHS}
LIMO2 + MO2 = HO2 + 0.192PRPE +
1.040CH2O + 0.308MACR + 0.250MOH +
0.250ROH : GCARR(3.56E-14, 0.0E+00, 708.0); {2017/07/14; Roberts1992; KRT,JAF,CCM,EAM,KHB,RHS}
LIMO2 + MCO3 = 0.500HO2 + 0.500MO2 +
0.192PRPE + 0.385CH2O + 0.308MACR +
0.500RCOOH : GCARR(7.40E-13, 0.0E+00, 765.0); {2017/07/14; Roberts1992; KRT,JAF,CCM,EAM,KHB,RHS}
LIMO2 + NO3 = HO2 + NO2 + 0.385PRPE +
0.385CH2O + 0.615MACR : GCARR(1.20E-12, 0.0E+00, 0.0); {2017/07/14; Roberts1992; KRT,JAF,CCM,EAM,KHB,RHS}
PIP + OH = 0.490OH + 0.440IR4O2 +
0.080RCHO + 0.410KET : GCARR(3.40E-12, 0.0E+00, 190.0); {2017/07/14; Goliff2013; KRT,JAF,CCM,EAM,KHB,RHS}
OLNN + NO = HO2 + NO2 + MONITS : GCARR(4.00E-12, 0.0E+00, 0.0); {2017/07/14; Browne2014,Goliff2013; KRT,JAF,CCM,EAM,KHB,RHS}
OLND + NO = 2.000NO2 + 0.287CH2O +
1.240RCHO + 0.464KET : GCARR(4.00E-12, 0.0E+00, 0.0); {2017/07/14; Goliff2013; KRT,JAF,CCM,EAM,KHB,RHS} {2018/07/16; Speciating C5 Ketone; JFB}
OLNN + HO2 = 0.700MONITS + 0.300MONITU : GCARR(1.66E-13, 0.0E+00, 1300.0); {2017/07/14; Browne2014,Roberts1992; KRT,JAF,CCM,EAM,KHB,RHS}
OLND + HO2 = 0.700MONITS + 0.300MONITU : GCARR(1.66E-13, 0.0E+00, 1300.0); {2017/07/14; Browne2014,Roberts1992; KRT,JAF,CCM,EAM,KHB,RHS}

OLNN + MO2 = 2.000HO2 + CH2O +
 0.700MONITS + 0.300MONITU : GCARR(1.60E-13, 0.0E+00, 708.0);
{2017/07/14; Browne2014,Roberts1992; KRT,JAF,CCM,EAM,KHB,RHS}
OLND + MO2 = 0.500HO2 + 0.500NO2 +
 0.965CH2O + 0.930RCHO + 0.348KET +
 0.250MOH + 0.250ROH + 0.350MONITS +
 0.150MONITU : GCARR(9.68E-14, 0.0E+00, 708.0); {2017/07/14;
Browne2014,Roberts1992; KRT,JAF,CCM,EAM,KHB,RHS} {2018/07/16; Speciating C5
Ketone; JFB}
OLNN + MCO3 = HO2 + MO2 + 0.700MONITS +
 0.300MONITU : GCARR(8.85E-13, 0.0E+00, 765.0); {2017/07/14;
Browne2014,Roberts1992; KRT,JAF,CCM,EAM,KHB,RHS}
OLND + MCO3 = 0.500MO2 + NO2 + 0.287CH2O +
 1.240RCHO + 0.464KET + 0.500RCOOH : GCARR(5.37E-13, 0.0E+00, 765.0);
{2017/07/14; Browne2014,Roberts1992; KRT,JAF,CCM,EAM,KHB,RHS} {2018/07/16;
Speciating C5 Ketone; JFB}
OLNN + NO3 = HO2 + NO2 + 0.700MONITS +
 0.300MONITU : GCARR(1.20E-12, 0.0E+00, 0.0); {2017/07/14;
Browne2014,Roberts1992; KRT,JAF,CCM,EAM,KHB,RHS}
OLND + NO3 = 2.000NO2 + 0.287CH2O +
 1.240RCHO + 0.464KET : GCARR(1.20E-12, 0.0E+00, 0.0); {2017/07/14;
Browne2014,Roberts1992; KRT,JAF,CCM,EAM,KHB,RHS} {2018/07/16; Speciating C5
Ketone; JFB}
OLNN + OLNN = HO2 + 1.400MONITS +
 0.600MONITU : GCARR(7.00E-14, 0.0E+00, 1000.0); {2017/07/14;
Browne2014,Roberts1992; KRT,JAF,CCM,EAM,KHB,RHS}
OLNN + OLND = 0.500HO2 + 0.500NO2 +
 0.202CH2O + 0.640RCHO + 0.149KET +
 1.050MONITS + 0.450MONITU : GCARR(4.25E-14, 0.0E+00, 1000.0);
{2017/07/14; Browne2014,Roberts1992; KRT,JAF,CCM,EAM,KHB,RHS} {2018/07/16;
Speciating C5 Ketone; JFB}
OLND + OLND = NO2 + 0.504CH2O +
 1.210RCHO + 0.285KET + 0.700MONITS +
 0.300MONITU : GCARR(2.96E-14, 0.0E+00, 1000.0); {2017/07/14;
Browne2014,Roberts1992; KRT,JAF,CCM,EAM,KHB,RHS} {2018/07/16; Speciating C5
Ketone; JFB}
MONITS + OH = HONIT : GCARR(4.80E-12, 0.0E+00, 0.0); {2017/07/14;
Browne2014; KRT,JAF,CCM,EAM,KHB,RHS}
MONITU + OH = HONIT : GCARR(7.29E-11, 0.0E+00, 0.0); {2017/07/14;
Browne2014; KRT,JAF,CCM,EAM,KHB,RHS}
MONITU + O3 = HONIT : GCARR(1.67E-16, 0.0E+00, 0.0); {2017/07/14;
Browne2014; KRT,JAF,CCM,EAM,KHB,RHS}
MONITU + NO3 = HONIT : GCARR(3.15E-13, 0.0E+00, -448.0); {2017/07/14;
Fisher2016; KRT,JAF,CCM,EAM,KHB,RHS}
MONITS + NO3 = HONIT : GCARR(3.15E-13, 0.0E+00, -448.0); {2017/07/14;
Fisher2016; KRT,JAF,CCM,EAM,KHB,RHS}

```
IONITA = INDIOL + HNO3 :                GCARR(2.78E-04, 0.0E+00, 0.0);      {2017/07/14;
Fisher2016; KRT,JAF,CCM,EAM,KHB,RHS}
MONITA = INDIOL + HNO3 :                GCARR(2.78E-04, 0.0E+00, 0.0);      {2017/07/14;
Fisher2016; KRT,JAF,CCM,EAM,KHB,RHS}
HONIT + OH = NO3 + HAC :                GC_OHHNO3(2.41E-14, 0.0E+00, 460.0, 2.69E-17,
0.E0, 2199., 6.51E-34, 0.E0, 1335.0); {2017/07/14; Browne2014;
KRT,JAF,CCM,EAM,KHB,RHS}
HC187 + OH = 0.500MCO3 + 0.500MGLY +
 0.500HO2 + 0.500CO + CH2O :            GCARR(1.40E-11, 0.0E+00, 0.0);      {2017/07/14;
Bates2014; KRT,JAF,CCM,EAM,KHB,RHS}
HPALD + OH = 0.365HPC52O2 + 0.085GLYX +
 0.085MCO3 + 0.550MGLY + 0.550CO +
 0.550CH2O + 0.635OH + 0.085CO2 :       GCARR(5.10E-11, 0.0E+00, 0.0);
{2017/07/14; Peeters2010,Wolfe2012; KRT,JAF,CCM,EAM,KHB,RHS}
DHPCARP + NO = GLYX + MGLY + NO2 + OH :    GCARR(2.70E-12, 0.0E+00, 360.0);
{2017/07/14; Jenkin2015; KRT,JAF,CCM,EAM,KHB,RHS}
HPC52O2 + NO = GLYX + MGLY + NO2 + OH :    GCARR(2.70E-12, 0.0E+00, 360.0);
{2017/07/14; Jenkin2015; KRT,JAF,CCM,EAM,KHB,RHS}
DHPCARP + HO2 = RCOOH :                 GCARR(2.05E-13, 0.0E+00, 1300.0);
{2017/07/14; Jenkin2015; KRT,JAF,CCM,EAM,KHB,RHS}
HPC52O2 + HO2 = RCOOH :                 GCARR(2.05E-13, 0.0E+00, 1300.0);
{2017/07/14; Jenkin2015; KRT,JAF,CCM,EAM,KHB,RHS}
DHPCARP = RCOOH + CO + OH :             GCARR(2.90E+07, 0.0E+00, -5300.0);
{2017/07/14; Crounse2012; KRT,JAF,CCM,EAM,KHB,RHS}
DHPCARP = DHDC :                        GCARR(1.28E+07, 0.0E+00, -5300.0);  {2017/07/14;
Crounse2012; KRT,JAF,CCM,EAM,KHB,RHS}
//
// Heterogeneous reactions
//
HO2 = O2 :                              HET(ind_HO2,1);                     {2013/03/22; Paulot2009;
FP,EAM,JMAO,MJE}
NO2 = 0.500HNO3 + 0.500HNO2 :           HET(ind_NO2,1);
NO3 = HNO3 :                            HET(ind_NO3,1);
N2O5 + H2O = 2.000HNO3 :                HET(ind_N2O5,1);
N2O5 + HCl = ClNO2 + HNO3 :             HET(ind_N2O5,2);                    {2017/09/22;
Sherwen2016b;TS,JAS,SDE}
N2O5 = ClNO2 + HNO3 :                   HET(ind_N2O5,3);                    {2017/09/22;
Sherwen2016b;TS,JAS,SDE}
BrNO3 + H2O = HOBr + HNO3 :             HET(ind_BrNO3,1);                   {2014/02/03;
Eastham2014; SDE}
BrNO3 + HCl = BrCl + HNO3 :             HET(ind_BrNO3,2);                   {2014/02/03;
Eastham2014; SDE}
ClNO3 + H2O = HOCl + HNO3 :             HET(ind_ClNO3,1);                   {2014/02/03;
Eastham2014; SDE}
ClNO3 + HCl = Cl2 + HNO3 :              HET(ind_ClNO3,2);                   {2014/02/03;
Eastham2014; SDE}
```

ClNO3 + HBr = BrCl + HNO3 : HET(ind_ClNO3,3); {2014/02/03; Eastham2014; SDE}
ClNO3 + BrSALA = BrCl + HNO3 : HET(ind_ClNO3,4); {2017/09/22; Sherwen2016b;TS,JAS,SDE}
ClNO3 + BrSALC = BrCl + HNO3 : HET(ind_ClNO3,5); {2017/09/22; Sherwen2016b;TS,JAS,SDE}
HOCl + HCl = Cl2 + H2O : HET(ind_HOCl,1); {2014/02/03; Eastham2014; SDE}
HOCl + HBr = BrCl + H2O : HET(ind_HOCl,2); {2014/02/03; Eastham2014; SDE}
HOBr + HBr = Br2 + H2O : HET(ind_HOBr,1); {2017/09/22; Sherwen2016b;TS,JAS,SDE}
HOBr + HCl = BrCl + H2O : HET(ind_HOBr,2); {2017/09/22; Sherwen2016b;TS,JAS,SDE}
HOBr = BrCl + H2O : HET(ind_HOBr,3); {2017/09/22; Sherwen2016b;TS,JAS,SDE}
HOBr + BrSALA = Br2 : HET(ind_HOBr,4); {2017/09/22; Sherwen2016b;TS,JAS,SDE}
HOBr + BrSALC = Br2 : HET(ind_HOBr,5); {2017/09/22; Sherwen2016b;TS,JAS,SDE}
HOBr = SO4H1 + HBr : HET(ind_HOBr,6); {2017/11/15; Chen2017; QJC}
HOBr = SO4H2 + HBr : HET(ind_HOBr,7); {2017/11/15; Chen2017; QJC}
HCl = O2 : HET(ind_HCl,1); {2017/09/22; Sherwen2016b;TS,JAS,SDE}
HCl = O2 : HET(ind_HCl,2); {2017/09/22; Sherwen2016b;TS,JAS,SDE}
O3 + HBr = HOBr : HET(ind_O3,1); {2017/09/22; Sherwen2016b;TS,JAS,SDE}
O3 + BrSALA = HOBr : HET(ind_O3,2); {2017/09/22; Sherwen2016b;TS,JAS,SDE}
O3 + BrSALC = HOBr : HET(ind_O3,3); {2017/09/22; Sherwen2016b;TS,JAS,SDE}
HBr = BrSALA : HET(ind_HBr,1); {2017/09/22; Sherwen2016b;TS,JAS,SDE}
HBr = BrSALC : HET(ind_HBr,2); {2017/09/22; Sherwen2016b;TS,JAS,SDE}
HI = AERI : HET(ind_HI,1); {2017/09/22; Sherwen2016b;TS,JAS,SDE}
HI = ISALA : HET(ind_HI,2); {2017/09/22; Sherwen2016b;TS,JAS,SDE}
HI = ISALC : HET(ind_HI,3); {2017/09/22; Sherwen2016b;TS,JAS,SDE}
HOI = ISALA : HET(ind_HOI,1); {2017/09/22; Sherwen2016b;TS,JAS,SDE}

HOI = ISALC : HET(ind_HOI,2); {2017/09/22; Sherwen2016b;TS,JAS,SDE}
I2O2 = 2.000AERI : HET(ind_I2O2,1); {2017/09/22; Sherwen2016b;TS,JAS,SDE}
I2O2 = 2.000ISALA : HET(ind_I2O2,2); {2017/09/22; Sherwen2016b;TS,JAS,SDE}
I2O2 = 2.000ISALC : HET(ind_I2O2,3); {2017/09/22; Sherwen2016b;TS,JAS,SDE}
I2O3 = 2.000AERI : HET(ind_I2O3,1); {2017/09/22; Sherwen2016b;TS,JAS,SDE}
I2O3 = 2.000ISALA : HET(ind_I2O3,2); {2017/09/22; Sherwen2016b;TS,JAS,SDE}
I2O3 = 2.000ISALC : HET(ind_I2O3,3); {2017/09/22; Sherwen2016b;TS,JAS,SDE}
I2O4 = 2.000AERI : HET(ind_I2O4,1); {2017/09/22; Sherwen2016b;TS,JAS,SDE}
I2O4 = 2.000ISALA : HET(ind_I2O4,2); {2017/09/22; Sherwen2016b;TS,JAS,SDE}
I2O4 = 2.000ISALC : HET(ind_I2O4,3); {2017/09/22; Sherwen2016b;TS,JAS,SDE}
IONO = ISALA : HET(ind_IONO,1); {2017/09/22; Sherwen2016b;TS,JAS,SDE}
IONO = ISALC : HET(ind_IONO,2); {2017/09/22; Sherwen2016b;TS,JAS,SDE}
IONO2 = ISALA : HET(ind_IONO2,1); {2017/09/22; Sherwen2016b;TS,JAS,SDE}
IONO2 = ISALC : HET(ind_IONO2,2); {2017/09/22; Sherwen2016b;TS,JAS,SDE}
IONO = 0.850ICl + 0.150IBr + HNO2 : HET(ind_IONO,3); {2017/09/22; Sherwen2016b;TS,JAS,SDE}
IONO2 = 0.850ICl + 0.150IBr + HNO3 : HET(ind_IONO2,3); {2017/09/22; Sherwen2016b;TS,JAS,SDE}
HOI = 0.850ICl + 0.150IBr : HET(ind_HOI,3); {2017/09/22; Sherwen2016b;TS,JAS,SDE}
GLYX = SOAGX : HET(ind_GLYX,1); {2017/06/15; Marais2016, EAM}
MGLY = SOAMG : HET(ind_MGLY,1); {2017/06/15; Marais2016, EAM}
IEPOXA = SOAIE : HET(ind_IEPOXA,1); {2017/06/15; Marais2016, EAM}
IEPOXB = SOAIE : HET(ind_IEPOXB,1); {2017/06/15; Marais2016, EAM}
IEPOXD = SOAIE : HET(ind_IEPOXD,1); {2017/06/15; Marais2016, EAM}
IMAE = SOAME : HET(ind_IMAE,1); {2017/06/15; Marais2016, EAM}

```
LVOC = LVOCOA :                    HET(ind_LVOC,1);              {2017/06/15;
Marais2016, EAM}
ISN1OG = ISN1OA :                  HET(ind_ISN1OG,1);            {2017/06/15;
Marais2016, EAM}
ISOPND = IONITA :                  HET(ind_ISOPND,1);            {2017/06/15;
Marais2016, EAM}
ISOPNB = IONITA :                  HET(ind_ISOPNB,1);            {2017/06/15;
Marais2016, EAM}
MACRN = IONITA :                   HET(ind_MACRN,1);             {2017/06/15;
Marais2016, EAM}
MVKN = IONITA :                    HET(ind_MVKN,1);              {2017/06/15;
Marais2016, EAM}
R6N2 = IONITA :                    HET(ind_R6N2,1);              {2017/06/15; Marais2016,
EAM}  {2019/11/21; Speciate Alk4; JFB}
IBN2 = IONITA :                    HET(ind_IBN2,1);              {2017/06/15; Marais2016,
EAM}  {2019/11/21; Speciate Alk4; JFB}
NBN2 = IONITA :                    HET(ind_NBN2,1);              {2017/06/15;
Marais2016, EAM}  {2019/11/21; Speciate Alk4; JFB}
IPN2 = IONITA :                    HET(ind_IBN2,1);              {2017/06/15; Marais2016,
EAM}  {2019/11/21; Speciate Alk4; JFB}
NPN2 = IONITA :                    HET(ind_NBN2,1);              {2017/06/15; Marais2016,
EAM}  {2019/11/21; Speciate Alk4; JFB}
DHDN = IONITA :                    HET(ind_DHDN,1);              {2017/06/15;
Marais2016, EAM}
MONITS = MONITA :                  HET(ind_MONITS,1);            {2017/07/14;
Fisher2016; KRT,JAF,CCM,EAM,KHB,RHS}
MONITU = MONITA :                  HET(ind_MONITU,1);            {2017/07/14;
Fisher2016; KRT,JAF,CCM,EAM,KHB,RHS}
HONIT = MONITA :                   HET(ind_HONIT,1);             {2017/07/14;
Fisher2016; KRT,JAF,CCM,EAM,KHB,RHS}
//
// Photolysis reactions
//
O3 + hv = OH + OH :                PHOTOL(3);
O3 + hv = HO2 + OH :               PHOTOL(103);
NO2 + hv = NO + O3 :               PHOTOL(11);
H2O2 + hv = OH + OH :              PHOTOL(9);
MP + hv = CH2O + HO2 + OH :        PHOTOL(10);
CH2O + hv = HO2 + HO2 + CO :       PHOTOL(7);
CH2O + hv = H2 + CO :              PHOTOL(8);
HNO3 + hv = OH + NO2 :             PHOTOL(16);
HNO2 + hv = OH + NO :              PHOTOL(15);
HNO4 + hv = OH + NO3 :             PHOTOL(17);
HNO4 + hv = HO2 + NO2 :            PHOTOL(18);
NO3 + hv = NO2 + O3 :              PHOTOL(12);   {2014/02/03; Eastham2014; SDE}
NO3 + hv = NO + O2 :               PHOTOL(13);
```

```
N2O5 + hv = NO3 + NO2 :                    PHOTOL(14);
ALD2 + hv = 0.880MO2 + HO2 + 0.880CO +
 0.120MCO3 :                              PHOTOL(61);     {2014/12/19; FAST-JX v7.0 fix; JMAO}
ALD2 + hv = CH4 + CO :                     PHOTOL(62);
PAN + hv = 0.700MCO3 + 0.700NO2 +
 0.300MO2 + 0.300NO3 :                     PHOTOL(59);     {2014/05/23; Eastham2014;
JMAO,SDE}
RCHO + hv = ETO2 + HO2 + CO :              PHOTOL(70);
ACET + hv = MCO3 + MO2 :                   PHOTOL(76);
ACET + hv = 2.000MO2 + CO :                PHOTOL(77);
MEK + hv = 0.850MCO3 + 0.850ETO2 +
 0.150MO2 + 0.150RCO3 + MEKZ :             PHOTOL(69);
KET + hv = 0.850MCO3 + 0.850ETO2 +
 0.150MO2 + 0.150RCO3 :                    PHOTOL(69);     {2018/07/16; Speciating C5 Ketone;
JFB}
GLYC + hv = 0.900CH2O + 1.730HO2 + CO +
 0.070OH + 0.100MOH :                      PHOTOL(68);     {2014/05/23; Eastham2014;
JMAO,SDE}
GLYX + hv = 2.000HO2 + 2.000CO :           PHOTOL(72);
GLYX + hv = H2 + 2.000CO :                 PHOTOL(73);
GLYX + hv = CH2O + CO :                    PHOTOL(74);
MGLY + hv = MCO3 + CO + HO2 :              PHOTOL(71);
MVK + hv = PRPE + CO :                     PHOTOL(63);
MVK + hv = MCO3 + CH2O + CO + HO2 :        PHOTOL(64);
MVK + hv = MO2 + RCO3 :                    PHOTOL(65);     {2014/05/23; Eastham2014;
JMAO,SDE}
MACR + hv = CO + HO2 + CH2O + MCO3 :       PHOTOL(66);     {2014/05/23;
Eastham2014; JMAO,SDE}
HAC + hv = MCO3 + CH2O + HO2 :             PHOTOL(75);
INPN + hv = OH + HO2 + RCHO + NO2 :        PHOTOL(78);
PRPN + hv = OH + HO2 + RCHO + NO2 :        PHOTOL(79);
ETP + hv = OH + HO2 + ALD2 :               PHOTOL(80);
RA3P + hv = OH + HO2 + RCHO :              PHOTOL(81);
RB3P + hv = OH + HO2 + ACET :              PHOTOL(82);
R6P + hv = OH + HO2 + RCHO :               PHOTOL(83); {2019/11/21; Speciate Alk4; JFB}
IBP + hv = OH + HO2 + RCHO :               PHOTOL(83); {2019/11/21; Speciate Alk4; JFB}
NBP + hv = OH + HO2 + RCHO :               PHOTOL(83); {2019/11/21; Speciate Alk4; JFB}
IPP + hv = OH + HO2 + RCHO :               PHOTOL(83); {2019/11/21; Speciate Alk4; JFB}
NPP + hv = OH + HO2 + RCHO :               PHOTOL(83); {2019/11/21; Speciate Alk4; JFB}
PP + hv = OH + HO2 + ALD2 + CH2O :         PHOTOL(84);
RP + hv = OH + HO2 + ALD2 :                PHOTOL(85);
RIPA + hv = 0.985OH + 0.985HO2 +
 0.710CH2O + 0.425MVK + 0.285MACR +
 0.275HC5 + 0.005LVOC :                    PHOTOL(86);     {2017/07/14;
KRT,JAF,CCM,EAM,KHB,RHS}
RIPB + hv = 0.985OH + 0.985HO2 +
```

```
 0.710CH2O + 0.425MVK + 0.285MACR +
 0.275HC5 + 0.005LVOC :                PHOTOL(86);     {2017/07/14;
KRT,JAF,CCM,EAM,KHB,RHS}
RIPD + hv = 0.985OH + 0.985HO2 +
 0.710CH2O + 0.425MVK + 0.285MACR +
 0.275HC5 + 0.005LVOC :                PHOTOL(86);     {2017/06/15;
KRT,JAF,CCM,EAM,KHB,RHS}
IAP + hv = OH + HO2 + 0.670CO + 0.190H2 +
 0.360HAC + 0.260GLYC + 0.580MGLY :        PHOTOL(87);
ISNP + hv = OH + HO2 + RCHO + NO2 :        PHOTOL(88);
VRP + hv = OH + 0.300HO2 + 0.300CH2O +
 0.700MCO3 + 0.700GLYC + 0.300MGLY :       PHOTOL(89);
MRP + hv = OH + HO2 + HAC + 0.500CO +
 0.500CH2O :                           PHOTOL(90);
MAOP + hv = OH + CH2O + MCO3 :             PHOTOL(91);
R6N2 + hv = NO2 + 0.320ACET + 0.0019MEK +
 0.180MO2 + 0.270HO2 + 0.320ALD2 +
 0.130RCHO + 0.050A3O2 + 0.180B3O2 +
 0.320ETO2 + 0.171KET :                PHOTOL(98); {2019/11/21; Speciate Alk4; JFB}
IBN2 + hv = NO2 + 0.415ACET +
 0.180MO2 + 0.270HO2 + 0.415ALD2 +
 0.130RCHO + 0.050A3O2 + 0.180B3O2 +
 0.320ETO2 :                           PHOTOL(98); {2019/11/21; Speciate Alk4; JFB}
NBN2 + hv = NO2 + 0.320ACET + 0.190MEK +
 0.180MO2 + 0.270HO2 + 0.320ALD2 +
 0.130RCHO + 0.050A3O2 + 0.180B3O2 +
 0.320ETO2 :                           PHOTOL(98); {2019/11/21; Speciate Alk4; JFB}
IPN2 + hv = NO2 + 0.320ACET + 0.019MEK +
 0.180MO2 + 0.270HO2 + 0.320ALD2 +
 0.130RCHO + 0.050A3O2 + 0.180B3O2 +
 0.320ETO2 + 0.171KET :                PHOTOL(98); {2019/11/21; Speciate Alk4; JFB}
NPN2 + hv = NO2 + 0.320ACET + 0.190KET +
 0.180MO2 + 0.270HO2 + 0.320ALD2 +
 0.130RCHO + 0.050A3O2 + 0.180B3O2 +
 0.320ETO2 :                           PHOTOL(98); {2019/11/21; Speciate Alk4; JFB}
IR4N2 + hv = NO2 + 0.320ACET + 0.190KET +
 0.180MO2 + 0.270HO2 + 0.320ALD2 +
 0.130RCHO + 0.050A3O2 + 0.180B3O2 +
 0.320ETO2 :                           PHOTOL(98);     {2018/07/16; Speciating C5 Ketone; JFB}
MAP + hv = OH + MO2 :                      PHOTOL(99);
MACRN + hv = NO2 + HAC + MGLY +
 0.500CH2O + HO2 + 0.500CO :               PHOTOL(92);     {2013/03/22; Paulot2009;
FP,EAM,JMAO,MJE}
MVKN + hv = GLYC + NO2 + MCO3 :            PHOTOL(93);     {2013/03/22; Paulot2009;
FP,EAM,JMAO,MJE}
```

```
ISOPNB + hv = HC5 + NO2 + HO2 :          PHOTOL(94);     {2013/03/22; Paulot2009;
FP,EAM,JMAO,MJE}
Br2 + hv = 2.000Br :                     PHOTOL(23);     {2012/06/07; Parrella2012; JPP}
BrO + hv = Br + O3 :                     PHOTOL(28);     {2014/02/03; Eastham2014; SDE}
HOBr + hv = Br + OH :                    PHOTOL(32);     {2012/06/07; Parrella2012; JPP}
BrNO3 + hv = Br + NO3 :                  PHOTOL(29);     {2012/06/07; Parrella2012; JPP}
BrNO3 + hv = BrO + NO2 :                 PHOTOL(30);     {2012/06/07; Parrella2012; JPP}
BrNO2 + hv = Br + NO2 :                  PHOTOL(31);     {2012/06/07; Parrella2012; JPP}
CHBr3 + hv = 3.000Br :                   PHOTOL(56);     {2012/06/07; Parrella2012; JPP}
CH2Br2 + hv = 2.000Br :                  PHOTOL(55);     {2014/02/03; Eastham2014; SDE}
CH3Br + hv = MO2 + Br :                  PHOTOL(50);     {2014/02/03; Eastham2014; SDE}
CH3Cl + hv = MO2 + Cl :                  PHOTOL(43);     {2014/02/03; Eastham2014; SDE}
CH2Cl2 + hv = 2.000Cl :                  PHOTOL(45);     {2017/09/22;
Sherwen2016b;TS,JAS,SDE}
BrCl + hv = Br + Cl :                    PHOTOL(33);     {2014/02/03; Eastham2014; SDE}
Cl2 + hv = 2.000Cl :                     PHOTOL(22);     {2014/02/03; Eastham2014; SDE}
ClO + hv = Cl + O3 :                     PHOTOL(27);     {2014/02/03; Eastham2014; SDE}
OClO + hv = ClO + O3 :                   PHOTOL(25);     {2014/02/03; Eastham2014; SDE}
Cl2O2 + hv = Cl + ClOO :                 PHOTOL(26);     {2014/02/03; Eastham2014; SDE}
ClNO2 + hv = Cl + NO2 :                  PHOTOL(21);     {2014/02/03; Eastham2014; SDE}
ClNO3 + hv = Cl + NO3 :                  PHOTOL(19);     {2014/02/03; Eastham2014; SDE}
ClNO3 + hv = ClO + NO2 :                 PHOTOL(20);     {2014/02/03; Eastham2014; SDE}
HOCl + hv = Cl + OH :                    PHOTOL(24);     {2014/02/03; Eastham2014; SDE}
ClOO + hv = Cl + O2 :                    PHOTOL(102);    {2014/02/03; Eastham2014; SDE}
I2 + hv = 2.000I :                       PHOTOL(115);    {2017/09/22; Sherwen2016b;TS,JAS,SDE}
HOI + hv = I + OH :                      PHOTOL(116);    {2017/09/22;
Sherwen2016b;TS,JAS,SDE}
IO + hv = I + O3 :                       PHOTOL(117);    {2017/09/22;
Sherwen2016b;TS,JAS,SDE}
OIO + hv = I + O2 :                      PHOTOL(118);    {2017/09/22;
Sherwen2016b;TS,JAS,SDE}
INO + hv = I + NO :                      PHOTOL(119);    {2017/09/22;
Sherwen2016b;TS,JAS,SDE}
IONO + hv = I + NO2 :                    PHOTOL(120);    {2017/09/22;
Sherwen2016b;TS,JAS,SDE}
IONO2 + hv = I + NO3 :                   PHOTOL(121);    {2017/09/22;
Sherwen2016b;TS,JAS,SDE}
I2O2 + hv = I + OIO :                    PHOTOL(122);    {2017/09/22;
Sherwen2016b;TS,JAS,SDE}
CH3I + hv = I :                          PHOTOL(123);    {2017/09/22; Sherwen2016b;TS,JAS,SDE}
CH2I2 + hv = 2.000I :                    PHOTOL(124);    {2017/09/22;
Sherwen2016b;TS,JAS,SDE}
CH2ICl + hv = I + Cl :                   PHOTOL(125);    {2017/09/22;
Sherwen2016b;TS,JAS,SDE}
CH2IBr + hv = I + Br :                   PHOTOL(126);    {2017/09/22;
Sherwen2016b;TS,JAS,SDE}
```

I2O4 + hv = 2.000OIO : PHOTOL(127); {2017/09/22; Sherwen2016b;TS,JAS,SDE}
I2O3 + hv = OIO + IO : PHOTOL(128); {2017/09/22; Sherwen2016b;TS,JAS,SDE}
IBr + hv = I + Br : PHOTOL(129); {2017/09/22; Sherwen2016b;TS,JAS,SDE}
ICl + hv = I + Cl : PHOTOL(130); {2017/09/22; Sherwen2016b;TS,JAS,SDE}
MPN + hv = CH2O + NO3 + HO2 : PHOTOL(104); {2012/02/12; Browne2011; ECB}
MPN + hv = MO2 + NO2 : PHOTOL(105); {2012/02/12; Browne2011; ECB}
ISOPND + hv = HC5 + NO2 + HO2 : PHOTOL(95); {2013/03/22; Paulot2009; FP,EAM,JMAO,MJE}
PROPNN + hv = CH2O + NO2 + CO + MO2 : PHOTOL(96); {2013/03/22; Paulot2009; FP,EAM,JMAO,MJE}
ATOOH + hv = OH + CH2O + MCO3 : PHOTOL(97); {2013/03/22; Paulot2009; FP,EAM,JMAO,MJE}
PIP + hv = RCHO + OH + HO2 : PHOTOL(106); {2017/03/23; Fischer2014; EVF}
IPMN + hv = 0.600IMAO3 + 0.600NO2 +
0.400CO2 + 0.400CH2O + 0.400MCO3 +
0.400NO3 : PHOTOL(107); {2017/06/15; Marais2016; EAM}
ETHLN + hv = NO2 + CH2O + CO + HO2 : PHOTOL(108); {2017/06/15; Marais2016; EAM}
DHDC + hv = MGLY + GLYX + 2.000OH : PHOTOL(109); {2017/07/14; Crounse2012; KRT,JAF,CCM,EAM,KHB,RHS}
HPALD + hv = 0.500MGLY + 0.390HAC +
0.110GLYC + 0.110MCO3 + 1.890CO +
0.890HO2 + 2.000OH : PHOTOL(110); {2017/07/14; Peeters2014; KRT,JAF,CCM,EAM,KHB,RHS}
ISN1 + hv = NO2 + HO2 + 0.500GLYC +
0.250GLYX + 0.250MGLY + CH2O + 0.500HAC : PHOTOL(111); {2017/07/14; Muller2014; KRT,JAF,CCM,EAM,KHB,RHS}
MONITS + hv = KET + NO2 : PHOTOL(112); {2017/07/14; Browne2014; KRT,JAF,CCM,EAM,KHB,RHS} {2018/07/16; Speciating C5 Ketone; JFB}
MONITU + hv = RCHO + NO2 : PHOTOL(113); {2017/07/14; Browne2014; KRT,JAF,CCM,EAM,KHB,RHS}
HONIT + hv = HAC + NO2 : PHOTOL(114); {2017/07/14; Browne2014; KRT,JAF,CCM,EAM,KHB,RHS}